DEVELOPMENT OF A RECYCLED COMPRESSION MOULDING COMPOUND

Adam W. Smith

Doctor of Philosophy

Department of Mechanical Engineering

McGill University
Montreal, Québec
March 2021

A thesis submitted to McGill University in partial fulfillment of the requirements of the degree of Doctor of Philosophy

For Tarah, Alistair and Kingsley

TABLE OF CONTENTS

ACKNOWLEDGEMENTS

Completing this work has taken me the better part of 8 years and so you can imagine that the list of people to whom I owe thanks is very long. It goes without saying that none of this would have been possible without the guidance of my supervisor Prof. Pascal Hubert. His unwavering support of me as a developing researcher and as a young father has meant the world to me and my family. I would also like to thank Lucie Riffard for being such a wonderful colleague and friend – I will cherish the memories of failed strain sweeps and broken load cells forever.

When I first joined the McGill Structures and Composite Materials Laboratory (SCML), I was part of the NSERC-funded G8 project that focused on making composite manufacturing more sustainable. I would like to thank the students and researchers from McGill, the University of Southern California, the University of Bristol and the Technical University of Munich that were involved in this project for being such great teammates and for making the composites learning curve truly enjoyable. Special mention goes to my desk mates Steven Payette, Stella Marissa Hughes and Marc Palardy-Sim.

Much of what I have presented here was made possible by the excellent work of Gilles-Philippe Picher-Martel, Marina Selezneva, Dominic LeBlanc, Benoit Landry and Caroline Collins. I owe them all a great debt for developing a versatile compression moulding apparatus and for generating top notch data upon which I built much of my own analysis and discussion.

I consider myself very lucky to have been able to collaborate with Daniel Poirier and the team of engineers, technicians and interns at the centre de développement des composites du Québec (CDCQ). I will always be grateful for how generous they were with their time and expertise.

As with any workplace, McGill and the SCML are both defined by the people that work there. I would like to thank Mathieu Beauchesne, Andreas Hoffman, Antonio (Tony) Micozzi, Lydia Dyda, Pascal Bourseguin, Jean-Philipe Guay and David Speller for embodying the spirit of McGill innovation and for being decent people. I would like to acknowledge the work of undergraduates Jasmine Tacneng, Matthias Rivollier, Elie Hymowitz, Ali Al-Taher, Adeola Odusanya and Celia Hameury. The process development and exploratory research you performed

were instrumental in helping me to create a coherent and mature story. I would also like to thank Mathieu Préau, Julieta Barroeta-Robles, Sanesh Iyer, Louis Grou and my other friends and peers in the SCML for their companionship. In particular, I would like to extend my sincere thanks to James Kratz and to the late Timotei Centea for being my mentors early on.

I must acknowledge the financial and in-kind support of the McGill Engineering Doctoral Award, the Natural Sciences and Engineering Research Council of Canada (NSERC), the Research Center for High Performance Polymer and Composite Systems (CREPEC), the Werner Graupe Distinguished Chair in Automation Engineering, Bell Flight, Bombardier Aerospace, and the Solvay Group.

Finally, I want to thank my parents for their love and for the sacrifices they have made over the years so that I could have so many opportunities to be successful. I also want to thank my in-laws for their encouragement and never-ending support. Lastly, thank you to my beautiful wife Tarah – you are my unwavering source of love and strength.

CONTRIBUTIONS OF THE AUTHOR

The author of this thesis has performed all of the work presented therein, with the following exceptions:

Chapter 4

The experiment designed to test the validity of the presented Cycom® 5276-1 cure kinetic model was performed by Nathan Hostettler as part of the exchange required for his Master en Science Matériaux from the École polytechnique fédérale de Lausanne (EPFL).

Chapter 5

A number of the flow-compaction experiments from this chapter were carried out by Jasmine Tacneng as part of her undergraduate research project (SURE) within the department of mechanical engineering.

Chapter 6

FT-IR experiments were performed by Nathan Hostettler (see above). Tack experiments and complementary rheometry were performed by Andreas Endruweit and Gabriel Choong from the University of Nottingham.

Chapter 7 & 8

Slitting, staging and cutting of prepreg offcuts was carried out by Celia Hameury, Farnaz Mazaheri Karvandian, David-Michael Phillips, Sidharth Sarojini Narayana, Lucas Marrone, Maxyme Simoneau and myself. The compression moulding of large flat plates and subsequent specimen cutting was carried out by Maxyme Simoneau. Specimen testing was performed by Mathieu Lapointe and Jean-Philippe Harvey of the CDCQ.

The author gratefully acknowledges these contributions.

ABSTRACT

Now more than ever, there is need for sustainable innovation in the composites industry. The next 10 years will likely see continued growth of composites within commercial aircraft and other transportation vehicles, resulting in alarming volumes of waste for which we do not have an adequate recycling infrastructure. The majority of structural aerospace parts are currently manufactured using carbon fibre textiles pre-impregnated with thermoset polymer matrix. These "prepregs" are typically cured in large-scale autoclaves, which is a process that represents a daunting cost to original equipment manufacturers. Furthermore, the cutting of prepreg templates, or plies, prior to layup generates large quantities of uncured prepreg offcuts which are nearly pristine when compared to other forms of composite waste. Disappointingly, these uncured offcuts are routinely treated in the same way as cured forms of composite waste, as they are sent to the landfill or pyrolyzed so that the carbon fibre can be reclaimed. The latter approach ignores the value of the uncured resin, produces a recycled fibre with reduced strength and bonding properties, and requires the introduction of a new resin and sizing for re-manufacturing. This thesis describes, in 5 sections, the development of a novel recycling methodology in which the behaviour of woven aerospace offcuts is tailored through elevated-temperature staging to create a highly versatile recycled prepreg moulding compound (rPMC).

In the first section, resin extracted from recovered prepreg was characterized using differential scanning calorimetry (DSC) and rheometry. Phenomenological models for cure, viscosity, and glass transition temperature (T_g) were then fit to the experimental data obtained.

Secondly, a compression moulding process map was developed using one-dimensional flow-compaction tests carried out at various speeds and for increasing levels of prepreg staging. The results showed that resin viscosity and moulding speed are key factors in determining what flow mechanisms are excited.

Thirdly, the effect of offcut state variability on the flow tailoring process was investigated. DSC, gel permeation chromatography, Fourier transform infrared spectroscopy, and tack testing were used to measure changes in resin degree-of-cure caused by progressively longer room-temperature ageing times. Each method was ranked based on the amount of material, time, and

money required to perform a baseline characterization. Furthermore, it was concluded that knowledge of the resin's initial degree-of-cure is essential for proper flow tailoring via staging.

Fourthly, two batches of rPMC with different fibre architectures were produced following the proposed staging methodology. These batches were used to manufacture two kinds of geometrically complex demonstrator panels at 140 °C in under 1 hour. The minimum required filling pressure for both material-part combinations was obtained by varying the moulding pressure from 1 – 9 MPa. A set of demonstrators was also made using lightly staged offcuts to simulate moulding with recently expired materials. Finally, the preliminary results of two different material hybridization trials were presented.

Lastly, an exploratory assessment of the rPMC's mechanical properties was carried out. ASTM standard tests for tensile, compressive, flexural, and short-beam strength properties were performed on plates manufactured using plain-weave and eight-harness satin offcuts. The results were then compared with the properties of some key commercial moulding compounds and metals showing that the rPMCs exhibit promising specific stiffnesses and strengths, despite featuring relatively small strands.

RÉSUMÉ

Plus que jamais, l'industrie des composites a besoin d'innovation durable. Les 10 prochaines années verront croître la quantité de matériaux composites utilisée dans les avions commerciaux et autres véhicules de transport. Ceci entraînera des volumes alarmants de déchets pour lesquels nous ne possédons pas d'infrastructure de recyclage assez mature. La majorité des pièces aérospatiales structurelles sont présentement fabriquées à l'aide de textiles en fibre de carbone préimprégnés d'une matrice polymère thermodurcissable. Ces «préimprégnés» sont généralement cuits dans une autoclave à grande échelle, ce qui représente un coût considérable pour les fabricants d'équipement d'origine. De plus, la découpe de gabarits préimprégnés génère de grandes quantités de retailles non polymérisées qui ont une valeur plus élevée comparée à d'autres formes de déchets composites. Ces retailles sont régulièrement traitées de la même manière que les déchets polymérisés: elles sont envoyées à la décharge ou pyrolysées afin que la fibre puisse être récupérée. Cette dernière approche ne tient pas compte de la valeur de la matrice, produit une fibre recyclée avec des propriétés réduites, et nécessite l'introduction d'une nouvelle résine et d'un nouvel encollage. Cette thèse décrit, en 5 sections, le développement d'une nouvelle méthodologie de recyclage grâce à laquelle le comportement des préimprégnés tissés est modulé en utilisant un conditionnement à température élevée; un composé de moulage préimprégné recyclé est ainsi créé.

Dans la première section, la résine extraite des retailles tissées a été caractérisée par analyse calorimétrique différentielle (DSC) et rhéométrie. Des modèles phénoménologiques de polymérisation, de viscosité et de température de transition vitreuse (T_g) ont ensuite été ajustés aux données expérimentales.

Une cartographie du processus a ensuite été développée à l'aide d'essais de compaction-écoulement 1-D effectués à différentes vitesses et pour des niveaux croissants de conditionnement. Les résultats ont montré que la viscosité de la résine et la vitesse de moulage sont des facteurs clés pour déterminer quels mécanismes d'écoulement sont en jeu.

Troisièmement, l’effet de la variabilité du taux de polymérisation sur l’adaptation du comportement compaction-écoulement a été étudié. La DSC, la chromatographie par perméation de gel, la spectroscopie infrarouge à transformée de Fourier et les tests d’adhésion ont été utilisés

pour mesurer les changements du taux de polymérisation de la résine causée par le vieillissement à température ambiante. Chaque méthode a été classée en fonction de la quantité de matière, temps, et fonds nécessaires pour compléter une caractérisation. Il a été conclu que la connaissance du taux de polymérisation initial est essentielle pour une adaptation appropriée des retailles.

Par la suite, la méthodologie de conditionnement a été utilisée pour produire deux lots de rPMC avec différentes architectures de fibre. Ces lots ont permis de fabriquer deux types de panneaux de démonstration à géométrie complexe à 140 °C en moins d'une heure. La pression de remplissage minimale requise pour les deux combinaisons matériau-pièce a été obtenue en faisant varier la pression de moulage de 1 à 9 MPa. Des démonstrateurs ont été réalisés en utilisant des retailles légèrement conditionnées afin de simuler un moulage avec des matériaux récemment expirés. Enfin, les résultats préliminaires de deux essais d'hybridation ont été présentés.

Finalement, une évaluation exploratoire des propriétés mécaniques du rPMC a été réalisée. En suivant les normes ASTM appropriées, des tests de traction, compression, flexion et cisaillement ont été effectués sur des plaques fabriquées à partir de retailles de satin huit-harness et plain-weave. En comparant avec les propriétés de certains composés de moulage commerciaux, les rPMC, bien que constituées de petits brins, présentent des raideurs et des résistances spécifiques prometteuses.

LIST OF TABLES

LIST OF FIGURES

LIST OF SYMBOLS & ABBREVIATIONS

Symbol	Designation
$[\ ]_S$	Denotes symmetric layup notation
$[\ ]_T$	Denotes total layup notation
α	Degree-of-cure
α_0	Initial degree-of-cure
α_{C0}	Critical degree-of-cure at absolute zero
α_{CT}	Rate of increase of critical degree-of-cure with temperature
α_{gel}	Degree-of-cure at gelation
α_{max}	Final degree-of-cure
α_{peak}	Degree-of-cure at the peak of the degree-of-cure vs. cure rate curve
α_{staged}	Post-staging degree-of-cure
α_t	Degree-of-cure for a given out-time
α_x	As-received degree-of-cure
β	Prepreg bulk factor
Δ	Denotes change of some quantity
Δd	Period of tack signal oscillation
$\Delta d'$	Plain weave fabric tow spacing
$\frac{\partial}{\partial t}$	Denotes a time rate of change
$\frac{\partial}{\partial x}$	Denotes a spatial rate of change in the x-direction
$\frac{\partial \alpha}{\partial t}$	Rate of polymerisation/curing (cure rate)
$\left(\frac{\partial \alpha}{\partial t}\right)_{peak}$	Cure rate at the maximum of the degree-of-cure vs. cure rate curve
$\frac{\partial T}{\partial t}$	Time rate of change of temperature
$\frac{\partial T}{\partial x}$	Spatial rate of change of temperature in the x-direction
ε	Specimen longitudinal strain
ε_1, ε_2	Strain gauge measurement from each side of a compressive specimen

ε_f	Specimen flexural strain
ε_t	Specimen transverse strain
η	Resin viscosity (dynamic)
η_0	Initial resin viscosity
η_i	Rheological Arrhenius term
η_{min}	Minimum resin viscosity
η_{target}	Target resin viscosity (staging)
λ	T_g model fitting parameter (Section 4.5.2), beam slenderness ratio (Section 8.5)
$\lambda_{Gel\text{-}Point}$	T_g model fitting parameter obtained using the ${}_{gel}T_g$
λ_{Ratio}	T_g model fitting parameter obtained using the ratio of initial and final T_g
ν	Poisson's ratio
ρ	Density
ρ_R	Resin density
σ	Specimen stress
σ_f	Specimen flexural stress
σ_{fM}	Flexural strength
σ_i	Instantaneous specimen stress
σ_{max}	Maximum normal stress experienced during a flow-compaction experiment
a_T	TTS shift factor
a_{T_g}	TTS shift factor using T_g as the reference temperature
A	Specimen cross-sectional area
A_i	Cure kinetic Arrhenius pre-exponential factor
$A_{\eta,i}$	Rheological Arrhenius pre-exponential factor
b	Flexural and short beam specimen width
B_y	Compressive specimen bending (buckling analysis)
C_1, C_2	WLF empirical fitting constants
C_P	Specific heat capacity
$C_{P,R}$	Resin specific heat capacity
$CV\%$	Coefficient of variation
d	Flexural specimen depth
D	Diffusion factor (Section 4.3.2), maximum beam deflection (Section 8.4)

$Đ$	Dispersity
e_x^S	Final flow-compaction specimen shear strain
E	Tack TTS activation energy coefficient
E_a	Cure kinetic activation energy
E_B	Flexural modulus of elasticity
E^c	Compressive modulus of elasticity
E^{chord}	Tensile chord modulus of elasticity
$E_{\eta,i}$	Rheological activation energy coefficient
F_{cr}	Theoretical Euler-buckling stress
F^{cu}	Compressive strength
F_{diss}	Force needed to overcome dissipative effects
F_{peel}	Total peel force
F^{sbs}	Short beam strength
F_t	Tack force
$F_{t,max}$	Maximum tack force
F^{tu}	Ultimate tensile strength
G'	Storage modulus
G''	Loss modulus
G_{xz}	Through-thickness interlaminar shear modulus
${}_{gel}T_g$	Temperature at which resin gelation and vitrification occur simultaneous
h	Compressive and short beam specimen gauge thickness
h_0	Initial flow-compaction specimen height
h_0'	Post preload flow-compaction specimen height
H_R	Total heat/enthalpy of reaction
I	Compressive specimen cross-sectional moment of inertia
k	Thermal conductivity
K_c	Cure rate prediction without diffusion considerations
K_e	Experimental cure rate
K_i	Cure kinetic Arrhenius coefficient
l_g	Compressive specimen gauge length
L	Flexural specimen support span

L_0	Initial flow-compaction specimen length
$\overline{L_0}$	Average initial flow-compaction specimen length
L_c	Critical fibre length
L_f	Final flow-compaction specimen length
m	Tangent slope of the elastic portion of the flexural load-deflection curve
m_0	Initial flow-compaction specimen mass
m_i, n_i	Cure kinetic reaction orders
n	Number of specimens tested
M_p	Peak of the molecular weight distribution
M_n	Number-average molecular weight
M_w	Weight-average molecular weight
M_z	"Z" average molecular weight
P	Instantaneous flexural load
P_f	Maximum compressive load at failure
P_i	Instantaneous specimen tensile load
P_m	Maximum testing load during a short beam strength test
P_{max}	Load at tensile specimen failure
r	Tack peel/feed rate
r_{max}	Feed/peel rate corresponding to maximum tack
R	Universal gas constant = 8.314 kJ $kmol^{-1}$ K^{-1}
R^2	Coefficient of determination
S	Heat generation/source term
S_{n-1}	Standard deviation
T	Temperature
t_{flow}	Flow-compaction flow window
T_g	Glass transition temperature
$T_{g,0}$	Initial glass transition temperature
$T_{g,\infty}$	Ultimate glass transition temperature
T_{gel}	Temperature at which resin gelation occurs
t_{gel}	Time at which resin gelation occurs
t_{out}	Out-time

$T_{g,staged}$	Post-staging glass transition temperature
$T_{g,x}$	As-received glass transition temperature
t_{min}	Time at minimum viscosity
T_{ref}	TTS reference temperature
V_f	Fibre volume fraction/content
w	Gaussian distribution width parameter (Section 6.2.5), compressive specimen gauge width (Section 8.5)
W_0	Initial flow-compaction specimen width
$\overline{W_0}$	Average initial flow-compaction specimen width
$\bar{x}$	Average property value
x_{max}	Maximum property value
x_{min}	Minimum property value
Abbreviation	**Meaning**
γ-BL	γ-Butyrolactone
5HS	5 harness satin
8HS	8 harness satin
ASTM	American Society for Testing Materials
ATR	Attenuated total reflectance
BMC	Bulk moulding compound
CF	Carbon fibre
CFRP	Carbon fibre reinforced polymer
CTTs	Carbon fibre tape-reinforced thermoplastics
DDS	Diaminodiphenyl sulfone
DGEBA	Diglycidylether of bisphenol A
DICY	Dicyandiamide
DLF	Discontinuous long fibre
DMA	Dynamic mechanical analysis/analyzer
DSC	Differential scanning calorimetry/calorimeter
FEP	Fluorinated ethylene propylene
FT-IR	Fourier transform infrared spectroscopy
GF	Glass fibre
GPC	Gel permeation chromatography

ILSS	Interlaminar shear strength
LCA	Life cycle analysis
LDF	Long discontinuous fibre
LVDT	Linear variable differential transformer
MIR	Medium infrared range
MW	Molecular weight
MWD	Molecular weight distribution
NCAMP	National Center for Advanced Materials Performance
NR	Neat resin
PEEK	Poly-ether-ether-ketone
PEI	Polyethylenimine
PID	Proportional-integral-derivative
PMMA	Poly(methyl methacrylate)
PPS	Polyphenylene sulfide
PTFE	Polytetrafluoroethylene
PW	Plain weave
QI	Quasi-isotropic
ROS	Randomly oriented strands
rPMC	Recycled prepreg moulding compound
SBS	Short beam strength
SMC	Sheet moulding compound
TMA	Thermo-mechanical analysis/analyzer
TGDDM	Tetraglycidyl-4,4'-diaminodiphenyl methane
TGMDA	Tetraglycidyl methylene dianiline
TPRC	Thermoplastic composites research centre
TTS	Time-temperature-superposition
UACS	Unidirectionally arrayed chopped strands
UD	Unidirectional
UT	Unidirectional tape
vCMC	Virgin compression moulding compound
WLF	Williams-Landel-Ferry

1 INTRODUCTION

1.1 A Growing Industry

The last decade has seen some of the most composite-intensive aircraft in history enter the commercial market. Wide-body programs like Boeing's 787 Dreamliner (first flight: Dec. 15, 2009 [1]) and Airbus' A350 (first flight: Jun. 14, 2013 [2]) were the first non-military aircraft to boast structural composite contents greater than 50 % [3]. Narrow-body programs like Bombardier's C-series (first flight: Sept. 16, 2013 [4]) and the Irkut MC-21 (first flight: May 28, 2017 [5]) have followed suit with respective structural composite contents of 46 % [6] and 30 % [7]. Composite materials are also becoming more common in the automotive industry, where the use of carbon fibre reinforcements is no longer limited to high performance vehicles like those of Formula One [8]. The same is true of various sporting industries, in which amateur level hockey sticks [9], baseball bats [10], and bicycles [11] all feature large amounts of carbon fibre composites.

At the same time as composites are being used more in structural and semi-structural aerospace applications, the market research network CAPA (Center for Aviation) reports increases in annual commercial aircraft deliveries for 14 of 17 years from 2000 to 2017 (Figure 1-1). It then comes as no surprise that numerous sources [12-16] report an exponentially increasing trend in the demand for carbon fibre over the same time period. Waste streams produced by aerospace material suppliers and aerospace original equipment manufacturers are, therefore, likely to become saturated with carbon fibre and carbon fibre reinforced materials.

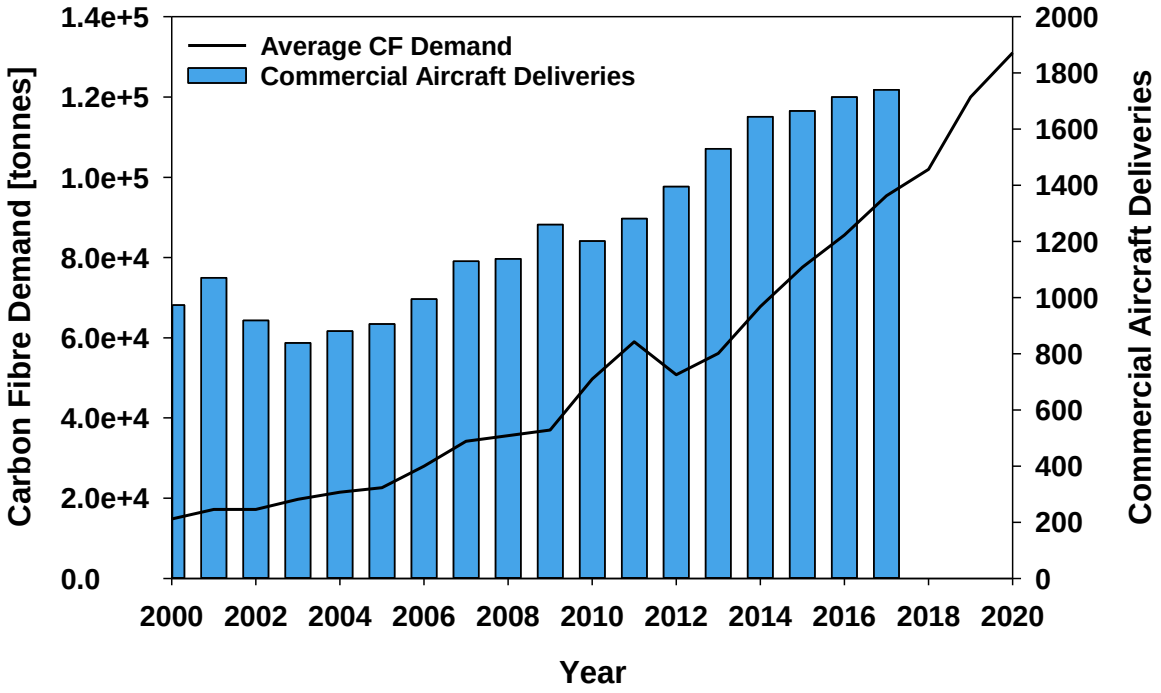

Figure 1-1. Average annual carbon fibre demand based on [12-16] and annual commercial aircraft deliveries reported by [17].

1.2 Uncured Prepreg Offcuts

Autoclave curing of prepregs is the most prevalent combination of process and material used to manufacture structural aerospace components. An autoclave's ability to maintain even part temperature during cure promotes uniform resin polymerization, which reduces non-uniform residual stress development. Elevated autoclave pressures ensure sufficient material consolidation and all but guarantee low levels of part porosity [18]. Contemporary prepregs feature relatively low-volatility resin systems in precisely controlled proportion with the reinforcing fibre, which provides excellent control over resin impregnation and final fibre volume fraction [19].

Despite these advantages, autoclave manufacturing is plagued by numerous cost-related factors which, cumulatively, limit its accessibility. Autoclaves represent an incredibly high non-recurring capital investment, as well as high running costs (e.g. nitrogen, energy for heating) which can easily exceed the initial value of the unit over its operational life [20, 21]. The production, handling and storage of prepregs make them one of the most expensive composite precursor materials available [22]. This cost is compounded by inefficient ply nesting patterns which lead to copious amounts of uncured prepreg waste (Figure 1-2) during the ply cutting phase of

manufacturing. This inefficiency is not a software limitation and is, instead, caused by restrictive production schedules, fixed prepreg roll widths, and limited material out-life. With ply cutter scrap rates reaching as high as 50 %, recycling of these uncured production offcuts remains an important aspect of improving the sustainability and economic appeal of this process [23, 24].

Figure 1-2. Uncured autoclave prepreg offcuts recovered from the ply-cutter of an aerospace original equipment manufacturer.

1.3 Composites Recycling

Until recently, composites recycling efforts have been restricted to academic investigations focused on treating the cured end-of-life waste that is expected to enter waste streams by 2040, as composites-intensive aircraft start being decommissioned [16]. Figure 1-3 provides the reader with an overview of the mechanical and thermochemical approaches to recycling that have already been studied and, in certain cases, commercialized (e.g. ELG Carbon Fibre's modified pyrolysis process [25]). The common thread running through each of these methods is the priority placed on fibre reclamation which typically results in the matrix being relegated to use as low-value chemical feedstock, filler or for energy recapture. Even the recycling of out-of-date prepreg rolls will generally involve some type of pyrolysis, followed by new resin impregnation.

Fibre reclamation methods may very well be the most efficient way to recycle end-of-life composite aircraft structures, given the high inherent value of carbon fibre. There should, however, be a more nuanced approach available for recycling of uncured production waste.

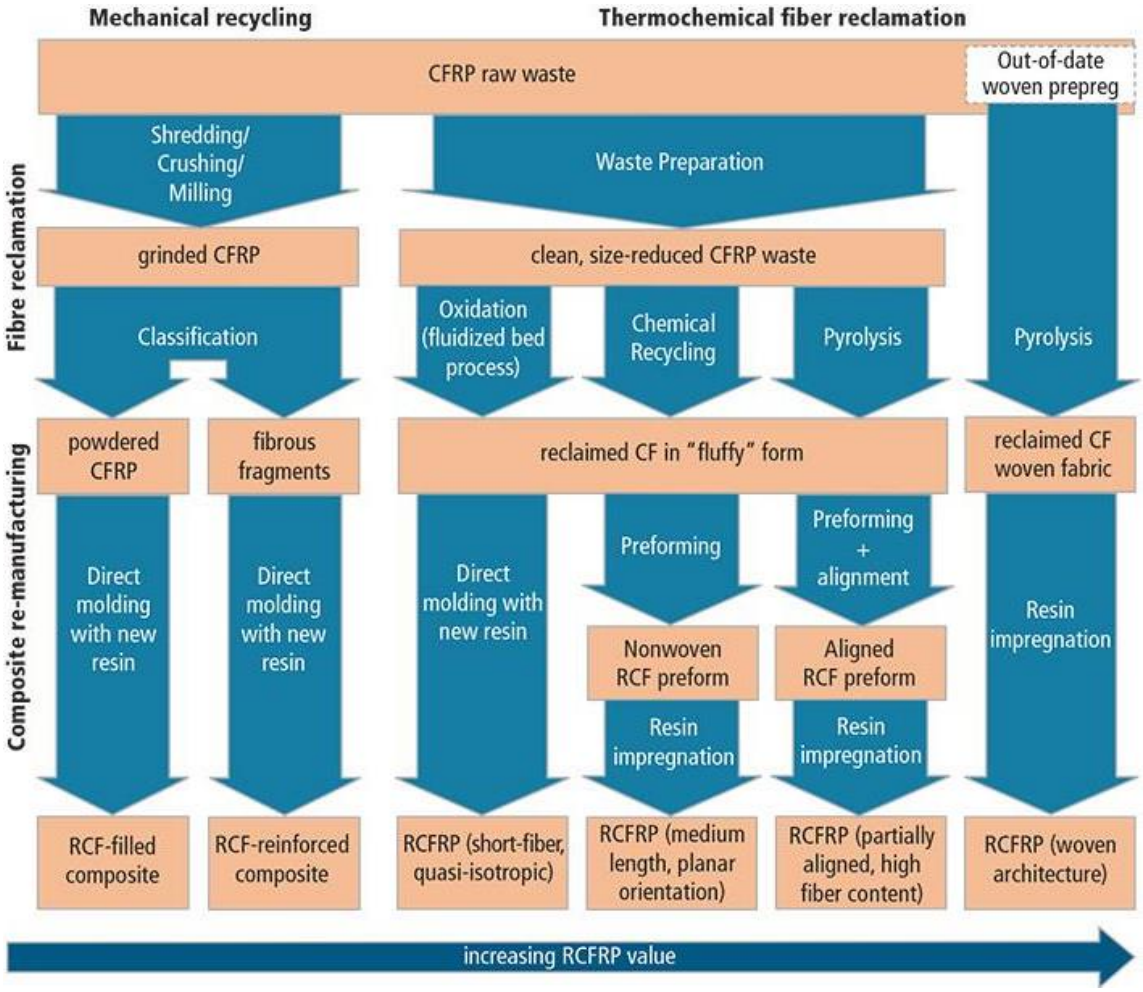

Figure 1-3. Overview of recycling technologies used to reclaim carbon fibre from CFRP waste and re-manufacture into recycled composites with increasing value [26].

1.4 A Recycled Prepreg Moulding Compound

The aim of this thesis is to demonstrate the feasibility of transforming uncured autoclave prepreg offcuts into a strand-based recycled prepreg moulding compound (rPMC) by carrying out the steps depicted in Figure 1-4. These steps include: (1) *waste inspection*, (2) a one-time *material characterization* including resin chemo-rheological and prepreg flow-compaction behaviours, (3) elevated temperature *staging*, and (4) *prepreg stranding*. This approach, referred to from this point onward as the *tailored staging method*, has several advantages when compared to pyrolysis, solvolysis, and other forms of fibre reclamation. First and foremost, there is no need to introduce a new resin system during re-manufacturing, nor be concerned with problems of resin-fibre compatibility. Second, thermochemical decomposition frequently causes a knock-down in the

fibre's mechanical properties due to fibre degradation and char deposition [27, 28]. Finally, tailored staging has the potential to be a much simpler approach to recycling, requiring no harsh chemical products, a more basic and non-specialized recycling infrastructure, and overall less energy consumption.

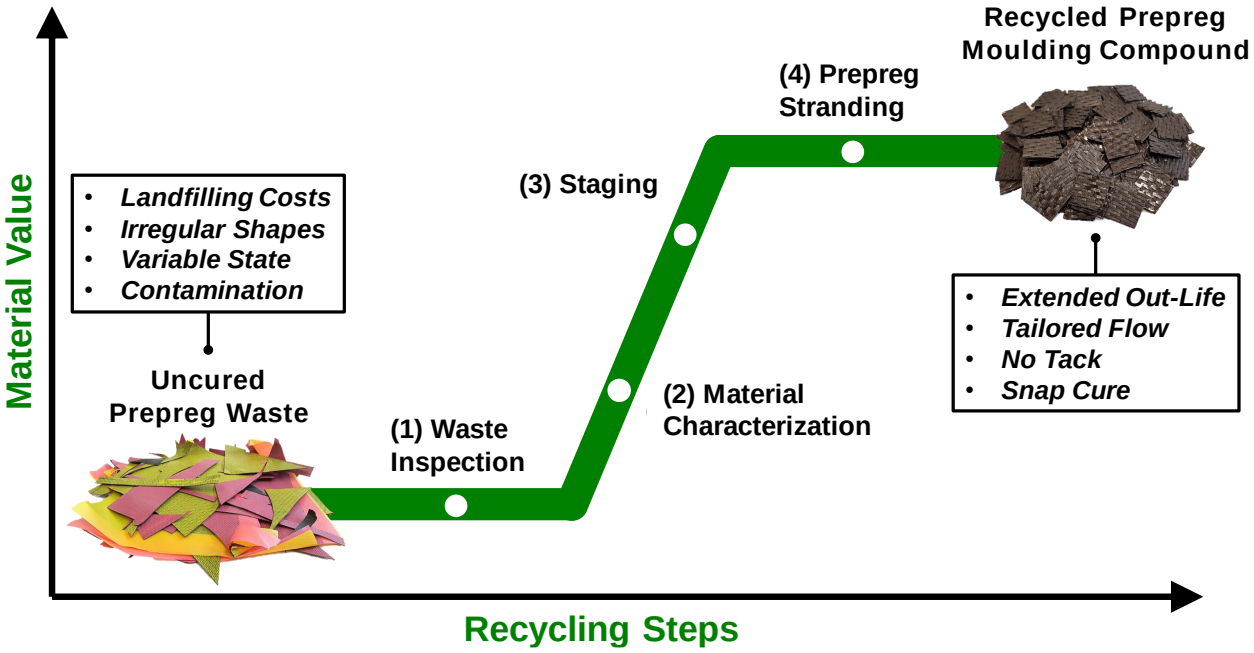

Figure 1-4. Schematic of the tailored staging method used to transform uncured autoclave prepreg offcuts into a recycled compression moulding compound.

1.5 Problem Statement

An rPMC must emulate certain characteristics of virgin compression moulding compounds (vCMCs) for it to be considered a viable alternative. Challenges, therefore, arise from the stark differences between commercially available vCMCs and autoclave prepreg systems. Standard vCMCs are used to produce geometrically challenging parts at high production rates with reliable mechanical properties [29]. This requires thermoset resins with short cure times, as well as relatively high moulding viscosities to promote coupled transport of fibre and resin through shear. Autoclave prepreg resins, on the other hand, are known for their long cure times and low processing viscosities which ensure complete fibre bed impregnation. Prepregs, in general, also feature high levels of tack which help to maintain adhesion between layers during layup.

The tailored staging method is a framework for modifying uncured prepreg offcuts, so that they behave more like a vCMC. Elevated temperature staging is used to increase the pre-gelation degree of cure of recovered offcuts, bringing about the desired changes in material behaviour. This includes increased moulding viscosities, reduced cure times, reduced tack for better handling, and increased room-temperature stability (extended out-life). A comprehensive understanding of prepreg constituent properties (e.g. cure, rheology, flow-compaction) and their relationship with compression moulding process parameters (e.g. temperature, pressure, mould closure rate) is vital in determining what staged degree of cure will yield the desired material response. Selection of appropriate staging parameters is further complicated by uncontrolled variations in offcut out-time, for which robust inspection techniques are needed.

1.6 Outline

This thesis is constructed as follows: the present chapter provides the reader with motivation and contextual information regarding composites recycling and the state of the aerospace industry. Chapter 2 presents a concise overview of the academic literature relevant to this topic and identifies areas where further study is needed. Chapter 3 explains the specific objectives of the thesis and outlines schematically how each of the chapters relates to them. Chapters 4 - 8 present the main findings of the thesis, while Chapter 9 summarizes its key contributions and recommends future work.

2
LITERATURE REVIEW

This chapter provides the reader with a concise review of the scientific literature pertaining to the recycling of fibre-reinforced polymer composites, as well as the processing and mechanical performance of long discontinuous fibre (LDF) materials. It summarizes the state-of-the-art in each area, identifies pertinent gaps, and proposes potential for expansion of knowledge.

2.1 Composites Recycling

The classification of fibre-reinforced polymer composites encompasses a broad range of materials in which any number of combinations of fibre type, reinforcement scale, and polymer type exist. Unsurprisingly, not all variations can be treated in the same way when it comes to recycling. Over the past 25 years, there have been a handful of review articles published that have, at their respective times, documented the state-of-the-art in composites recycling technology. In each case, the authors discuss *recycling methods*, which refers to processes in which waste composites are collected and treated to produce recycled precursor materials, and *re-manufacturing methods*, which refers to the fabrication of new composite parts using recycled precursors. Table 2-1 summarizes the recycling and re-manufacturing methods presented in each of the review articles found. This list was used as the starting point for the review presented here. Subsequent sections will discuss methods omitted, as well as some more recent commercial recycling efforts.

Table 2-1. Summary of relevant composites recycling review articles.

Year	Authors	Recycling Methods Discussed
1996	Henshaw *et al.* [30]	Pyrolysis, hydrolysis, regrind, energy recovery
2006	Pickering [31]	Mechanical recycling, combustion for energy recovery, fluidised bed process, pyrolysis
2011	Pimenta and Pinho [32]	Mechanical recycling, pyrolysis, fluidised bed, chemical solvolysis
2012	Yang *et al.* [33]	Mechanical recycling, thermal recycling, chemical recycling, re-melting (thermoplastic)
2015	Oliveux *et al.* [34]	Mechanical recycling, thermal processes, solvolysis

2.1.1 Mechanical Recycling

Mechanical recycling involves the physical breakdown of materials that feature either cured thermoset, or thermoplastic resins. Makenji [35] describes the steps of mechanical recycling as: waste collection, initial sorting, size reduction, additional separation, and preparation into a usable recycled material. While this framework appears consistently throughout the literature, the equipment and method used to carry out each step varies significantly. For example, Inoh *et al.* [36] and Perrin *et al.* [37] both performed size reduction operations on similar GF-reinforced SMCs. However, Inoh *et al.* [36] used a two step approach in which SMC waste was granulated using a screen classifier-type hammer mill, and then ground using an impact-board-type jet mill. Perrin *et al.* [37], on the other hand, employed consecutive grinding and sieving operations using a rotary cutter mill and progressively finer grids. Similar diversity exists for waste sorting, where material classification has been performed using flotation [38], hydro-cyclone [39], electrostatic [35], near infrared and optical [38, 40], and sequential sieve [41] techniques. The purpose of the size reduction and sorting is to physically separate fibre from matrix [42, 43], so that the resulting fibre-rich and resin-rich products can then be introduced into other materials as either reinforcements or fillers.

Schinner *et al.* [44] showed that it is possible to improve the mechanical properties of injection moulding pellets made of neat PEEK by incorporating as much as 50 % by weight of fibre-rich by-product of ground CF-PEEK prepreg tape. When compared with a standard CF-PEEK pellet (Victrex PEEK 450 CA30), the recycled material was stronger and stiffer with a similar elongation at break. Palmer *et al.* [43] showed that a by-content, instead of a by-weight, substitution of virgin GF with ground GF-SMC along with improved separation and mixing

techniques resulted in better flexural and impact properties. Saccani *et al.* [45] and Li *et al.* [46] both looked at recycling CFRP waste. The former obtained improved flexural strength and toughness when adding cured and shredding CFRP to different types of cement. The latter performed a life-cycle-analysis (LCA) to determine the financial viability of replacing virgin short CF with end-of-life CFRP in a United Kingdom context. Ultimately, they concluded that poor fibre recovery rates, degraded fibre properties and excessive recycling costs associated with dismantling, shredding, transport, etc. limited the potential for this type of recycling.

2.1.2 Incineration

Incineration is perhaps the most straightforward approach to recycling composite waste, whether it be cured or uncured. Yang *et al.* [33] notes that incineration for energy recapture without material recovery is not considered a recycling method by some of the European directives. Palmer [47] acknowledges that, in certain cases, it is also possible to recover inorganic fillers and reinforcements following polymer burn-off; however, this falls more within the realm of fibre reclamation, which is the topic of the next section.

2.1.3 Fibre Reclamation

Unlike mechanical recycling and incineration, fibre reclamation techniques endeavour to remove the matrix in a way that preserves fibre length and mechanical performance. Pairing the recovered fibres with a new resin system is usually the main objective, while finding meaningful avenues for the resulting organic and inorganic compounds is secondary.

Pyrolysis

Pyrolysis is a process in which waste is heated in the absence of oxygen to a sufficiently high temperature such that the organic matrix undergoes chemical decomposition [48]. It is arguably the most widely studied fibre reclamation method. The reclaimed solid waste, which typically consists of fibre and fillers, can be paired with another resin system and used to manufacture a new composite component. The gaseous and aqueous products that come from the matrix decomposition are used as chemical feedstock [27, 28]. Pyrolysis is a high energy and high cost process when compared with some other methods, thereby limiting its application to materials with high intrinsic value such as carbon fibre [49]. Decomposition of the organic matrix also leads to the contamination of the reclaimed fibre surfaces with carbon char as shown in Figure 2-1.

Studying post-pyrolysis treatments that can effectively clean the fibre surface and improve their mechanical performance remains the focus of this field. Giorgini *et al.* [50], for example, have demonstrated the effectiveness of a secondary high temperature (500 – 600 °C) oxidation step to burn off char and other residue. Kim *et al.* [51] applied a similar two-step approach using superheated steam (700 °C) to remove char-contamination, which they refer to as carbonaceous residue. Both authors showed significant gains in mechanical strength relative to unclean fibres.

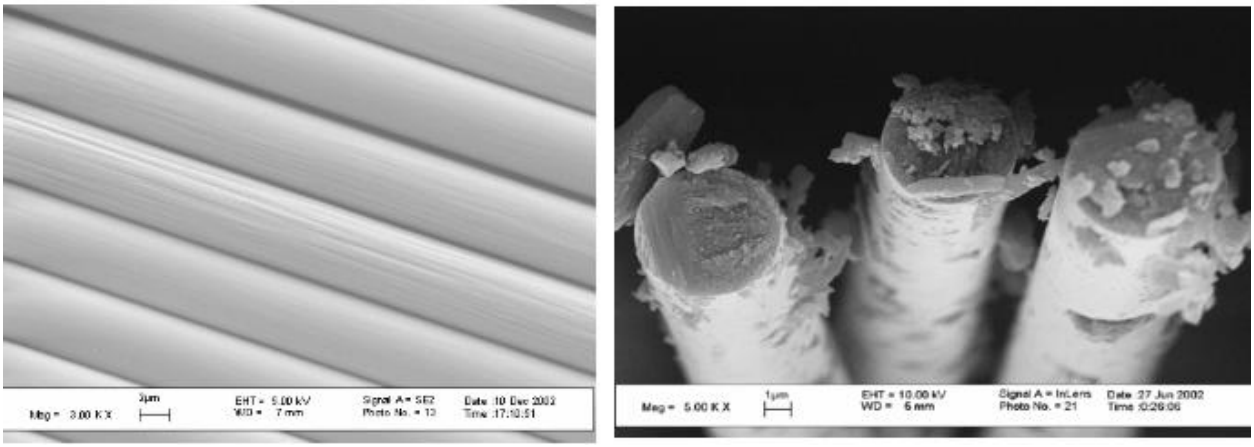

Figure 2-1. Untreated, unsized IM7 carbon fibre (left) and NBASR-1 (pyrolyzed) ANL recovered carbon fibre (right) [52][1].

Fluidised Bed

Reactors based on the principle of particle bed fluidisation have garnered a lot of interest due to their ability to process large amounts of scrap [27, 53]. Pioneers in the field Meng *et al.* [54] describe the process schematically in Figure 2-2. CFRP waste that has been shredded to a size of 6 – 20 mm is fed into the reactor, hot air passing through a bed of silica both decomposes the polymer matrix and elutriates the fibres, leaving behind any inorganic contaminants. A cyclone separation system then removes the fibre-rich products from the gas stream which continues into a combustion chamber where any remaining compounds are incinerated and the energy recaptured is used to run the system. Applications for the recyclates generated using this process include injection moulding pellets [55] and random non-woven aligned commingled mats for compression moulding [56].

[1] NBASR-1 refers to carbon fibres that were recovered using the process developed by the Argonne National Laboratory (ANL). The images in this figure are reprinted by permission from the Society for the Advancement of Material and Process Engineering (SAMPE).

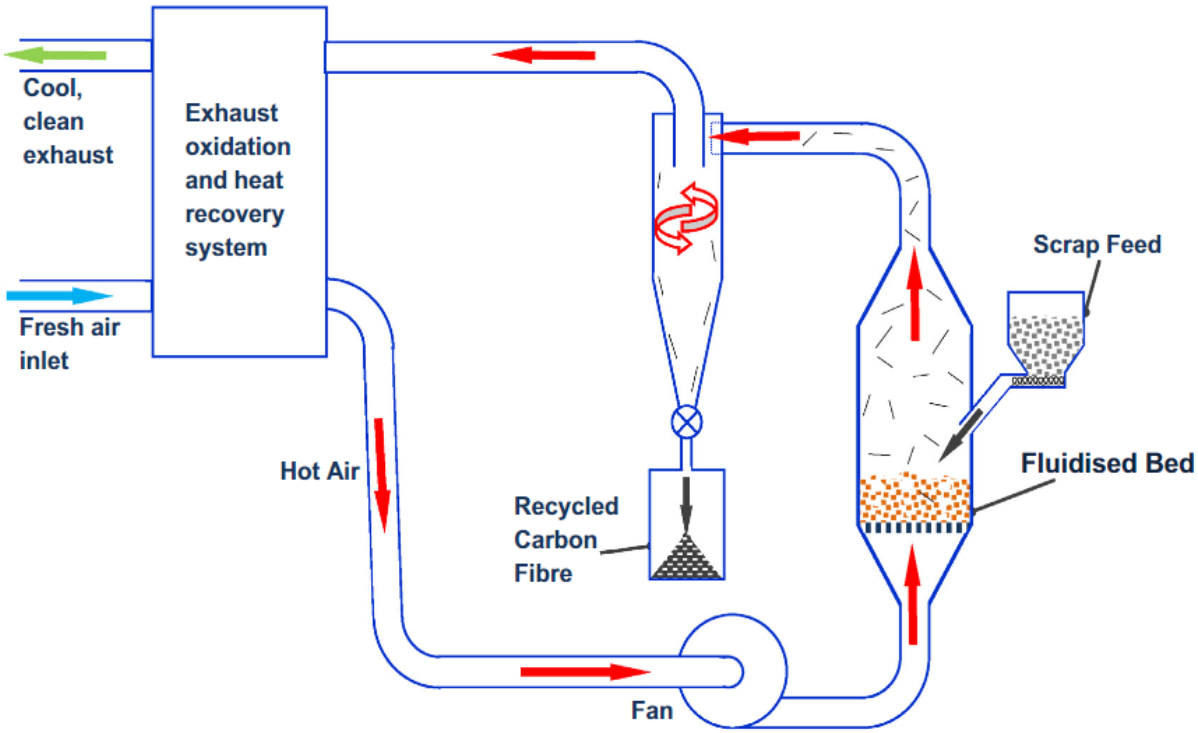

Figure 2-2. Overview of the fluidised bed CFRP recycling process [54].

Solvolysis

According to Pimenta and Pinho [32], chemical recycling methods involve the decomposition of a polymeric matrix using reactive media such as catalytic solutions, benzylalcohol, or supercritical fluids at temperatures under 350 °C. Feraboli *et al.* [57] were successful in extracting carbon fibres from recovered automotive parts, some of which included aluminum inserts, using a mixture of sulfuric acid and hydrogen peroxide along with constant mechanical agitation (Figure 2-3). Without additional fibre manipulation or preforming considerations, re-manufactured panels yielded an average fibre volume fraction of 33 % compared to 62 % for the virgin parts. This result exemplifies the current limitations of solvolysis as a recycling method for polymer-matrix composites. Investigations like those of Sokoli *et al.* [58] and Jiang *et al.* [59] found that it is possible to recover carbon fibre with mechanical strength and stiffness similar to the original fibre as long as significant size reduction is avoided. Drawbacks associated with chemical recycling include reduced fibre adhesion to new resins, low fibre volume fractions for re-manufactured parts, difficulty of process-scaling, and environmental concerns [32].

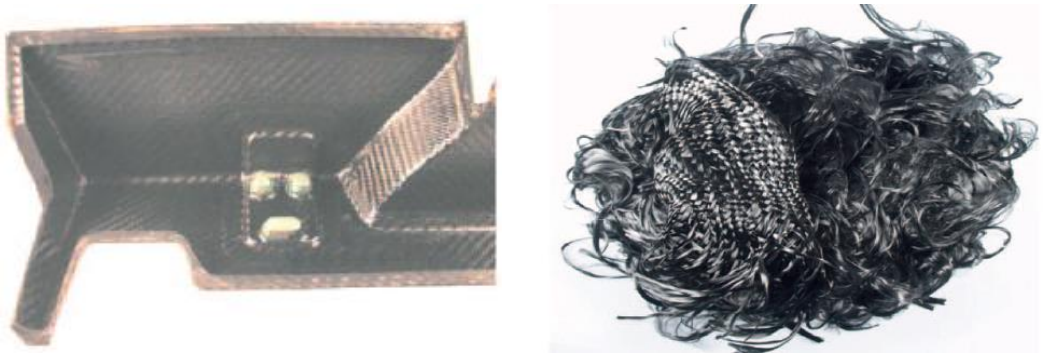

Figure 2-3. CF-epoxy part manufactured by vacuum-assisted resin transfer moulding (left) the recovered CFs following acid digestion (right) (adapted from [57]).

2.1.4 Reforming of Thermoplastic Composites

Thermoplastic-matrix composites are often touted as being recyclable due to their ability to melt and solidify numerous times. This makes it possible to break down existing thermoplastic parts and/or production waste (e.g. trimmings, offcuts) into a recyclate that can be incorporated into injection moulding pellets or a BMC for compression moulding. Variation in the literature comes from the type of size-reduction technique(s) employed to produce a given recyclate. Both Roux *et al.* [60] and Eguémann [61] used a technique referred to as electrodynamic fragmentation to break down rotorcraft door-hinges made of CF/PEEK as shown in Figure 2-4. This approach involved placing door-hinges between two electrodes and inducing voltages between 50 – 200 kV in pulses of less than 5 μs. Door-hinges manufactured using the fragmented material exhibited a 17 % reduction in failure load and a transition from elasto-plastic to brittle failure due to shorter fibre lengths and irregular fibre surfaces [60].

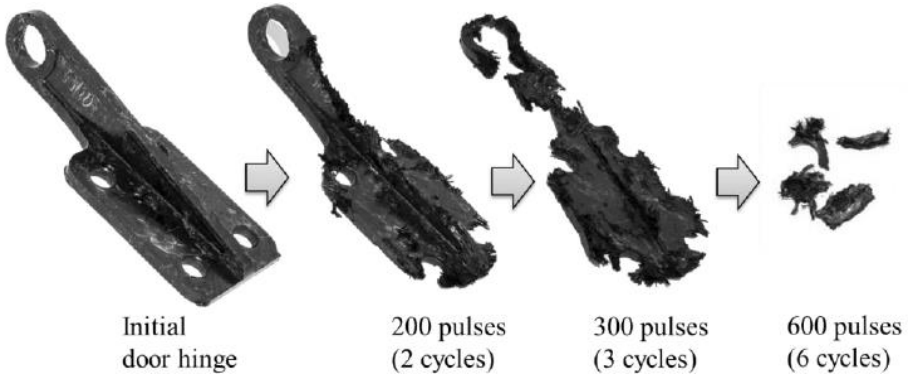

Figure 2-4. Evolution of a CF/PEEK door-hinge during electrodynamic fragmentation [60].

Leblanc *et al.* [62] used two different recycling strategies on T-brackets that they had compression moulded using CF/PEEK strands. The first method involved mixing tested short-

beam strength (SBS) specimens taken from the T-bracket's rib with different quantities of virgin strands as shown in Figure 2-5 (left). The second method involved stacking pieces of the T-bracket flange at the centre of the mould as shown in Figure 2-5 (right). The authors reported that up to 20 % by weight of SBS specimens could be used without causing a reduction in the recycled panel's flexural strength. They also found that using 25 % mould coverage for the manufacturing of their second recycled panel resulted in a more uniform mesostructure and a 25 % increase in flexural strength relative the baseline panel.

Figure 2-5. Mould cavity filled with 80 wt% SBS specimens and 20 wt% virgin strands (left). Stacked pieces of T-bracket flange at the mould cavity centre (right) [62].

In 2016, TenCate Advanced Composites in collaboration with the Thermoplastic Composites Research Center (TPRC) and GKN Fokker, developed a closed-loop recycled access door panel (Figure 2-6) for the leading edge of the Gulfstream G650 rudder. Their process involved chopping up CF/PPS prepreg waste that had been recovered from the elevator and rudder production followed by isothermal compression moulding [63].

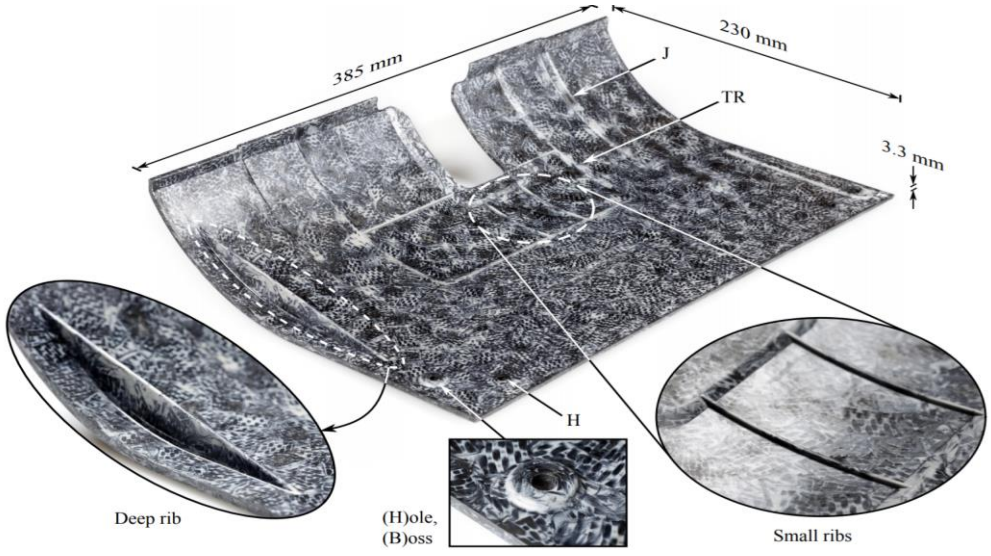

Figure 2-6. Access door panel demonstrated in 2016 made from scrap Cetex CF/PPS material and features stiffening ribs and moulded-in holes with bosses [63].

2.1.5 Uncured Prepreg Recycling

Efforts to treat uncured thermoset prepreg waste in the same manner as its thermoplastic counterpart can be found in the literature going back to the mid-nineties when Buggy *et al.* [64], Michaeli and Oelgarth [65], and Pannkoke *et al.* [66] all used different cutting methods to convert production offcuts into injection and compression moulding compounds. At that time, excessive resin percolation during moulding often necessitated the introduction of new resins and fillers [65, 66]. More recently, authors like Nilakantan and Nutt [67], Jin *et al.* [68], Blanco *et al.* [69], and Sultana *et al.* [70] have chosen to focus on turning prepreg waste into a strand-based recyclate similar to some commercially available sheet moulding compounds (Figure 2-7). This approach leverages longer fibre lengths and potentially higher fibre volume fractions to obtain better mechanical performance.

Figure 2-7. SMC sheet prepared from "fresh" prepreg trim waste tapes (left) and chopped "dry" prepreg trim waste tapes (right) [70].

However, a number of processing challenges associated with these techniques have been reported including: difficulties with prepreg cutting and clumping during handling due to high levels of tack [68-70]; insufficient shear flow, excessive resin percolation, and long processing times due to the low reactivity of the original resin systems [24]. Significantly lower and more variable strength values when compared with continuous laminates [67, 68, 71] and even some commercially available SMCs [69] have also been reported.

Other investigations have shown that splicing recovered prepreg plies together to form a semi-continuous laminate as shown in Figure 2-8 can reduce the loss of tensile strength and, in some cases where overlaps were used, even improve flexural properties [72]. For example, de Souza *et al.* [73] reported knockdowns in the tensile (-13 %), compressive (-23 %), and flexural (- 56 %) strengths of autoclave cured laminates composed of recovered CF/epoxy prepregs. Their method of randomly positioning prepreg offcuts with 5 – 10 mm overlaps did, however, increased

the interlaminar shear strength (ILSS) measured using the ASTM 2344 [74] standard for short-beam specimens.

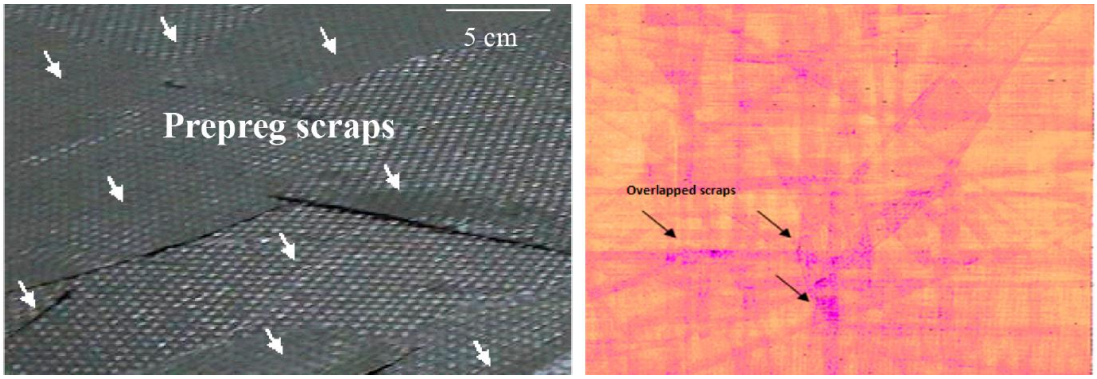

Figure 2-8. Panel lay-up with randomly positioned scraps with different sizes and shapes (left) and a typical ultrasonic inspection image of a cured panel (right). Adapted from [73].

2.1.6 Commercial Efforts

Of the many recycling methods presented here, only a handful have been implemented on an industrial scale. ELG Carbon Fibre Ltd. is a company based in the United Kingdom that uses a modified pyrolysis process to generate a number of reclaimed fibre products like those shown in Figure 2-9. ELG's choice of recycling process and target recyclate types allows them to use a variety of post-industrial waste to produce their products. They have also recently secured a 5-year agreement with The Boeing Co. to recycle both cured and uncured waste from 777X wing manufacturing facilities in the United States [75].

Figure 2-9. Recycled products offered by ELG including carbon fibre nonwoven mats (left), chopped tow (middle) and milled carbon fibre pellets (right).

121c Pure Carbon is a company based in the United States that has also targeted aerospace composite waste. Since 2015, they have been using a simple hot press process and prepreg offcuts recovered from local aerospace companies to manufacture a variety of recycled skateboards (Figure 2-10) [76, 77].

Figure 2-10. Co-founders Ryan Olliges and Jaysen Harries unloading fresh carbon fibre scraps at 121c in Gardena (left) and Olliges showing off one of their skateboards (right) [76, 77].

Lavoisier® Composites (Chassieu, France) is yet another company that has developed a pathway for discarded aerospace prepregs. Their recylate Carbonium® has been showcased in the case of the Ulysse Nardin Skeleton X luxury watch shown in Figure 2-11. According to their patent [78], the Carbonium® product line is a combination of uncured unidirectional offcuts which have been "stabilized" and an additional resin component. Stabilization in this case refers to imparting energy into the prepreg offcuts so as to advance their degree of cure and make them less tacky and less reactive at room-temperature.

Figure 2-11. Ulysse Nardin Skeleton X watch with Carbonium® Gold case (left) and a picture of a Carbonium® Gold billet (right) [79].

2.2 Long Discontinuous Fibre Composites

2.2.1 Definition

Continuous reinforcements found in most structural aerospace composites provide unbroken paths through which applied loads can be efficiently transmitted. This characteristic

yields materials with high strength and modulus. However, the relative inextensibility of most high-performance fibres makes it difficult to manufacture parts with even moderate geometric complexity [80, 81]. In contrast, short-fibre materials paired with a process like injection moulding can be used to produce incredibly complex yet low-performance structures. The trade-off between performance and processability is described schematically by Chang and Pratte [82] (Figure 2-12).

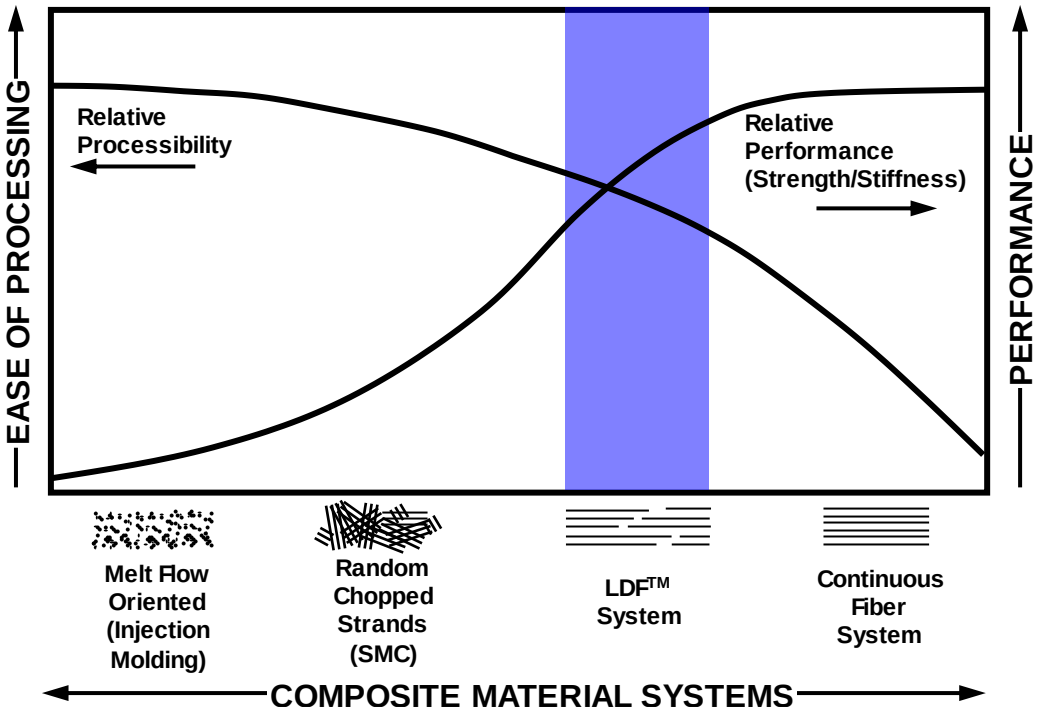

Figure 2-12. Performance and processability of LDF compared with other materials systems [82].

The synergistic relationship that occurs within a polymer matrix composite is, in large part, dictated by the length of the reinforcing fibres relative to the critical fibre length (L_c) which is given by Equation (2.1):

$$L_c = \frac{\sigma d}{2s}, \tag{2.1}$$

where σ, d, and s are the maximum fibre tensile stress, the fibre diameter, and the fibre/matrix shear strength, respectively. By definition, this parameter represents the length at which load transferred to the fibre along the fibre/matrix interface reaches the fibre's ultimate tensile strength [83, 84]. Chang and Pratte [82] claim that maximum reinforcement efficiency occurs "when the average fiber stress integrated over the fiber length is equal to the ultimate fiber strength, [which] is mathematically achieved when the fiber length exceeds 50 times [L_c] (*sic*)". Discontinuous

materials that satisfy this criterion are often referred to as long discontinuous fibre (LDF) composites. This classification encompasses a number of terminologies found in the literature such as: randomly oriented strand composites (ROS – McGill University), prepreg platelets (Purdue University), discontinuous long fibre composites (DLF – Greene Tweed), CF tape-reinforced thermoplastics (CTTs – University of Tokyo), unidirectionally arrayed chopped strands (UACS – Toray), flakes (University of Twente), etc.

To provide some length-scale context, Sager *et al.* [84] reported an approximate critical fibre length of 383 μm for sized T650 carbon fibres embedded in EPIKOTE 862 epoxy resin. It may, therefore, be possible to achieve the much sought-after balance between mechanical properties and processability with an LDF composite consisting of similar constituent materials and featuring fibre lengths around 19.2 mm (50 L_c).

2.2.2 Flow-Compaction

Experimental

A number of deformation mechanisms have been observed during the compression moulding of LDF materials including initial preform consolidation [85, 86], resin percolation [87], and various types of shearing (e.g. intraply shear, interply shear) [88, 89]. A material's flow-compaction behaviour is defined by the specific combination of these mechanisms excited during the manufacturing process.

The relationship between processing parameters and the flow-compaction of LDF systems has been studied using a variety of experimental techniques. LeBlanc [90], Bae *et al.* [91], and Abdul Rasheed [92] have each studied the filling of ribbed panels using different prepreg strand sizes and moulding pressures. These authors reported that larger strands were more resistant to shearing at lower pressures and that increasing the moulding pressure was needed to both improve filling and mitigate the formation of voids [93-95]. However, Evans *et al.* [93] warned that forcing LDF compounds to flow over too great a distance may lead to fibre/matrix separation also known as resin percolation. Martulli *et al.* [96] showed that using minimal charge coverage to induce large flow distances can also lead to preferential fibre orientation and highly anisotropic in-plane mechanical properties.

Several studies have shown that mould closure rate is another processing parameter that can influence strand behaviour. Abdul Rasheed [92] found that woven CF/PPS strands are more

likely to experience localised jamming as shown in Figure 2-13 when very slow closure rates (0.005 mm/s) are used. They attributed this phenomenon to an increase in strand nesting and a greater number of fibre-to-fibre contacts. Picher-Martel [97] observed a strong rate dependence in the interply friction of CF/PEEK prepregs and suggested that a better understanding of this phenomenon would result in more representative values of yield stress associated with their proposed flow model.

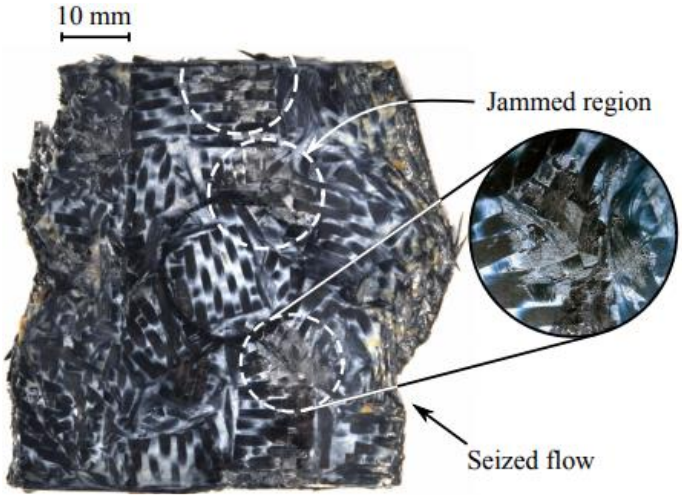

Figure 2-13. Jamming observed in squeeze flow experiments. Due to jamming, the flow in the bottom right side has seized. (Inset) Dry fabric visible in the jammed spot [92].

In addition to strand size and moulding pressure, moulding temperature was identified by LeBlanc [90] as another key process parameter for the filling of their T-brackets. They showed that, regardless of the strand size used, increasing the moulding temperature reduced the pressure needed to completely fill their T-bracket's main rib. It is important to note that numerous authors discuss the importance of resin viscosity on flow without quantitatively studying this relationship.

Modelling

Modelling of LDF compression moulding involves the definition of the initial charge structure, the material's flow-compaction behaviour including curing effects for thermoset systems, and the problem's boundary conditions. While most authors choose to approximate charge structure as layers of randomly distributed strands with no out-of-plane orientation [83], Favaloro *et al.* [98] made use of micro-CT measurements to obtain a more accurate representation as shown in Figure 2-14. The use of pre-consolidated specimens has also been used to remove the need for modelling of the initial fibre bed compaction [97, 98].

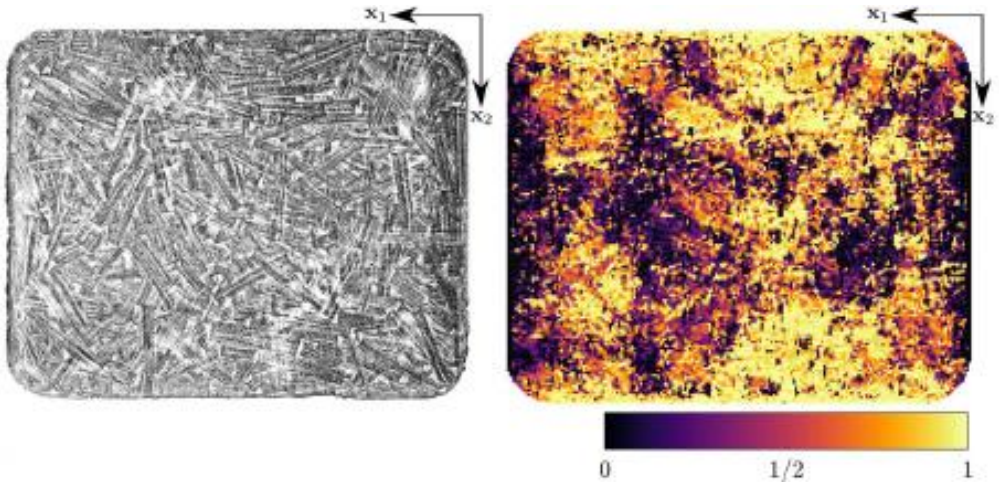

Figure 2-14. CT scan density field of a pre-consolidated preform (left) and corresponding orientation analysis result (right). Adapted from [98].

The choice of flow-compaction behaviour model and boundary conditions varies throughout the literature. Favaloro *et al.* [98] elected to use a coupled anisotropic viscosity model paired with an orientation evolution method implemented in ABAQUS/EXPLICIT to describe the flow of CF/thermoplastic strands. A pure slip (no friction) boundary condition allowed them to limit computational cost; however, it resulted in an underprediction of strand movement at the entrance of their rib features. Picher-Martel *et al.* [99] lumped the micromechanics of CF/PEEK strands during 2-D squeeze flow into a homogenous modified Bingham plastic model and used a no-slip (infinite friction) boundary condition which was supported by previous experimentation [97]. This modelling approach was implemented in COMSOL Multiphysics and it allowed them to improve their predictions of final specimen strain when compared to previous modelling efforts using Newtonian or Carreau models. Unfortunately, treating LDF materials like homogenous fluids does not provide any information regarding the final strand orientation distribution of a compression moulded part.

2.2.3 Mechanical Performance

This section is based on the review article written by Visweswaraiah *et al.* [83] which provides a comprehensive summary of the literature related to the mechanical characterization and modelling of LDF composites. A variety of techniques, such as manual placement [61, 100, 101], water/air dispersion [101, 102], and mat-layups [68], have been used to study the effect of initial strand distribution on the mechanical performance of LDF parts. Commonly observed defects in

compression moulded components include porosity at the surface and in resin rich pockets near the edge of strands [24, 103], excessive warpage and thickness variations in thin parts [104], and non-uniform strand/fibre orientations induced by large flow distances [96]. As previously mentioned, the discontinuous nature of these materials provides improved flow-compaction characteristics at the expense of mechanical performance when compared with continuous laminate groups. Table 2-2 summarizes the work of various authors who have experimentally measured the mechanical properties of LDF coupons and compared them with corresponding quasi-isotropic (QI) laminates.

Table 2-2. A comparison of LDF coupon properties against corresponding QI continuous laminates. Percentage values are calculated as the LDF properties normalized by the QI properties.

In-plane		
Tensile	Modulus	Similar [83]
	Strength	15 – 35 % [105], 50 % [68], 70 % [101]
	Fatigue	More resistant [106]
	OHT	Notch insensitive [107], 5 – 9 mm critical hole size [108]
Compressive	Modulus	Similar [83]
	Strength	45 – 60 % [105]
	OHC	Notch insensitive [107]
Out-of-plane		
Flexure	Modulus	117 – 130 %* or 30 – 34 %** [105]
	Strength	67 – 120 %* or 28 – 50 %** [105]

* compared to QI laminate with 90° plies at the outer surface

** compared to QI laminate with 0° plies at the outer surface

In the studies presented, specimen failure was most commonly attributed to matrix failure with some secondary fibre failures. With this in mind, Eguémann *et al.* [109] showed that the tensile properties of LDF coupons were higher when a resin with higher shear strength was used. Improvements in tensile strength have also been achieved by improving the uniformity of initial strand distributions as was reported by both Yamashita *et al.* [101] and Jin *et al.* [68]. Compressive failure of panels manufactured using CF/PEEK strands has been shown to be particularly sensitive to surface porosity according to the work of Landry [94]. Finally, the findings of both Feraboli *et al.* [107] and Qian *et al.* [108] show significant notch insensitivity for LDF materials due to their heterogeneous mesostructure.

2.3 Expansion of Knowledge

The review presented herein details the state-of-the-art in composites recycling technology and in the processing of LDF material systems by compression moulding. Gaps in the literature have been identified for both fields of research and are discussed below.

Of the many recycling methods presented within the literature, none have given appropriate attention to the inherent value of the resin found in uncured composite waste. Thermal fibre reclamation methods such as pyrolysis and fluidised bed are the furthest along in terms of large-scale commercialisation and yet they break down the polymer matrix to be used a low-value chemical feedstock or to be burned for energy recapture. Only a handful of academic studies have attempted to reuse uncured prepregs without first stripping them of their resin. Those who have attempted to transform uncured prepreg waste some type of compression moulding compound, without the adding a new resin or filler, have faced a slew of processing challenges related to non-ideal material flow and unacceptably long and inflexible cure windows.

The importance of resin viscosity on the flow-compaction behaviour of LDF composite systems is acknowledged in the literature, however, a quantitative investigation into this relationship across a broad range of viscosities does not exist. The need for low resin viscosities to ensure sufficient resin percolation during vacuum-bag processing of prepregs and resin infusion of dry preforms is well documented. Dominant shear-induced material transport has been observed for materials that exhibit orders-of-magnitude larger viscosities such as compression and injection moulding compounds. A more complete understanding of the relationship between resin viscosity and the prevalence of these competing flow-compaction mechanisms is needed to enable accurate predictions of the material evolution during manufacturing.

Supporting experimental techniques and characterization methods are desirable. A combination of experiments and resin behaviour modelling is needed to address the goals described above. An abundance of experimental techniques exists within the literature that could be used to study the flow-compaction behaviour of these materials. However, improvements to existing methods are needed to allow for a more in-depth analysis of deformation mechanism contributions. Furthermore, the staging framework described in Chapter 1 will require models to

accurately predict the curing and rheology of the resin being studied. The use of phenomenological models in the literature has been limited, for the most part, to resins with low initial degrees-of-cure. Additional considerations will be needed to both collect data related to resin degree-of-cure and extend the accuracy of these models to resins that have undergone extensive room-temperature ageing, as well as elevated temperature staging.

A concise summary of the existing knowledge and the proposed expansion of knowledge is given in Table 2-3.

Table 2-3. Existing knowledge and proposed expansion of knowledge.

Existing Knowledge
• A variety of methods for recycling both cured and uncured composite waste • Relationships between primary processing parameters, such as temperature and pressure, and LDF material flow-compaction • A basic understanding of the mechanical behaviour and failure of LDF materials
Expansion of Knowledge
• Approach to recycling uncured prepreg offcuts that preserves the original resin and does not require additional resin or filler components • Quantitative relationship between resin viscosity and LDF flow-compaction • Evaluation of inspection techniques for tracking extensive room-temperature ageing of prepregs • Extended validity of resin behaviour models

3
THESIS OBJECTIVES AND STRUCTURE

3.1 Thesis Objectives

As the volume and diversity of composite waste streams continue to grow, there is increasing urgency to find more versatile and economically viable recycling technologies. The goal of this thesis is to develop and validate a methodology for transforming uncured prepreg waste into an LDF compression moulding compound referred to here as an rPMC. Thusly, the following thesis objectives have been defined:

1. Develop a recycling framework that uses elevated temperature staging to selectively increase a prepreg resin's degree-of-cure, thereby modifying both the flow-compaction and curing behaviours to suit a compression moulding process.
2. Characterize the relationship between resin viscosity and prepreg flow-compaction using simplified compression moulding trials and determine the optimum viscosity range for inducing shear flow.
3. Validate the recycling framework by manufacturing geometrically complex demonstrator panels using appropriately staged prepreg offcuts cut into strands.
4. Characterize the mechanical performance of compression moulded coupons and compare the results with properties from the literature.
5. Throughout the proposed research, develop and improve experimental methods to address the gaps identified in the literature.

3.2 Thesis Structure

The objectives outlined in the previous section are addressed in the five chapters shown in Figure 3-1and described below:

- **Chapter 4** presents the experimental characterization of the Cycom® 5276-1 resin system found in the recovered autoclave prepreg. Phenomenological models for cure, viscosity, and glass transition temperature are populated and validation experiments carried out.
- **Chapter 5** presents the methodology used to investigate the relationship between resin viscosity and prepreg flow-compaction. Specimens subjected to increasing levels of staging were tested and optical micrographs were used to quantify specimen shear flow.
- **Chapter 6** evaluates the ability of different inspection techniques to accurately measure the degree-of-cure of specimens subjected to extensive room-temperature ageing.
- **Chapter 7** presents the results of compression moulding trials in which staged prepreg strands are used to produce geometrically complex panels in a shortened cure time.
- **Chapter 8** presents a mechanical characterization of rPMC panels and compares the measured properties with common aerospace CMCs and metals.

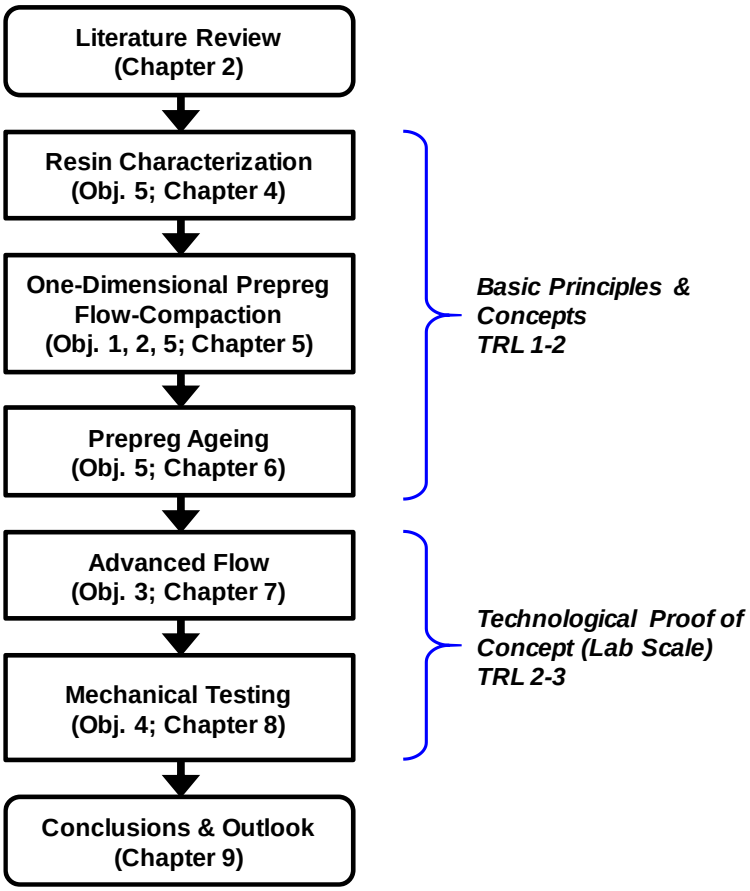

Figure 3-1. Thesis organization with related objectives.

4
RESIN CHARACTERIZATION

In this chapter, thermo-chemical and chemo-rheological characterizations of Cytec's aerospace epoxy resin system Cycom® 5276-1 are presented. Semi-empirical phenomenological models for cure, viscosity, and glass transition temperature are fit to the experimental data obtained through calorimetry and rheometry. The selection of each model and the non-linear least-squares regression used for fitting is discussed briefly in the context of similar studies found in the literature. Finally, model goodness of fit is evaluated for both the cure and viscosity models using additional validation experiments.

4.1 Materials

Two types of uncured prepreg waste were studied here. Plain weave (PW) and eight-harness satin (8HS) offcuts were obtained from production ply-cutters of Bell Helicopter Textron Canada and Bombardier Aerospace, respectively. Both materials are impregnated with Cytec's Cycom® 5276-1 toughened epoxy; a system designed for primary aircraft structures with a specified service temperature range of -59 °C to 121 °C and high damage tolerance [110]. All offcut batches recovered were within the manufacturer-specified out-life; however, the exact out-time was not known. 8HS offcuts from Bombardier Aerospace are pictured in Figure 4-1 to give the reader an idea of the general size and shape of the materials studied. Additionally, select technical specifications for each prepreg system are shown in Table 4-1.

Figure 4-1. Ply-cutter production offcuts provided by Bombardier Aerospace.

Table 4-1. Technical specifications for recovered 5276-1 prepreg offcuts.

Material Specification	Bell Helicopter	Bombardier Aerospace
Fibre Type	Thornel T650 – PAN	Thornel T650 – PAN
Fibre Architecture	Plain weave	8 harness satin
Tow Size	3K	3K
Areal Weight	312 gsm	370 gsm
Resin Content	36 % wt	42 % wt
Cured Resin Density	1.29 g/cc	1.29 g/cc
Out-Life (22 °C)	N/A	15 days
Shelf-Life (< -18 °C)	N/A	6 months

4.2 Resin Extraction

Using prepreg to study resin cure kinetics by differential scanning calorimetry (DSC) is not recommended, as they often feature highly non-uniform resin morphologies which promote unpredictable variations in measured cure evolution magnitude. Pictures taken of the PW and 8HS prepreg surfaces (Figure 4-2) using a Dino-Lite digital microscope revealed that this is particularly true of prepregs based on woven reinforcements. Furthermore, prepreg cannot be used to measure resin viscosity by parallel plate rheometry, as the presence of fibre increases the apparent viscosity by several orders of magnitude. For these reasons, and because it was not possible to procure resin film for this work, a resin extraction technique was used to obtain enough neat resin (NR) to complete all necessary testing.

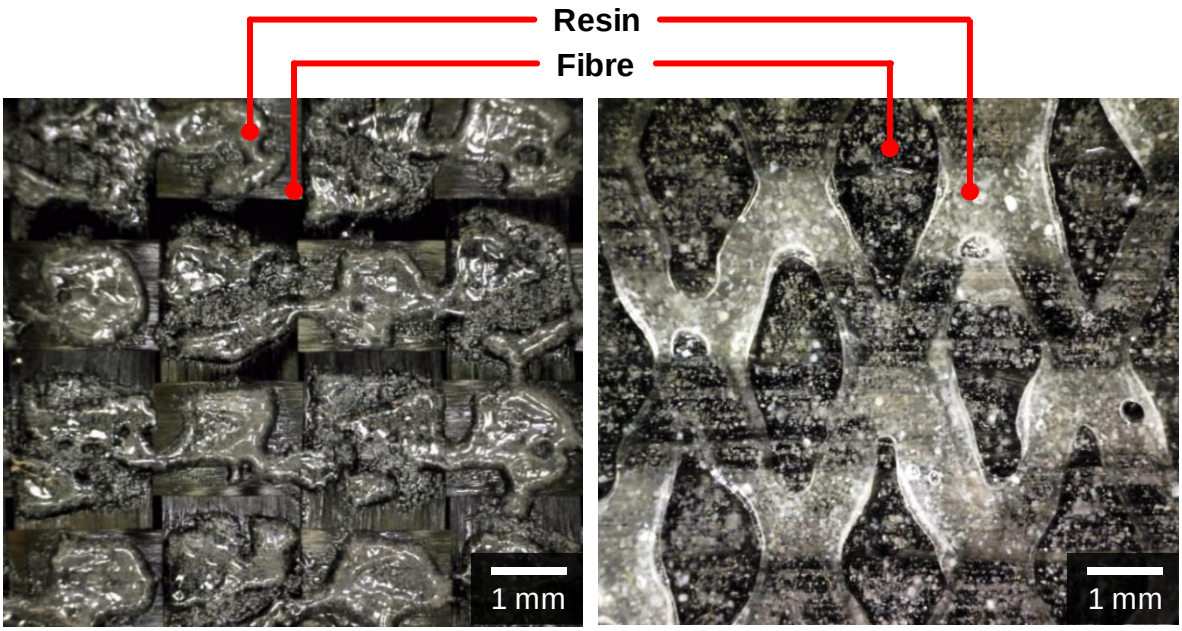

Figure 4-2. Pictures of PW (left) and 8HS (right) prepreg surfaces, showing the non-uniform resin surface distribution caused by the prepregging process.

Siddiqui et al. [111] briefly describe a method for extracting resin from a quartz/cyanate-ester prepreg using a heated steel substrate and pressure applied with a spatula. Building on their description, a procedure appropriate for the 5276-1 prepregs was developed: A single ply of 8HS/5276-1 is placed on an aluminium plate preheated to 70 °C, a temperature determined through trial and error to be the lowest temperature at which resin could be easily extracted. A razor blade is then drawn across the ply surface at 45° from the warp or weft directions with moderate pressure applied (Figure 4-3 – left). After each pass, the recovered resin is immediately placed on a cool metal surface to avoid unwanted conversion (Figure 4-3 – right).

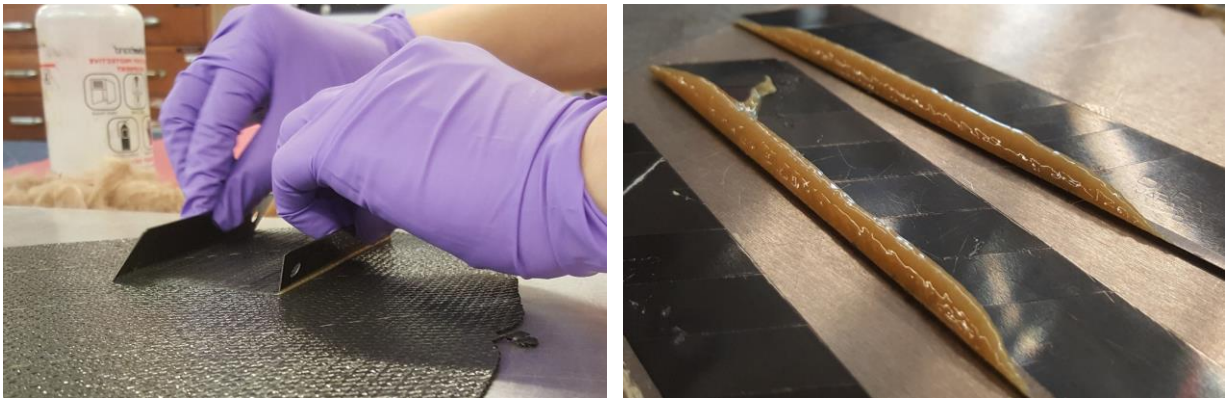

Figure 4-3. A razor blade being drawn across the hot prepreg surface (left) and some of the corresponding resin obtained cooling on a steel plate (right).

Each ply is exposed to 60 – 70 °C for roughly 30 seconds during extraction. Total heat of reactions (H_R) and ungelled glass transition temperatures (T_g), measured by modulated DSC and summarized in Figure 4-4, were used to assess cure advancement due to these elevated temperature conditions. An average increase in T_g of 2.36 °C indicates that resin extraction did indeed cause some increase in degree-of-cure; however, the magnitude of change is small given that the datasheet for 5276-1 specifies a maximum T_g of 188 °C [110]. There is also an apparent increase in H_R by 43 J/g (13%) which would normally indicate a reduction in degree-of-cure. This is, of course, not feasible. Instead, the increase in H_R, along with the 42.3% decrease observed in the H_R interquartile range, supports the assumption that prepreg DSC specimens are highly heterogeneous and not suitable for cure kinetic measurements.

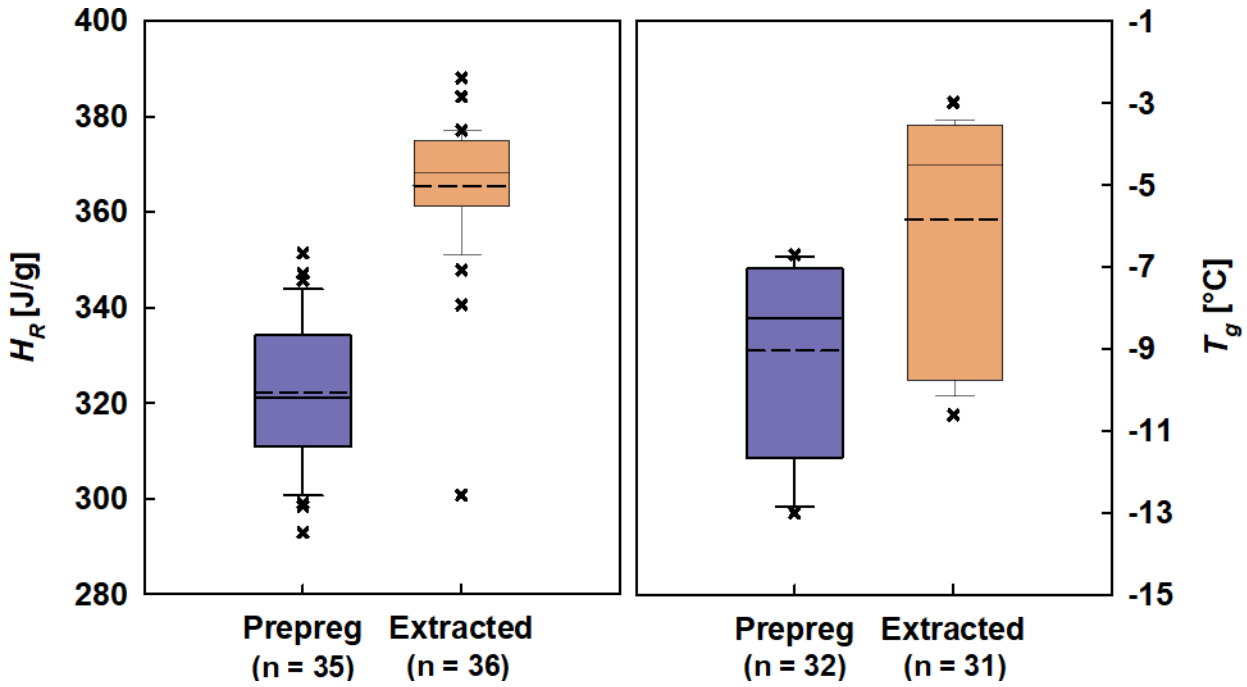

Figure 4-4. Box and whisker plots of H_R and T_g measurements for prepreg and extracted resin specimens. The plot shows the mean (dashed-line), median (solid line), interquartile distance (boxes), 25th and 75th percentiles (whiskers), outliers ("x"), and sample sizes (n).

4.3 Cure Kinetics

4.3.1 Test Matrix

The curing behaviour of extracted 5276-1 resin was studied using a combination of conventional and modulated DSC. Dynamic and isothermal scans were carried out on a Q100 DSC

from TA Instruments to track the evolution of the resin cure rate under different time-temperature conditions. A summary of the tests performed is shown below in Table 4-2.

Table 4-2. DSC test matrix for extracted 5276-1 resin.

Test Type	Conditions	Repetitions
Dynamic Ramp	2 °C/min	3-5
Isothermal Dwell	120, 140, 160, 180 °C	3-5

4.3.2 Model Fitting

Physics-based phenomenological cure modelling often provides a simple and effective way of approximating the behaviour of complex proprietary polymer systems for which a mechanistic approach would not be feasible. The method of isoconversional visualization described by Dykeman [112] was used here to determine the model form best suited to 5276-1. Isoconversional curves constructed using isothermal DSC data and shown in Figure 4-5 – left, reveal the following insights: First, cure rate reaches a maximum at a degree-of-cure greater than zero ($\alpha \approx 0.3$), suggesting that 5276-1 polymerization may follow an autocatalytic behaviour; Second, two groups

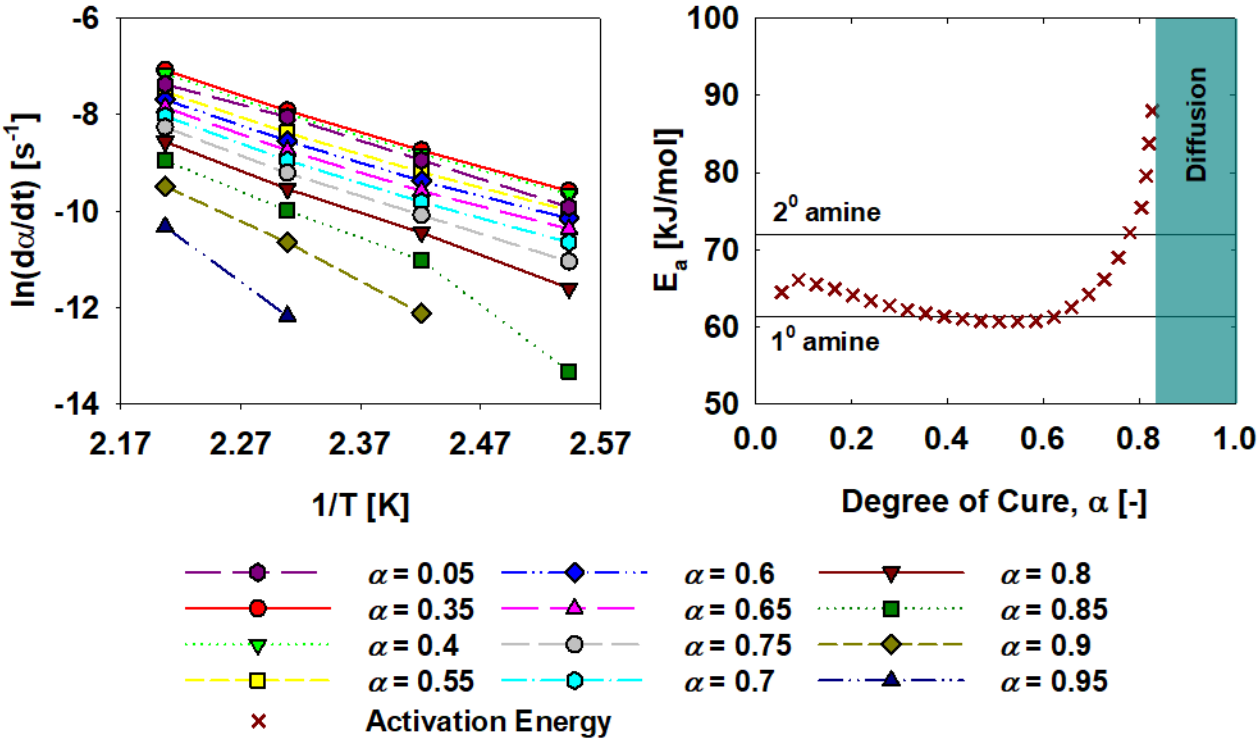

Figure 4-5. Isoconversional curves obtained from experimental DSC data (left) and corresponding activation energies (right) for extracted 5276-1.

of isoconversional curves with different slopes are observed indicating a possible secondary reaction; Finally, a drop-off in cure rate is observed at higher degrees-of-cure ($\alpha > 0.8$) and lower temperatures ($T = 120$ °C) indicating a reduction in molecular mobility commonly associated with resin vitrification and a switch from kinetic to diffusion dominated cure [112, 113].

Drawing from these observations, a two-reaction autocatalytic model including a diffusion factor (Equation (4.1)) was selected to represent the curing behaviour of 5276-1:

$$\frac{d\alpha}{dt} = K_1\alpha^{m_1}(1-\alpha)^{n_1} + \frac{K_2\alpha^{m_2}(1-\alpha)^{n_2}}{1+\exp(D(\alpha-(\alpha_{C0}+\alpha_{CT}T)))}\ , \tag{4.1}$$

where α is the degree-of-cure, K_1 and K_2 are Arrhenius coefficients given by Equation (4.2), n_1, n_2, m_1, and m_2 are reaction orders, D is the diffusion factor, α_{C0} is the critical degree-of-cure at absolute zero, α_{CT} is the rate of increase of critical degree-of-cure with temperature, and T is temperature in units of Kelvin. The Arrhenius coefficients are given by Equation (4.2):

$$K_i = A_i \exp\left(\frac{-E_{a,i}}{RT}\right), \tag{4.2}$$

where A_i is the pre-exponential factor, $E_{a,i}$ is the activation energy, R is the universal gas constant, and T is, once again, temperature in units of Kelvin. Appropriate values for the parameters in Equations (4.1) and (4.2) were determined through the following steps:

(1) $E_{a,1}$ and $E_{a,2}$ were fixed at 61.4 kJ/mol and 71.0 kJ/mol, respectively, based on the observations made using the activation energy evolution shown in Figure 4-5 – right.

(2) Linear fits were obtained for each isoconversional curve (Figure 4-5 – left) and the vertical intercepts were extracted to later serve as limits on the pre-exponential factors A_1 and A_2.

(3) The maximum T_g obtained for each isotherm was plotted versus the corresponding degree-of-cure (Figure 4-6 – right) and a linear fit provided an estimate of the critical degree-of-cure parameters α_{C0} and α_{CT}[2].

(4) A weighted non-linear least-squares regression was performed with Equation (4.1) and the experimental cure rate data obtained for each isothermal test.

(5) The diffusion and critical degree-of-cure parameters were refined by performing another regression on Equation (4.3):

$$\frac{K_e}{K_c} = \frac{1}{1+\exp(D(\alpha_{C0}+\alpha_{CT}T))}, \tag{4.3}$$

[2] A discussion of the critical degree-of-cure and its dependence on temperature is presented by Cole *et al.* [113]

where K_e is the experimental cure rate and K_c is a diffusion-less version of Equation (4.1).

Figure 4-6 – left illustrates the effectiveness of Equation (4.1) (solid red curves) at predicting the drop-off in cure rate due to diffusion, once steps 1-5 have been successfully completed.

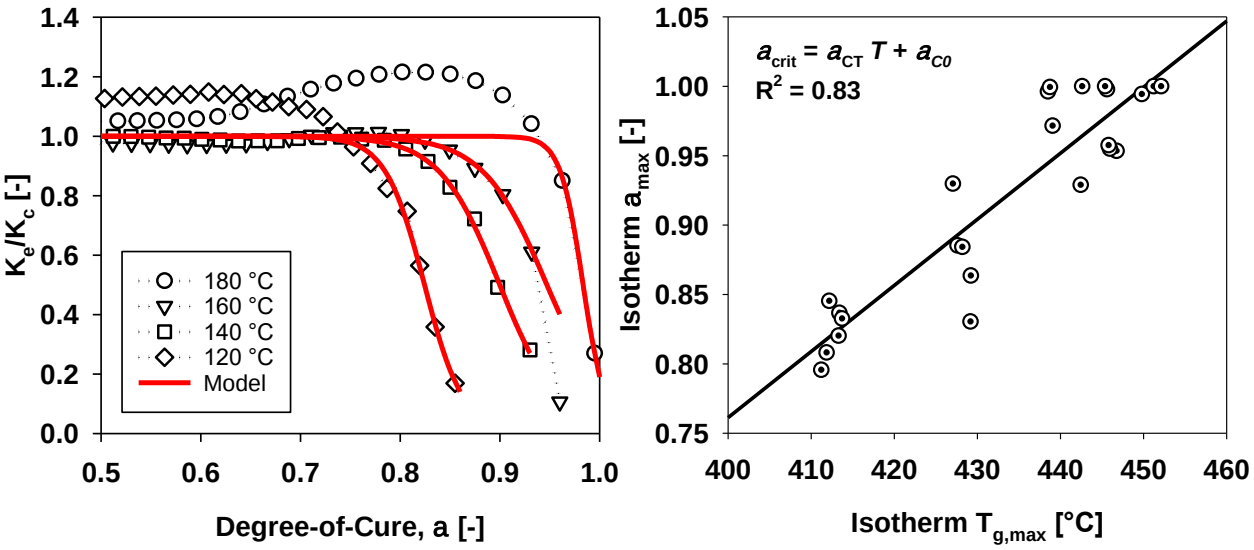

Figure 4-6. Diffusion and critical degree-of-cure parameter approximation (right) and refinement (left) using the approach outlined by Cole *et al.* [113].

The overall model fit is shown in Figure 4-7, where experimental cure rate data and corresponding model predictions are compared for both isothermal and dynamic test conditions. The final cure model parameters are summarized in Table 4-3.

Table 4-3. Summary of 5276-1 cure kinetic model parameters.

Parameter	Reaction 1	Reaction 2
A_i (s^{-1})	3.50×10^4	2.50×10^4
$E_{a,i}$ (J/mol)	6.14×10^4	7.20×10^4
m_i	0.50	0.20
n_i	2.00	0.50
D	-	40
α_{C0}	-	-7.03×10^{-1}
α_{CT} (K^{-1})	-	3.73×10^{-3}

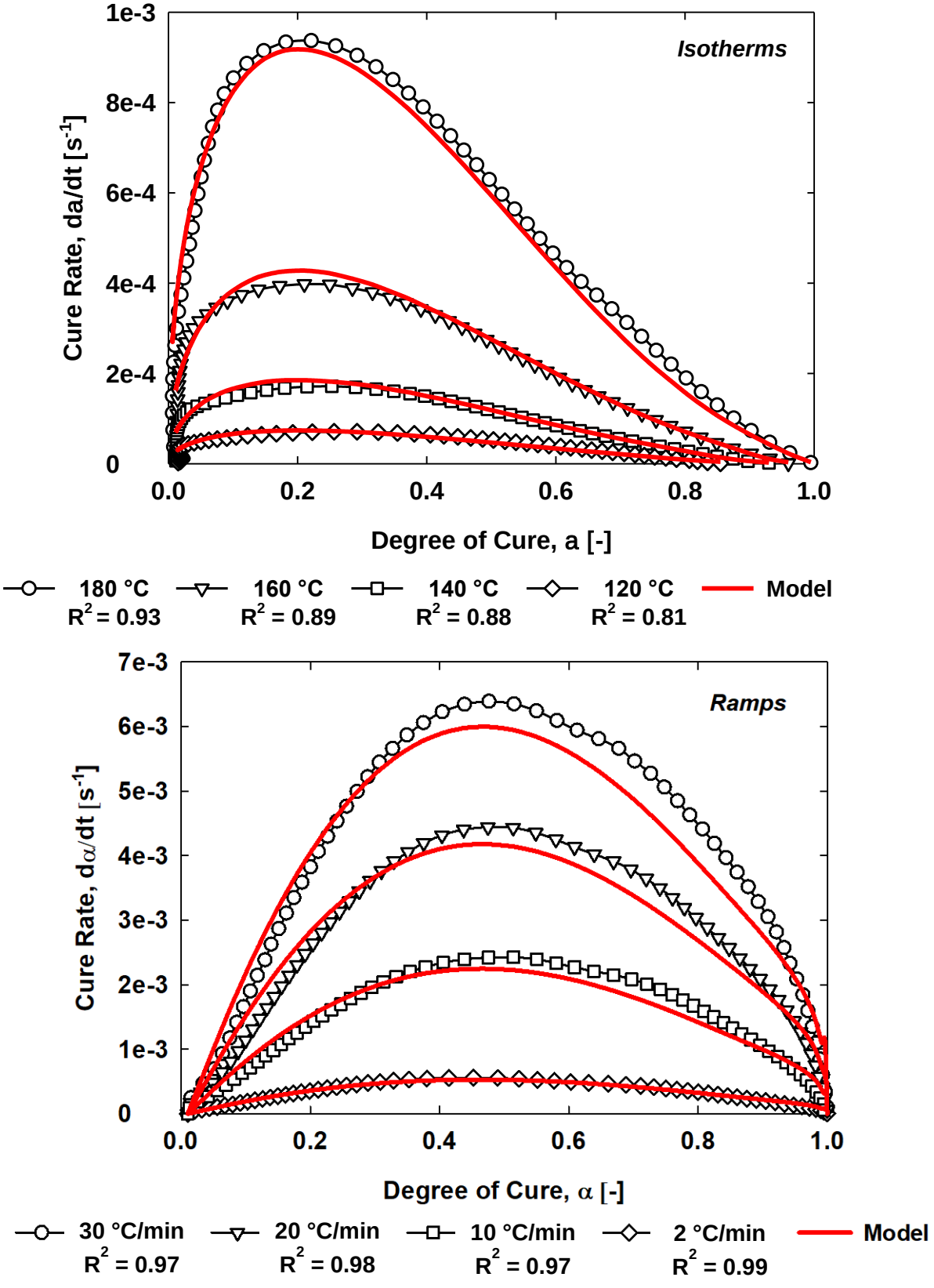

Figure 4-7. Measured and predicted cure rate curves for extracted 5276-1 resin.

4.3.3 Goodness of Fit

The quality of the model fit was assessed using the coefficient of determination (R^2) as well as the model deviation at two key points: the peak of the cure rate versus degree-of-cure curve and the final degree-of-cure (α_{max}). The R^2 values obtained for the isothermal predictions range from 0.81 to 0.93, indicating a strong correlation. Interestingly, the R^2 values obtained for the dynamic predictions are higher at 0.97 to 0.99, despite those tests not being used during the model fitting. A summary of all the R^2 values obtained, as well as both model and experiment values associated with each of the two key points chosen is shown in Table 4-4 for completeness.

Table 4-4. Goodness of fit summary table – Cure Model

Test	R^2	Peak Cure Rate α_{peak}, $d\alpha/dt\|_{peak}$		Final Degree-of-Cure α_{max}	
		Exp.	Model	Exp.	Model
120 °C	0.81	0.27, 7.14 x 10^{-5} s^{-1}	0.20, 7.40 x 10^{-5} s^{-1}	0.86	0.98
140 °C	0.88	0.24, 1.72 x 10^{-4} s^{-1}	0.21, 1.86 x 10^{-4} s^{-1}	0.93	0.99
160 °C	0.89	0.23, 3.98 x 10^{-4} s^{-1}	0.20, 4.28 x 10^{-4} s^{-1}	0.96	1.00
180 °C	0.93	0.21, 9.38 x 10^{-4} s^{-1}	0.20, 9.19 x 10^{-4} s^{-1}	1.00	1.00
2 °C/min	0.99	0.44, 5.59 x 10^{-4} s^{-1}	0.46, 5.29 x 10^{-4} s^{-1}	1.00	1.00
10 °C/min	0.97	0.50, 2.40 x 10^{-3} s^{-1}	0.47, 2.30 x 10^{-3} s^{-1}	1.00	1.00
20 °C/min	0.98	0.49, 4.40 x 10^{-3} s^{-1}	0.47, 4.20 x 10^{-3} s^{-1}	1.00	1.00
30 °C/min	0.97	0.48, 6.40 x 10^{-3} s^{-1}	0.46, 6.00 x 10^{-3} s^{-1}	1.00	1.00

The percent difference between the experimental data and model prediction was also calculated for each key point and is referred to as the *percent model deviation*. This analysis is presented in Figure 4-8, showing that the cure model predictions are better at higher cure temperatures and under dynamic testing conditions. At lower temperatures, the percent model deviations increase, culminating in a maximum at 120 °C, where α_{peak}, $d\alpha/dt|_{peak}$, and α_{max} reach - 9.8 %, 3.6 %, and 13.0 %, respectively. Peak cure rate magnitude deviations hover consistently around ± 5 %, while the location of the peak is almost always underpredicted, or early. The model does a good job of predicting the final degree-of-cure for most of the tests performed; however, it fails to adequately capture the effect of cure temperature on α_{max} as evidenced by a progressively larger percent deviation at 160, 140, and 120 °C. It is likely that these deviations stem from an

inadequate description of diffusion-driven curing at lower temperatures. It may be possible to improve the model predictions in these areas by including more low-temperature trials, by obtaining better diffusion parameters, or by considering a different diffusion model form.

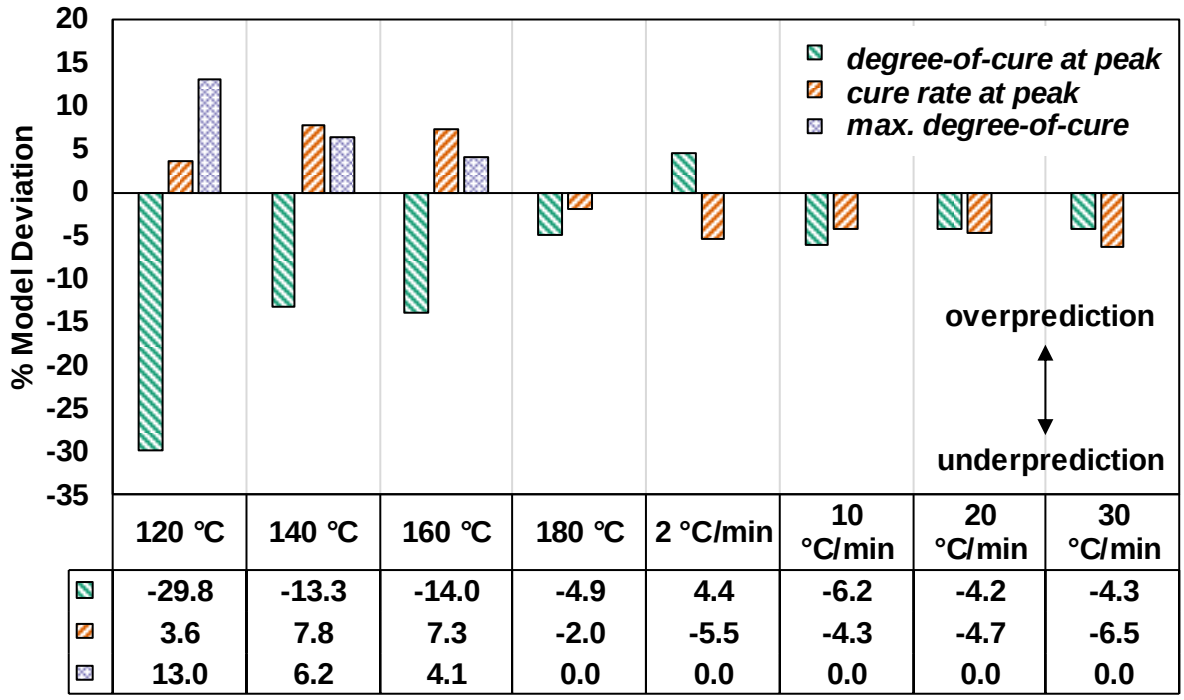

	120 °C	140 °C	160 °C	180 °C	2 °C/min	10 °C/min	20 °C/min	30 °C/min
degree-of-cure at peak	-29.8	-13.3	-14.0	-4.9	4.4	-6.2	-4.2	-4.3
cure rate at peak	3.6	7.8	7.3	-2.0	-5.5	-4.3	-4.7	-6.5
max. degree-of-cure	13.0	6.2	4.1	0.0	0.0	0.0	0.0	0.0

Figure 4-8. Percent model deviation summary – Cure Model.

Goodness of fit metrics like those presented here are most useful when making comparisons between model fits, which is why a detailed summary has been included above. It is difficult, however, to obtain a quantitative stand-alone conclusion from this type of analysis. This is particularly true when it comes to evaluating how accurate a cure model's predictions will be when applied to situations other than idealised DSC trials. This motivated the decision to perform a secondary model validation, which is described in the next section.

4.3.4 Model Validation

Slesinger [114] developed an experiment which tests a cure model's ability to predict the heat generated within an idealised 1-D heat transfer system. The method consists of measuring the temperature evolution within a composite laminate bounded by two rubber bricks of known thermo-physical properties during a cure cycle designed to excite a substantial exotherm. A schematic of the validation setup is shown below in Figure 4-9.

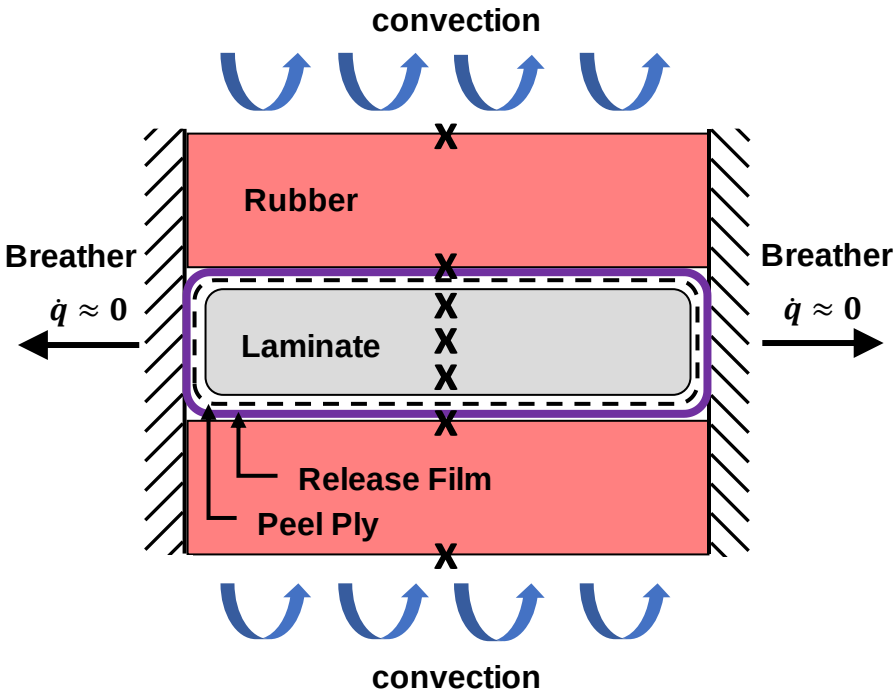

Figure 4-9. Schematic of the cure model validation experiment developed by Slesinger [114]. Thermocouple placement denoted by "x".

Laminate temperature can be predicted using thermocouple data from the outer surface of each rubber brick and by solving the governing equation for one-dimensional unsteady heat conduction within an isotropic material through each component layer:

$$\frac{\partial}{\partial t}\left(\rho C_P T\right) = \frac{\partial}{\partial x}\left(k\frac{\partial T}{\partial x}\right) + S\,, \tag{4.4}$$

where ρ is density, C_P is specific heat capacity, k is thermal conductivity, T is temperature, and S is the heat generation or source term. Relying on the assumption of proportionality between resin cure rate and the rate of heat release [115], the source term becomes:

$$S = H_R \cdot \frac{\partial \alpha}{\partial t}\left(1 - V_f\right)\rho_R C_{P,R}\,, \tag{4.5}$$

where H_R is taking from the extracted resin DSC tests as 366 J/g, V_f is the laminate fibre volume fraction, ρ_R is the resin density, and $C_{P,R}$ is the resin specific heat capacity.

The composite processing simulation software RAVEN (Convergent Manufacturing Technologies) was used to implement and solve the 1-D heat transfer problem depicted in Figure 4-9. A summary of the thermos-physical properties of each material is included in Table 4-5: The

properties of the peel ply and the fluorinated ethylene propylene (FEP) release film used were taken from Kratz et al. [116], who performed the same validation on two other aerospace epoxy systems. Properties for T650 carbon fibre were obtained from the COMPRO model documentation [117]. The rubber [118] and resin [110] properties were either taken from the manufacturer data sheet or obtained experimentally.

Table 4-5. Thermo-physical properties of materials used in validation simulations

Property	Rubber	5276-1	T650-CF	Peel Ply	FEP
Density (kg/m^3)	1540*	1300*	1770	1600	1720
Heat Capacity (J/kg-K)	1019 + 1.97T‡	1525 + 5.48T‡	712	900	775
Conductivity (W/m-K)	0.51‡	0.2‡	14/5	0.1	0.5

* Supplier data sheet, ‡ Obtained experimentally

The cure model validation results are presented in terms of the through-thickness temperature profile (Figure 4-11) and the laminate middle temperature (Figure 4-10) evolutions. From Figure 4-10, the ability of the cure model to predict the laminate middle temperature evolution is impressive. With an R^2 of 0.96 and only 0.9 % and 0.07 % deviations in the peak temperature time and magnitude, respectively, the correlation is undoubtedly strong.

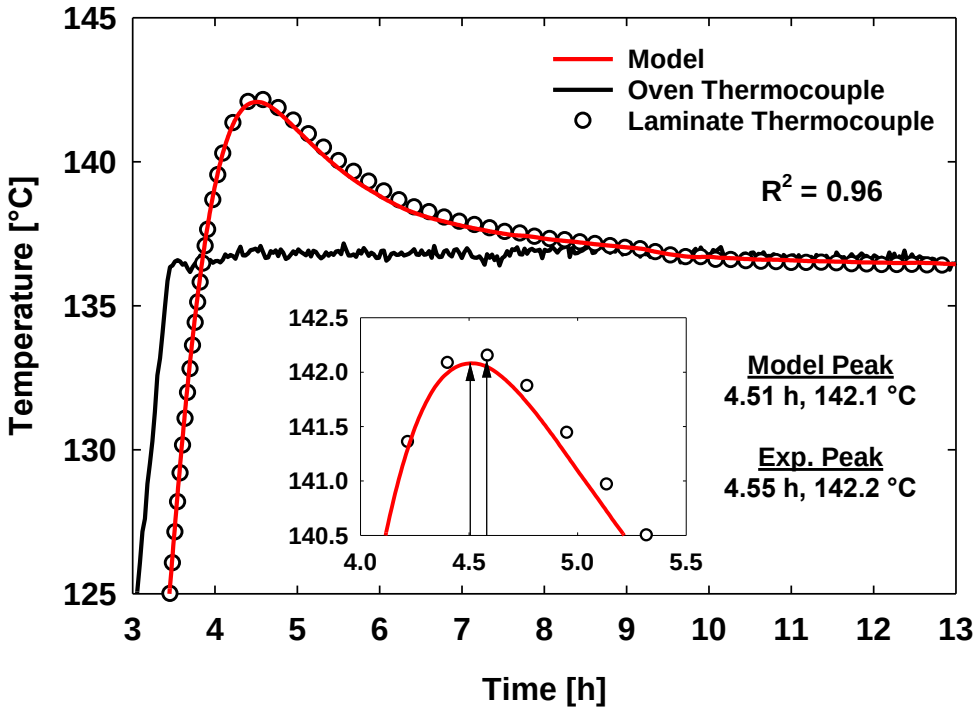

Figure 4-10. Measured and predicted laminate temperatures during cure model validation.

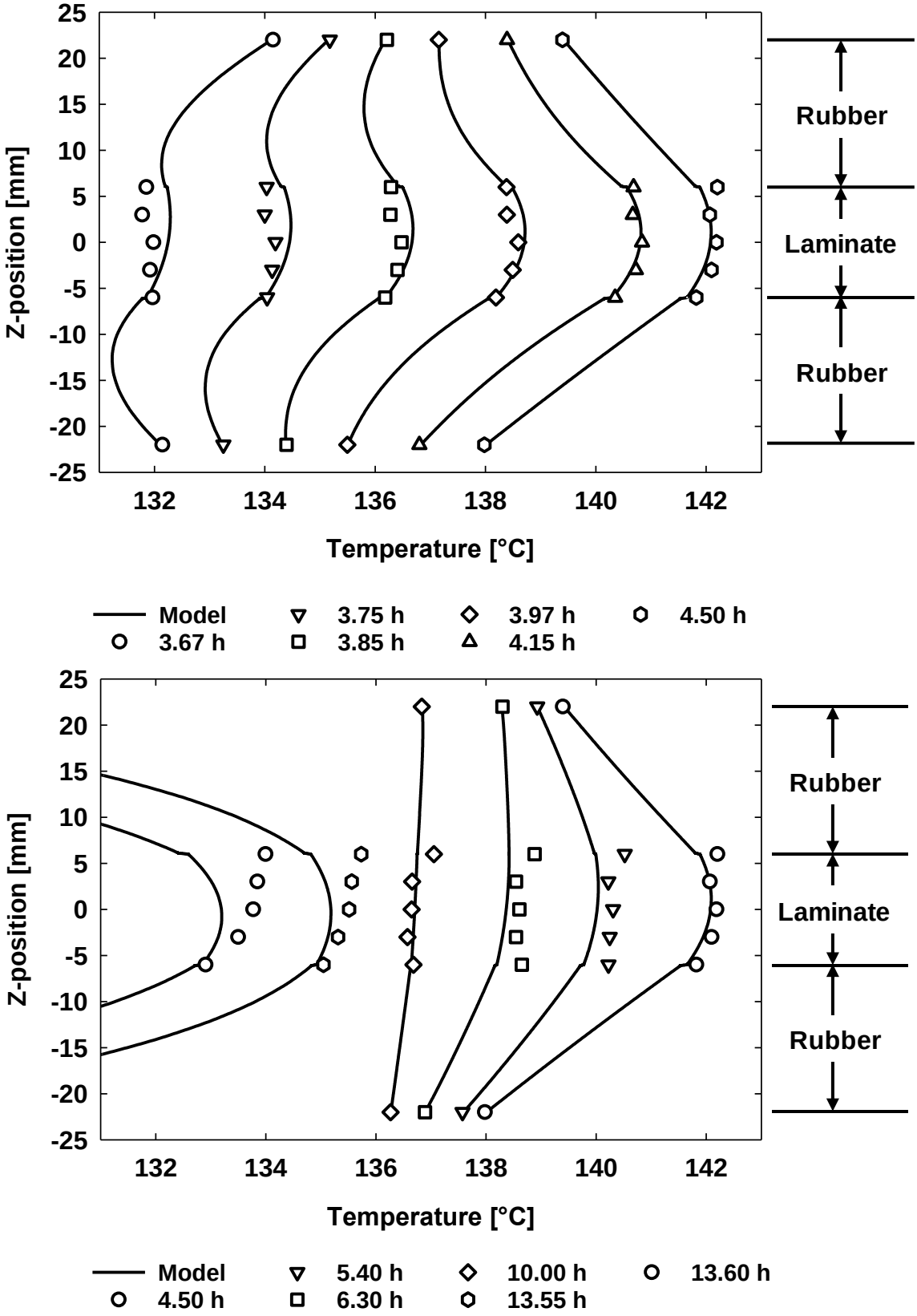

Figure 4-11. Measured and predicted through-thickness temperature profiles.

From Figure 4-11, the cure model does a good job of capturing the slight curvature of the experimental data during heat-up. The model seems to struggle somewhat during the laminate cooldown, where the model predicts faster cooling than what is measured via thermocouple. However, measurements taken at a time of 10 hours show that the thermocouple located between the upper rubber brick and release film may not have been functioning properly, as it read 1 °C above all the others despite the system being in equilibrium. Furthermore, the largest difference observed between model and experiment was under 2 °C.

4.4 Rheology

4.4.1 Test Matrix

The rheology of 5276-1 was studied by parallel plate rheometry using an AR2000 rheometer from TA Instruments. Dynamic and isothermal scans were used track the evolution of resin viscosity with respect to different time-temperature conditions. A summary of the tests performed is shown in Table 4-6 below.

Table 4-6. Rheometry test matrix for extracted 5276-1 resin.

Test Type	Conditions	% Strain	Repetitions
Dynamic Ramp	0.5, 1, 2 °C/min	1.0%	1-4
Isothermal Dwell	80, 100, 120, 140, 160 °C	1.0%	2

4.4.2 Model Fitting

Khoun et al. [119] proposed a modification to the gel model originally developed by Castro and Macosko [120, 121], suggesting that the addition of an Arrhenius temperature-dependent term and a quadratic degree-of-cure term would help to capture complex resin behaviour near gelation (Equation (4.6)).

$$\eta = \eta_1 + \eta_2 \left(\frac{\alpha_{gel}}{\alpha_{gel} - \alpha} \right)^{A + B\alpha + C\alpha^2}, \tag{4.6}$$

where η is the dynamic resin viscosity, η_1 and η_2 are Arrhenius terms given by Equation (4.7), α is the degree-of-cure, α_{gel} is the degree-of-cure at gelation, and A, B, and C are fitting parameters.

$$\eta_i = A_{\eta i} \exp\left(\frac{E_{\eta i}}{RT} \right), \tag{4.7}$$

where $A_{\eta i}$ is the Arrhenius pre-exponential factor, $E_{\eta,i}$ is the amount of energy required to overcome the polymer's internal resistance to strain, R is the ideal gas constant, and T is the temperature in units of Kelvin.

Initial fitting of Equation (4.6) to the isothermal data was unsuccessful despite following similar procedures to those found in the literature [116, 122]. Attempting regression at each temperature individually revealed a strong linear dependence of the fitting parameters B and C with temperature, which is shown in Figure 4-12.

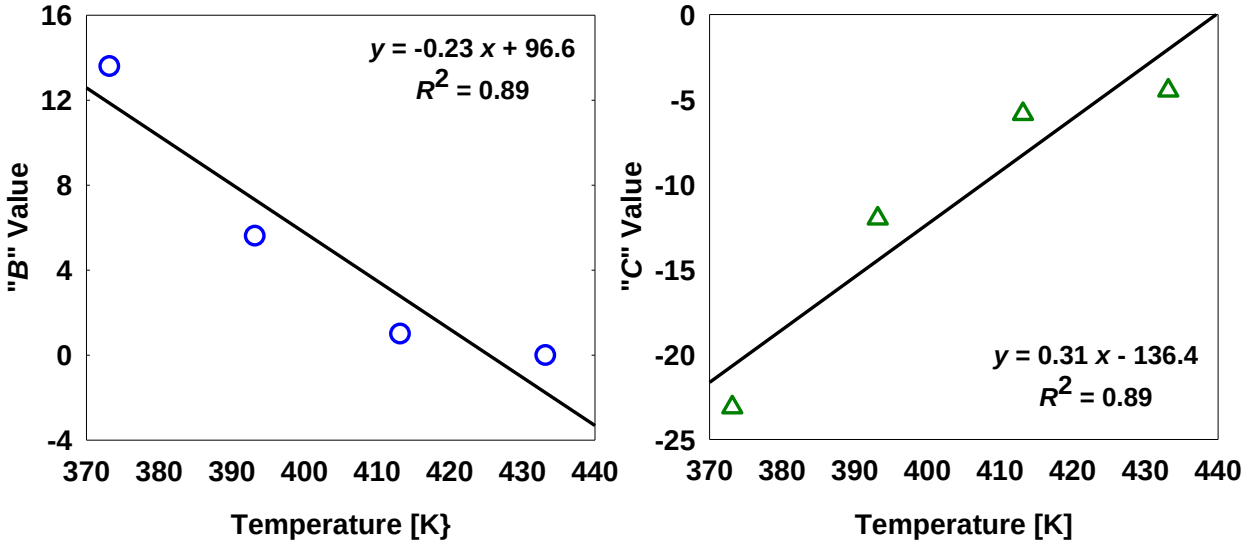

Figure 4-12. *B* and *C* values for best individual temperature fits.

Incorporating this behaviour into the "gel effects" term of Equation (4.6), acknowledges that changes in resin viscosity over time depend on both the instantaneous degree-of-cure and temperature. With the newly modified viscosity model, a global fit was obtained and is shown in Figure 4-13. The final model parameters are summarized in Table 4-7.

Table 4-7. Summary of 5276-1 viscosity model parameters.

Parameter	Term 1 (Viscous Behaviour)	Term 2 (Gel Effects)
$A_{\eta,i}$ (Pa-s)	1.00×10^{-13}	9.37×10^{-3}
$E_{\eta,i}$ (J/mol)	1.01×10^{5}	2.11×10^{4}
α_{gel}	-	0.63
A	-	4.06
B	-	$-0.23T + 96.6$
C	-	$0.31T - 136.4$

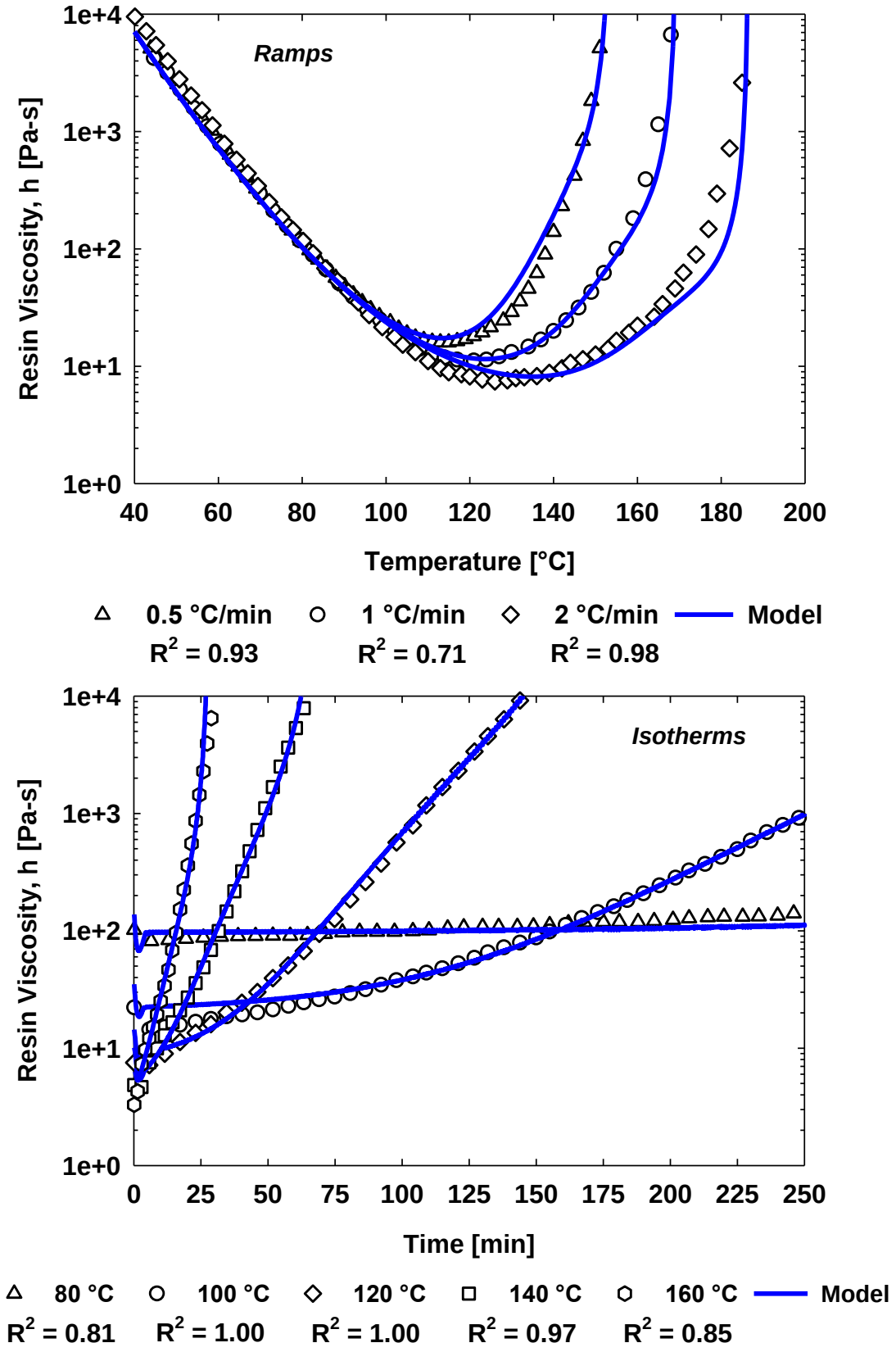

Figure 4-13. Measured and predicted isothermal viscosity curves for extracted 5276-1.

4.4.3 Goodness of Fit

As in Section 4.3.3, model goodness of fit was assessed using the coefficient of determination and the model predictions at two key points. Specifically, the minimum viscosity (time and viscosity) and the gel-point (time or temperature) were chosen as appropriate key points. A summary of all the R^2 values obtained, as well as both model and experiment values corresponding to each key point chosen is shown in Table 4-8.

Table 4-8. Goodness of fit summary table – Viscosity Model

Test	R^2	Minimum Viscosity t_{min}, η_{min}		Gel Point t_{gel} or T_{gel}	
		Exp.	Model	Exp.	Model
80 °C	0.81	1.60 min, 56.5 Pa-s	1.67 min, 67.6 Pa-s	16.00 h	27.50 h
100 °C	1.00	1.83 min, 11.1 Pa-s	1.83 min, 18.5 Pa-s	5.72 h	8.82 h
120 °C	1.00	1.13 min, 4.1 Pa-s	2.03 min, 8.0 Pa-s	2.89 h	3.18 h
140 °C	0.97	1.19 min, 3.1 Pa-s	2.23 min, 5.5 Pa-s	1.10 h	1.23 h
160 °C	0.85	0.41 min, 3.2 Pa-s	1.39 min, 5.3 Pa-s	0.49 h	0.50 h
0.5 °C/min	0.93	113 °C, 15.4 Pa-s	113 °C, 17.4 Pa-s	152 °C	153 °C
1 °C/min	0.71	119 °C, 11.1 Pa-s	124 °C, 11.5 Pa-s	168 °C	169 °C
2 °C/min	0.98	126 °C, 7.4 Pa-s	135 °C, 8.2 Pa-s	186 °C	185 °C

The R^2 values obtained for the isothermal and dynamic predictions range from 0.81 to 1.00 and 0.71 to 0.98, respectively. With the exception of $R^2 = 0.71$ for the 1 °C/min tests, these values indicate a strong model correlation to the data. The percent model deviation was again calculated for each key point and is shown in Figure 4-14. In all cases, the model overpredicted the time at which minimum viscosity is reached (late), as well as the magnitude of the minimum viscosity (high). The largest model deviation in terms of viscous behaviour prediction was observed at 160 °C, where the viscosity time and magnitude deviated by 108.4 % and 49.1 %, respectively. For the gel-point, a distinct increase in the percent model deviation was observed for test temperatures outside of the cure kinetic characterization window (80 °C, 52.9 %; 100 °C, 42.6 %). Dynamic model predictions were noticeably better at both key points, though no obvious explanation for this improved fit quality was found.

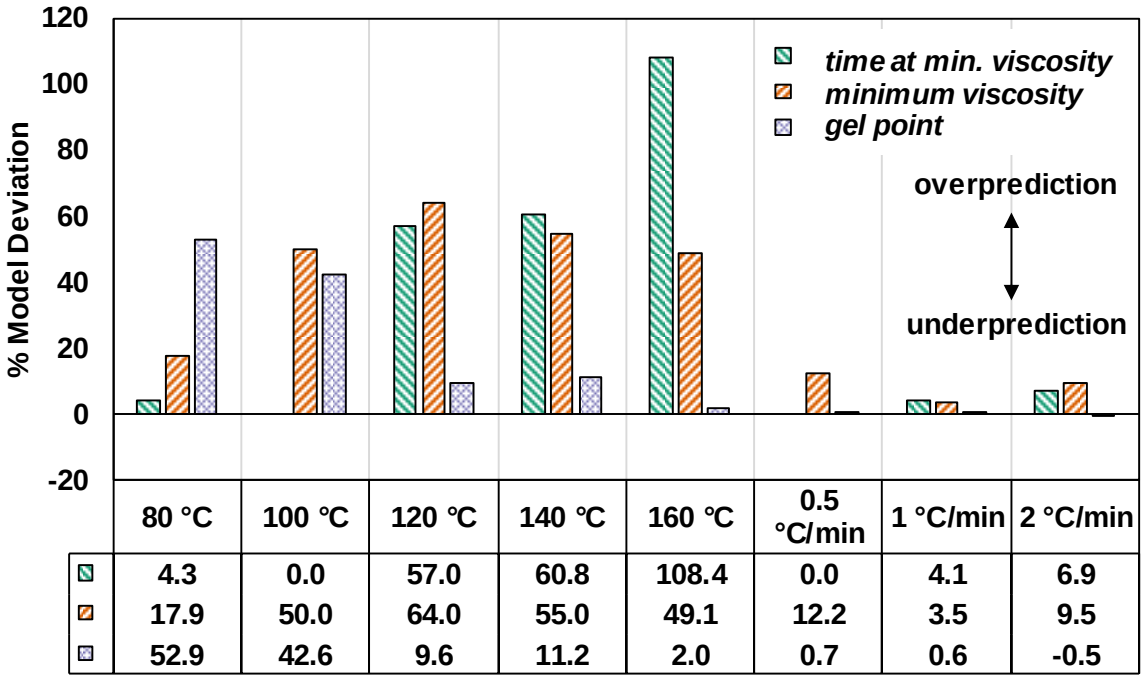

	80 °C	100 °C	120 °C	140 °C	160 °C	0.5 °C/min	1 °C/min	2 °C/min
time at min. viscosity	4.3	0.0	57.0	60.8	108.4	0.0	4.1	6.9
minimum viscosity	17.9	50.0	64.0	55.0	49.1	12.2	3.5	9.5
gel point	52.9	42.6	9.6	11.2	2.0	0.7	0.6	-0.5

Figure 4-14. Percent model deviation summary – Viscosity Model.

4.4.4 Model Validation

Following the logic outlined at the end of Section 4.3.3, a validation experiment was employed as a secondary evaluation of the viscosity model's robustness. In this case, a complex

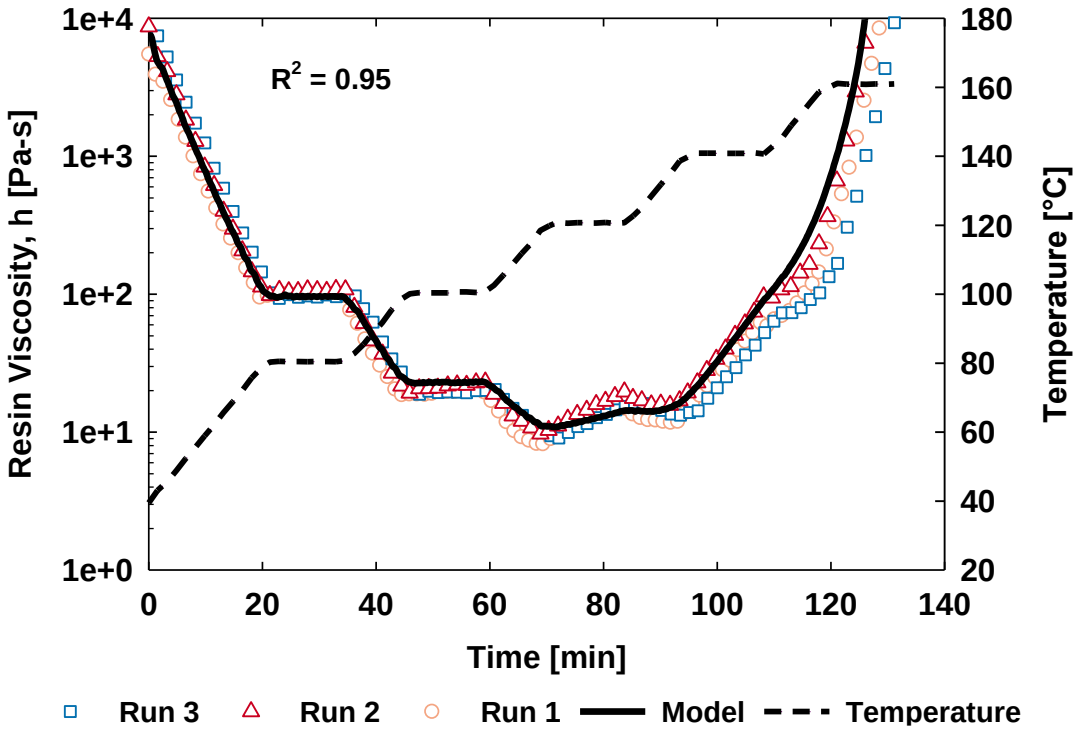

Figure 4-15. Viscosity model verification cycle for extracted 5276-1.

rheometer test cycle consisting of numerous ramps and dwells was chosen to simulate non-idealised curing conditions in which compounding error are promoted. The results of three experiment repetitions, as well as the corresponding model prediction (R^2 = 0.95) are shown in Figure 4-15. Visually speaking, the model captures the magnitude and timing of the viscosity changes associated with each step of the test within the repeatability of the experimental data.

4.5 Glass Transition Temperature

4.5.1 Test Matrix

The relationship between degree-of-cure and glass transition temperature for 5276-1 was explored by modulated DSC. Specimens of extracted NR and of both 8HS and PW prepregs were processed under a series of different time-temperature conditions to obtain incremental levels of cure from 0 to 1. A summary of the tests performed is shown below in Table 4-9.

Table 4-9. DSC test matrix for 5276-1 glass transition temperature characterization.

Test Type	Form	Test Conditions
Dynamic Ramp	NR 8HS	2 °C/min
Isothermal Dwell	NR	80, 100, 120, 140, 160 °C
Sequential Ramps	PW	150, 155, 160, 175, 275 °C
Interrupted Isotherms	NR	5 – 60 min; Δt = 5 min
	8HS	32, 87, 107, 122, 130.5 min

4.5.2 Model Fitting

The classic DiBenedetto relationship [123], shown in Equation (4.8), was chosen to model the glass transition temperature versus degree-of-cure behaviour:

$$\frac{T_g - T_{g0}}{T_{g\infty} - T_{g0}} = \frac{\lambda\alpha}{1-(1-\lambda)\alpha}, \tag{4.8}$$

where T_{g0}, $T_{g\infty}$, and T_g are the initial (α = 0), final (α = 1), and intermediate ($0 < \alpha < 1$) glass transition temperatures, respectively.

Normally used as an empirical fitting parameter, λ is said to vary between 0 and 1 based on the experimental findings of Adabbo and Williams [124] and Enns and Gillham [125].

However, Pascault and Williams [126] defined λ as "the ratio of segmental mobilities for a certain extent of reaction [α] with respect to the mixture of monomers [$\alpha = 0$]". They used a fundamental approach to show that λ could be computed using the ratio of the initial and final glass transition temperatures (Equation (4.9)) provided the corresponding ratio of lattice energies is equal to unity, which Nielsen [123] argued should be true. Pascault and Williams also showed that it is possible to approximate λ using the gel-point glass transition temperature ($_{gel}T_g$), defined as the "temperature at which gelation and vitrification occur simultaneously" [126] (Equation (4.10)).

$$\lambda_{Ratio} = \frac{T_{g0}}{T_{g\infty}} \tag{4.9}$$

$$\lambda_{Gel-Point} = \frac{2\left({}_{gel}T_g - T_{g0}\right)}{3\left(T_{g\infty} - {}_{gel}T_g\right)}, \tag{4.10}$$

All three of these approaches were implemented for comparison's sake. In each case, the λ obtained resulted in a fit with an R^2 value of 0.99 (Table 4-10). With no obvious reason to favour one result over the other, an average λ was computed and the corresponding model curve is shown in Figure 4-16 along with the DSC data collected from Table 4-9.

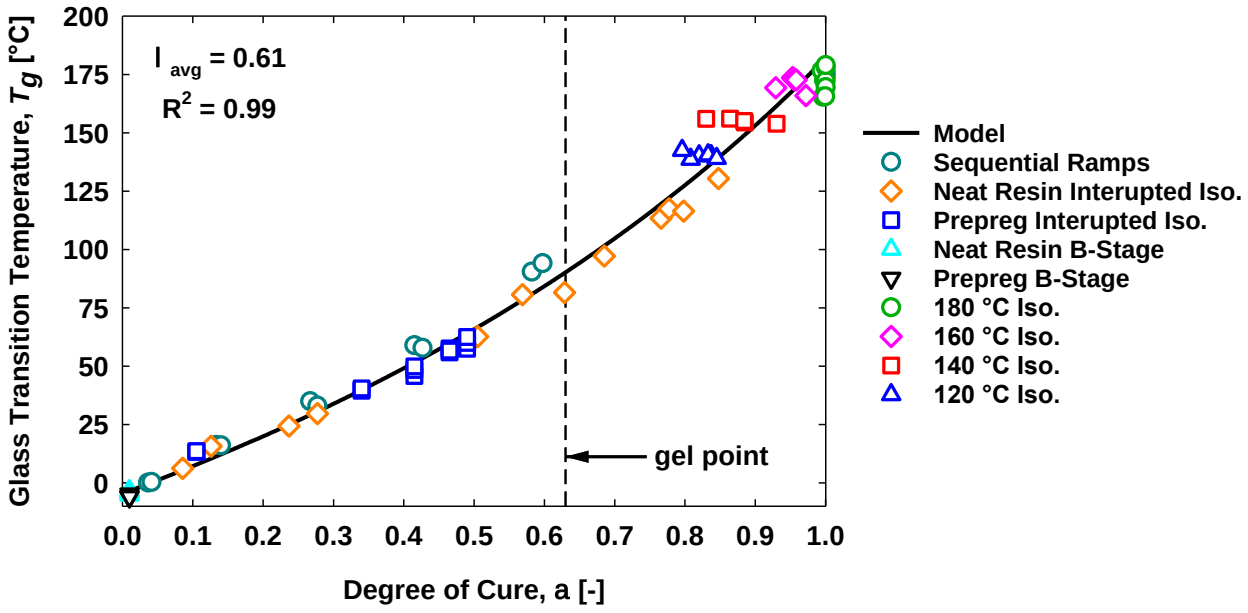

Figure 4-16. Measured (DSC) and predicted (DiBenedetto) glass transition temperatures of 5276-1 at various degrees of cure.

Table 4-10. Summary of 5276-1 DiBenedetto model parameters.

Parameter	Value	R^2
$T_{g,0}$	-4.6 °C	-
${}_{gel}T_g$	81.6 °C	-
$T_{g,\infty}$	182 °C	-
λ - Best Fit	0.66	0.99
λ - Gel Point	0.57	0.99
λ - Ratio	0.59	0.99

Given the variety of approaches used to determine λ and the strong correlations obtained, a validation experiment was deemed unnecessary. That being said, quite a few techniques that do not depend on changes in heat flow to determine T_g, including dynamic mechanical analysis (DMA), thermo-mechanical analysis (TMA), and rheometry would be interesting candidates for such a validation.

4.6 Summary

In this chapter, semi-empirical phenomenological models have been shown to adequately describe the curing, rheology, and glass transition behaviour of the 5276-1 resin system, within the scope of testing presented. Goodness of fit assessments and independent validation experiments revealed that Equation (4.1) has some difficulty capturing diffusion-related curing, resulting in increasing model deviations at lower temperatures as shown in Figure 4-8. This inaccuracy has undoubtedly carried over into the viscosity model predictions of gel-point as shown in Figure 4-14. That being said, Equation (4.6) does an admirable job at capturing the effect of temperature on resin viscosity. Finally, the DiBenedetto equation was found to easily capture the relationship between 5276-1 degree-of-cure and glass transition temperature with a coefficient of determination of 0.99.

5
ONE-DIMENSIONAL PREPREG FLOW-COMPACTION

In this chapter, an instrumented compression moulding apparatus and an electro-mechanical testing frame were used to study the one-dimensional flow-compaction behaviour of woven prepreg strands under different moulding conditions. An elevated temperature staging technique was used to alter resin initial degree-of-cure as a means to investigate the effect of resin viscosity on the magnitude and nature of prepreg flow. Mould closure rates of 0.01, 0.1, and 1 mm/s were then used to explore the rate-dependency of prepreg flow-compaction. A compression moulding process map was built based on the results of both viscosity and rate-dependence testing.

5.1 Flow-Compaction Mechanisms

Two distinct, yet often coupled, mechanisms contribute to the flow-compaction behaviour of fibre-reinforced polymers: The first is *percolation flow*, which is characterized by the movement of resin relative to a quasi-static fibre bed and which is dominant in processes like resin transfer moulding, resin film infusion, and prepreg autoclave curing. The second is *shear flow*, which features coupled movement of fibre and matrix and which is dominant in processes like compression moulding, injection moulding, and thermoforming. Figure 5-1 provides a generalized schematic representation of both mechanisms; however, each mechanism will manifest at different length scales depending on the type of forces present and on the material structure. For example,

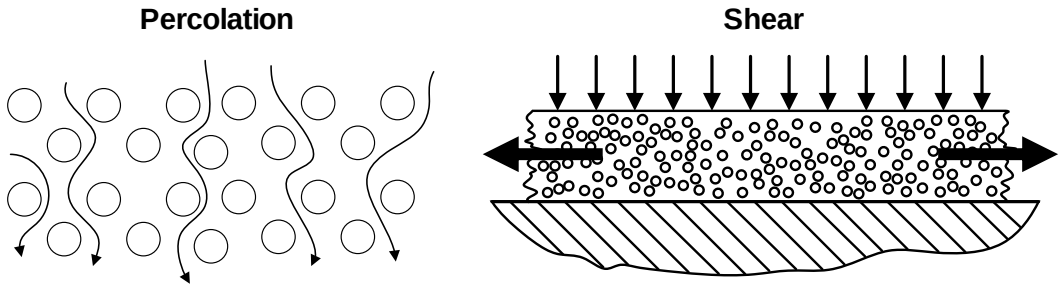

Figure 5-1. Resin percolation (left) and generalized shear flow (right) [127].

both macroscopic and microscopic (capillary) resin percolation are observed in the infusion of continuous fibre preforms and must be accounted for using appropriate infusion speed. Similarly, different modes of shear flow exist (e.g. interply shearing, inraply shearing, squeeze flow) and will affect the manufacturing outcome.

5.2 Processing-Related Defects

There is a strong relationship between the design of a composite precursor material, how that material is processed, and final part quality [18, 128]. Changes in material state prior to manufacture, or in processing conditions can cause unintended excitation of flow mechanisms which cause part defects. Figure 5-2 shows two such examples: In example A, a lack of resin percolation has resulted in incomplete prepreg tow impregnation. In example B, insufficient interlaminar slippage during part consolidation has caused convex corner wrinkling.

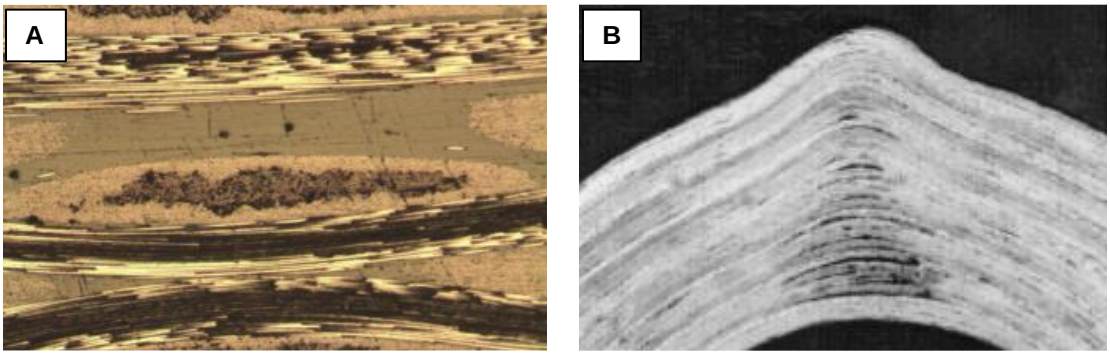

Figure 5-2. Incomplete resin impregnation of prepreg tows due to extended out-time (A) [129][3]. Convex corner wrinkling due to a lack of interply slippage in flanges (B) [88].

This same principle applies to the compression moulding of woven prepreg strands, where fibres in both 0° and 90° directions restrict shear flow and make successful feature filling and

[3] Image reprinted by permission from the Society for the Advancement of Material and Process Engineering (SAMPE)

excessive resin bleed realistic processing challenges (Figure 5-3). This is, in fact, the reason that most prepreg-based moulding compounds are made using unidirectional tapes. Nonetheless, fabrics make up the majority of prepreg production waste, so their flow-compaction behaviour should be understood for recycling to be successful.

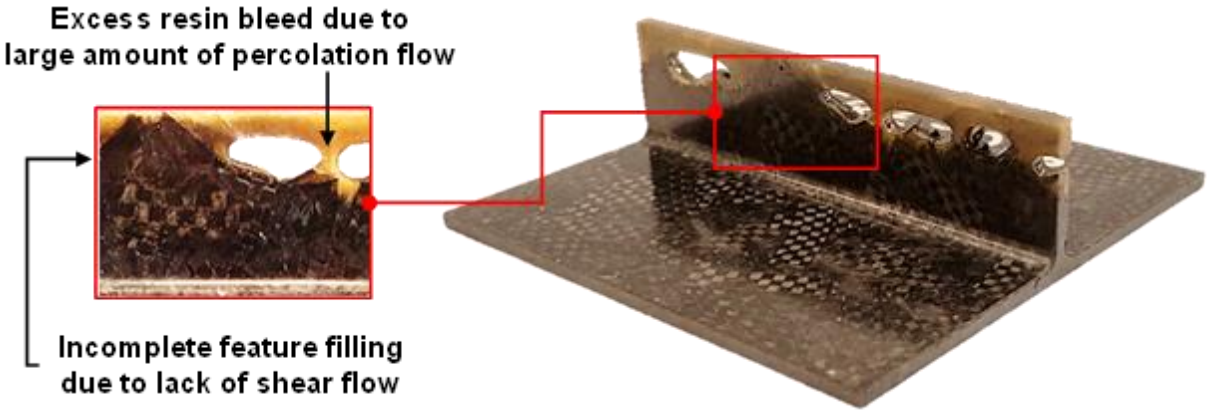

Figure 5-3. Attempt at moulding a rib-stiffened panel using expired woven prepreg.

5.3 Flow-Compaction Method

As the literature review in Chapter 2 discusses, compression moulding of prepreg strands has been studied using a variety of different experimental approaches. The method used here, henceforth referred to as simply *flow-compaction method*, is based on the work of Hubert [88] who studied the consolidation of various autoclave prepreg tapes using a heated channel compression mould. A detailed description of this flow-compaction method, including the specimen design, apparatus, and experiment workflow is present in this section.

5.3.1 Specimen Design

The decision was made early on to keep strand size constant for all 1-D flow-compaction tests, advanced flow trials (Chapter 7), and mechanical characterization (Chapter 8). Previous studies have shown that strand size has an effect on bulk material flow [90], residual stress development and warpage [104], as well as part mechanical strength and stiffness [83, 100]. Square strands measuring approximately 12.7 mm by 12.7 mm were chosen to balance these three characteristics and all flow-compaction specimens consisted of a $[0_6]_T$ stack of these strands. The flow of these specimens will be restricted to one longitudinal axis by the walls of the heated channel mould described in the next section. This is shown schematically in Figure 5-4.

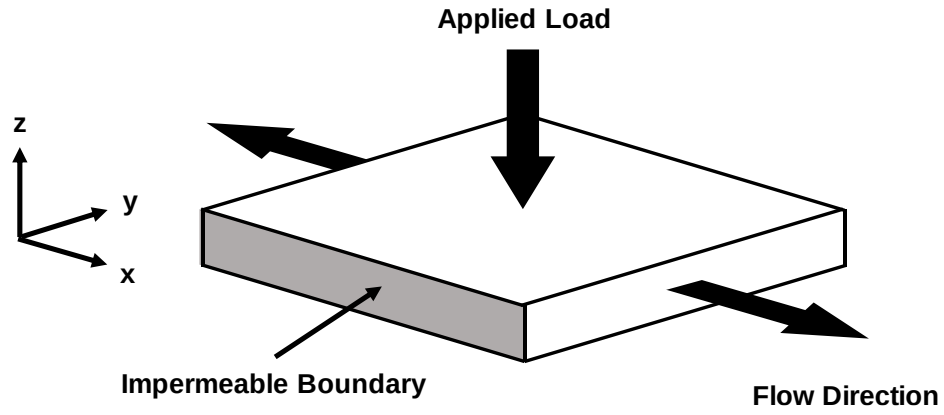

Figure 5-4. Schematic of flow-compaction specimen adapted from [88].

5.3.2 Apparatus

A detailed view of the apparatus that was developed for the flow-compaction method is shown in Figure 5-5. The main component of the apparatus is a 12.7 mm wide rectangular piston-channel mould made from AISI 4140 alloy steel. A gap tolerance of 0.0127 mm between the piston

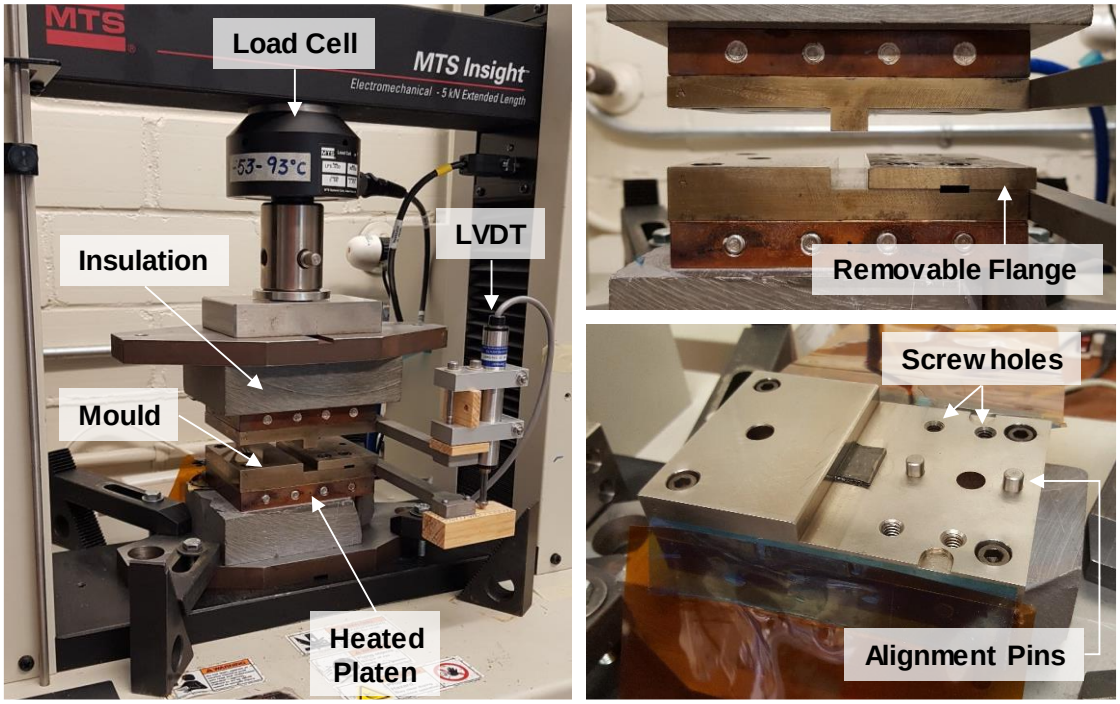

Figure 5-5. Instrumented flow-compaction apparatus.

and channel walls prevents material from escaping in the z-direction during testing. The mould also includes a removable flange to facilitate cured specimen removable. Temperature was controlled using resistive cartridges heaters, a PID limit controller, and a K-type thermocouple from Watlow Electric Manufacturing Co. The cartridge heaters are fit into copper plates using heat

transfer paste to promote in-plane temperature uniformity across the mould surfaces. The apparatus is mounted on an Insight 5 kN table-top electromechanical testing frame from the MTS Corporation. Force is measured using the frame's 5 kN load cell, and displacement of the upper and lower tooling surfaces is measured using an HS25 LVDT from Vishay Precision Group. Finally, blocks of machinable insulation prevent excessive heating of the load cell, which has a maximum operating temperature of 93 °C, as well as the surrounding work surfaces for safe operation.

5.3.3 Experiment Workflow

A schematic of the experiment workflow is presented in Figure 5-6, followed by an in-depth description of each step and the corresponding outcomes.

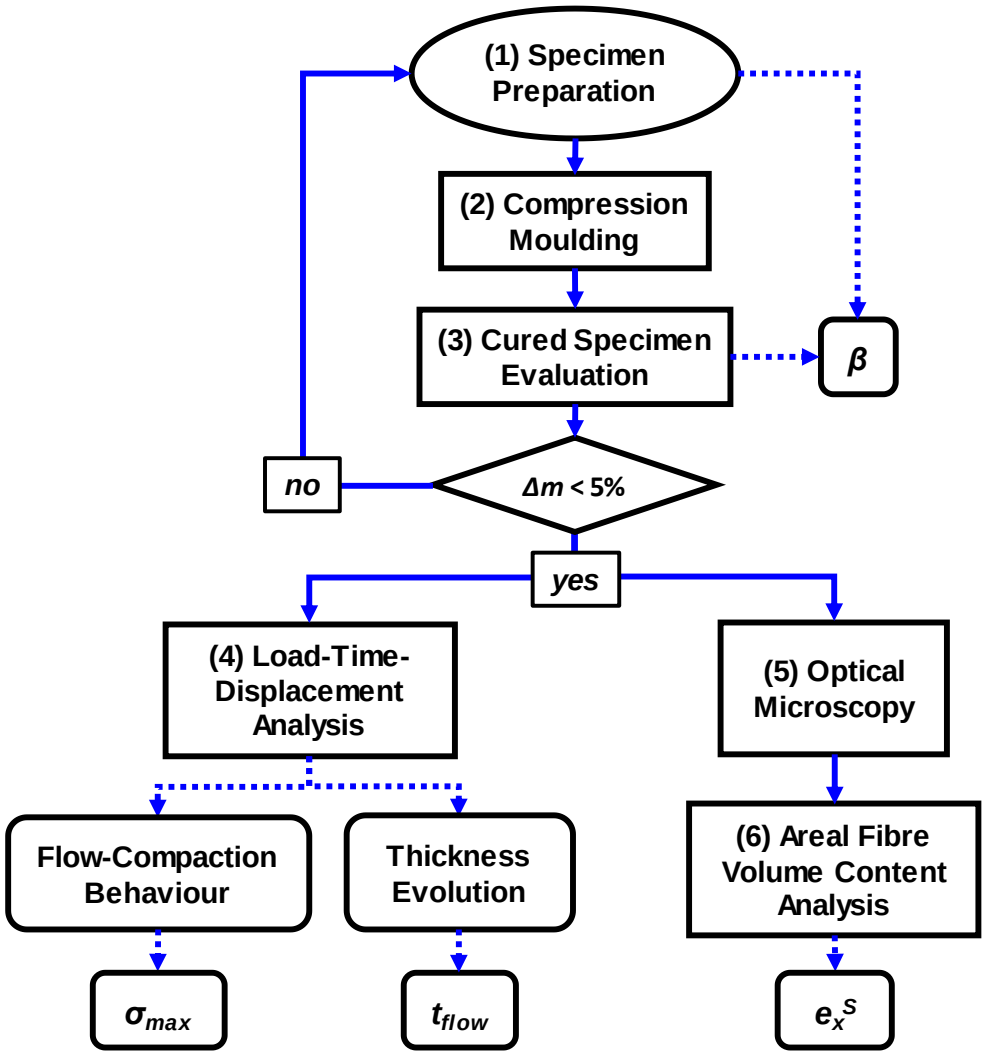

Figure 5-6. Flow-compaction experiment workflow.

Specimen Preparation

Prepreg strands are stored in sealed bags at -18 °C prior to testing to preserve the state of the resin. Shortly before testing, the strands are thawed at room temperature. Moisture contamination is avoided by opening the sealed bag only after condensation is no longer observed on the bag surface and it is no longer cool to the touch. The length (L_0) and width (W_0) of each strand, which correspond to the *x* and *y* axes shown in Figure 5-4, respectively, are measured using a digital caliper and then stacked according the aforementioned $[0_6]_T$ layup. The uncompressed specimen thickness (h_0) is also measured and is used to calculate the bulk factor. Finally, the specimen's initial mass (m_0) is measured using a precision scale.

Compression Moulding

Once a specimen has been prepared, it is placed inside the channel mould which has been preheated to the testing temperature. The frame's crosshead is then lowered at 0.5 mm/s until a preload of 25 N is applied to the specimen. This corresponds to a pressure of 0.16 MPa for a 12.7 mm square specimen, assuming negligible in-plane deformation. Once the preload is reached, the crosshead position is held constant for 60 seconds to ensure that each test is performed under uniform temperature conditions.

At this point, it is assumed that (1) spaces between strands have been completely removed, (2) no significant deformation or change in the fibre bed architecture has occurred, (3) no significant quantity of resin has bled from the specimen, and (4) the specimen constituents, fibre and liquid matrix, are effectively incompressible. Assumptions 1-3 were verified visually using pictures of specimens before and after preloading (Figure 5-7). Notice that empty spaces between

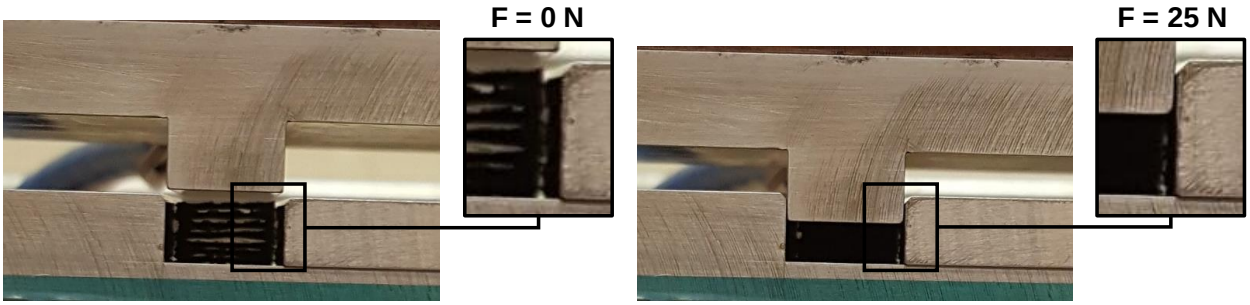

Figure 5-7. Flow-compaction specimen before (left) and after (right) preloading.

the stack strands have disappeared following preloading, while the gap between the specimen edge and mould wall is still discernible, indicating consolidation without significant flow. The specimen volume is therefore given by Equation (5.1):

$$V = \overline{L_0} \cdot \overline{W_0} \cdot h_0', \tag{5.1}$$

where $\overline{L_0}$ is the average initial strand length, $\overline{W_0}$ is the average initial strand width, and h_0' is the specimen thickness which was measured using the LVDT after preloading. The instantaneous normal stress given by Equation (5.2) can be computed using the specimen volume from Equation (5.1), the instantaneous specimen thickness ($h(t)$) and applied force ($F(t)$), along with the assumption of incompressibility.

$$\sigma(t) = \frac{F(t) \cdot h(t)}{\overline{L_0} \cdot \overline{W_0} \cdot h_0'} \tag{5.2}$$

Following preloading and temperature equilibration, the crosshead is lowered at a constant displacement rate until the prescribed test force is reached, at which point the frame switches to PID force-control for the remainder of the test. The cure dwell and final cooling ramp are chosen, with the help of the 5276-1 cure and viscosity models from Chapter 4, such that gelation and vitrification occur prior to demoulding (Figure 5-8).

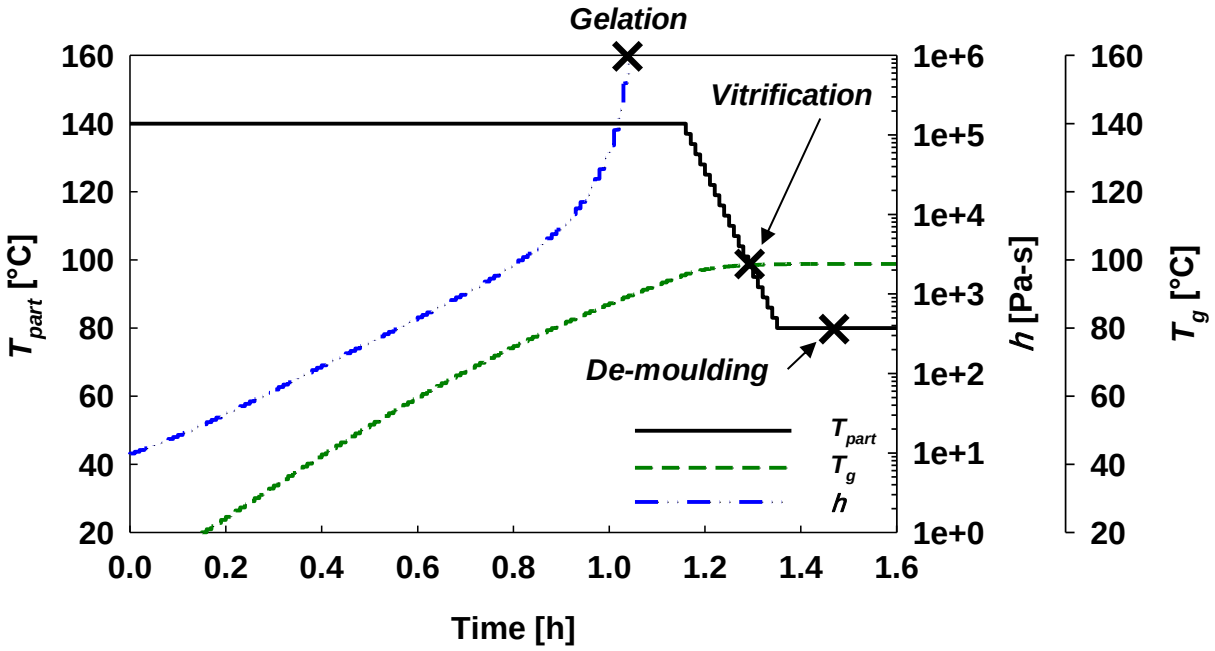

Figure 5-8. Idealised representation of a flow-compaction test cure cycle.

Cured Specimen Evaluation

Any flashing is removed from the cured specimen and it is weighed to determine the amount of material lost due to percolation in the z-direction (Δm). If the mass loss surpasses 5% of the original specimen mass, the test is deemed a failure and a new specimen is prepared.

Optical Microscopy

The final specimen length (L_f) was measured using optical micrographs of specimen midplane sections. This approach was chosen instead of using traditional calipers of micrometer because, when using woven prepregs, the final specimen edge (transition between fibre and resin) is often difficult to determine with a basic visual inspection [130].

Preparation of optical microscopy samples was carried out according to the recommendations outlined by Hayes and Gammon [131]: Several flow-compaction specimens were cured in Amazing Clear Cast potting resin from Alumilite under ~80 psi (550 kPa) to mitigate the presence of air bubbles. The resulting "puck" was sectioned using a Struers Secotom-50 precision saw to expose the specimens' midplane (Figure 5-4: x-z plane). These sections were then progressively ground and polished on a metkon Forcipol automated polishing unit with abrasive sizings of 220 – 1200 grit and 12.5 – 0.3 µm, respectively. Once a satisfactory surface finish was obtained, specimens were imaged at X200 magnification using a Nikon microscope equipped with a USB vision camera from Sentech. Mosaics were then created using the stitching function built into the Image Capture software offered by DCI Microscopy.

Areal Fibre Volume Content Analysis

Both fibre-counting and area-based algorithms have been used in the literature to optically measure the fibre volume fraction (V_f) of fibre-reinforced polymers [132-134], though no international standard has yet been adopted. An area-based algorithm, written in MATLAB, was used here to measure V_f along flow-compaction specimens' x-axis. The decision to use an area-based approach was made because of the method's practicality and ease of implementation. The author does, however, acknowledge that fibre counting methods are more accurate when compared to the ASTM acid digestion standard [135]. N.B.: Image thresholding operations were carried out in Fiji (ImageJ) using Otsu's method to remove human bias.

Strain Measurement

Next, L_f is determined using a minimum fibre volume content limit of 20%, as shown in Figure 5-9. This cut-off reflects fibre volume contents typical of SMC (20-30%) and BMC (10-20 %) compression moulded parts [136]. Thus, anything below 20 % was considered to be resin percolation. In many of the specimens tested, a dip below 20 % was observed immediately after the edge of the original prepreg stack. This often coincided with the end of a large concentration

of 0° fibres. In almost all cases, V_f quickly increased to over 20 % for the remainder of the specimen length and, for this reason, only the final dip below the 20 % was used to determine L_f.

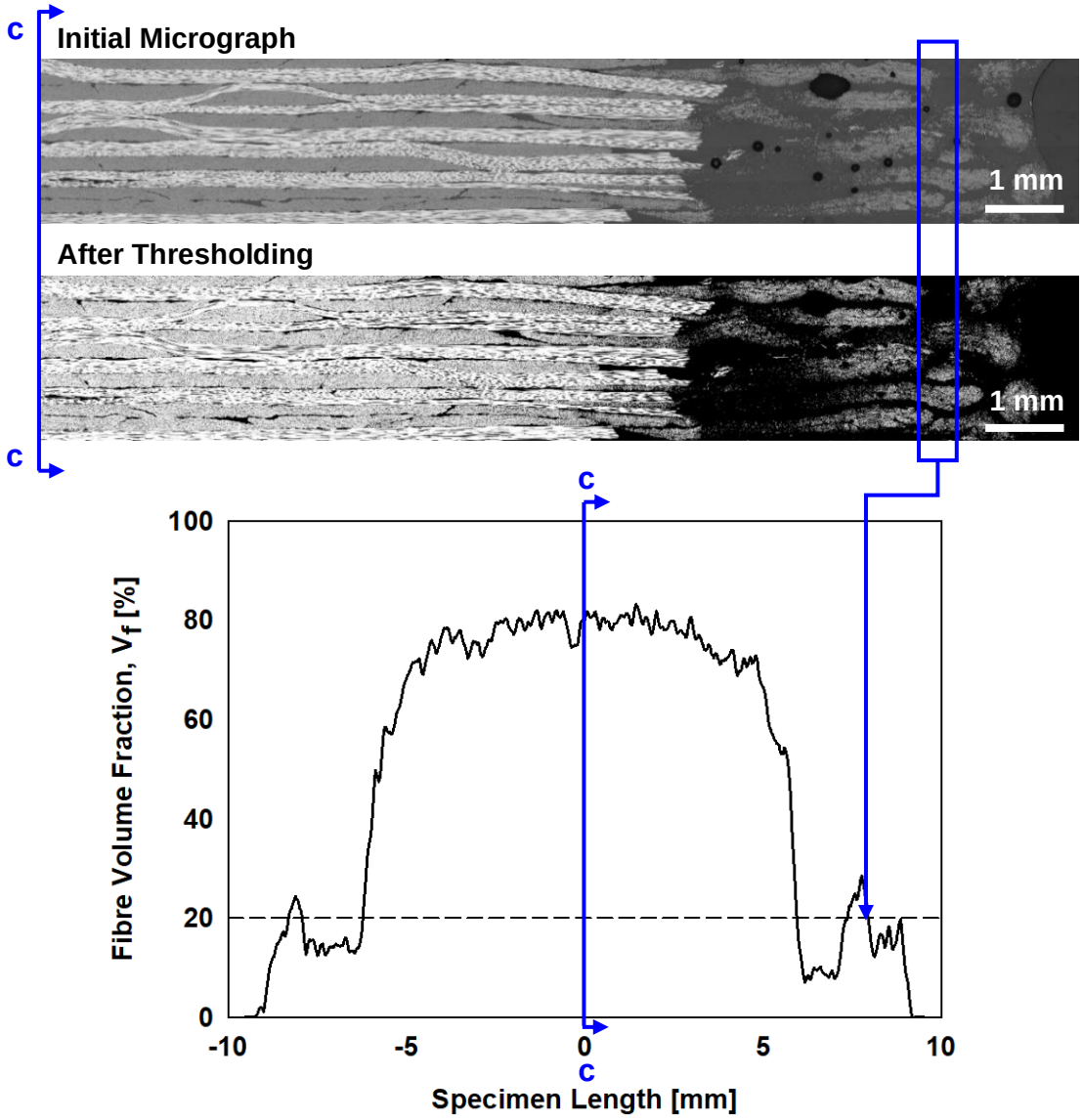

Figure 5-9. Illustration of the method used to determine the final specimen length.

Next, the final shear strain (e_x^S) was calculated using x-direction scalar component of the Green strain tensor, given by Equation (5.3). The Green strain tensor includes quadratic terms in

$$e_x^S = \frac{1}{2}\left[\left(1+\frac{L_f-\overline{L_0}}{\overline{L_0}}\right)^2-1\right] \tag{5.3}$$

addition to the small strain terms more commonly known as engineering strain, making it rotation independent and better suited for quantifying large deformations.

Load-Time-Displacement Analysis

The data captured by the electromechanical testing frame and LVDT are processed using another MATLAB script to obtain the flow-compaction behaviour (σ vs. h/h_0) and the thickness evolution (h/h_0 vs. time). The maximum specimen normal stress (σ_{max}) and the flow window (t_{flow}) are then obtained from these two curves. The flow window was defined here as the time required for 95% of the total specimen deformation to occur and is used to calculate the average resin viscosity of a specimen during testing.

5.4 Effect of Resin Viscosity

Significant deviations in resin viscosity during manufacturing can alter resin-reinforcement interactions and lead to defects (see Section 5.2). Table 5-1 shows that some very well-established autoclave curing resins have processing viscosities within a 0.4 – 50 Pa-s window, while traditional thermoplastic compression moulding polymers feature melt viscosities in the range of 70 – 1500 Pa-s. This large difference gives an indication of the importance of resin viscosity, although it is unclear what effect it will have on the flow-compaction behaviour of woven 5276-1 offcuts. This section endeavours to answer the following questions: (1) How can the processing viscosity of an autoclave prepreg resin such as 5276-1 be elevated to within 100 – 1000 Pa-s, a level comparable to systems designed for compression moulding (Sections 5.4.1 and 5.4.2)? (2) What is the relationship between resin viscosity and the relative amounts of percolation and shear flows excited during compression moulding (Sections 5.4.3 and 5.4.4)? These questions need to be addressed if defects like the ones shown in Figure 5-3 are to be avoided.

Table 5-1. Viscosity comparison of autoclave and compression moulding resin systems.

Autoclave Curing		**Compression Moulding**	
System	***Viscosity***	***System***	***Viscosity***
Hexcel 3501-6	0.4 Pa-s [88]	TORELINA PPS	150 – 400 Pa-s [137]
Hexcel 8552	1 – 10 Pa-s [138]	Vitrex PEEK 151	300 – 700 Pa-s [139]
MTM45-1	5 – 50 Pa-s [116]	ULTEM 1000 PEI	70 – 1500 Pa-s [140]

5.4.1 Temperature Reduction Trials

Perhaps the most straightforward way to increase resin processing viscosity is by lowering the cure temperature. This approach was explored by carrying out flow-compaction tests on 8-ply

8HS/5276-1 specimens at 180, 160, 140, 120, and 100 °C. Micrographs prepared from these specimens revealed an excessive amount of resin percolation and no shear flow [130]. A representative example from the 100 °C tests is shown in Figure 5-10.

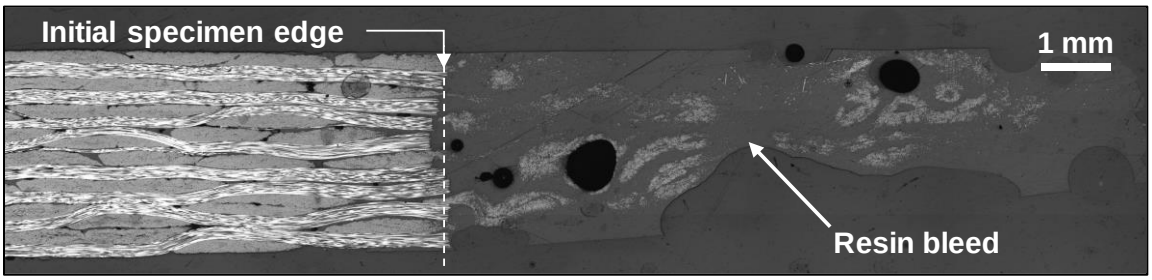

Figure 5-10. Micrograph of a flow-compaction specimen made using as-received prepreg and moulded at a temperature of 100 °C and applied force of 4 kN.

Figure 5-11 shows that even cure temperatures as low as 100 °C could not produce initial resin viscosities (η_0) in the range of the compression moulding thermoplastics shown in Table 5-1. Furthermore, lowering the cure temperature results in a reduction in resin reactivity leading to unrealistically long gel-times. For example, if the cure temperature was lowered to 80 °C, resin viscosity would be approximately 150 Pa-s and gelation would occur after 24 hours.

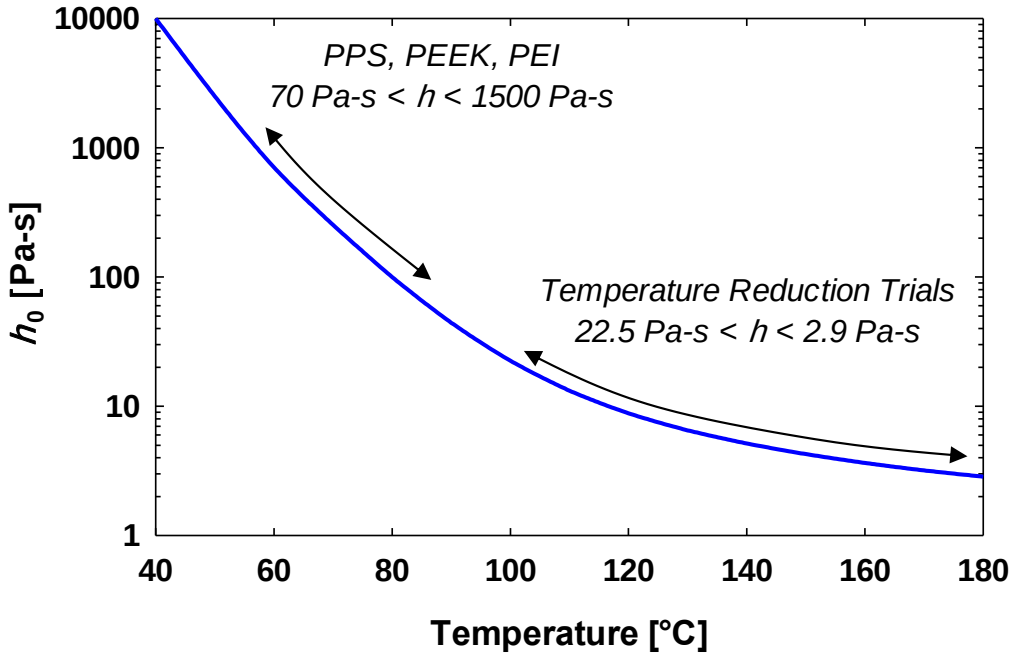

Figure 5-11. Initial resin viscosities obtained using the viscosity model for 5276-1 developed in Chapter 4 plotted against the corresponding cure temperatures.

5.4.2 Prepreg Staging

Alternatively, increasing a resin's initial degree-of-cure (α_0) can bring about an increase in processing viscosity at a given temperature without lengthening the cure window. This is commonly observed with vacuum-bag-only prepregs subjected to extended periods of room temperature out-time [141] and during the B-staging phase of both solution-dip and hot-melt prepregging [19, 142]. The potential for prepreg *staging*, or partial curing, to bring about the necessary increase in 5276-1 viscosity was assessed by generating a map of η_0 versus α_0 for different cure temperatures: This map is shown in Figure 5-12.

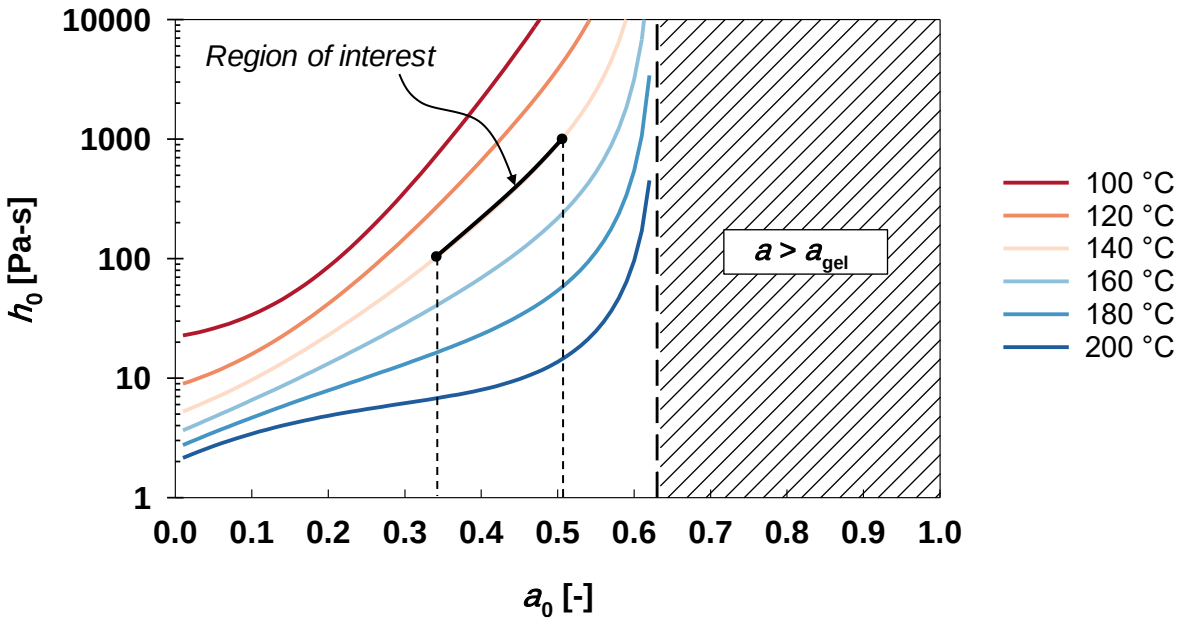

Figure 5-12. Initial resin viscosity versus initial degree-of-cure of 5276-1 at different temperatures.

At first glance, Figure 5-12 offers a wide range of possible α_0 – temperature combinations that correspond to viscosities in the compression moulding region of interest discussed at the beginning of Section 5.4. For example, choosing $0.35 < \alpha_0 < 0.5$ and a temperature of 140 °C gives an approximate viscosity window of 100 – 1000 Pa-s. Because 140 °C is within the range of temperatures used to characterize and model the 5276-1 cure and viscosity behaviours, these parameters were chosen as a starting point for the flow-compaction testing of 8HS/5276-1 strands. The steps followed to achieve these levels of α_0, now referred to as α_{staged}, are presented below:

Step 1

Dynamic modulated DSC scans were performed on samples taken from a batch of recovered 8HS/5276-1 offcuts. The batch's as-received glass transition temperature ($T_{g,x}$), taken as the half-

height transition temperature on the reversible heat flow signal, was measured to be -3.29 ± 1.08 °C. Corresponding α_x values were then obtained from the 5276-1 T_g model.

Step 2

Having selected a cure temperature of 140 °C, the 5276-1 viscosity model and α_x from step 1 were used to determine values of α_{staged} corresponding to moulding viscosities in the range of interest (i.e. 10 – 1000 Pa-s). Arbitrarily choosing a staging temperature within the cure model's characterization window of 120 °C, the necessary staging times were then calculated.

Step 3

Having decided to focus on 12.7 mm x 12.7 mm strands (see Section 5.3.1), offcuts were cut into 12.7 mm wide strips using a standard utility knife. These strips were placed side-by-side between two layers of non-perforated PTFE release film and the edges sealed with tape to create a "staging envelope" (Figure 5-13 – left). This envelope was placed in a convection oven between two aluminium plates that had been preheated to between 118 – 120 °C (Figure 5-13 – right).

Figure 5-13. Preparation of a staging bag (left) and preheated aluminium staging plates (right).

Step 4

The staging envelope was removed from the oven after the staging time had elapsed and immediately placed between another two aluminium plates at room-temperature to avoid further polymerization. This step also reduced the post-staging prepreg thickness for which an increase had been observed during preliminary staging trials. It was hypothesized that this increase in ply thickness was caused by a relaxation of the fibre bed due to a drop in resin viscosity during staging.

Step 5

Post-staging glass transition temperatures ($T_{g,staged}$) were obtained using dynamic modulated DSC scans and compared with the expected values from step 2[4].Figure 5-14 shows that these values

[4] Due to intermittent oven availability, three different convection ovens were used for staging.

deviated significantly from the cure model predictions even when the variations in $T_{g,x}$ and oven temperature were used to expand the prediction space. This discrepancy can be related to the overprediction of the 5276-1 cure model at 120 °C shown in Figure 4-8, which is associated with an inadequate description of the diffusion phenomenon. A linear fit (R^2 = 0.96) was found to yield more reliable predictions of staging time and was used for all subsequent material preparation.

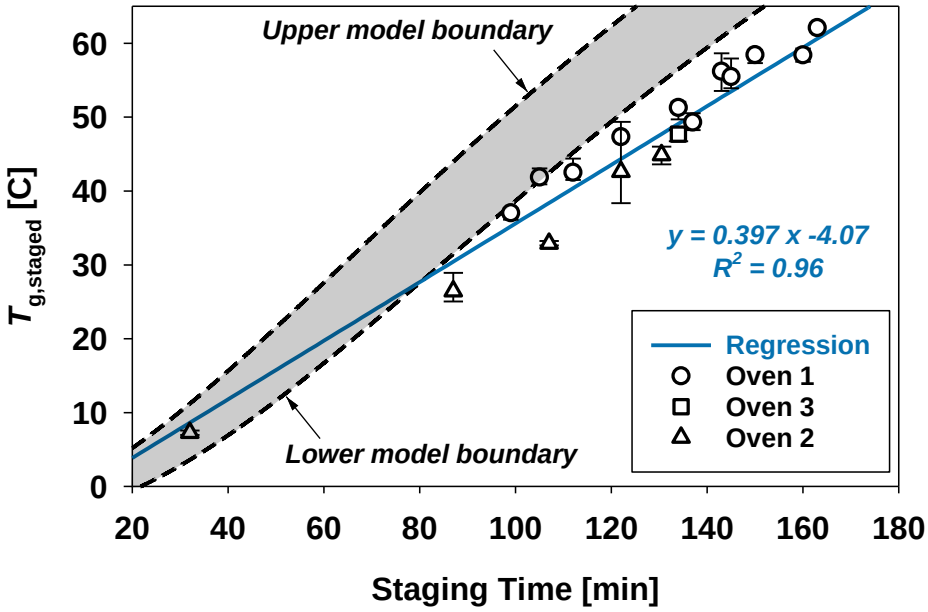

Figure 5-14. Summary of all measured glass transition results from oven staging compared with cure model predictions. The lower model boundary corresponds to $T_{g,x}$ = - 4.37 °C, T = 118 °C. The upper model boundary corresponds to $T_{g,x}$ = - 2.21 °C, T = 120 °C

Step 6

Staged prepreg strips were cut into 12.7 mm x 12.7 mm strands using an automatic tape cutter from Taizhou Foxsew (FX-110L). A picture of some representative 8HS/5276-1 strands is shown in Figure 5-15. N.B.: All staging trials produced strands with no tackiness at room-temperature.

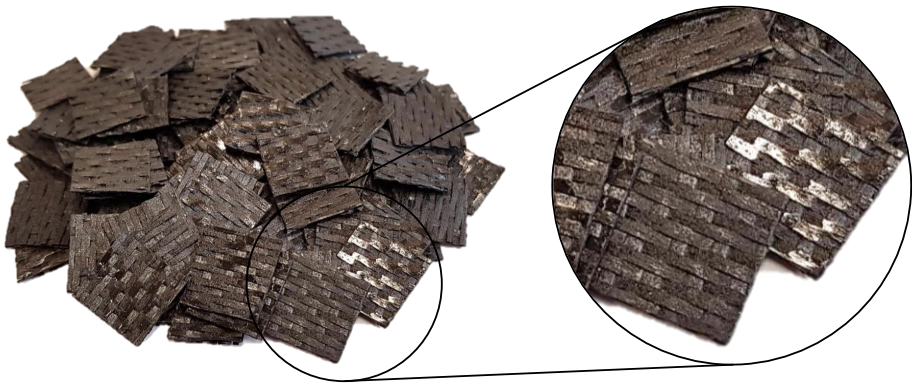

Figure 5-15. Staged 8HS/5276-1 strands.

5.4.3 Test Matrix

Having developed a procedure for modifying prepreg resin viscosity, the relationship between viscosity and the flow-compaction behaviour of 8HS/5276-1 offcuts was explored. Batches of 8HS/5276-1 were staged to different levels of cure corresponding to progressively higher resin viscosities at the selected cure temperature of 140 °C. Strands from each batch were tested using the flow-compaction method described in Section 5.3.3 using the same mould closure rate (0.1 mm/s) and applied force (1 kN). A summary of the batches prepared for testing is given in Table 5-2.

Table 5-2. Staging configurations used to study the effect of viscosity on flow-compaction.

Code	Staging	$T_{g,\,staged}$	α_{staged}	Avg. Viscosity	Repetitions
S1	32 min at 120 °C	7.3 °C	0.104	10.9 Pa-s	5
S2	87 min at 120 °C	26.5 °C	0.253	44.3 Pa-s	5
S3	107 min at 120 °C	32.9 °C	0.299	73.3 Pa-s	5
S4	122 min at 120 °C	42.6 °C	0.365	158 Pa-s	4
S5	131 min at 120 °C	44.9 °C	0.380	191 Pa-s	5
S6	137 min at 120 °C	49.3 °C	0.420	268 Pa-s	5
S7	145 min at 120 °C	55.5 °C	0.446	446 Pa-s	5
S8	160 min at 120 °C	58.4 °C	0.464	576 Pa-s	5

The spacing of the average resin viscosity values for configurations S1 – S6 was made intentionally small in comparison to the S7 and S8 configurations, so that the transition between percolation-dominant flow and shear-dominant flow could be better captured. From previous experience, this transition was expected to take place at lower viscosities. A much larger difference in the average resin viscosity between S7 and S8 was chosen, so that relevant comparisons could be made with materials like PPS and PEEK, which feature higher melt viscosities.

When relatively fresh resin is used to populate a phenomenological viscosity model, as is the case here, then predicting changes in viscosity due to changes in initial degree-of-cure by replacing α_0 with other values of α is not guaranteed to yield accurate results Kim *et al.* [141]. The staging of S1 and S2 configurations was replicated using a rheometer and extracted 5276-1 resin to see whether a modification to the viscosity model would be necessary to capture the effects of

staging. The results of these two runs are shown Figure 5-16 and with such little deviation between model and experiment, it was decided that no action was needed to improve the robustness of the 5276-1 viscosity model.

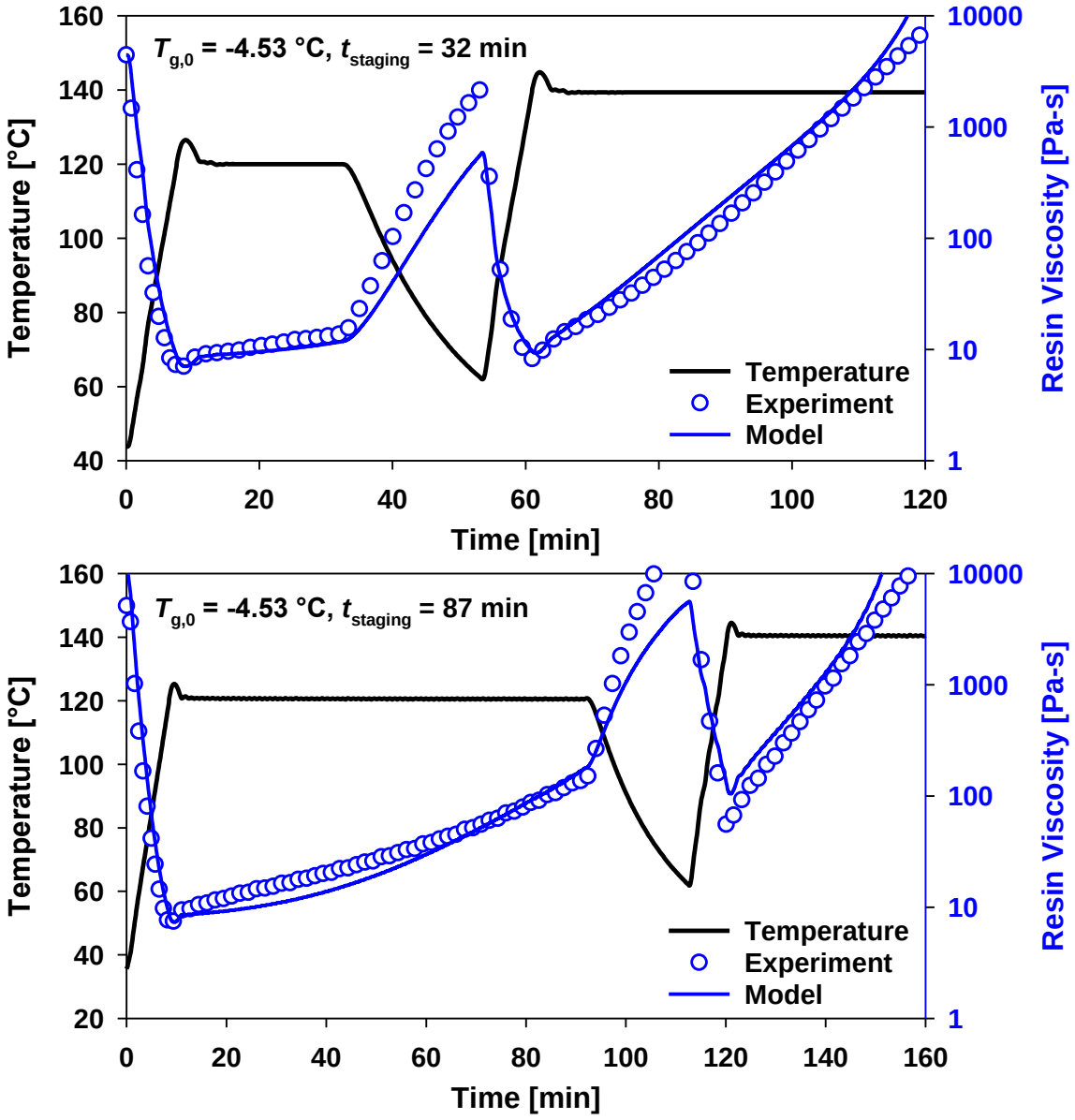

Figure 5-16. Resin staging rheometer validation for S1 (top) and S2 (bottom) configurations.

A nominal mould closure rate of 0.1 mm/s was selected for these experiments based on the work of Rasheed [92], who observed local fibre jamming of 5HS/PPS flakes in squeeze flow tests performed at low speeds such as 0.005 mm/s. Rasheed [92] did not observe jamming, however, during test that were performed at 0.05 mm/s or faster. 0.1 mm/s was chosen for the 8HS/5276-1 flow-compaction tests to avoid similar jamming.

5.4.4 Results

Shear Strains

For each of the test configurations presented in Table 5-2, final specimen shear strains were calculated using Equation (5.3) and the averages were then plotted against their corresponding resin viscosities in Figure 5-17. Optical micrographs of the specimens most representative of the shear strain averages from Figure 5-17 are shown in Figure 5-18 to provide a visual reference. Together, these two figures reveal three phases of flow-compaction behaviour.

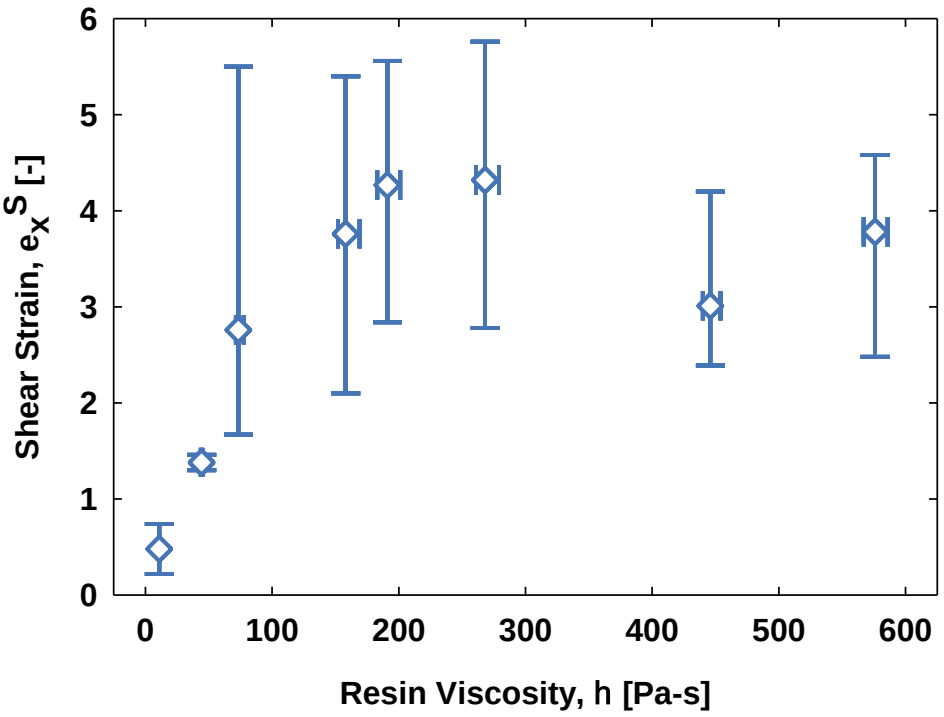

Figure 5-17. Final shear strain versus average resin viscosity for prepreg specimens staged to different levels of cure.

The first (I) phase is observed in the lowest resin viscosity configuration (S1), for which micrographs consistently show a significant amount of resin loss through the specimen edge along with a small amount of fibres from the outermost 90° tows. This clearly represents percolation-dominant behaviour and is very similar to what was observed during the un-staged flow-compaction trials discussed in Section 5.4.1. The viscosity range associated with Phase I is therefore defined by both S1 and the un-staged trials as 2.9 – 22.5 Pa-s.

The second (II) phase is observed in the S2 configuration, where the average resin viscosity was estimated to be 44.3 Pa-s. This phase was defined by a noticeable increase in shear flow when

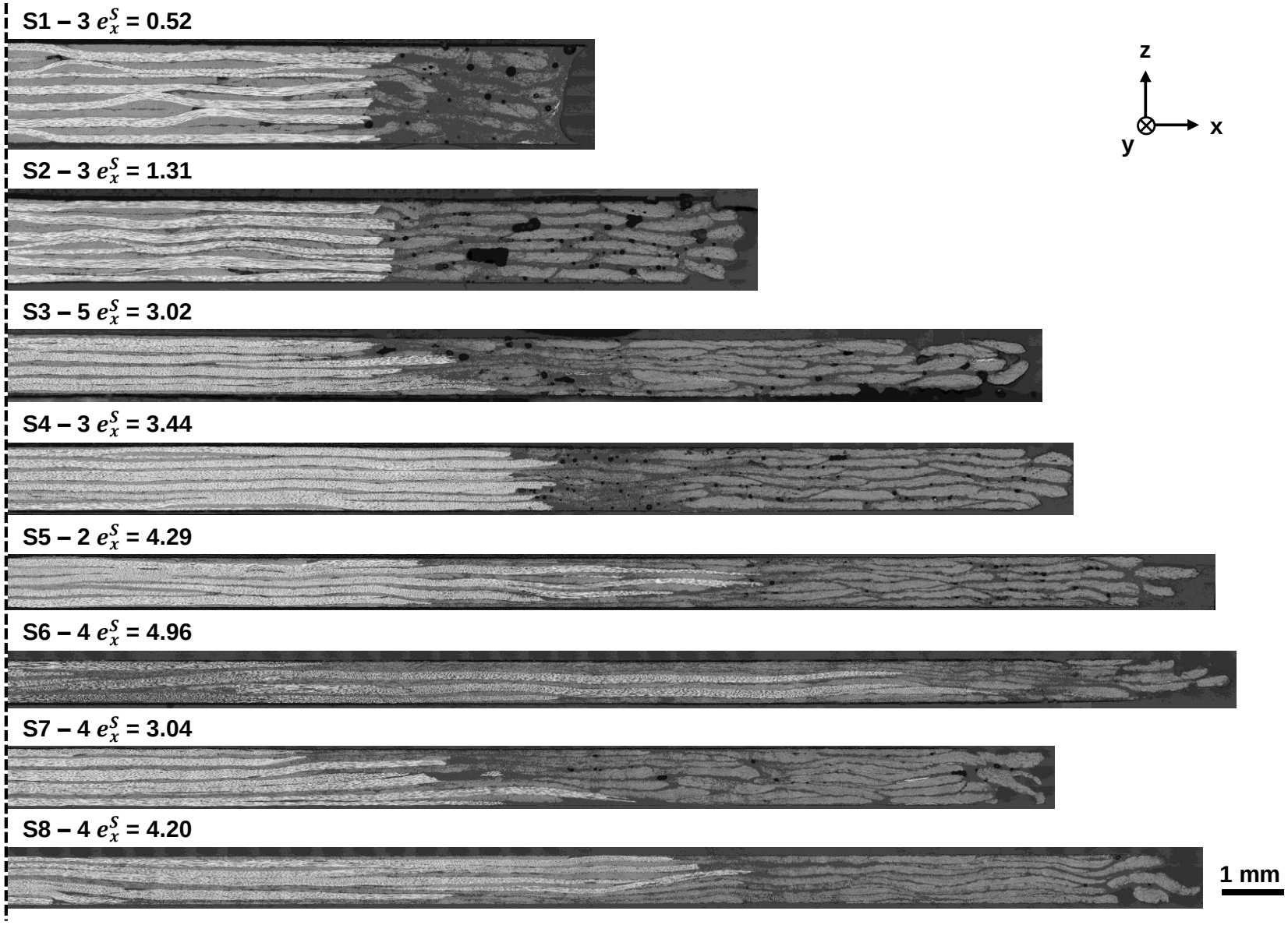

Figure 5-18. Representative micrographs for each staging configuration, where the black dashed line represents the specimen centreline.

compared to phase I and was found to be similarly repeatable in terms of both e_x^S and micrograph characteristics. Interestingly, the only fibres that were swept along by the resin flow in phase II were those belonging to tows initially oriented at 90° (y-direction). These fibres remained in tow form despite having moved such a large distance from their original position. Close inspection of S2 micrographs showed the presence of thermoplastic toughening particles dispersed in the resin surrounding each tow (Figure 5-19), which may have acted as "bumpers" explaining this limited tow deformation.

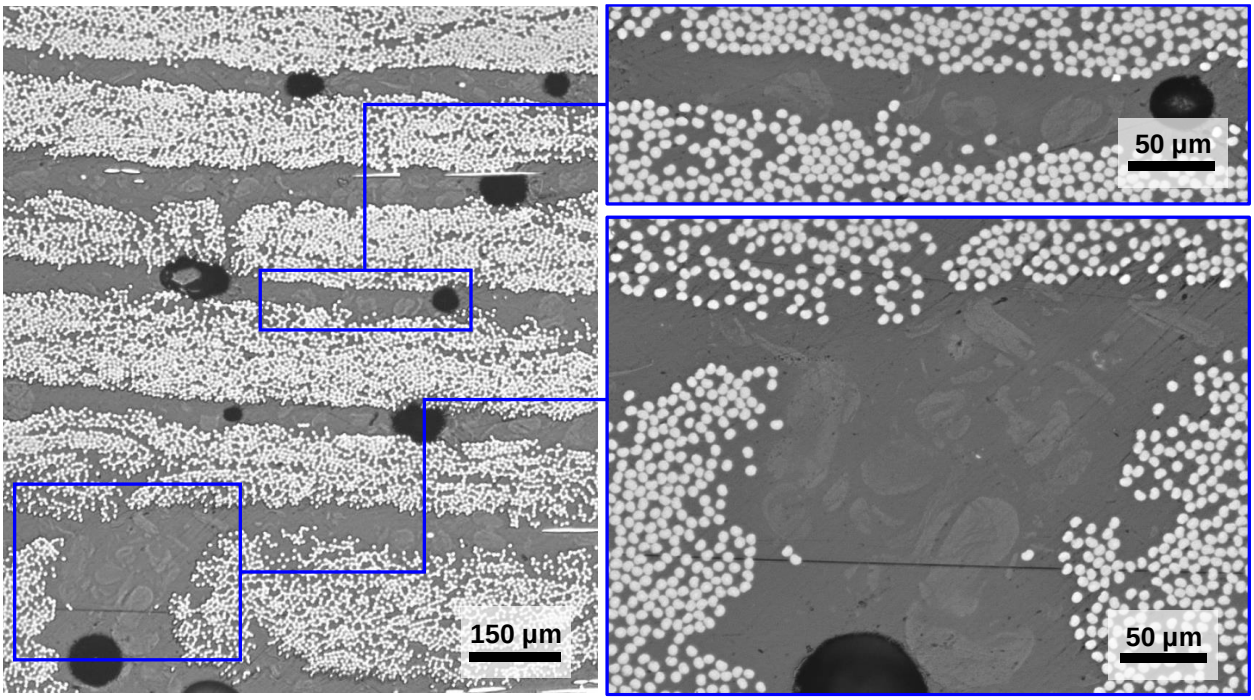

Figure 5-19. Close up images of the S2-1 optical micrograph (left side) showing interlaminar particles surrounding each 90° tow.

The third (III) and final phase of flow-compaction behaviour was observed in the remaining S3 – S8 test configurations, where resin viscosity was estimated to vary from 73.3 – 576 Pa-s. Unlike in phase II, where only 90° tow movement was observed, the micrographs from phase III show progressively larger movement of 0° fibres. This is a strong indication that shear flow is becoming more dominant within this higher range of resin viscosity. This is further supported by the visual evidence of transverse fibre movement show in Figure 5-20 where 0° fibres go from appearing as long bright bands in phase II to mildly eccentric ellipses in phase III, suggesting they have undergone a rotation toward the 90° direction.

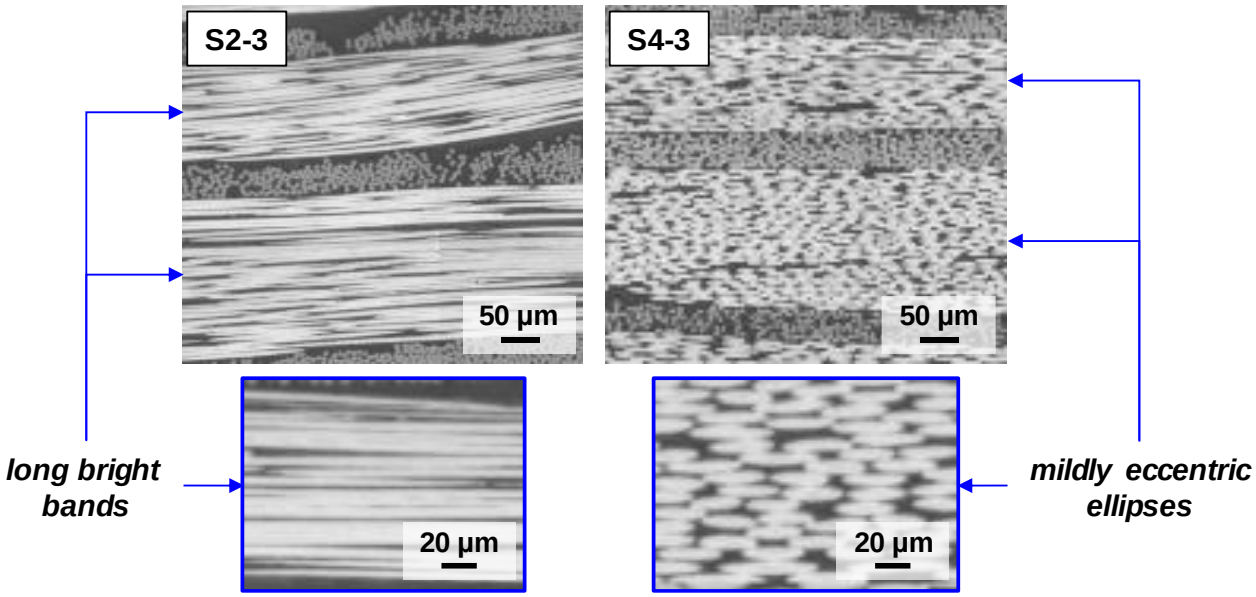

Figure 5-20. Optical micrographs for S2-3 and S4-3 specimens showing evidence of transverse fibre movement in Phase III relative to Phase II.

Phase III also features a substantial increase in the variability of e_x^S. This variability remains somewhat constant from S3 – S5, while the magnitude of e_x^S increases steadily, and then decreases slightly from S6 – S8, where e_x^S seems to plateau. It is unclear what exactly causes this inconsistent behaviour to occur, although it does coincide with the onset of 0° fibre movement. It is possible that the 0° fibre movement described above is sensitive to changes in initial strand placement and fibre orientation, as these are both parameters that are difficult to control and evaluate given the scale of the flow-compaction experiment. If this is the case, then the shear strain variability observed may be more so an artifact of the experiment design rather than a scalable aspect of the prepreg flow-compaction behaviour.

Load-Time-Displacement Curves

Normalized specimen thickness evolutions (h/h_0 vs. time) and flow-compaction curves (σ_{zz} vs. h/h_0) for the tests representative of the shear strain averages from Figure 5-17 are shown in Figure 5-21[5]. These curves complement the quantitative shear strain data obtained through optical microscopy from the last section by providing insight into the material's response throughout the compression moulding process.

It took between 34 min (S6) and 63 min (S1) for the resin in these flow-compaction specimens to gel, as per the 5276-1 cure model. Despite such long gel times, the normalized

[5] S7 and S8 load-time-displacement data was lost due to a software failure and could not be included.

thickness evolutions from Figure 5-21 show that most of the specimen deformation occurs within the first 30 seconds of the test. This was consistently captured using the flow window metric discussed in Section 5.3.3 with an average t_{flow} of 26.2 ± 12.2 seconds across all configurations. This suggests that the cycle time for a part made using this material would be limited by the resin curing time and not by the time required for material to fill a mould cavity.

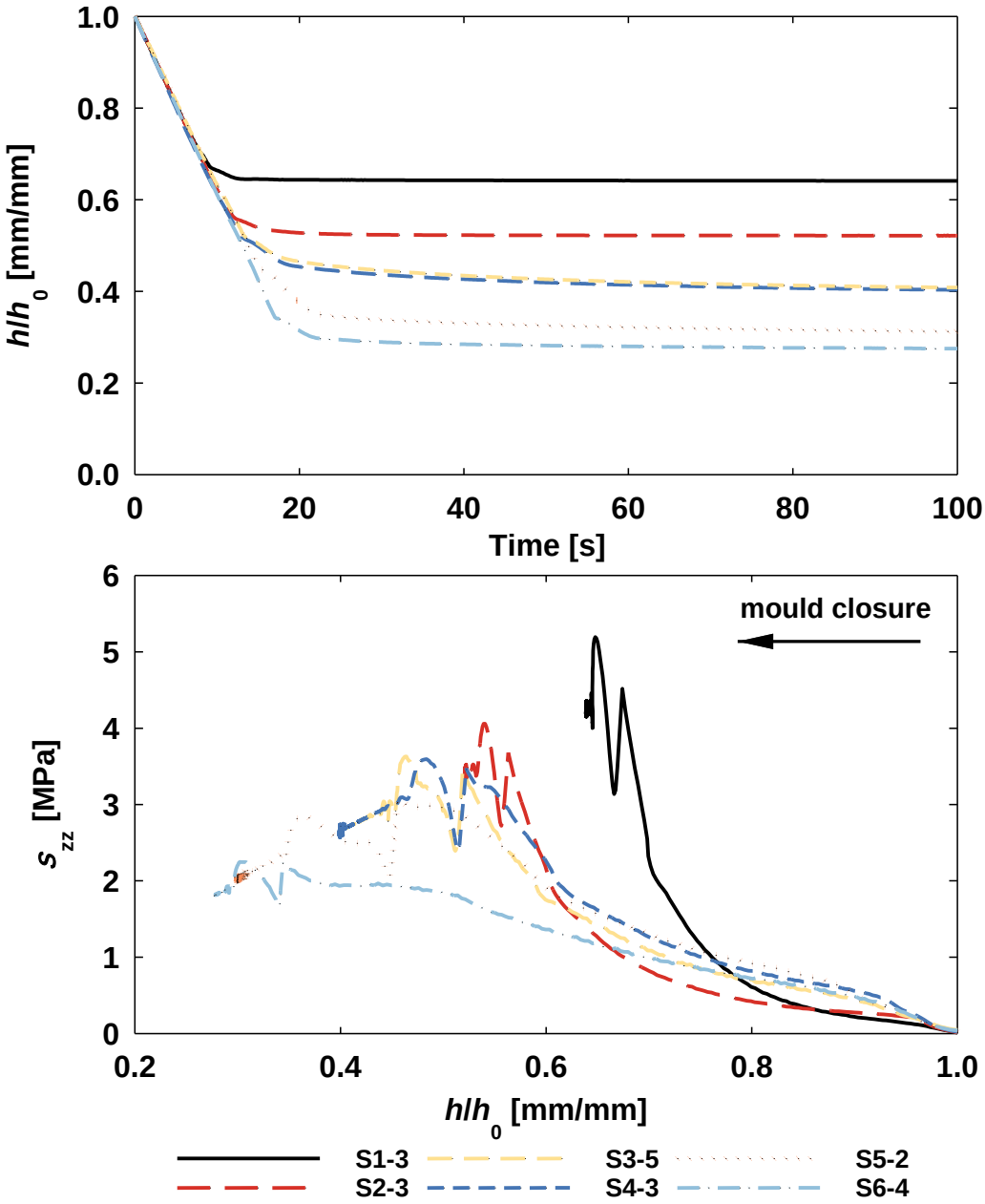

Figure 5-21. Representative normalized specimen thickness evolutions (top) and flow-compaction curves (bottom) for each of the staging configurations tested.

Figure 5-21 also shows that, by changing the resin viscosity through staging, the general shape of the flow-compaction curves also changes. For S1-3, which lies in phase I where percolation is the primary mechanism observed, the flow-compaction curve resembles a traditional prepreg compaction curve in which stress increases exponentially with fibre volume fraction [Hubert]. The S2-3 (phase II) flow-compaction curve has a similar exponential shape, though the increase in normal stress is less aggressive and the overall thickness reduction is larger. These two changes are likely due the loss of 90° fibre tows seen in the S2-3 micrograph and which caused an increase the specimen area. The S2-3 curve retaining its exponential shape despite losing these 90° fibres is probably due to the fact that the rest of the fibre bed remains intact during phase II similar to a quasi-static fibre bed. The remaining flow-compaction curves, which all correspond to tests in phase III, exhibit an almost linear behaviour with a slope that decreases as viscosity increases.

Mechanism Map

It is now possible to create a mechanism map to show the transition between the three phases of flow-compaction behaviour observed in the micrographs and flow-compaction curves. Recall that phase I features visual evidence of dominant percolation flow, an exponential flow-compaction curve shape, and covers an estimated viscosity range of 2.9 – 22.5 Pa-s. In phase II, micrographs gave an indication that shear flow was more prevalent as a substantial increase in 90° fibre movement was observed. Defined by a resin viscosity of 44.3 Pa-s, phase II flow-compaction curves were also less aggressively exponential in appearance. Finally, in phase III, micrographs

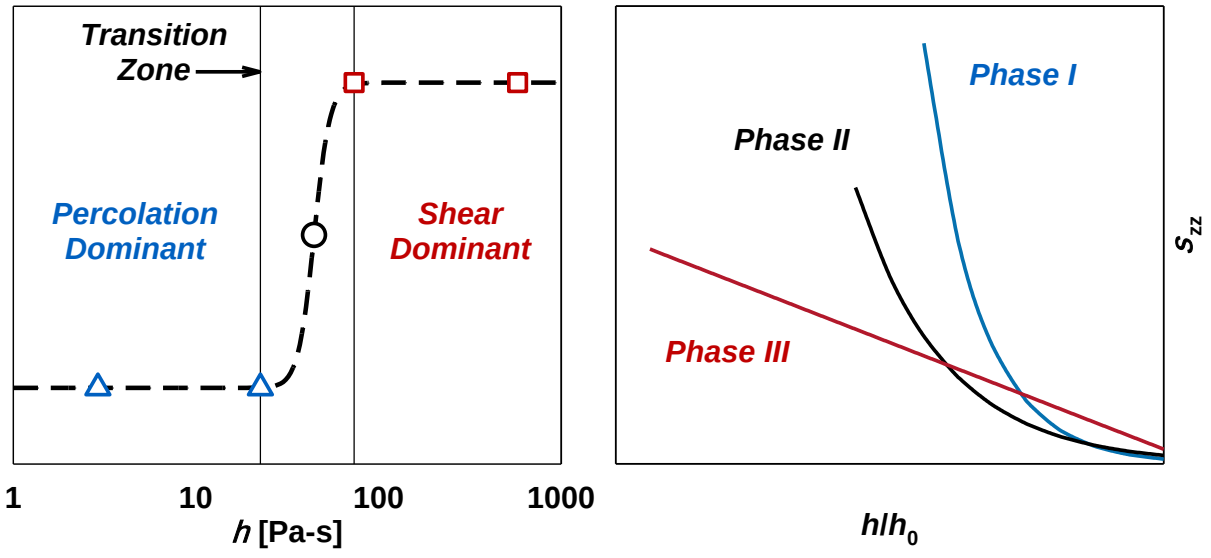

Figure 5-22. Map of the transition between percolation and shear dominant zones as a function of resin viscosity (left) and the corresponding changes in flow-compaction curve shape (right).

show a complete switch to shear flow dominant behaviour and flow-compaction curves becomes progressively more linear in shape over a resin viscosity range of 73.3 – 576 Pa-s. Figure 5-22 gives a visual representation of the transitioning between phases plotted against resin viscosity (left), as well as a schematic illustration of the flow-compaction curves evolution (right).

The range of viscosity over which the mechanism transition occurs will undoubtedly depend on the specimen fabric architecture, as well as the magnitude and speed of loading. One could easily imagine that a unidirectional tape would present much less resistance to shear deformation and result in a transition at lower viscosities and lower moulding forces, while a tighter fabric like a plain weave would experience the opposite effect.

5.5 Effect of Mould Closure Rate

5.5.1 Test Matrix

Additional flow-compaction tests were performed at two different mould closure rates (0.01 mm/s & 1 mm/s) to investigate the impact of test speed on the behaviour of staged 8HS/5276-1 strands. The details of these tests are summarized in Table 5-3.

Table 5-3. Staging configurations and mould closure rates used to study the effect of test speed on flow-compaction of 8HS/5276-1 strands.

Code	Closure Rate	$T_{g,\,staged}$	Avg. Viscosity	Repetitions
S3-0.01	0.01 mm/s	32.4 °C	79.7 Pa-s	5
S4-0.01	0.01 mm/s	41.3 °C	172 Pa-s	4
S5-0.01	0.01 mm/s	45.8 °C	208 Pa-s	3
S6-0.01	0.01 mm/s	48.8 °C	311 Pa-s	5
S7-0.01	0.01 mm/s	55.5 °C	539 Pa-s	5
S3-1	1 mm/s	32.4 °C	72.8 Pa-s	5
S4-1	1 mm/s	41.3 °C	157 Pa-s	5
S5-1	1 mm/s	45.8 °C	188 Pa-s	5
S7-1	1 mm/s	55.5 °C	459 Pa-s	5
S8-1	1 mm/s	58.9 °C	582 Pa-s	5
S9-1	1 mm/s	62.1 °C	834 Pa-s	4

5.5.2 Results

Shear Strains

Shear strain versus resin viscosity (Figure 5-23) and representative micrographs (Figure 5-24) provide insight into the final state of the specimens tested, as in Section 5.4.4. Only staging configurations which resulted in phase III flow-compaction behaviour at 0.1 mm/s were also tested at 0.01 mm/s and 1 mm/s, as fully developed shear flow is needed to produce fully filled high-flow compression moulded parts.

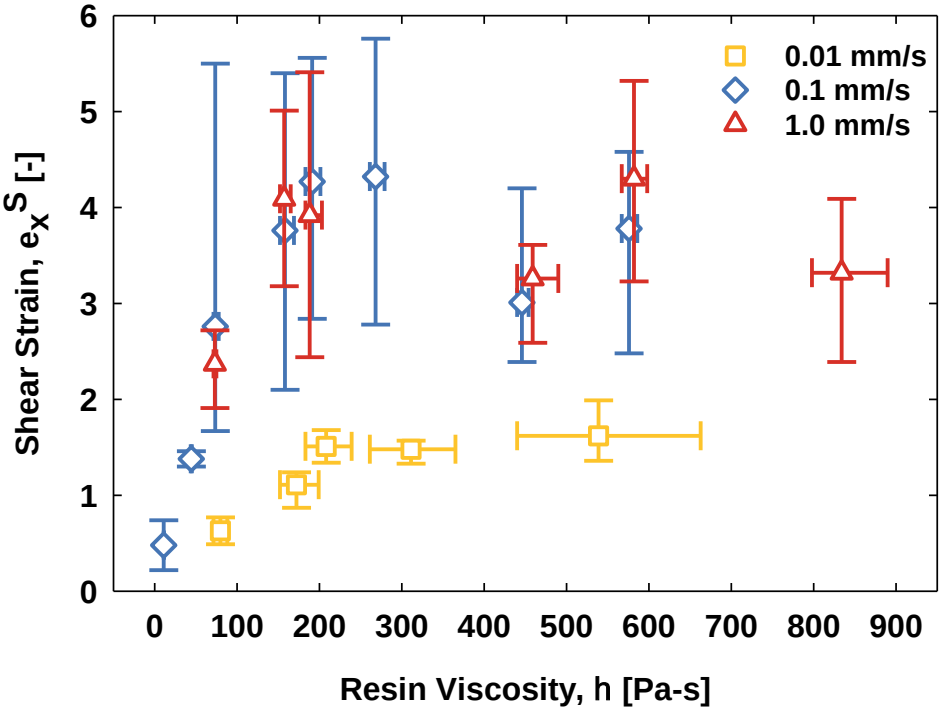

Figure 5-23. Final shear strain versus average resin viscosity for prepreg specimens staged to different levels of cure and tested under different speeds.

The shear strain versus resin viscosity data for each of the mould closure rates tested all follow a similar trend; increasing steadily at lower resin viscosities until about 200 Pa-s, then reaching somewhat of a plateau. The magnitude and variability of e_x^S for the specimens moulded at 0.1 mm/s and 1 mm/s are almost identical, whereas the values measured at the slowest speed (0.01 mm/s) are significantly and consistently lower. Micrographs of specimens moulded at 0.01 mm/s show that the observed decrease in e_x^S corresponds to a reduction in the movement of 0° fibres. In fact, most of the 0.01 mm/s micrographs resemble phase II (transitional) behaviour from the previous section, indicating that strand flow-compaction is indeed rate-dependent. The mechanism map presented in Figure 5-22 should, therefore, have a third degree-of-freedom.

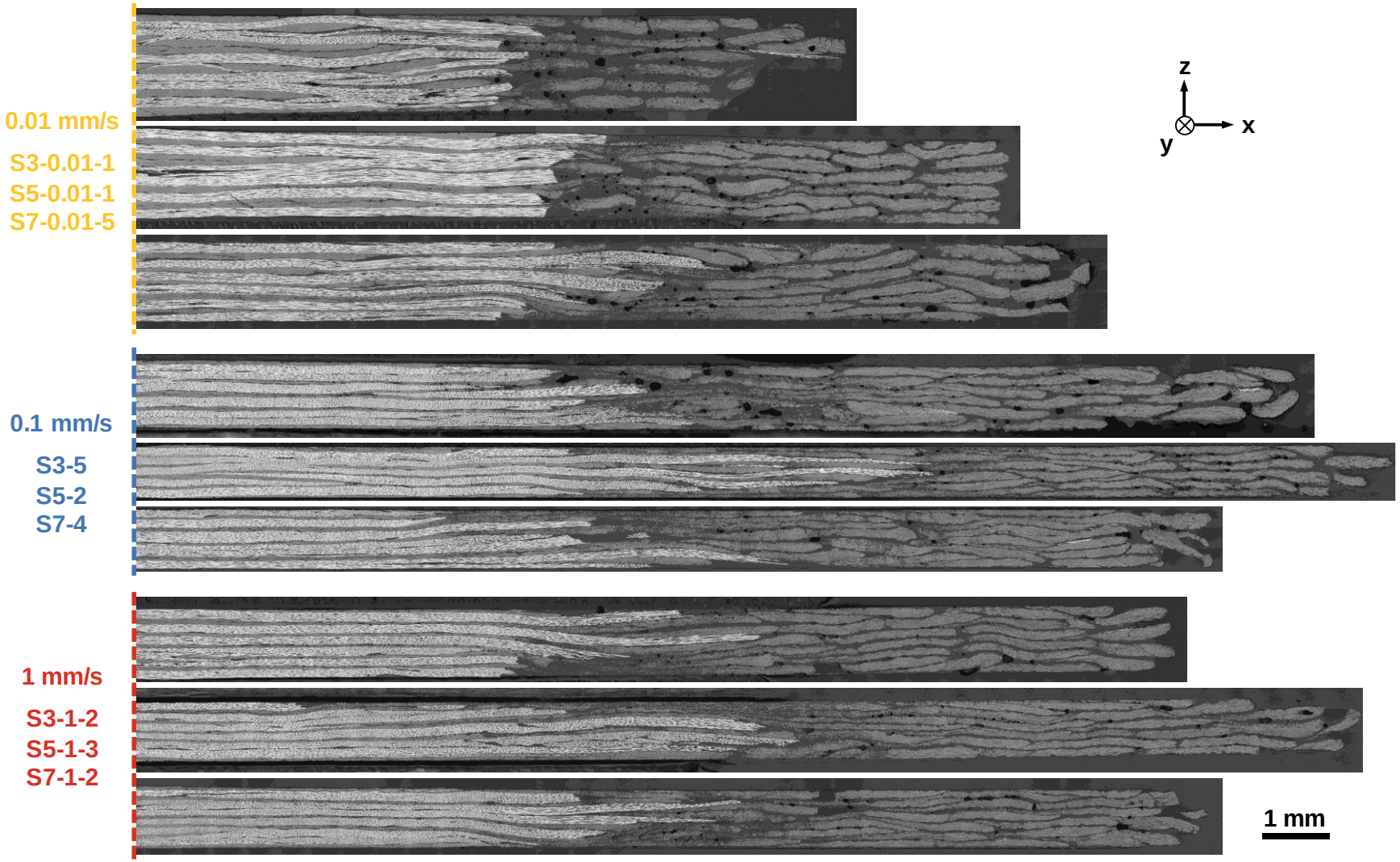

Figure 5-24. Representative micrographs at S3, S5, and S7 staging configurations from each of the closure rate trials.

It is not immediately obvious what has caused the observed reduction in shear flow at 0.01 mm/s; however, evidence of nesting between adjacent strands, shown in Figure 5-25, suggests that slower testing speeds may give strands more of an opportunity to settle in to each other. An increase in the number of contact points between 0° tows could then, possibly, lead to reduced fibre-bed mobility and 90° tow entrapment. Alternatively, 5276-1 exhibiting viscoelastic characteristics over the range of temperatures and degrees-of-cure tested could have also contributed to the rate-dependency observed, although this hypothesis would have to be verified using a more in-depth rheological study.

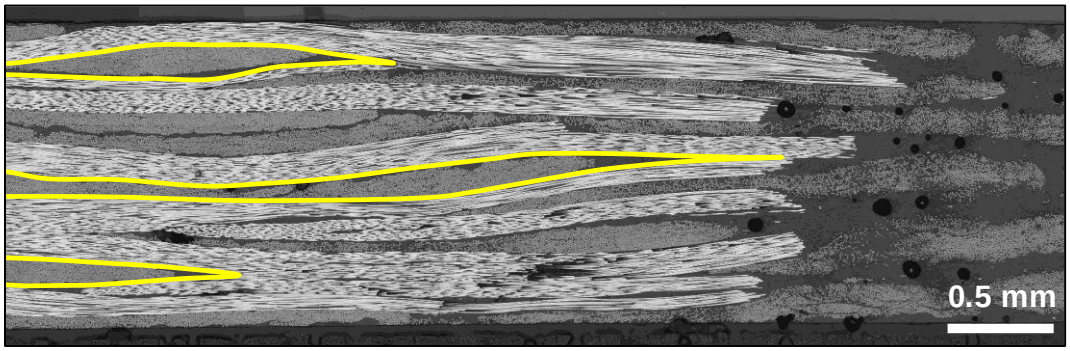

Figure 5-25. S3-0.01-1 micrograph showing evidence of strand nesting causing 90° tow entrapment highlighted in yellow.

Load-Time-Displacement Curves

Test frame and LVDT data from the mould closure rate trials were used to compute flow-compaction curves which, as in Section 5.4.4, serve as a complement to the optical micrograph analysis. Recall that tests performed at the nominal test speed of 0.1 mm/s showed that fully developed shear flow (phase III) is observed for resin viscosities above 73.3 Pa-s (≥S3) and that this type of behaviour results in flow-compaction curves that are approximately linear in shape. How mould closure rate affects strand behaviour is presented visually in Figure 5-26 which includes select curves from S3 and S5 rate trials.

Lowering the test speed to 0.01 mm/s resulted in distinctly exponential flow-compaction curves, corroborating the shift from phase III to phase II behaviour observed in S3-0.01 and S5-0.01 micrographs. Increasing the test speed to 1 mm/s produced curves consisting of two discrete regions: The first region features a linear loading segment which is more steeply sloped than the nominal (0.1 mm/s) case and that quickly reaches the prescribed target load of 1 kN. The second region begins as the test frame switches to PID force-control and is similar in shape to the nominal

test case. Nearly half of the total change in specimen thickness occurs during the force-controlled region at speeds much slower than the targeted 1 mm/s. Figure 5-27 shows that, extensive PID

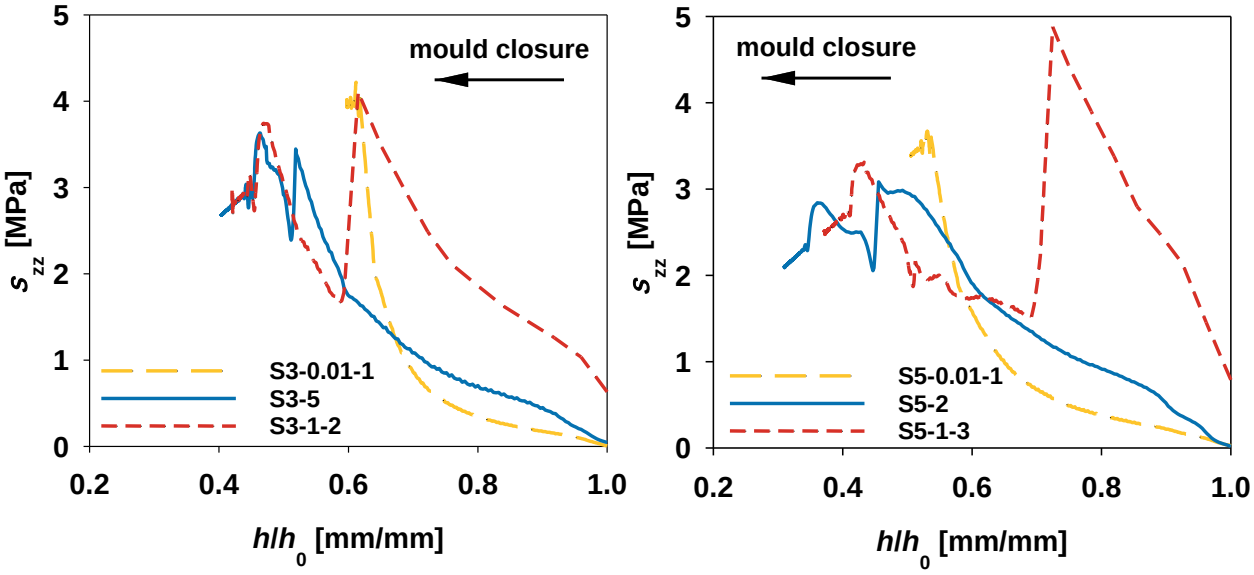

Figure 5-26. Flow-compaction curve comparison for S3 and S5 staging configurations tested at different mould closure rates: 0.01 mm/s, 0.1 mm/s, and 1 mm/s.

tuning notwithstanding, the testing frame was unable to maintain the desired test speed in the second half of the experiment. This resulted in a secondary test speed of approximately 0.05 mm/s. Despite this departure from the idealized closure rate, specimens moulded at 1 mm/s still represent

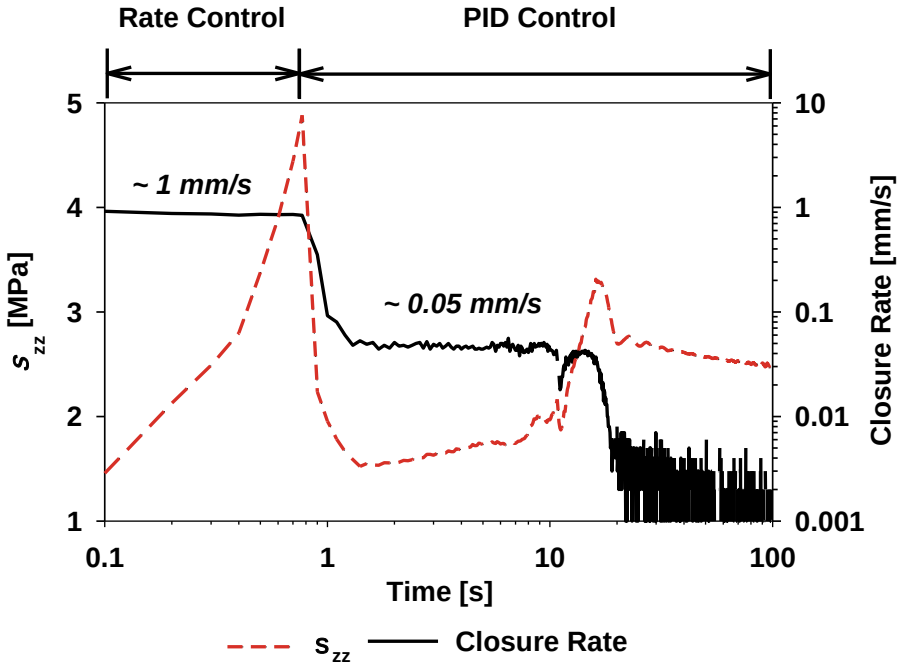

Figure 5-27. Normal stress and closure rate evolution for S5-0.01-1.

a more aggressive moulding strategy than the experiments carried out at 0.1 mm/s. Most compression moulding occurs in multiple segments and at different rates. The fact that final e_x^S values and micrographs for both 1 mm/s and 0.1 mm/s cases were similar indicates that nesting may be the primary obstacle to achieving large amounts of shear flow. Once overcome, it is likely that strand deformation will become less sensitive to changes in closure rate.

5.6 Compression Moulding Process Map

The impact of key processing parameters on the final shear strain of 8HS/5276-1 strands has been determined through a comprehensive 1-D flow-compaction study. The e_x^S data collected was used to create a compression moulding map to guide users in using strands based on these uncured offcuts. Piecewise cubic splines were fit to each of the data sets from Figure 5-23 and linear interpolation was used to create a three-dimensional surface of resin viscosity, closure rate, and e_x^S. Values of e_x^S were normalized with respect to the largest value observed, so that the map shows flow as a percentage of the maximum. While the study did not include strands of different fibre architectures, the general behaviours should still have value in determining appropriate processing parameters for a variety of other materials.

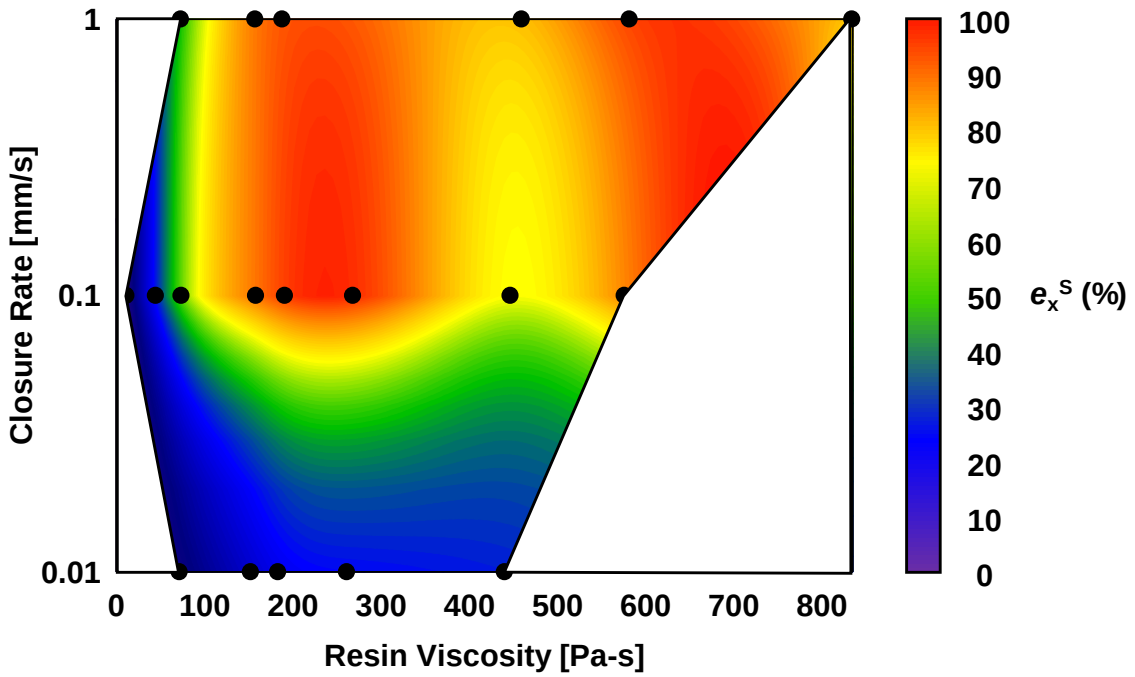

Figure 5-28. Compression moulding process map for 8HS/5276-1 strands measuring 12.7 mm x 12.7 mm linking resin viscosity and mould closure rate to the amount of shear strain.

5.7 Summary

In this chapter, a flow-compaction methodology based on the work of Hubert [88], along with a new strain measurement technique based on optical microscopy, was used to study the effect of resin viscosity and mould closure rate on the excitation of shear flow in 8HS/5276-1 specimens. Prepreg staging was shown to be an effective way to incrementally change resin degree-of-cure and, as a result, resin processing viscosity. Figure 5-17 and Figure 5-23 show that the shear strain defined by Equation (5.3) is directly proportional to viscosity and that slower closure rates can bring about reduced fibre mobility. Optical micrographs (Figure 5-18) taken from tested specimens show this evolution of fibre movement with resin viscosity, which is likely dependent on the viscous drag (friction) which the fibres experience as resin moves around them. This would also account, in part, for the decreased shear flow observed at lower mould closure rates, as resin velocity relative to the fibre would be decreased. Finally, these results have been combined to create the processing map shown in Figure 5-28, which may to aid in the selection of compression moulding parameters.

6
PREPREG AGEING

In this chapter, the effect of prolonged room-temperature ageing on the state of 5276-1 prepreg is investigated using a variety of techniques including: differential scanning calorimetry (DSC), gel permeation chromatography (GPC), Fourier transform infrared spectroscopy (FT-IR), and tack peel-testing. Metrics for tracking the resin's out-time were chosen for each method and their reliability discussed. Finally, the amount of material, time, and money needed to characterize the material's ageing behaviour were used to provide a ranking of the methods.

6.1 Offcut Variability & Staging

A staging methodology was described in the previous chapter in which the degree-of-cure of prepreg offcuts is increased to a level where, for a chosen cure temperature, a specific resin viscosity and curing timeframe are achieved. Idealized compression moulding trials carried out on 8HS/5276-1 specimens showed that viscosities of 200 – 600 Pa-s excite large amounts of shear deformation. Deviation from this viscosity range can lead to higher levels of resin percolation (< 200 Pa-s) or restricted shear mobility (> 600 Pa-s), both of which can hinder proper mould filling. Variability in the as-received degree-of-cure (α_x) of offcuts represents a significant obstacle to producing a recyclate with a consistent viscosity behaviour, as α_x determines what staging parameters are needed to yield the desired staged degree-of-cure (α_{staged}). Figure 6-1 shows that variations as small as 5 °C in the as-received glass transition temperature ($T_{g,x}$) translates to ± 50 % deviations in the initial isothermal viscosity predicted by the 5276-1 viscosity model from

Chapter 4. This highlights the need for better tools to track resin ageing and for a better understanding of how resin properties and structure evolve with exposure to ambient conditions.

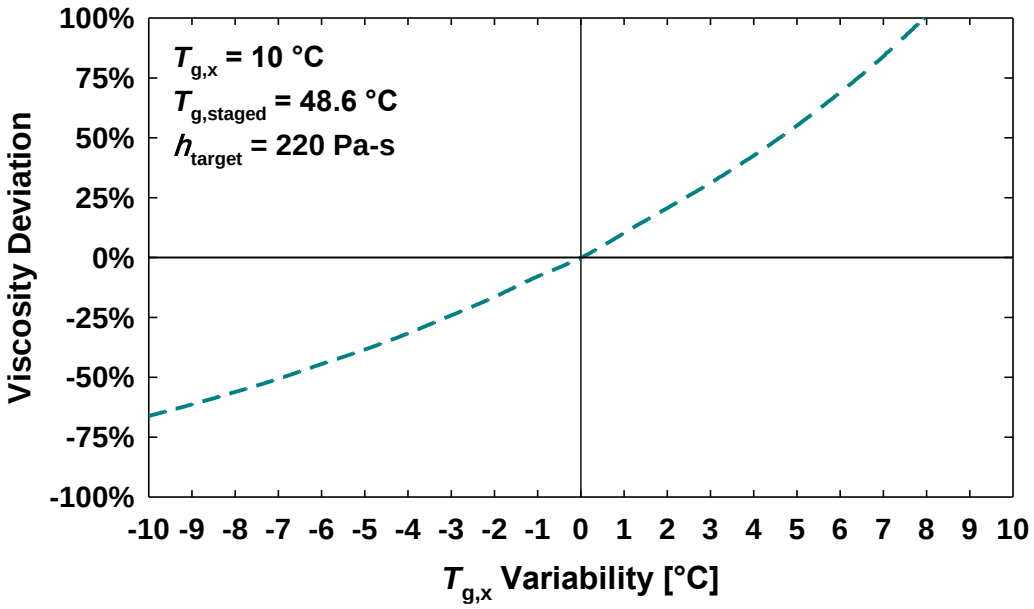

Figure 6-1. Deviation of initial isothermal viscosity of staged 5276-1 caused by variability in offcut $T_{g,x}$ for constant staging parameters.

6.2 Methodology

6.2.1 Offcut Ageing

Three batches of offcuts were aged under ambient laboratory conditions for extended periods: Batch 1 consisted of 8HS/5276-1 offcuts stored at an average temperature of 21 °C for up to 70 days, Batch 2 consisted of PW/5276-1 offcuts stored under the same conditions as Batch 1 for up to 375 days, and Batch 3 consisted of PW/5276-1 offcuts stored at an average temperature of 17.7 °C for up to 35 days. Specimens were taken from each batch at regular intervals for evaluation by either DSC, FT-IR, Tack testing, or GPC as summarized in Table 6-1.

Table 6-1. Summary of specimen ageing and method evaluation.

Testing Method	Batch 1 (8HS)	Batch 2 (PW)	Batch 3 (PW)
DSC	0 – 70 days	0 – 375 days	0 – 35 days
GPC	0 – 36 days	-	0 – 35 days
FT-IR	0 – 53 days	-	-
Tack	-	-	0 – 35 days

6.2.2 DSC

Modulated DSC was used to measure changes in resin T_g brought about by the ageing described in Table 6-1. Following the convention outlined in ASTM D3418 – 15 [143], the T_g of each specimen was measured as the half-height temperature of the step change observed in the reversible heat capacity signal shown in Figure 6-2. Dynamic tests were performed on specimens from each batch using Q2000 (Batch 1 & 2) and Q2500 (Batch 3) DSCs from TA instruments. All tests were carried out at a heating rate of 2 °C/min with a temperature modulation of ± 1.27 °C every 60 seconds. Specimens were encapsulated in hermetically-sealed aluminum pans and weighed between 5 and 15 mg. A minimum of three repetitions were performed for each of the ageing conditions.

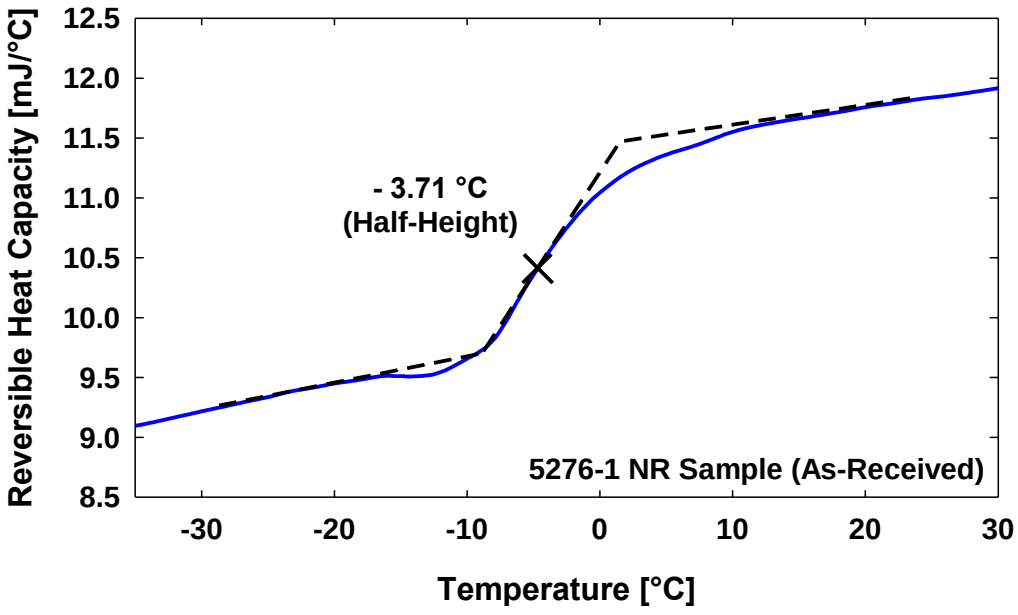

Figure 6-2. A representative DSC reversible heat capacity versus temperature curve for an as-received neat resin sample demonstrating the method used to determine T_g.

6.2.3 FT-IR

Fourier transform infrared spectroscopy in the medium infrared range (MIR) was used to measure changes in the concentrations of key chemical species of Batch 1 specimens subjected to room-temperature ageing from 0 to 40 days (Table 6-1). All tests were performed using a Spectrum II FT-IR from Perkin Elmer featuring a standard room-temperature LiTaO3 (lithium tantalate) MIR detector and a single-bounce diamond crystal attenuated total reflectance (ATR)

accessory. The instrument resolution was 4 cm^{-1} over a range of 4000-400 cm^{-1} and each specimen spectrum was taken as the average of six sequential scans against a steel anvil background.

Spectrum analysis was performed using Perkin Elmer's Spectrum IR software (version 10.6.2). Basic post-processing steps performed included: (1) unit conversion from transmittance (%) to absorbance (a.u.), (2) spectrum baselining to account for drift at lower wavenumbers, and (3) spectrum normalization with respect to an internal standard. Figure 6-3 shows post-processed spectra for both as-received and fully cured specimens. In both cases, the spectrum shown is the average result of 5 independent specimen scans.

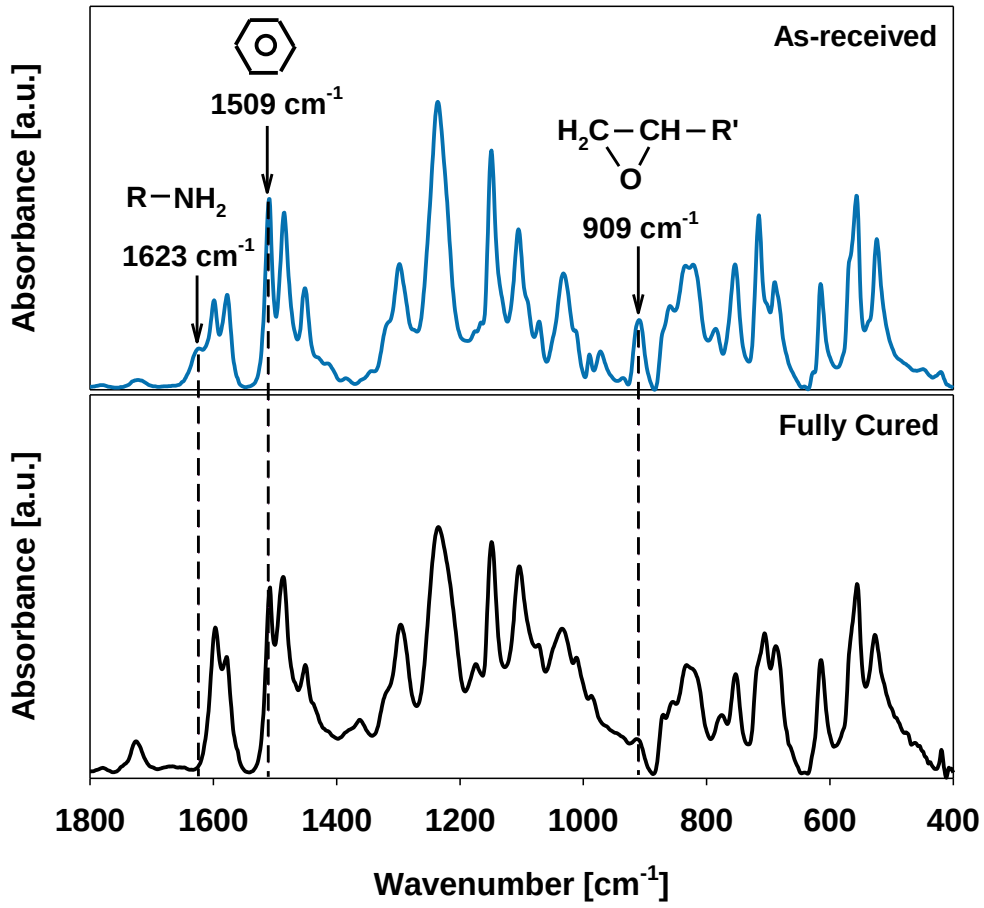

Figure 6-3. Average spectra for as-received (top) and fully cured (bottom) 8HS/5276-1 specimens. Spectrum normalization was taken with respect to the peak at 1509 cm^{-1}. Epoxy (oxirane) and primary amine bands are highlighted at 909 cm^{-1} and 1623 cm^{-1}, respectively.

A literature survey of studies in which the curing of epoxy resins were investigated by FT-IR was carried out and the key absorbance bands used as internal standards and for tracking conversion are summarized in Table 6-2. Excitation of a phenyl group's aromatic carbon ring is

observed at ~1510 cm^{-1} in all of the studies surveyed and serves as a reliable internal standard. A similar band is shown in Figure 6-3 at 1509 cm^{-1} and was used to normalize all 5276-1 spectra.

Characteristic primary amine and epoxy (oxirane) bands are visible in the as-received spectra at 1623 cm^{-1} and 909 cm^{-1}, respectively. After curing, the primary amine band has completely disappeared, while the epoxy band has decreased significantly. These observations suggest that 5276-1 is comprised of an epoxy monomer and an amine curing agent. According to Mijovic *et al.* [144], the only reactions that can occur given an epoxy-amine mixture are: (1) primary amine-epoxy, (2) secondary amine-epoxy, (3) hydroxyl-epoxy, (4) epoxy-epoxy. Each of these reactions will produce or consume certain functional groups thereby changing the intensity of peaks within the MIR spectrum. The chemical species common to all of these reactions is the epoxy monomer, which is why the band at 909 cm^{-1} is frequently used to track total polymerization. The degree-of-cure for a given out-time (α_t) can therefore be expressed in terms of the epoxy band absorbance (Equation (6.1)) by invoking the Beer-Lambert law which states that absorbance is directly proportional to the concentration of the absorbing chemical species [145].

$$\alpha_t = \left(\frac{A^t_{909} - A^x_{909}}{A^\infty_{909} - A^x_{909}} \right) + \alpha_x \tag{6.1}$$

In Equation (6.1), A^x_{909}, A^∞_{909}, and A^t_{909} correspond to the normalized 909 cm^{-1} peak areas of as-received, fully cured, and intermittently aged specimens, respectively. The as-received degree-of-cure was calculated using DSC measurements performed on as-received Batch 1 specimens and the 5276-1 T_g model. It is also possible to convert values of α_t to glass transition temperatures ($T_{g,t}$) by rearranging the DiBenedetto equation as shown in Equation (6.2):

$$T_{g,t} = T_{g,0} + \frac{\lambda \alpha_t (T_{g,\infty} - T_{g,0})}{1 - (1-\lambda)\alpha_t}, \tag{6.2}$$

where T_{g0}, $T_{g\infty}$, and T_g are the initial ($\alpha = 0$), final ($\alpha = 1$), and intermediate ($0 < \alpha < 1$) glass transition temperatures, respectively, and λ is the fitting parameter discussed in Chapter 4, Section 4.5.2.

Table 6-2. Summary of key absorbance bands used to study the curing of epoxy-based resins by FT-IR.

Reference	Material	Key Bands	Attribution	Band Change	Use
Sprouse *et al.* [146]	TGMDA/DICY	910 cm^{-1}	epoxide ring	↓	total polymerization
		1510 cm^{-1}	aromatic carbon	none	internal standard
		1740 cm^{-1}	aliphatic carbonyl	↑	thermal oxidation
Smith *et al.* [147]	TGDDM/DDS	906 cm^{-1}	epoxide ring	↓	total polymerization
		1072 cm^{-1}	ether	↑	rate of homopolymerization
		1190 cm^{-1}	phenyl	none	internal standard
		1517 cm^{-1}	phenyl	shift to 1512 cm^{-1}	internal standard
		3409 cm^{-1}	secondary amine	↑	heteropolymerization
		3507 cm^{-1}	hydroxyl	↑	total polymerization
George *et al.* [148]	MY721/DDS	648 cm^{-1}	primary amine	↓	heteropolymerization
		906 cm^{-1}	epoxy cyclic ether	↓	total polymerization
		1100 cm^{-1}	ether or hydroxyl	↑	cross-linking
		1515 cm^{-1}	aromatic carbon	none	internal standard
		1652 cm^{-1}	primary amine	↓	heteropolymerization
Ramis *et al.* [149]	DGEBA/γ-BL + ytterbium triflate	915 cm^{-1}	epoxy	↓	total polymerization
		1509 cm^{-1}	phenyl	none	internal standard
		1736 cm^{-1}	carbonyl (aliphatic linear ester)	↑	SOE conversion
		1773 cm^{-1}	carbonyl (cyclic ester)	↓	γ-BL consumption

6.2.4 GPC

Gel permeation chromatography, a common type of size exclusion chromatography, was used to measure changes in the apparent molecular size distribution of 5276-1 specimens that had been aged according to Table 6-1. Specimens from Batch 1 were tested using a Breeze GPC from Waters with a differential refractive index RI 2414 detector and 2 ResiPore (3 m, MULTI pore type, 250 mm x 4.6 mm) columns with a ResiPore guard column (3 m, 50 mm x 4.6 mm) from Polymer Laboratories. Specimens from Batch 2 were tested using a PL50 GPC from Polymer Laboratories, again with a refractive index detector and two mixed bed (D) columns. Resin solutions were prepared using dimethylformamide (DMF) at a concentration of approximately 2 mg ml^{-1} with 0.1 % lithium bromide. Tests were performed with a mobile phase flow rate of 0.3 mL min^{-1} at a temperature of 50 °C. Molecular weight distributions (MWDs) were computed using linear narrow molecular weight distribution poly(methyl methacrylate) calibration standards.

Figure 6-4 shows a representative chromatogram obtained for a Batch 1 specimen with the molecular weight calibration standard superimposed. Each chromatogram was processed according to the guidelines put forth by Malawer and Senak [150]. One repetition per ageing condition was performed, unless otherwise specified.

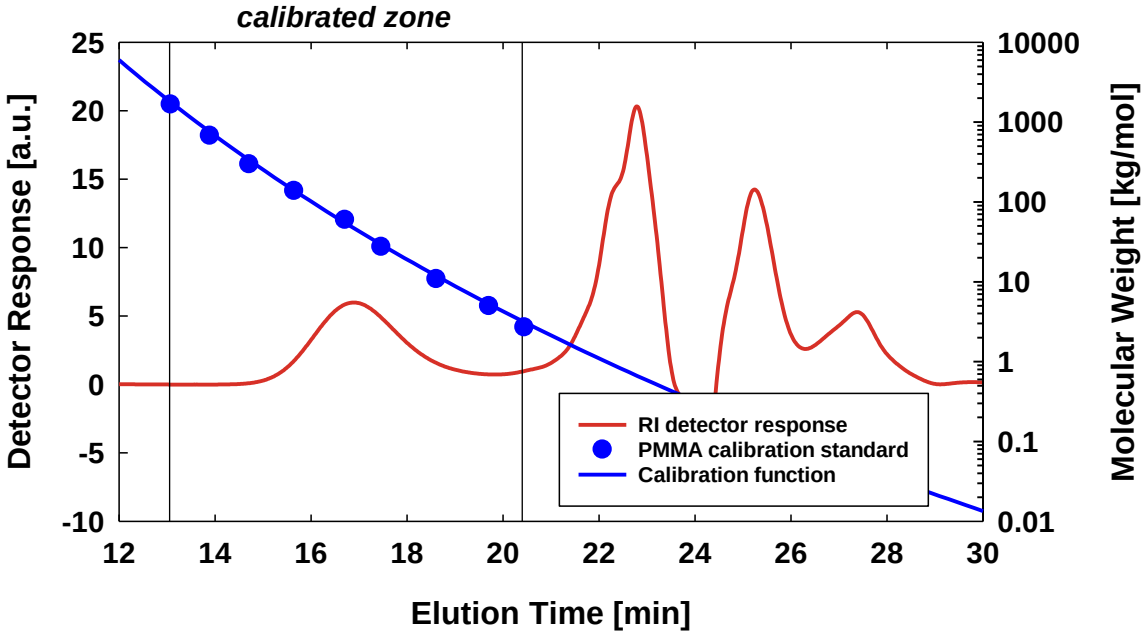

Figure 6-4. Representative unprocessed GPC signal for a 5276-1 specimen showing the peak of interest and the region encompassed by the calibration standard.

Molecular weight averages, also known as the moments of the distribution [150], are used to quantify changes to MWDs like the one shown in Figure 6-5. The number-average molecular weight (M_n), the weight-average molecular weight (M_w), and the "Z" average molecular weight (M_z) were calculated for each specimen tested according to Equations (6.3), (6.4), and (6.5):

$$M_n = \frac{\sum_i n_i M_i}{\sum_i n_i} = \frac{\sum_i A_i}{\sum_i A_i / M_i}, \tag{6.3}$$

$$M_w = \frac{\sum_i n_i M_i^2}{\sum_i n_i M_i} = \frac{\sum_i A_i M_i}{\sum_i A_i}, \tag{6.4}$$

$$M_z = \frac{\sum_i n_i M_i^3}{\sum_i n_i M_i^2} = \frac{\sum_i A_i M_i^2}{\sum_i A_i M_i}, \tag{6.5}$$

where, n_i is the number of molecules with weight M_i and A_i is the area of the i^{th} time slice of a chromatogram signal like the one shown in Figure 6-4. These molecular weight averages, the molecular weight at the distribution's peak (M_p), and the dispersity ($Đ$) given by Equation (6.6), provide different information regarding a polymer's expected properties.

$$Đ = \frac{M_w}{M_n} \tag{6.6}$$

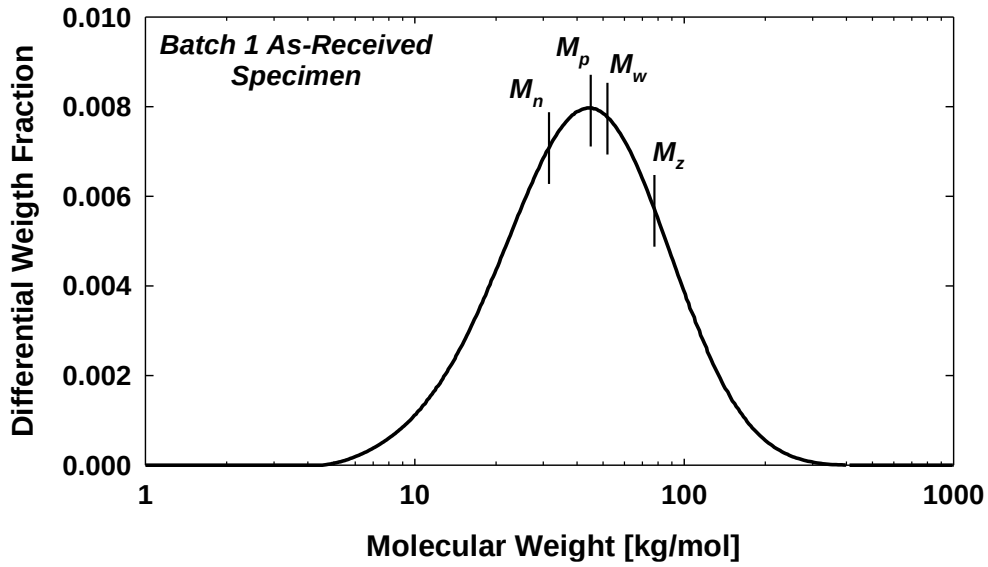

Figure 6-5. Representative MWD showing the different molecular weight averages and the molecular weight at the distribution's peak.

6.2.5 Tack

The evolution of prepreg tack with extended periods of out-time has been studied by Ahn *et al.* [151], Endruweit *et al.* [152], Budelmann *et al.* [153], and Smith *et al.* [154], to name a few. Small to moderate increases in resin degree-of-cure have been consistently shown to cause measurable shifts in a material's viscoelastic response. Here, changes to the tack behaviour in the time-temperature domain have been used to determine the degree-of-cure and, by extension, the age of PW/5276-1 prepregs.

Continuous Application-Peel Method

The continuous application-peel method discussed in detail by Crossley *et al.* [155] was used here to measure prepreg tack. In this method, a rectangular prepreg specimen is first laid up by hand on a rectangular substrate measuring 140 mm × 80 mm. Substrate and specimen are then loaded into a test fixture where a stiff compaction roller presses the prepreg against the substrate and against a stiff peel roller at a controlled force. The fixture is mounted on the base of a universal testing machine and the free end of the prepreg specimen is attached to the crosshead and load cell of the testing machine through a material clamp. During a tack test, the crosshead moves vertically at a set speed, which translates into horizontal movement of specimen and substrate through the fixture. As a result, the prepreg is bonded to and peeled from the substrate in a single continuous motion at a rate which corresponds to the crosshead speed. Pictures of the tack testing fixture with a specimen ready for testing is shown in Figure 6-6.

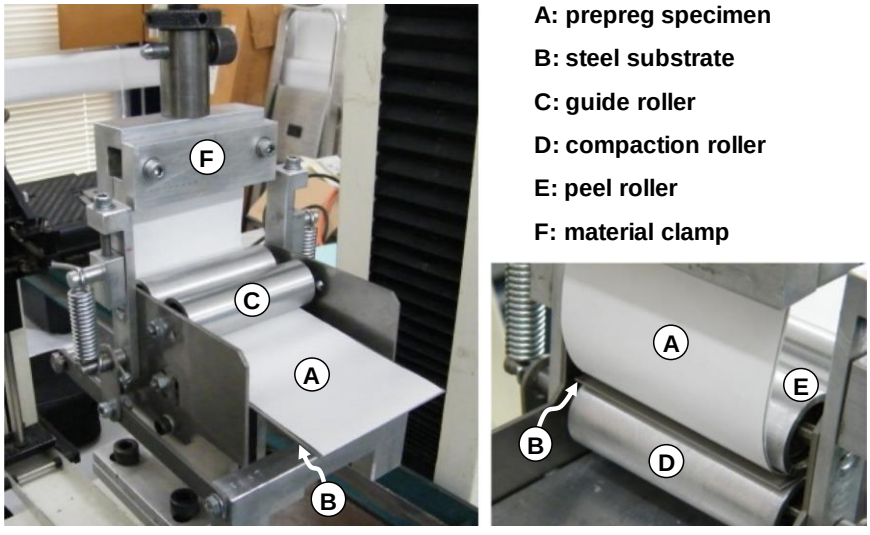

Figure 6-6. Picture of the tack test fixture designed by Crossley *et al.* [155] and setup with a prepreg specimen ready for testing (adapted from [152]).

The test procedure described above was used to measure tack between plies of the recovered PW/5276-1 and a polished steel substrate at peel rates of 25 mm min^{-1}, 70 mm min^{-1}, 180 mm min^{-1}, and 500 mm min^{-1}. With the help of an environmental chamber, tests were performed at temperatures of 18 °C, 28 °C, 38 °C, and 50 °C. All tests were carried out on specimens measuring 215 mm x 75 mm with a compaction force of 100 N. The testing side of each specimen was partially covered with backing film resulting in a contact length of only 80 mm. As such, there was no adhesion between the specimen and substrate during the first phase of each tack test. The tack force was quantified as the difference between the total peel force (F_{peel}) and the force needed to overcome the dissipative effects (F_{diss}) arising from friction and bending the prepreg ply (Figure 6-7).

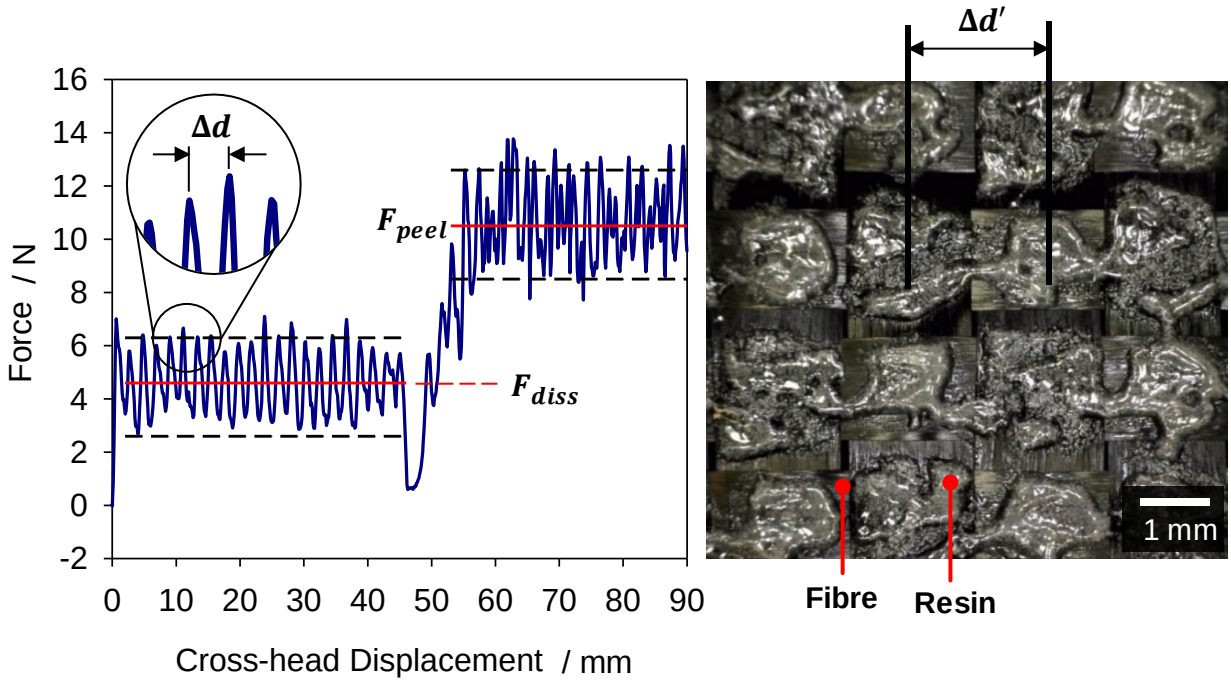

Figure 6-7. Measured tensile force versus cross-head displacement during a representative tack test (left) showing the period of signal variation, Δ*d*, and a picture of the plain-weave tow spacing, Δ*d'* (right).

Prepreg Surface Morphology

Large oscillations were measured during the PW/5276-1 tack trials which had not previously been observed during tack tests performed on unidirectional prepregs [152]. This periodic behaviour cannot be related to the tack phenomenon as it is observed in the dissipative regime, where prepreg and substrate are separated by a backing film. Furthermore, the period of the oscillation (Δ*d*) was found to closely match the plain-weave tow spacing (Δ*d'*) as shown in

Figure 6-7. This suggests that some component of the variability observed in the ply peel regime is caused by the periodic thickness variations of the prepreg's plain-weave architecture. Further investigation into this phenomenon was deemed outside the scope of this study and so only average tack force values are reported here.

Given the in-plane symmetry of the plain weave architecture, one would not expect the different sides of the PW/5276-1 prepreg to yield different tack results. However, Endruweit *et al.* [152] showed that backing films can affect the distribution of resin on a prepreg's surface and, as a consequence, the measured tack. Two preliminary tack tests were performed using an arbitrary set of conditions (t_{out} = 0 days, T = 28 °C, r = 180 mm min^{-1}) to see whether the side used for testing needed to be controlled. The results showed no obvious difference with average values of 6.72 N and 6.30 N. Nevertheless, subsequent tests were performed with the same prepreg surface in contact with the steel substrate.

Time-Temperature Superposition

Crossley *et al.* [155] have shown that the principle of time-temperature superposition is applicable to tack data acquired in continuous application-and-peel tests. In essence, this means that the tack force (F_t) measured at given temperature (T) and feed rate (r) should be equivalent to the tack force measured at some reference temperature (T_{ref}) and shifted feed rate ($a_T r$):

$$F_t(T, r) = F_t(T_{ref}, a_T r). \tag{6.7}$$

Endruweit *et al.* [152] obtained these shift factor for a unidirectional CF/epoxy prepreg using parallel plate rheometry and were able to fit their data to the Williams, Landel and Ferry (WLF) relation shown in Equation (6.8) [156]. The WLF equation uses the empirical constants C_1 and C_2 to describe the relationship between a shift factor (a_T) and temperature for a given T_{ref}.

$$\log_{10} a_T = \frac{-C_1(T - T_{ref})}{C_2 + (T - T_{ref})} \tag{6.8}$$

Endruweit *et al.* [152] also showed that tack master curves generated using WLF shift factors can be approximated by Gaussian curves described by:

$$F_t(T_{ref}, a_T r) = F_{t,max} \exp\left(-\left(\frac{\log(a_T r) - \log(a_T r_{max})}{w} \right)^2 \right), \tag{6.9}$$

where, $F_{t,max}$ is the maximum tack force, $a_T r_{max}$ is the shifted rate at maximum tack, and w indicates the width of the curve. The shape of these tack master curves reflects the competing effects of increasing cohesion within the resin and decreasing adhesion between resin and substrate with increasing feed rates.

Rheometry

Isothermal frequency sweeps were performed using an Anton Paar MCR 302 rheometer fitted with a CTD 450 environmental chamber and a Grant Instruments LTD6 refrigerated circulator. Due to the limited availability of neat resin specimens, frequency sweeps were performed directly on plain weave prepreg specimens cut to a size of 30 mm × 30 mm. Although the magnitude of the viscoelastic measurements is strongly affected by the presence and distribution of the fibres, changes in the storage modulus G' with temperature can be attributed to the resin system alone, since the fibres do not exhibit any significant temperature dependent behaviour in the range examined. All tests were carried out using a standard 25 mm diameter parallel plate geometry in an air atmosphere. At the beginning of each test, the specimen is subjected to a normal force of 20 N at the lowest test temperature. This step promotes contact between the rheometer plates and the specimen prior to fixing the gap distance. Isothermal frequency sweeps are then carried out between 15 °C and 60 °C (in increments of 5 °C) at logarithmically increasing frequencies from 1 Hz to 10 Hz, and at a fixed strain amplitude of 0.01%. The amplitude was kept small in order to avoid disrupting the fibre arrangements. It is to be noted that the range of test temperatures for t_{out} = 35 days was limited to 25 °C to 60 °C due to an increase in T_g.

6.3 Results

6.3.1 DSC

The results of the DSC tests described in Section 6.2.2 are presented in Figure 6-8 shown below and in Table A-1 of Appendix A. Specimen T_g was found to increase with out-time at a similar rate for all batches tested, despite Batch 3 ageing conditions being 3.3 °C lower on average than the other two. The inset of Figure 6-8 shows that offcuts reach a T_g of 2.8 – 6.4 °C before surpassing the manufacturer-specified out-life of 14 days. This corresponds to a degree-of-cure of approximately 0.06 – 0.10. Recall that $T_{g,staged}$ values of 45 – 58 °C yielded desirable flow-

compaction behaviour for the strands tested at 140 °C in Chapter 5. The findings presented here indicate that aged 5276-1 prepregs would eventually surpass these levels making it impossible to achieve the desired strand behaviour without adjusting the cure temperature. Fortunately, it seems unlikely that offcuts subjected to similar room-temperature ageing would ever reach gelation given the ${}_{gel}T_g$ of 81.6 °C that was measured in Chapter 4. Finally, the T_g measurements obtained by DSC were very repeatable with T_g values varying by 1.29 °C, 2.14 °C, and 1.24 °C on average for batches 1 – 3, respectively.

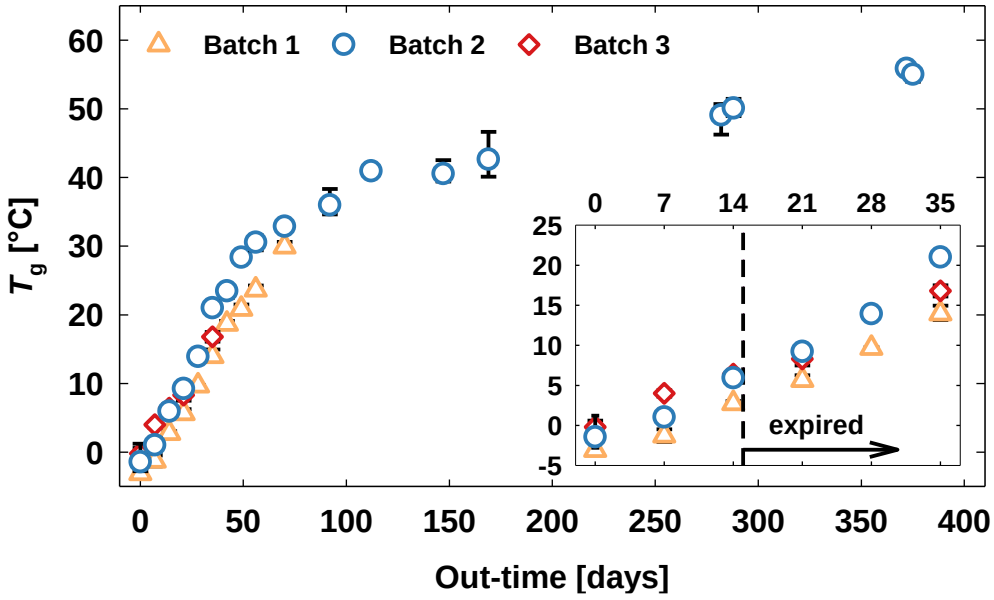

Figure 6-8. T_g values measured by DSC for prepreg specimens subjected to increasing periods of out-time. Error bars represent the minimum and maximum values measured for batches 1 and 2, and standard deviations for Batch 3.

6.3.2 FT-IR

The band absorbances measured from the FT-IR tests described in Section 6.2.3 along with degrees-of-cure calculated using Equation (6.1) are presented in Figure 6-9 shown below and in Table A-2 of Appendix A. The area of the epoxy (oxirane) band at 909 cm^{-1} was found to decrease with increasing out-time producing a progressive increase in the calculated degree-of-cure. The epoxy band was also shifted to higher wavenumbers as curing progressed, reaching 913 cm^{-1} for fully cured specimens. α_t was found to vary more in specimens subjected to longer out-times with the largest variabilities occurring in 40-day and fully cured specimen measurements. Difficulty in achieving adequate contact between the FT-IR crystal and increasingly aged prepreg specimens is

likely the cause of this observation. This is a common problem when using an ATR approach and future considerations should include grinding or pulverizing of the specimens.

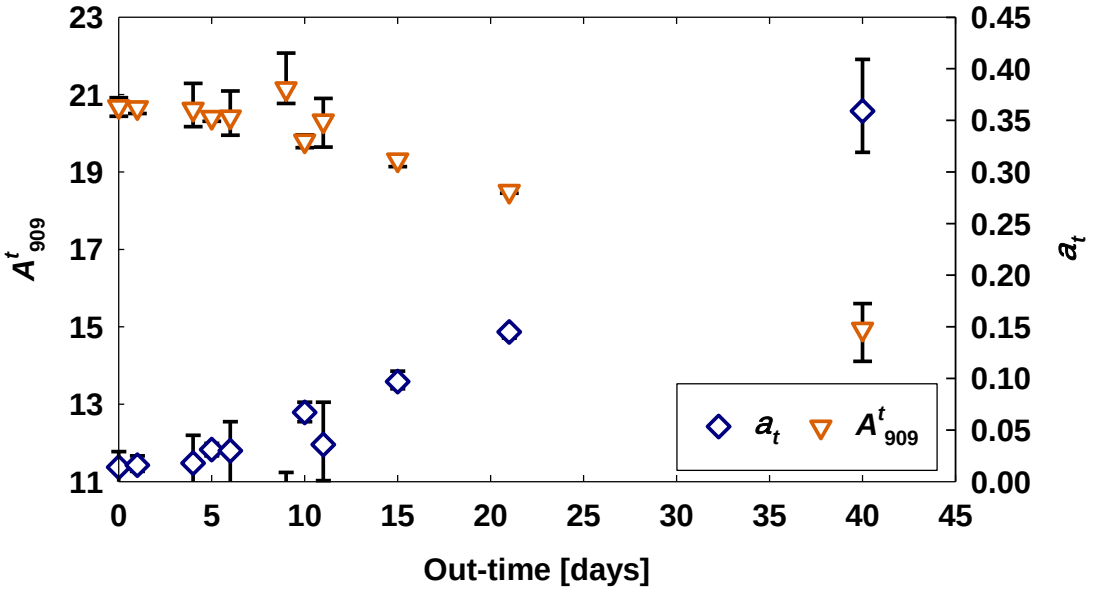

Figure 6-9. Evolution of the 909 cm^{-1} epoxy band absorbance and the corresponding degree-of-cure with increasing room-temperature out-time.

Several of the tests performed – namely 16, 47, and 53 days – exhibited large amounts of scatter in the 900 – 1200 cm^{-1} range, as shown in Figure 6-10. These tests were disregarded due to the proximity of the scatter to the epoxy band and because it was unclear what had caused the

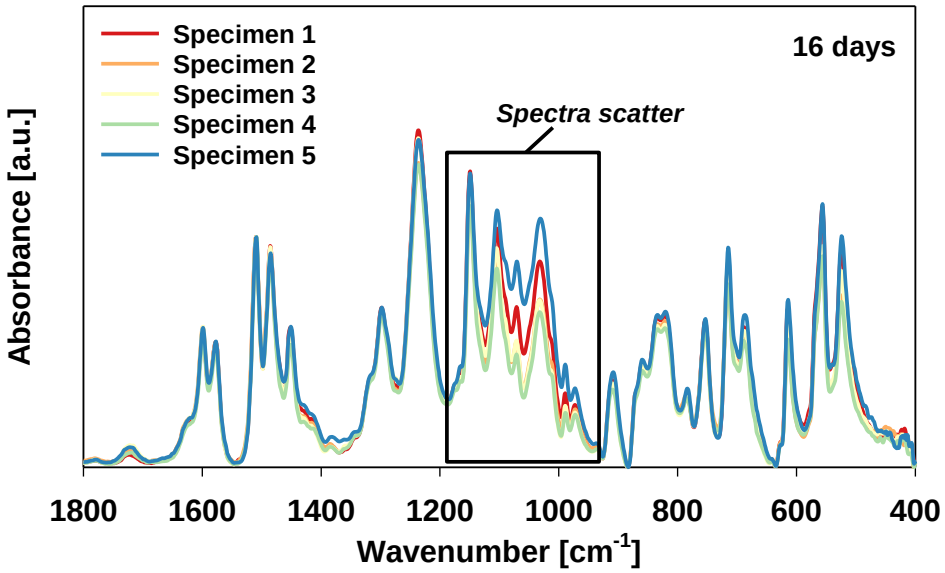

Figure 6-10. FT-IR scans of prepreg specimens aged 16 days at room-temperature. Scatter in the spectra around 900 – 1200 cm^{-1} is highlighted.

observed variation. Specimens aged for 9 and 11 days produced repeatable spectra, however, the calculated degrees-of-cure deviated significantly from the overall trend observed in the other data. In fact, the 9-day specimen exhibited a non-physical degree-of-cure of -0.014.

6.3.3 GPC

The MWDs obtained from the tests performed on specimens from batches 1 and 3, as described in Section 6.2.4, are presented in Figure 6-11. For specimens exposed to longer out-times, the left-hand-side tail of the MWD was found to shift towards higher molecular weights and the differential weight fraction of the peak was found to intensify. These observations suggest that curing of the 5276-1 resin system at room temperature consists primarily of small polymer chain growth. Larger molecules remain largely unaffected, as little change is observed in the peak molecular weight (M_p) and the right-hand-side tail of the distribution.

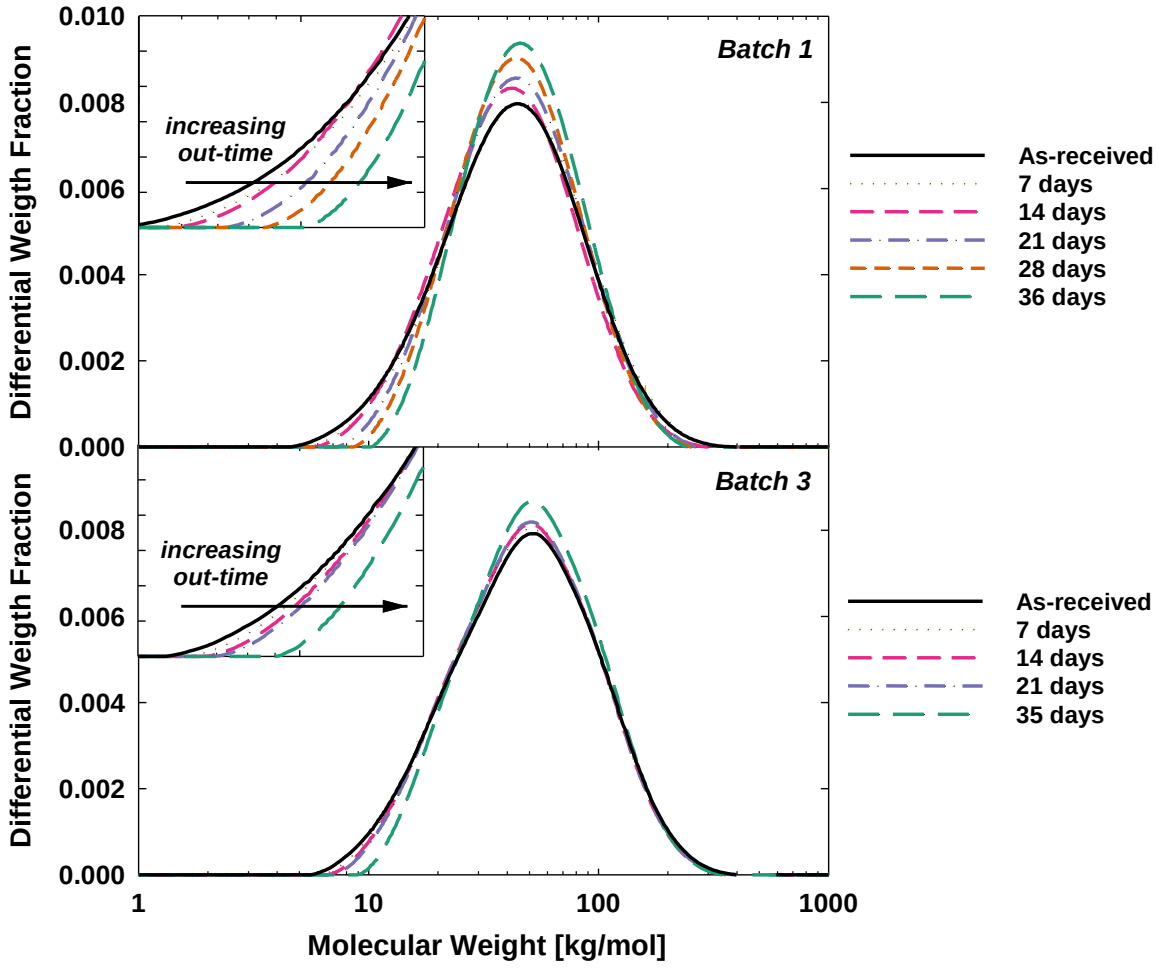

Figure 6-11. MWDs obtained for aged specimens from Batch 1 and Batch 3. Insets highlight the shifting observed in the lower molecular weight tail of the distributions.

Changes to the MWDs obtained were quantified using the molecular weight average metrics described in Section 6.2.4 and are summarized in Table 6-3. The relationship between M_n, M_w, M_z, $Đ$, and out-time are plotted in Figure 6-12.

Table 6-3. Summary of the molecular weight averages and *Đ* calculated for each MWD.

t_{out} [days]	*Batch 1*					*Batch 3*				
	M_p	M_n	M_w	M_z	$Đ$	M_p	M_n	M_w	M_z	$Đ$
0	44.8	31.7	51.0	77.9	1.61	51.9	34.9	57.7	88.9	1.65
7	44.8	33.1	52.4	79.2	1.58	50.4	35.2	56.5	84.1	1.61
14	41.8	32.0	48.2	70.3	1.51	50.4	35.9	56.9	84.3	1.58
21	43.6	34.8	50.1	65.9	1.44	51.1	36.5	57.8	87.4	1.58
28	43.6	36.2	50.7	69.3	1.40	-	-	-	-	-
35	-	-	-	-	-	51.9	39.9	59.8	87.0	1.50
36	45.5	39.0	53.0	70.8	1.36	-	-	-	-	-

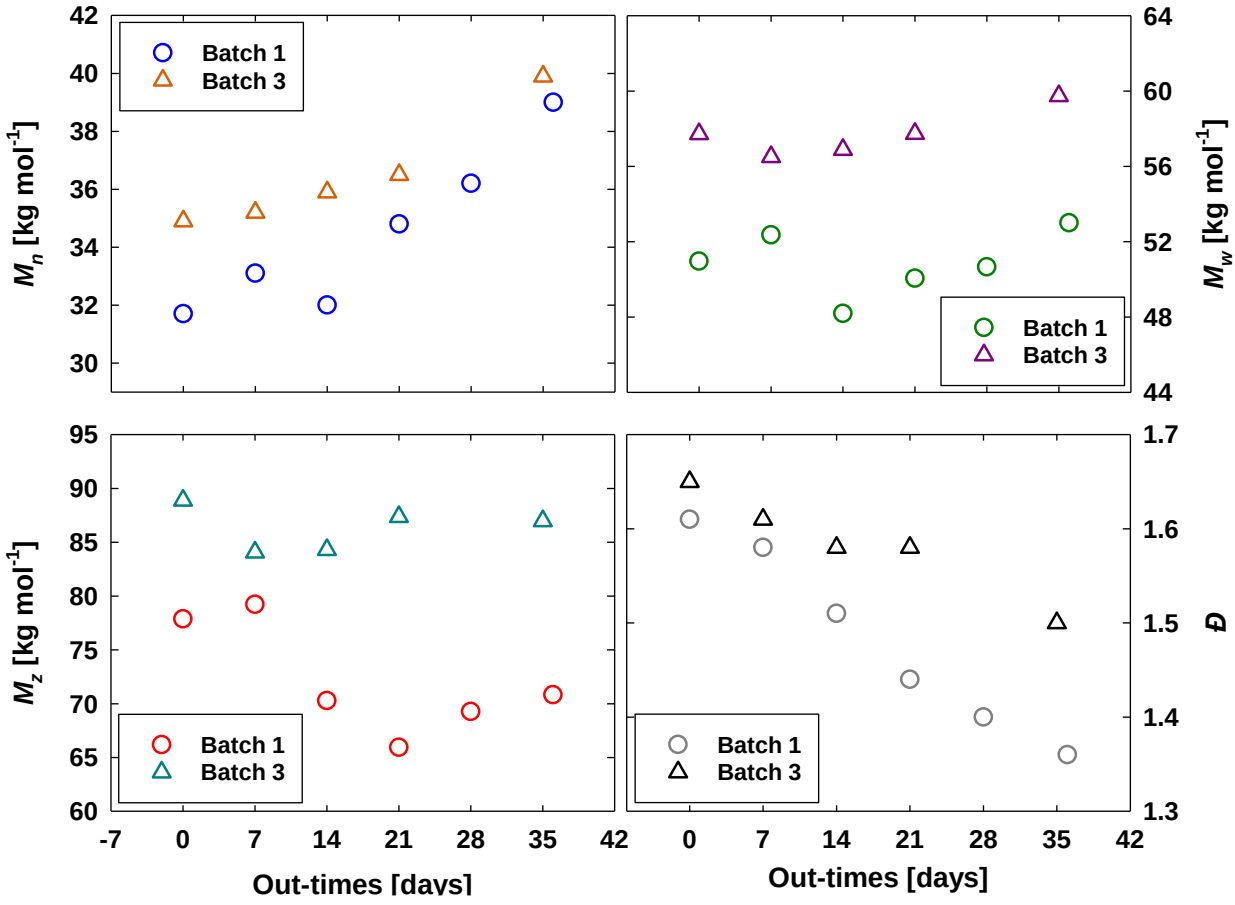

Figure 6-12. Molecular weight averages and *Đ* for Batch 1 and Batch 3 specimens plotted against their corresponding out-time.

Only M_n and $Đ$ showed noticeable trends with out-time, most likely due to their particular dependence on the presence of lower molecular weight molecules. To properly compare the trends observed in each specimen batch, the shifting caused by different α_x values must be considered. Figure 6-13 shows M_n and $Đ$ plotted against the corresponding specimen T_g values measured by DSC in Section 6.3.1 with linear regressions applied. The results indicate that M_n is a better indicator of specimen ageing with a coefficient of determination of 0.85 compared to 0.44 for $Đ$.

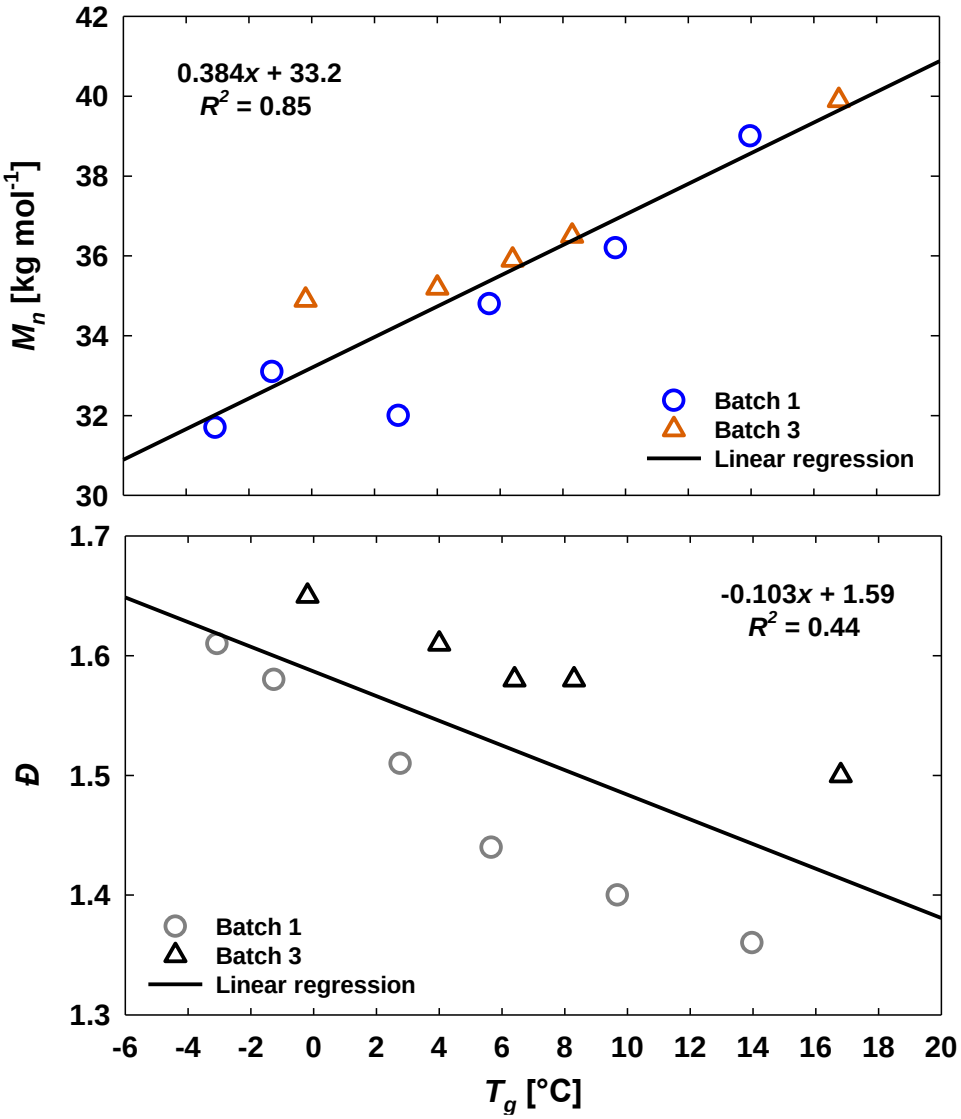

Figure 6-13. Number average molecular weight and dispersity values obtained from Batch 1 and Batch 3 MWDs plotted against corresponding specimen T_g values.

6.3.4 Tack

Viscoelastic Shifting Parameters

Figure 6-14 illustrates a typical frequency sweep, as described in Section 6.2.5, on a prepreg specimen aged to 7 days. All out-times investigated exhibited the same general trend of the moduli with respect to frequency. Temperatures were limited to 60 °C, while the frequency range used included relatively high values to reduce test duration and avoid significant cure advancement during elevated temperature measurements. The high moduli ($>10^5$ Pa) in the low frequency region (i.e. the high temperature measurements), where a neat resin system is expected to flow, are attributed to the presence of the fibres.

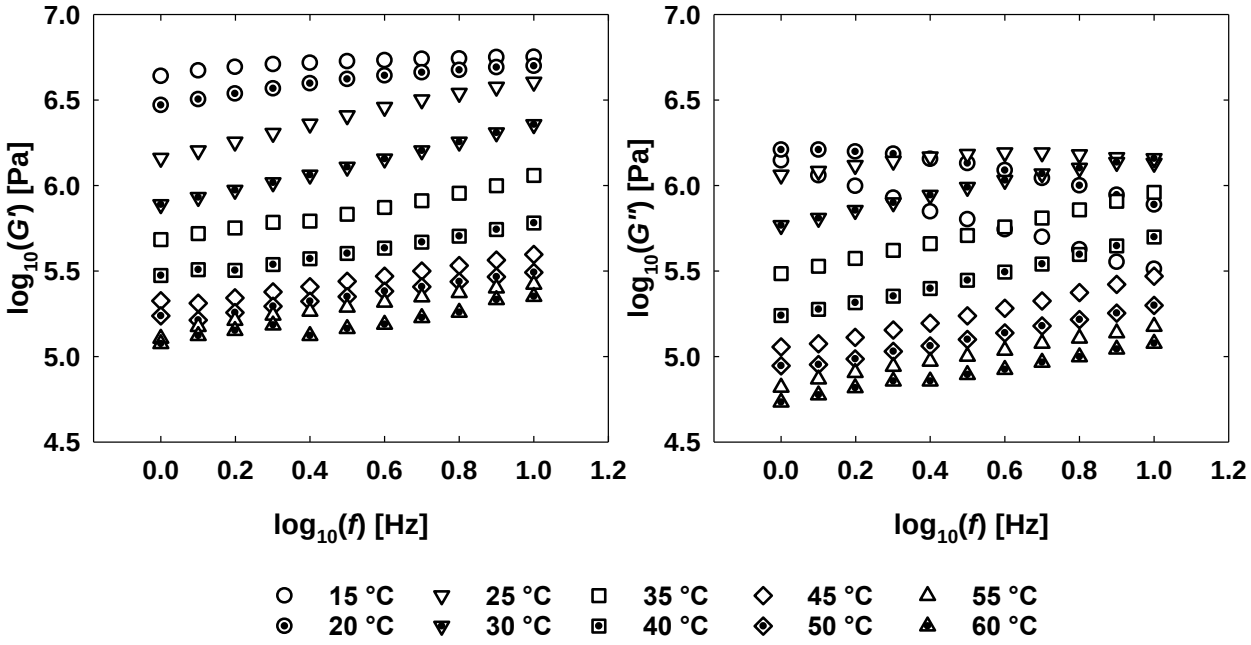

Figure 6-14. Storage modulus *G'* (left) and loss modulus *G''* (right) frequency sweeps performed on aged prepreg specimens with t_{out} = 7 days at temperatures 15 °C – 60 °C with a strain amplitude of 0.01 %.

Employing the principle of time-temperature equivalence, the rheological measurements shown in Figure 6-14 were shifted along the frequency axis to an arbitrary reference temperature of 25 °C to produce the master curve shown in Figure 6-15 (left). The corresponding horizontal shift factors (*a*) were obtained using the automated procedure described by Choong *et al.* [157] which seeks to minimize the area enclosed by adjacent data sets. The data obtained at different temperatures overlapped to yield coherent master curves for all out-times and for as-received prepreg, confirming that the rheometry carried out provides insight into the time-temperature

dependence of 5276-1. Figure 6-15 (right) shows that the relationships between shift factor and test temperature follow a very similar trend for each of the out-times investigated.

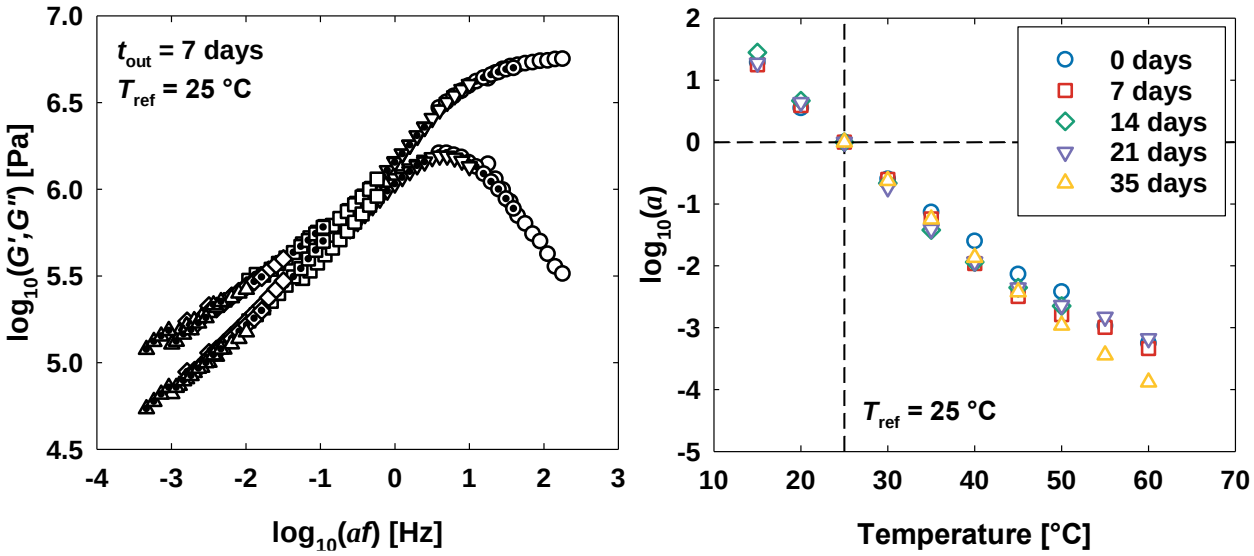

Figure 6-15. Rheological master curve for t_{out} = 7 days obtained through minimization of area technique (left); Corresponding horizontal shift factors obtained for all out-times considered (right).

With resin viscous behaviour so closely related to changes in testing temperature, it is suggested that the changes to prepreg tack commonly observed with increased out-time [151-153] can be related to the changes in resin T_g reported in Section 6.3.1. Shift factors linked to both testing temperature and T_g are defined here in the form of Arrhenius relationships as opposed to the WLF equations discussed in Section 6.2.5:

$$\log_{10} a_T = \frac{E}{R}\left(\frac{1}{T} - \frac{1}{T_{\text{ref}}}\right), \tag{6.10}$$

$$\log_{10} a_{T_g} = \frac{E}{R}\left(\frac{1}{T_{\text{g,0}}} - \frac{1}{T_{\text{g}}}\right), \tag{6.11}$$

where R is the universal gas constant (8.31 J K^{-1} mol^{-1}), E is an activation energy, T and T_{ref} are the test and reference temperatures and $T_{g,0}$ is the glass transition temperature at 0 days, all expressed in Kelvin. By letting $T_{\text{ref}} = T_{g,0}$, a combined shift factor ($a_T a_{Tg}$) that accounts for the difference between testing temperature and T_g at any out-time can be defined as:

$$\log_{10} a_T a_{T_g} = \frac{E}{R}\left(\frac{1}{T} - \frac{1}{T_g}\right) \tag{6.12}$$

where E can be obtained from the Arrhenius plot shown in Figure 6-16. Since rheometer tests were not performed directly at T_g, combined shift factors had to, instead, be calculated from individual Arrhenius plots for each out-time.

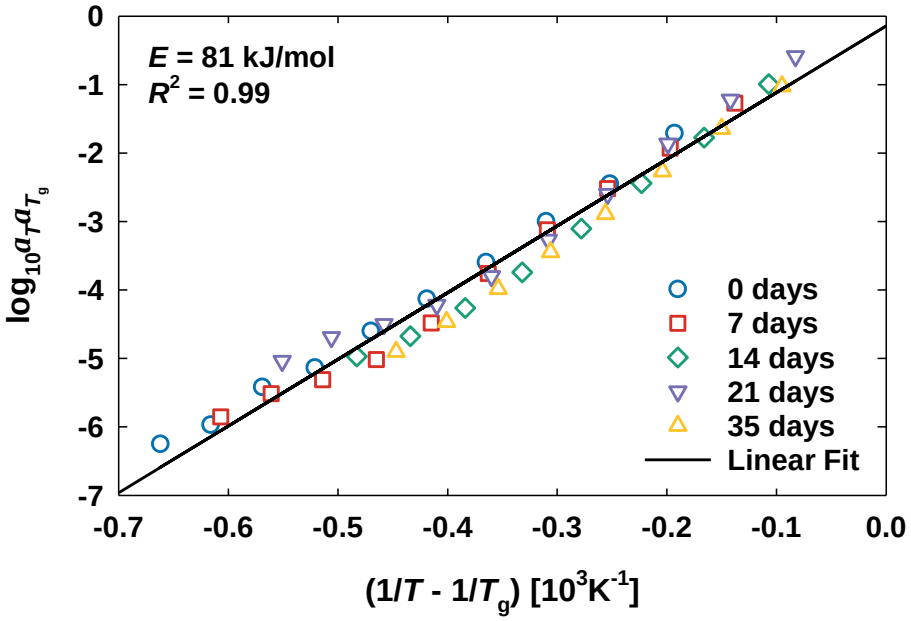

Figure 6-16. Arrhenius plot obtained for as-received and aged prepreg specimens showing the dependence of the combined shift factor on the distance from T_g.

Figure 6-16 shows that the observed shifts in prepregs with out-time can be accounted for through the additional shift factor a_{Tg}. Linear regression through the data yielded E = 81 kJ mol^{-1} with a coefficient of determination R^2 = 0.99. E is essentially employed here as a parameter representing the observed temperature dependence instead of a chemical or physical activation energy, as E is affected by several processes such as polymer relaxation and partial curing induced by elevated temperatures.

Tack Curve Evolution

Applying Equation (6.10) to shift tack data obtained for each out-time to a reference temperature of 25 °C gives the tack master curves plotted in Figure 6-17. The Gaussian curves obtained by applying Equation (6.9) to the master curve data allows $F_{t,max}$ and $a_T r_{max}$ to be determined and used as quantitative descriptors of tack for the chosen reference temperature. These descriptors are presented in Table 6-4.

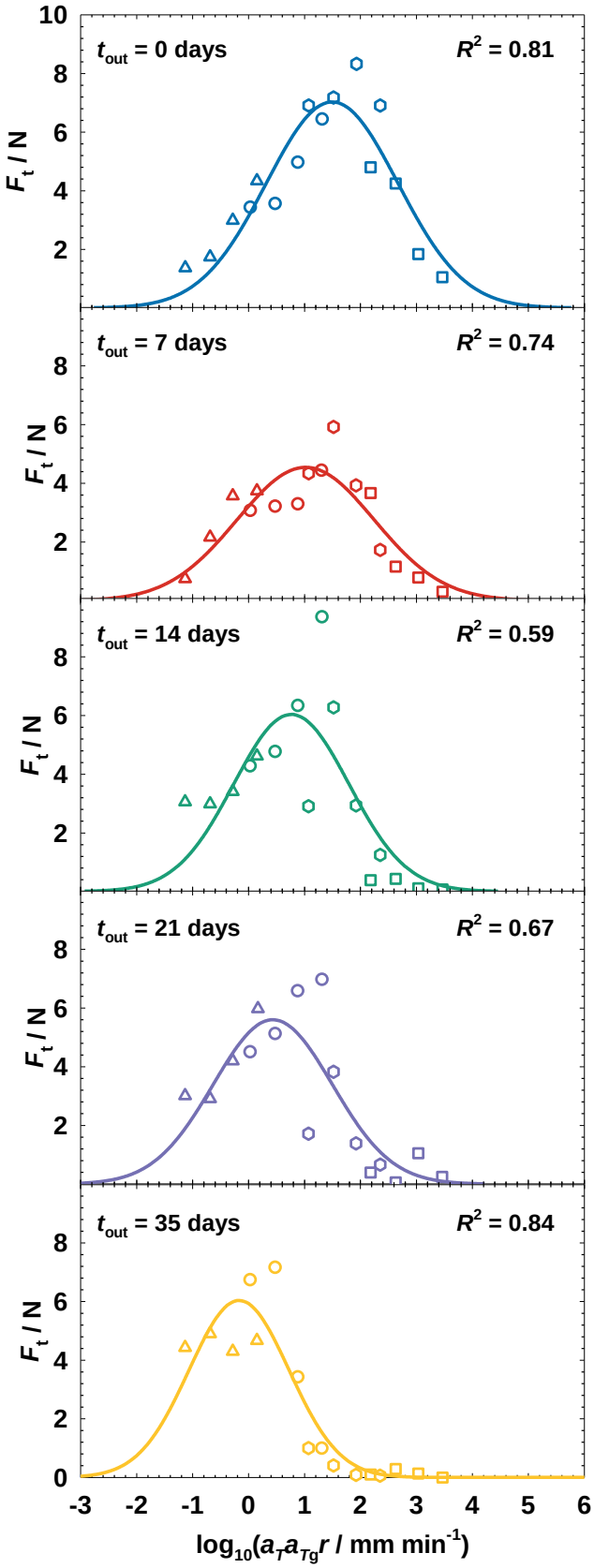

Figure 6-17. Tack master curves obtained by shifting tack data to 25 °C.

Table 6-4. Tack descriptors obtained from tack master curve Gaussian fits.

t_{out} [days]	$F_{t,max}$ [N]	$a_T r_{max}$ [mm min^{-1}]	$a_T a_{Tg} r_{max}$ [mm min^{-1}]
0	7.03	31.67	31.67
7	4.55	10.64	37.01
14	6.03	5.92	41.31
21	5.60	2.74	32.86
35	6.05	0.68	84.58

As out-time increased, $a_T r_{max}$ was found to decrease consistently, while only small changes in $F_{t,max}$ were observed. This result is consistent with the findings reported by Endruweit *et al.* [152] who studied the tack behaviour of unidirectional CF/epoxy prepreg using the same method. The shifting of master curves to lower feed rates for specimens subjected to longer out-times is even more evident when the tack data for all out-times is shifted to 25 °C and plotted together as shown in Figure 6-18 (left). The combined shift factor given by Equation (6.12) was used to shift the tack data for each ageing condition to the corresponding T_g, resulting in the master curves for all out-times to approximately coincide as shown in Figure 6-18 (right). This is also reflected in the values of $a_T a_{Tg} r_{max}$ shown in Table 6-4 with the exception of the 35-day case.

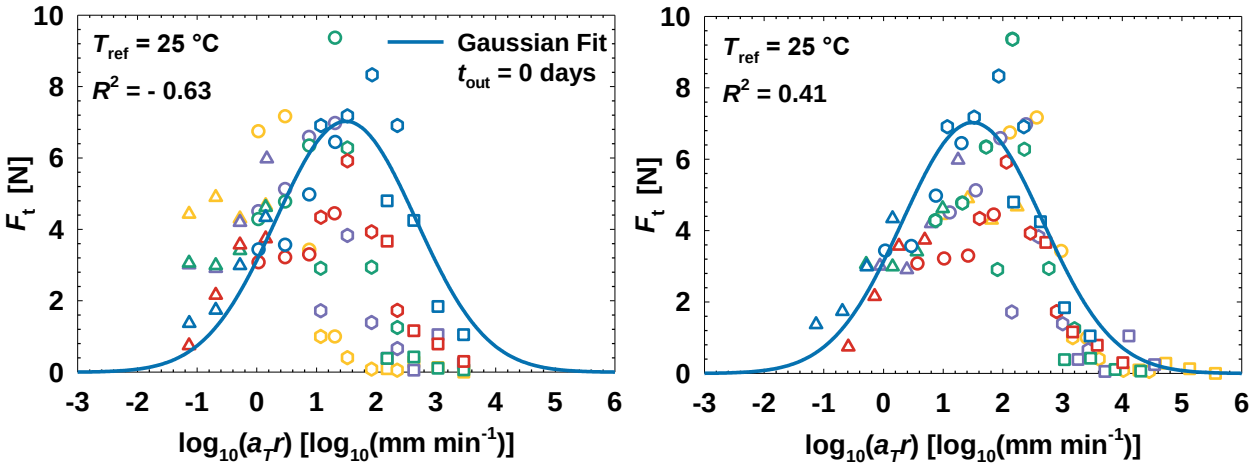

Figure 6-18. Tack data shifted to 25 °C showing the effect of out-time (left); Tack data shifted to 25 °C and to respective T_g, showing a more collapsed curve (right).

In summary, the evolution of prepreg tack with ageing has been linked to changes in resin T_g through the principle of TTS. This relationship has been expressed using the Arrhenius relation described in Equation (6.12). The shifted feed rate at maximum tack was found to be a good indicator of specimen ageing and is shown plotted against out-time in Figure 6-19 along with an exponential regression (R^2 = 0.99).

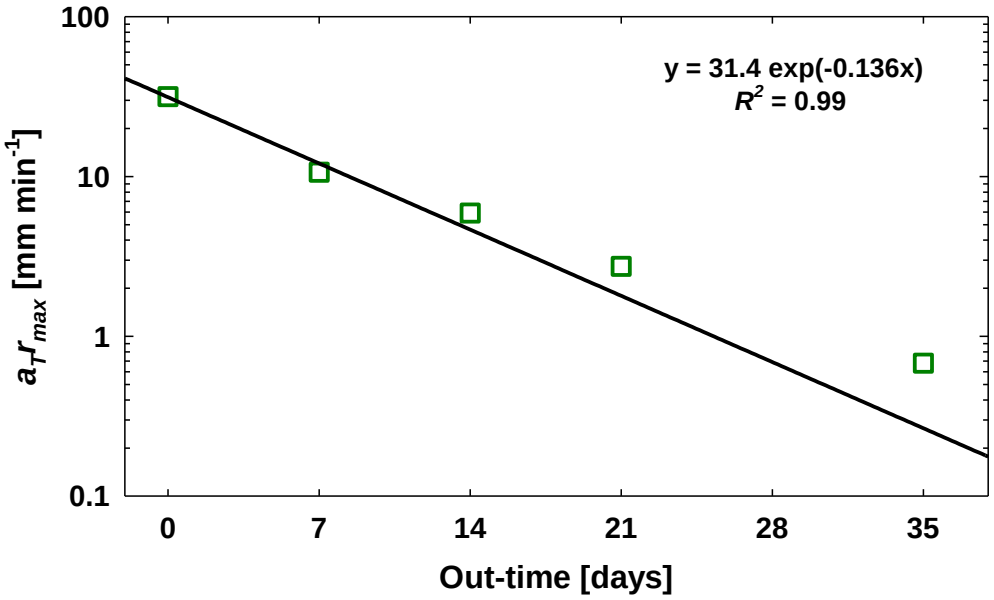

Figure 6-19. Shifted federate at maximum tack against specimen out-time.

6.4 Conclusions

6.4.1 Material Identification

Within the manufacturer's technical data sheet [110], 5276-1 is described as a highly toughened epoxy resin with a shelf life of 6 months at -18 °C, an out-life of 14 days, and 2 hour cure cycle at a temperature of 177 °C. Once fully cured, it boasts a dry T_g of 188 °C with a recommended service temperature range of -59 °C to 121 °C. The characterization presented in this chapter has revealed additional information regarding the composition and properties of the 5276-1 system. Regarding its composition, FT-IR testing has revealed that 5276-1 consists of an epoxy monomer and an amine curing agent (Section 6.2.3), while the optical micrographs presented in Chapter 5 showed what appear to be thermoplastic toughening particles dispersed between the fibre tows (Section 5.4.4). DSC scans of as-received prepreg specimens showed that 5276-1 features an initial glass transition temperature as low as -3.08 °C, assuming out-time of the

recovered offcuts was minimal. Finally, GPC performed on similar specimens produced fairly symmetric MWDs with number-average molecular weights between 31.7 kg mol^{-1} to 34.9 kg mol^{-1}.

6.4.2 Effect of Ageing

The different methods used here to study the room temperature ageing of 5276-1 prepreg specimens have revealed progressive changes to either the resin's structure, or its thermo-physical behaviour with increasing out-time. These changes include:

1. The consumption of epoxy monomer and primary amine molecules as measured by the disappearance of the 909 cm^{-1} and 1623 cm^{-1} absorbance bands, respectively.
2. The disappearance of lower molecular weight molecules and the simultaneous increase in the number of molecules around the peak of the MWD obtained through GPC.
3. The progressive increase in the pre-gelation T_g measured by DSC.
4. The shifting of peak tack to lower peel rates, or higher temperatures, measured using the continuous application-peel method described in Section 6.2.5.

Within the periods of out-time studied, no significant change in the concentration of larger MW molecules was observed, nor did any of the specimens experience gelation.

6.4.3 Method Ranking

Material inspection must be efficient and economically viable, as well as technically robust for the recycling methodology discussed in this thesis to be effective. This chapter has illustrated the promise of each inspection technique in terms of their ability to measure changes in resin state with out-time. Next, each method was ranked based on the amount of material, time, and money are required to complete a hypothetical 35-day characterization of PW/5276-1. It is assumed that data collection occurs every 7 days and includes 3 repetitions, except for tack testing for which one repetition is sufficient. A technician hourly rate of 50 $/hr was considered when estimating the operation costs[6].

[6] All dollar figures provided in this discussion are given in Canadian dollars (CAD) and do not include taxes.

DSC

A DSC specimen size of 10 mg was considered given the TA Instruments recommendation of 5 – 15 mg. The testing window used to calculate scan duration was ± 30 °C about the expected T_g. A Discovery 250 DSC with an RCS90 cooling system and a specimen preparation press from TA were used to calculate the capital investment associate DSC testing. Operational costs included 10 minutes of technician time, while consumables included DSC pans (DSC Consumables, Inc.) at 1.69 $ each and nitrogen gas at 30 $ per 8.44 m^3 cylinder and a testing flow rate of 50 mL/min.

FT-IR

An FT-IR specimen size of 4 mm x 4 mm was considered as the ATR crystal size is 2 mm x 2 mm. Testing time was taken as 30 seconds, approximately the amount of time needed to obtain an average spectrum from 6 scans. The Spectrum II FT-IR with diamond ATR accessory from Perkin Elmer was considered for the capital investment and 5 minutes of technician time for the operational cost. No consumables were considered for this method.

GPC

A minimum required GPC specimen size of 28 mg was determined based on the recommendations outlined in Mulvenna [158] and using the fibre volume fraction of the PW/5276-1 (312 gsm). Testing time was approximated as 30 min, the maximum retention time obtained. A Breeze GPC from Waters equipped with an isocratic pump, a cooled autosampler, RI 2414 and UV 2489 detectors, and a set of high-resolution Styragel columns was considered for the capital investment. Operational costs included 15 minutes of technician time. Consumables included 135 mL of DMF at 0.15 $/mL.

Tack & Rheometry

As mentioned in Section 6.2.5, tack testing and rheometry specimens measured 215 mm x 75 mm and 30 mm x 30 mm, respectively. Generating each tack master curve without repetitions requires a total of 16 tests of 4, 1.43, 0.56, and 0.20 minutes depending on the feed rate used. This means that one tack master curve requires 24.7 minutes of testing. The rheometer tests performed to obtain TTS shift factors for each out-time take approximately 30 minutes each to run. A 10 kN Criterion C43.104 testing frame with an Advantage environmental chamber from the MTS Corporation was considered for the capital investment for tack testing, while the MCR302 rheometer from Anton Parr was considered for the rheometry. Operational cost considered include

20 minutes for preparing the tack specimens, 124 minutes of tack testing time, and 10 minutes per rheometer test of technician time. No consumables were considered for this method.

Summary

A detailed summary of the information used to compare inspection techniques is provided in Table 6-5. A more streamlined comparison including only the total material, time, and cost needed to carry out the aforementioned characterization is given in Figure 6-20.

Table 6-5. Detailed summary of inspection technique comparison.

	DSC	FT-IR	GPC	Tack/Rheometry
Specimen Size [mm^2]	32	16	89	16,125/900
Number of Tests	15	15	15	80/15
Material Needed [m^2]	4.81 x 10^{-4}	2.40 x 10^{-4}	1.34 x 10^{-3}	1.29/0.0135
Test Time [min]	30	0.5	30	24.7/30
Characterization Time [min]	450	7.50	450	124/450
Capital Investment [$]	120,900	26,925	118,422	88,400/125,090
Operational Cost [$]	125	62.5	188	120/125
Consumables [$]	25	0	20	0/0
Total Cost [$]	121,050	26,988	118,630	88,520/125,215

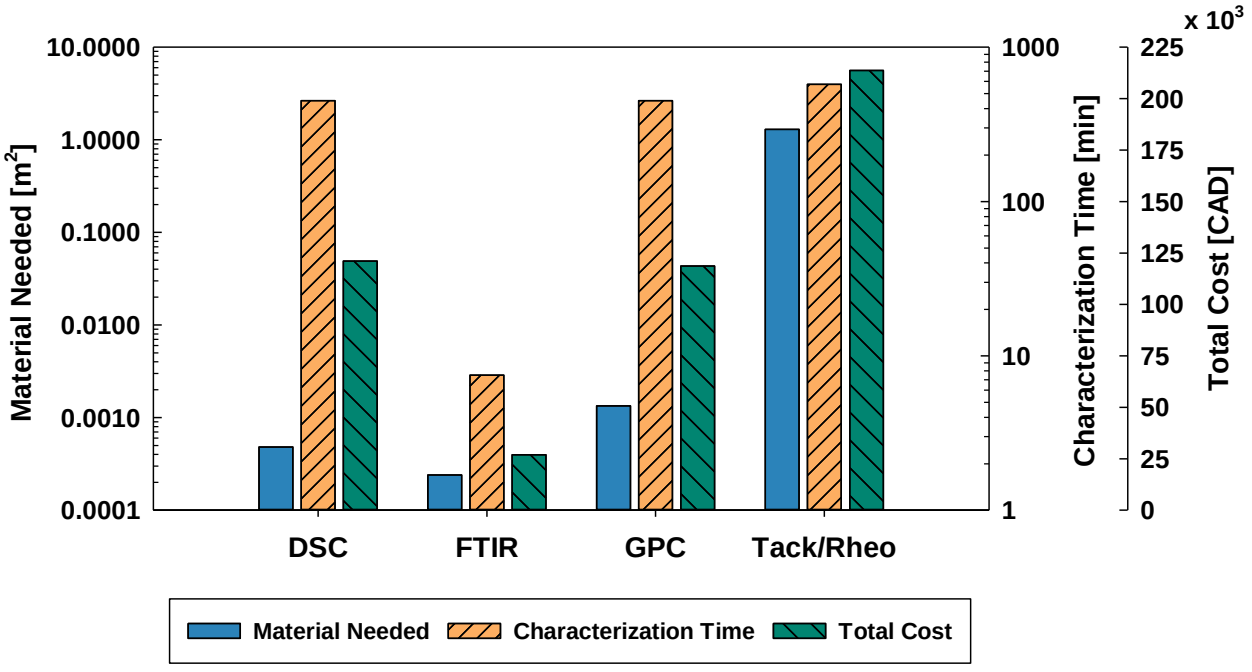

Figure 6-20. Material, time, and cost needed to characterize PW/5276-1 using each of the inspection techniques presented.

For each of the three comparison categories, simple rankings from 1st to 4th were assigned to each method and, with each category being weighted equally, the results were combined to obtain the following overall rankings:

- First Overall: FT-IR (1st, 1st, 1st)
- Joint Second: DSC (2nd, 2nd, 3rd)
- Joint Second: GPC (3rd, 2nd, 2nd)
- Fourth Overall: Tack (4th, 4th, 4th)

While FT-IR presents itself as by far the most cost effective and efficient method studied here, additional work is required to improve the quality of the spectra obtained from specimens with more advanced degrees-of-cure. Furthermore, it must be shown that the degree-of-cure obtained from the analysis of spectral bands correlates directly to the degree-of-cure measured by DSC, as the latter was used to characterize the resin's curing behaviour as well as the staging methodology.

7
ADVANCED FLOW

In this chapter, the staging methodology presented in Chapter 5 was used to produce two batches of rPMC with both PW and 8HS fibre architectures. These batches were used to manufacture two complex demonstrator panels to show process scalability. The minimum required filling pressure for both material-part combinations was obtained by varying the moulding pressure from 1 – 9 MPa. Some general characteristics of properly filled parts are discussed and compared with observations from the literature. The power of flow-compaction tailoring through staging was reinforced by making a set of demonstrator parts using strands with degrees-of-cure similar to recently expired offcuts. Finally, the preliminary results of two different material hybridization trials are presented.

7.1 Process Scale-up

The previous two chapters have laid the groundwork for preparing an rPMC that can be used to produce components with complex geometries using a cure cycle different from the standard options supplied by the material manufacturer. More specifically, they showed the feasibility of taking expired prepreg offcuts, performing an inspection according to the guidelines from Chapter 6, carrying out staging to increase the resin degree-of-cure, and achieving a desirable flow-compaction behaviour and curing timescale for a chosen moulding temperature (see Chapter 5). The purpose of this chapter is to show that this recycling methodology can be scaled to accommodate larger quantities of prepreg with different temperature histories, and to show that

the amount of shear deformation observed during the 1-D flow-compaction trials from Chapter 5 will translate to 3-D.

7.1.1 Demonstrator Parts

The two demonstrator parts shown in Figure 7-1 were chosen to test the rPMC's ability to completely fill a complex mould cavity. The first part, referred to as the *multi-ribbed panel* features four parallel ribs of increasing size and was developed by Collins [104] during her work on the dimensional stability of a CF-PEEK randomly oriented strand material. The second demonstrator panel referred to as the *compound T-bracket* features a primary and secondary rib, a moulded hole, two raised bosses, and several aggressive corner radii. This second demonstrator was developed during the consortium for research and innovation in aerospace in Québec's (CRIAQ) project COMP412: Thermoplastic Composites Forming Technology for Complex and Integrated Aerospace Components [90]. The overall size of both demonstrator panels is 100 mm x 100 mm with thicknesses that depend on the quantity of material used. Dimensions of each panel feature are given in Table 7-1.

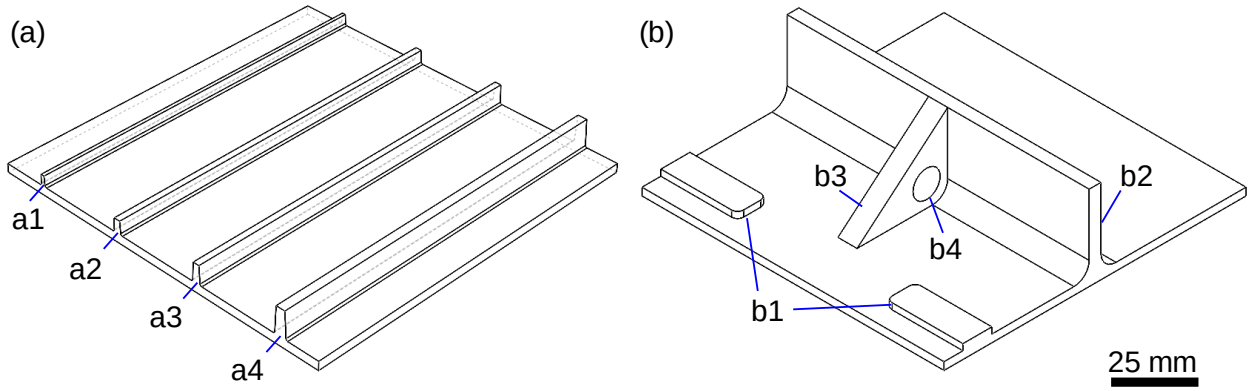

Figure 7-1. The multi-ribbed (a) and compound T-bracket (b) demonstrator panels.

Table 7-1. Key feature dimensions in millimetres for each demonstrator panel.

Multi-Ribbed Panel [104]		Compound T-Bracket	
Rib (a1)	3.1H x 1.0W, R = 0.5 Draft = 3°	Raised Bosses (b1)	3.2H x 9.6W x 25.4L
Rib (a2)	3.8H x 1.8W, R = 0.5 Draft = 3°	Main Rib (b2)	25.4H x 4.0W, R = 6.0
Rib (a3)	5.3H x 1.8W, R = 0.5 Draft = 3°	Compound Rib (b3)	25.4H x 6.4W x 31.5D
Rib (a4)	7.6H x 2.5W, R = 0.5 Draft = 3°	Moulded Hole (b4)	Ø 9.5

H = height; W = width; L = length; R = radius; D = depth; Ø = diameter

7.1.2 Manufacturing

Two batches of recovered 5276-1 prepreg with different fibre architectures (PW and 8HS) were used to manufacture the demonstrator parts described in the previous section. The 8HS specimens test as part of the Chapter 5 flow-compaction trials experienced maximum levels of shear deformation over a resin viscosity range of 191 – 268 Pa-s. Therefore, a target moulding viscosity of 250 Pa-s was chosen for the advanced flow trials presented here. This decision assumes that the flow-compaction behaviour of PW strands is similarly dependent on resin viscosity. Keeping the same cure cycle from Figure 5-8, the staging map shown in Figure 5-14 was used to select staging parameters that would yield the desired moulding viscosity. A slight difference in the as-received T_g of each batch meant that different staging times were needed to bring each batch to the target $T_{g,staged}$ of approximately 48 °C. 8HS offcuts were staged for 134 min at 120 °C which yielded $T_{g,staged}$ values of 46.7 – 48.3 °C. PW offcuts were staged for 145 min at 120 °C which yielded $T_{g,staged}$ values of 48.7 – 50.3 °C. Remnants of prepreg backing film were found clinging to the edges of 8HS strands following staging as shown in Figure 7-2. These pieces were removed by hand before moulding.

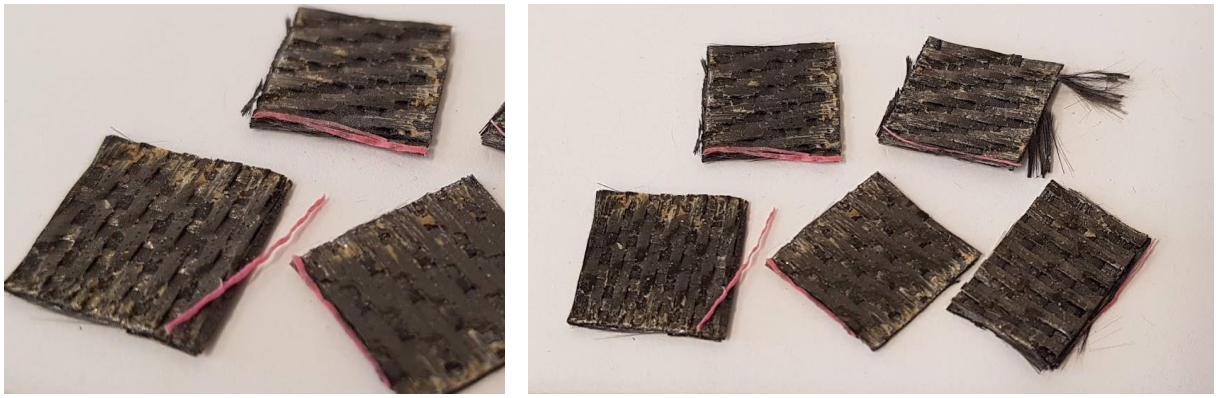

Figure 7-2. Backing film remnants (pink) found attached to staged 8HS strands.

An instrumented steel picture-frame mould with custom inserts was installed on an Instron 5985 universal testing frame equipped with a 250 kN-capacity load cell. The mould inserts provided the geometries needed to produce each demonstrator part without having to change the entire apparatus. Figure 7-3 shows the mould installed on the testing frame before and after rPMC charge placement. The procedure for making each part involved the following six steps:

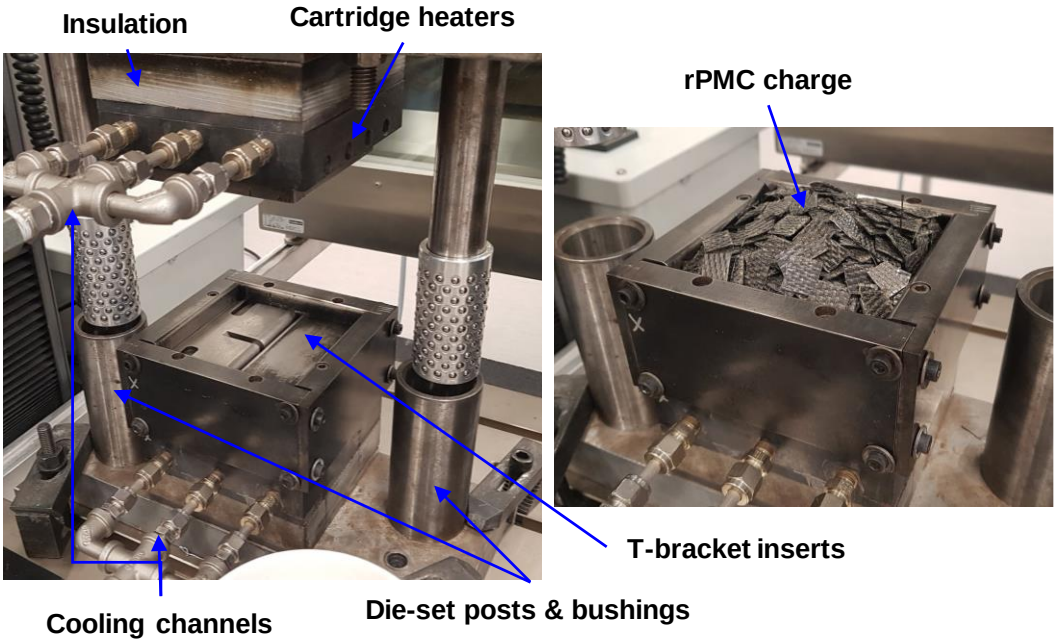

Figure 7-3. The instrumented picture frame mould with compound T-bracket inserts installed (left) and following the placement of an rPMC charge (right).

Step 1

The compression moulding apparatus was preheated to the desired curing temperature of 140 °C. Offset controller setpoint values were needed to obtain an accurate moulding temperature due to the distance between the control thermocouples and the tooling surfaces. The upper mould-half was set to 143 °C and the lower mould-half was set to 150 °C. It was important to avoid having the mould walls interfere with each other by ensuring that the lower half of the mould was 2 – 3 °C hotter than the upper half. A thermocouple was placed on the bottom mould surface during this step to determine when the system had reached thermal equilibrium.

Step 2

With the mould at temperature, 1 – 2 coats of the water-based release agent Chemlease 2627W from Chemtrend were applied to all the moulding surfaces depending on how easily the previous part was demoulded. Each application was allowed to cure for approximately 1 minute before moving to the next coat.

Step 3

The crosshead of the testing frame was lowered until a small preload of 100 – 300 N was measured indicating the two tooling surfaces were in contact. The crosshead displacement value was then tared and the crosshead was raised to a safe working distance.

Step 4

The rPMC charge was placed within the mould taking care to spread strands out evenly and to avoid having them spill over. Charges of 50 g and 65 g were used for the multi-ribbed panels and compound T-brackets, respectively, based on previous work [90, 104].

Step 5

With the charge in place, a procedure previously constructed in the BlueHill control software was initiated. This moulding procedure is made up of six segments:

1- The crosshead is lowered at a speed of 0.5 mm/s until a preload of 1.5 kN, which corresponds to approximately 0.15 MPa of pressure, is reached.
2- The crosshead is held in position for 1 minute to allow the charge temperature to stabilize. Relaxation of the preload was observed during this segment, presumably caused by movement of the rPMC into the mould cavity.
3- The crosshead is lowered at a speed of 0.1 mm/s until the prescribed moulding force is attained.
4- The crosshead position is held constant for a period of 45 min while the rPMC cures and eventually reaches gelation.
5- The temperature controller setpoints for the upper and lower mould-halves are changed to 83 °C and 90 °C, respectively and compressed air is forced through the mould's cooling channels.
6- Once the controller setpoints are attained, the crosshead is raised at a speed of 0.5 mm/s until it reaches the initial starting position.

Figure 7-4 provides an example of segments 1 – 4 that were executed during the moulding of a multi-ribbed panel at 3 MPa. The 5276-1 viscosity model from Chapter 4 (Section 4.4) was used, along with the range of $T_{g,staged}$ values given above, to approximate the resin viscosity during the critical phase of moulding (segment 3) assuming a constant temperature of 140 °C. This range, shown in blue in Figure 7-4, agrees with the target viscosity of 250 Pa-s.

Step 6

The screws anchoring the picture frame to the base of the mould are removed and the picture frame, moulding inserts, and part are removed using a magnet and heat-resistant gloves. A rubber mallet and a brass scraper are then used to dislodge the mould inserts from the part.

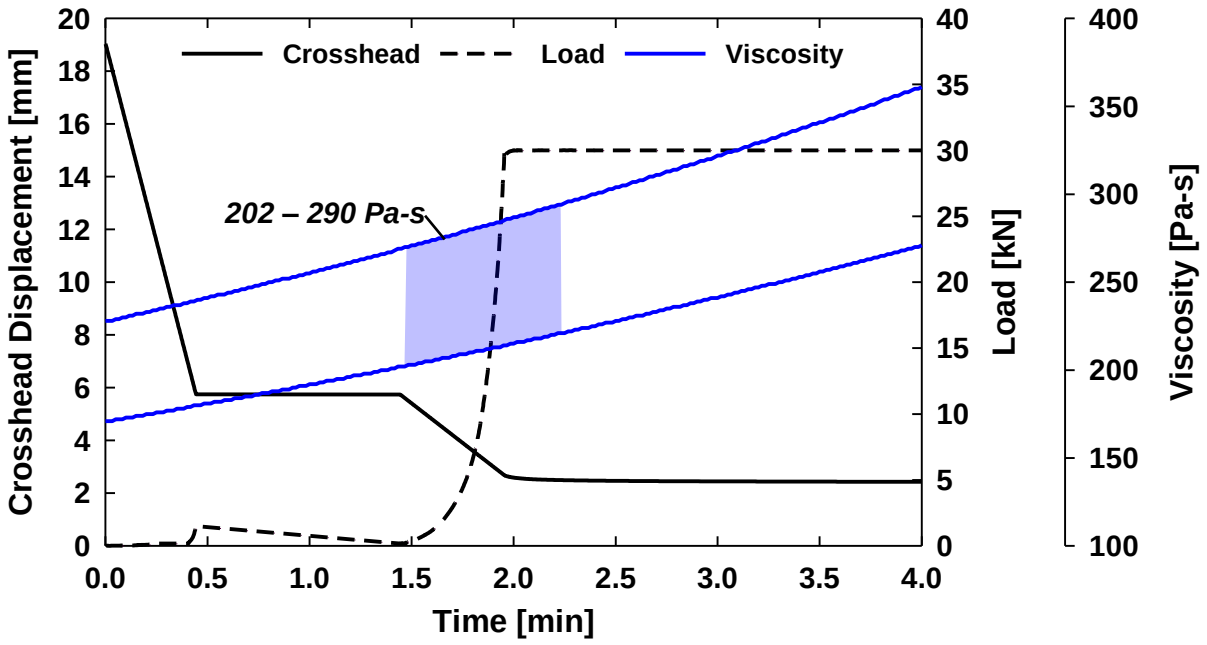

Figure 7-4. The crosshead displacement and load recorded during the manufacture of a PW/rPMC multi-ribbed panel. A moulding pressure of 3 MPa was used. The moulding viscosity was approximated using the 5276-1 viscosity model and is shown in blue.

7.2 Effect of Moulding Pressure

The amount of pressure needed to form a defect free part, referred to here as the *filling pressure*, depends on a number of parameters such as the part geometry, strand size, resin viscosity, and mould closure rate. Filling pressure plays an important role in economies of scale for part manufacturing, as it determines the number of parts that can be moulded concurrently for a given press capacity. Both multi-ribbed panels and compound T-brackets were manufactured using increasing levels of pressure. A summary of the trial parameters is given in Table 7-2.

Table 7-2. Summary of the moulding pressure trial parameters.

	Multi-Ribbed Panel	Compound T-bracket
Material	PW, 8HS	PW, 8HS
Charge Mass	50 g	65 g
Moulding Pressure	1, 3, 6, 9 MPa	3, 6, 9 MPa
Mould Closure Rate	0.1 mm/s	
Cure Temperature	140 °C	
Cure Time	45 min	
Demould Temperature	80 °C	

The filling of each part was evaluated visually. Pictures of the multi-ribbed panels are shown in Figure 7-5 (PW) and Figure 7-6 (8HS), while pictures of the compound T-brackets are shown in Figure 7-7 (PW) and Figure 7-8 (8HS). Detail callouts show the progression of key feature filling with increased moulding pressure.

Ribs *a1* and *a2* of the multi-ribbed panels were the first to fill, whereas the filling of the two larger ribs *a3* and *a4* required higher moulding pressures. This progression is best captured in the images of the PW strand parts moulded at 3 MPa and 6 MPa. In general, it was more difficult to produce fully filled parts with PW strands compared to 8HS strands. This suggests that the "tightness" of the fabric weave plays an important role in strand deformation and explains why commercially available prepreg-based compression moulding compounds always consist of unidirectional tapes. In terms of the compound T-bracket, the raised bosses (*b1*) were the first features to fill followed by the two main rib features *b2* and *b3*. The top corners of the main rib (*b2*) and the outer surface of the secondary rib (*b3*) were the most troublesome areas to fill.

There was no difference observed in the minimum filling pressures required for each demonstrator part when using the same type of strands. Both parts filled between 3 – 6 MPa when using 8HS strands, and 6 – 9 MPa when using PW strands.

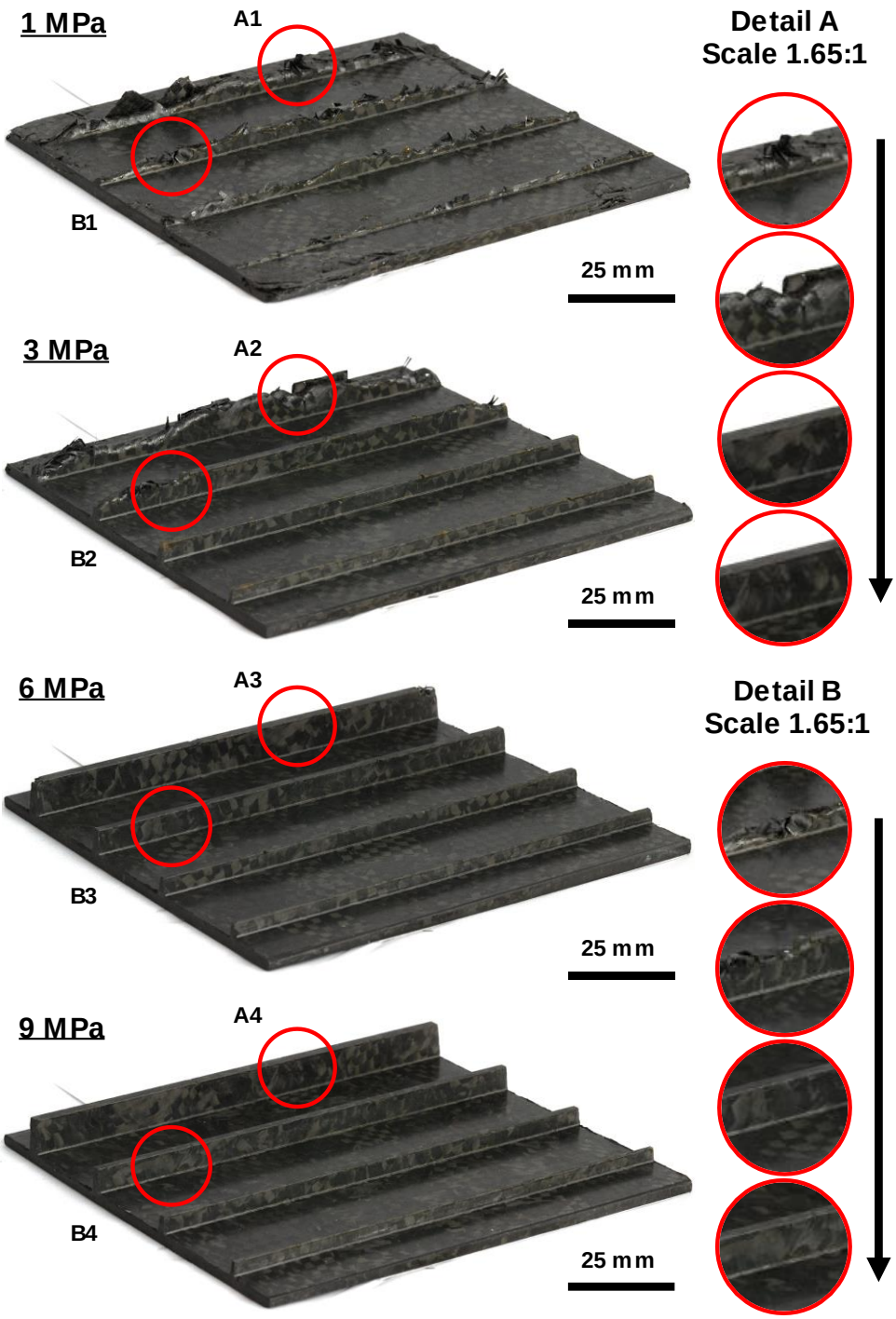

Figure 7-5. PW/rPMC multi-rib panels moulded with increasing pressure (1, 3, 6, 9 MPa).

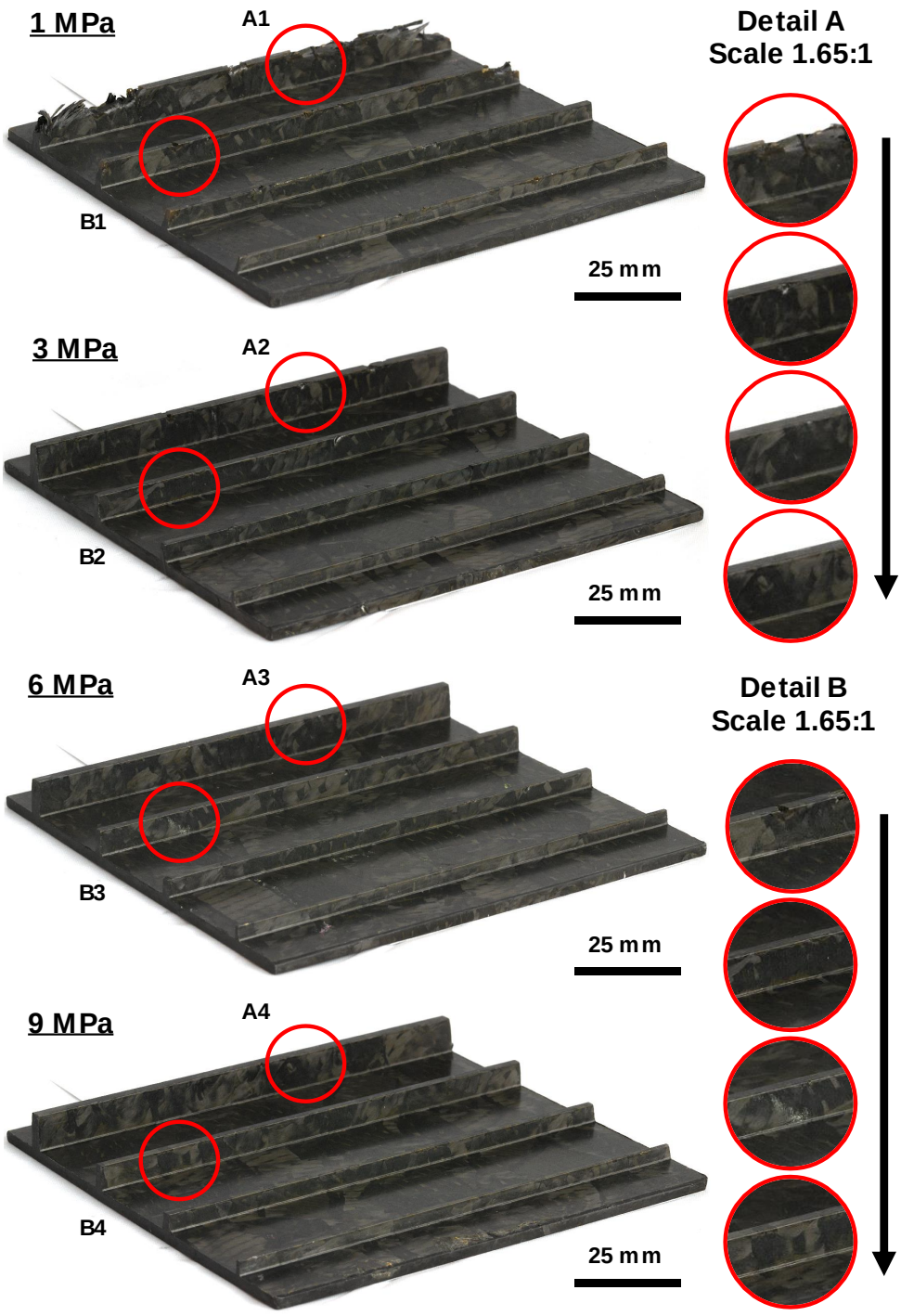

Figure 7-6. 8HS/rPMC multi-rib panels moulded with increasing pressure (1, 3, 6, 9 MPa).

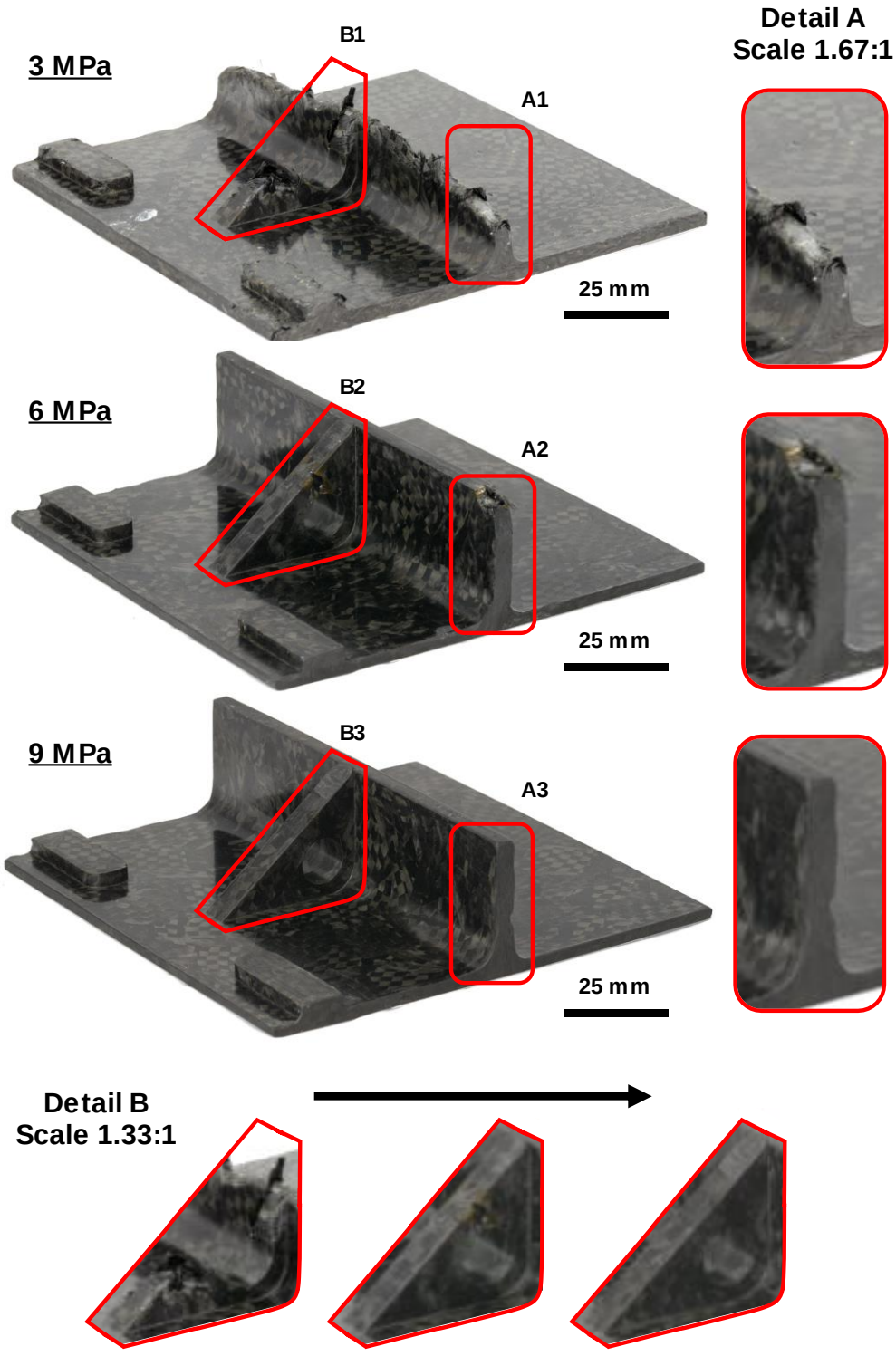

Figure 7-7. PW/rPMC compound T-brackets moulded with increasing pressure (3, 6, 9 MPa).

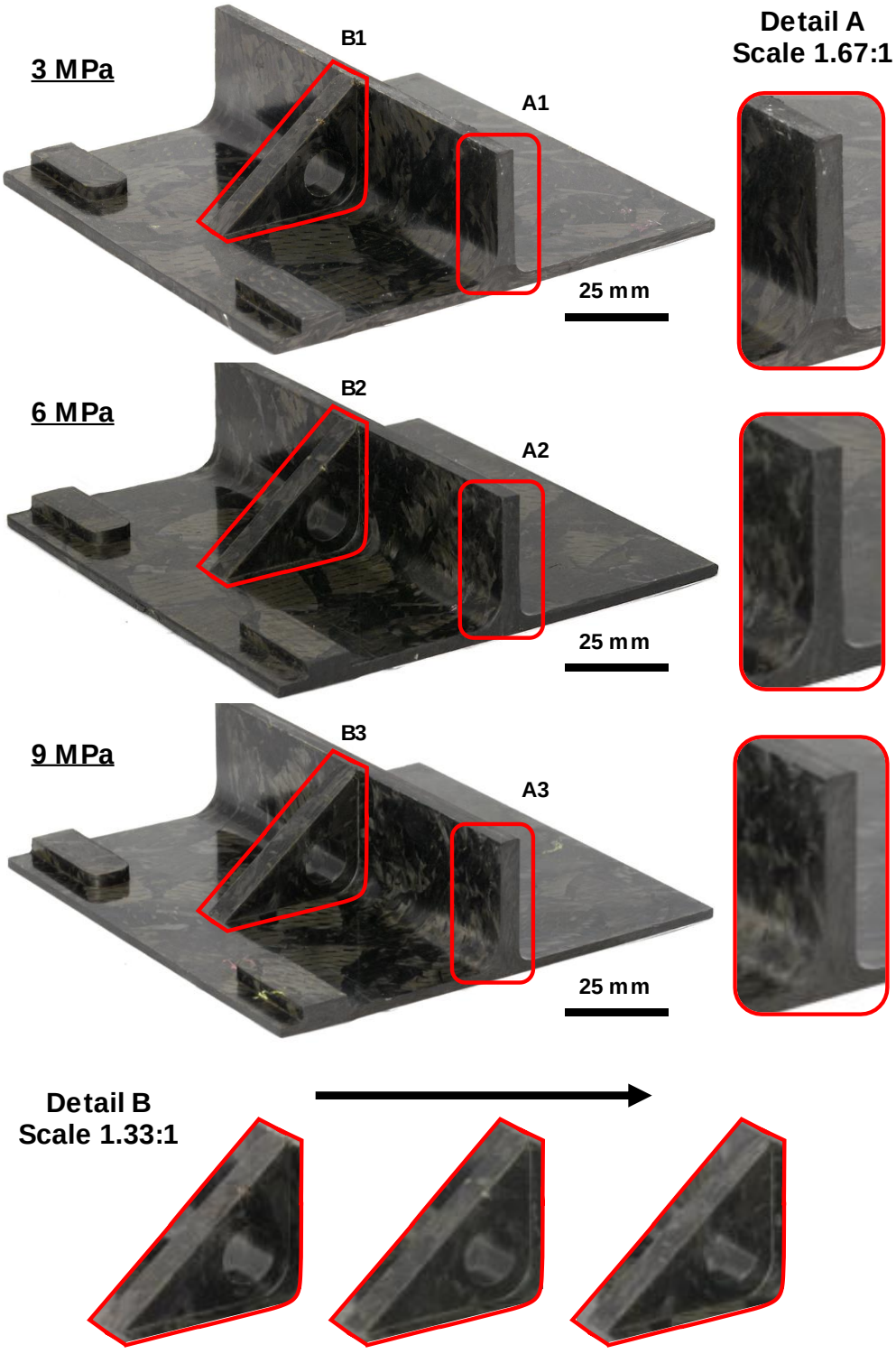

Figure 7-8. 8HS/rPMC compound T-brackets moulded with increasing pressure (3, 6, 9 MPa).

7.2.1 Filling Pressure Analysis

A similar study was performed by LeBlanc [90], who used the same equipment but with different mould inserts to produce simple T-brackets (i.e. without a secondary rib or raised bosses) out of unidirectional CF/PEEK strands. Given the simple geometry of these brackets, LeBlanc was able to use a straightforward image thresholding technique to quantify the filling of his brackets as shown in Figure 7-9.

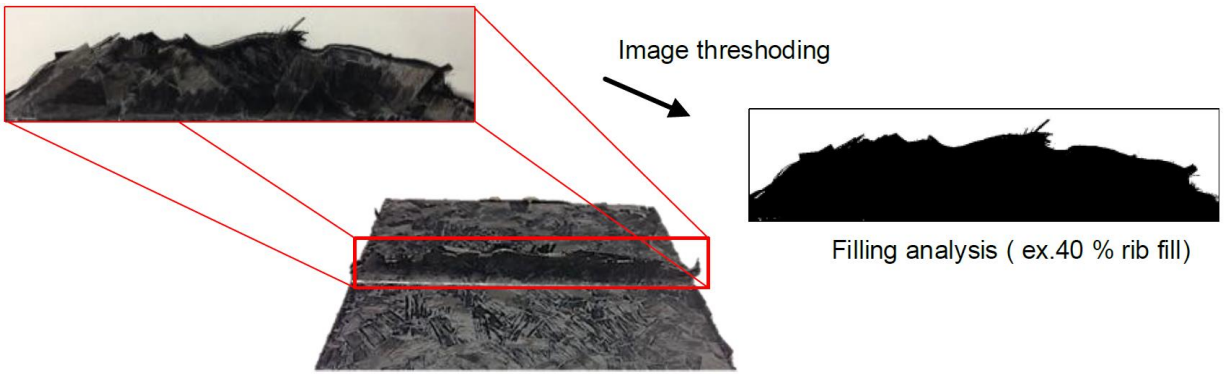

Figure 7-9. Image thresholding technique used to measure percent rib filling [90].

LeBlanc recognized that lower melt viscosities were likely the cause of better rib filling at higher moulding temperatures, although they did not measure the viscosity directly. Fortunately, a characterization of the same PEEK resin was carried out by Bangarusampath *et al.* [139] using parallel plate rheometry, the results of which are shown in Figure 7-10.

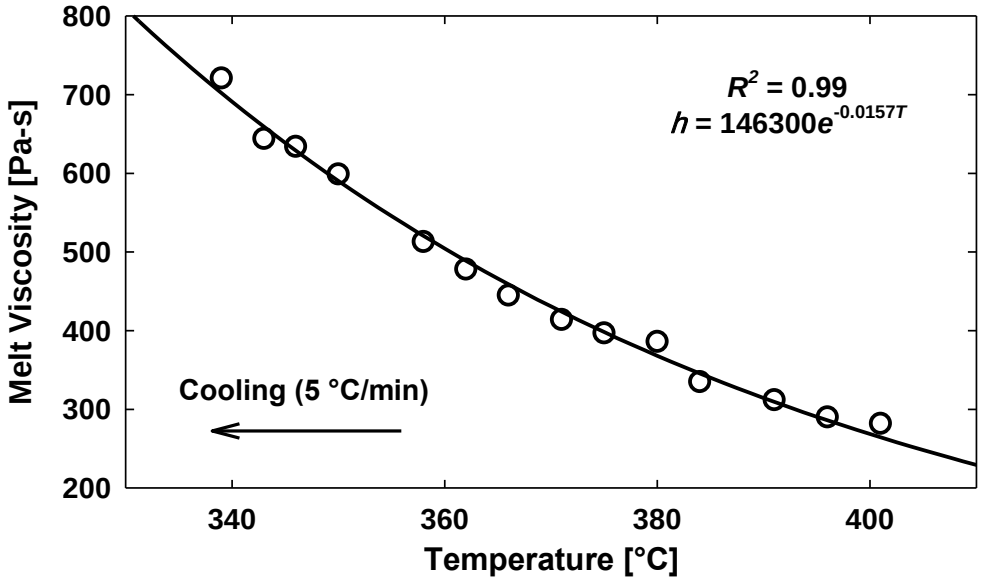

Figure 7-10. PEEK melt viscosity evolution during cooling (data extracted from [139]).

The data collected by Bangarusampath shows that, for temperatures in the range of 395 – 420 °C, PEEK exhibits viscosities similar to that of the staged 5276-1. An interesting comparison can, therefore, be made between the simple T-brackets moulded by LeBlanc at 400 °C (~ 275 Pa-s) and the compound T-brackets presented in this chapter. Figure 7-11 shows filling pressure ranges for T-brackets made using strands with increasing fibre length. The plot provides the reader with a clear picture of the impact that strand fibre architecture has on the ability flow this type of material.

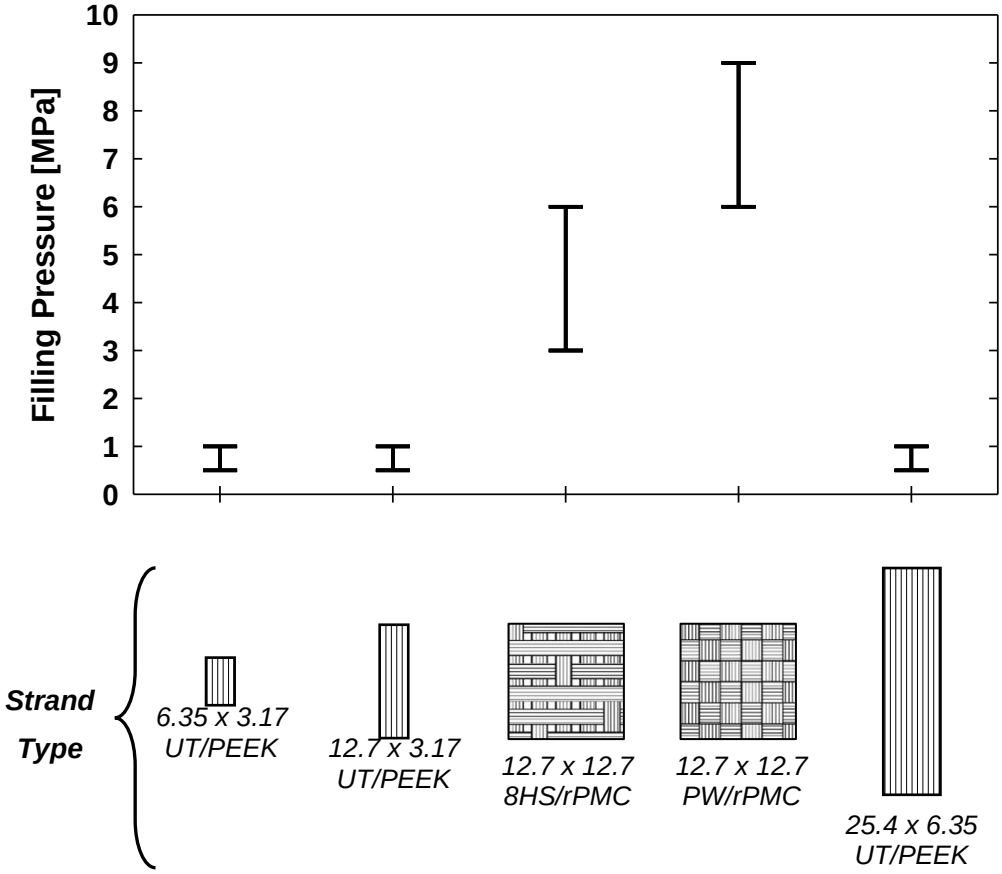

Figure 7-11 explain that these are for T-brackets and compound T-brackets. Note the difference in processing viscosity

7.3 Observed Defects & Artifacts

Backing film residue was found on the surface of several parts that were made using 8HS strands (Figure 7-12). These remnants were likely missed during the strand preparation from Section 7.1.2 and should be removed in future to avoid a possible knockdown in mechanical performance.

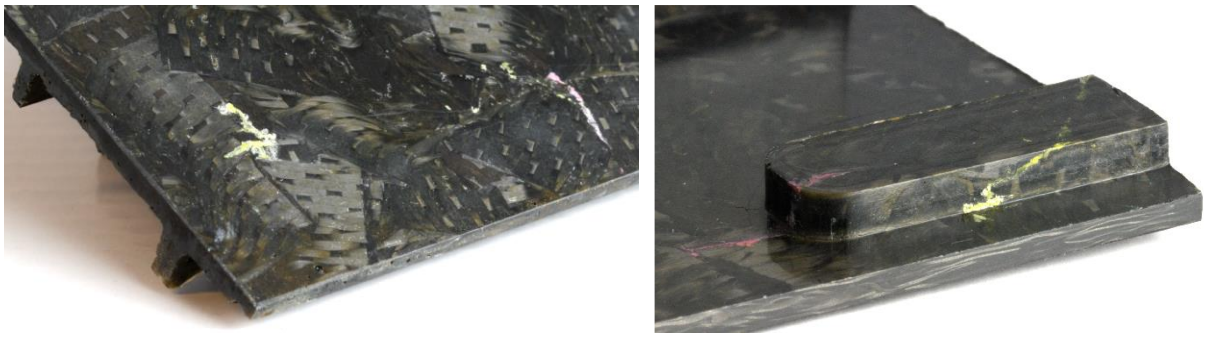

Figure 7-12. Backing film residue observed on the surface of a multi-ribbed panel (left) and a compound T-bracket (right).

Print-through artifacts corresponding to the base of the two rib features were observed on the underside of each compound T-bracket. These artifacts are shown in Figure 7-13 and are likely the result of large strand displacements into the ribs during charge compaction. Further testing is needed to determine what role this artifact will play in the mechanical response of the parts.

Figure 7-13. Print-through artifacts caused by the flow of fibre into the two rib features of a compound T-bracket: 8HS-strand part on the left and PW-strand part on the right.

A region of resin richness, sometimes accompanied by surface pitting, was consistently observed on the compound T-bracket's secondary rib (*b3*) just above the moulded hole (*b4*). Figure 7-14 shows several variations of this defect on brackets made at different pressures and using different strand types. It is the opinion of the author that these defects were caused by the formation of a knit line. The red arrows in Figure 7-14 indicate the paths likely taken by the strands during manufacturing that led to the formation of this knit line. It is important to highlight that this type of defect does not stem from improper processing and, instead, should be rectified with a different mould design.

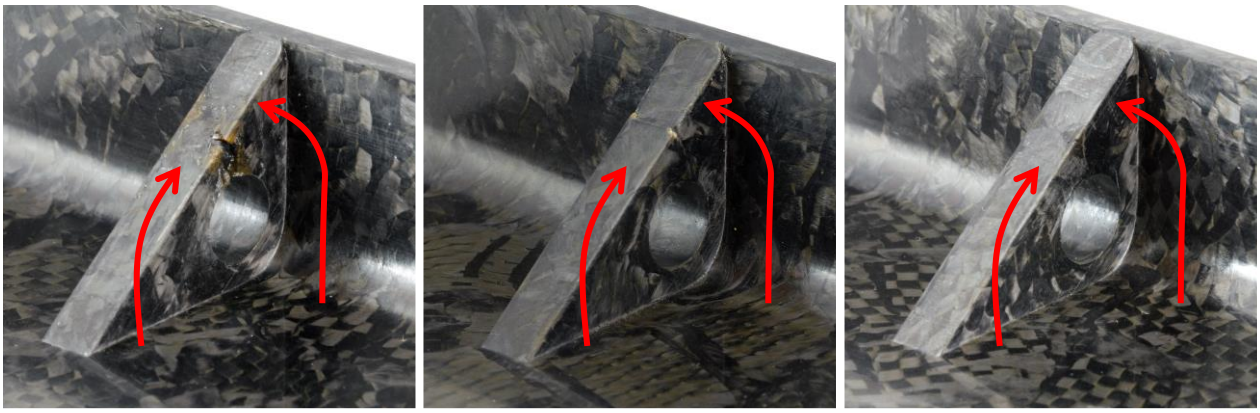

Figure 7-14. Close-up images of compound T-bracket secondary ribs showing the possible formation of a knit line. From left to right: PW strands moulded at 6 MPa; 8HS strands moulded at 6 MPa; PW strands moulded at 9 MPa.

7.4 Flow-Compaction Tailoring Validation

The pressures needed to completely fill each demonstrator part, as well as some general observations regarding the final parts' characteristics have been presented in the previous two sections. Now, the effectiveness of the flow-compaction tailoring methodology will, once again, be demonstrated. Recall that in Chapter 5, flow-compaction trials carried out on minimally staged strands resulted in excessive amounts of resin loss with very little shear deformation. A similar approach was taken here, as two additional prepreg batches were staged for 30 minutes at 120 °C. This amount of staging resulted in $T_{g,staged}$ values of 4 – 7 °C and a estimated moulding viscosity of 10 Pa-s. Invoking the discussion from Chapter 6, this range of T_g is representative of 5276-1 that has been subjected to room-temperature ageing for about 2 weeks. The strands produced in this fashion were noticeably more pliable than those that had been more aggressively staged, as well as being slightly tacky when handled.

Using these lightly staged strands, additional demonstrator parts were manufactured at 6 MPa with all other processing conditions kept constant. The resulting parts are compared to their corresponding baselines in Figure 7-15. It is clear that the lower resin viscosities have, as in the 1-D trials, shifted the strand behaviour to favour percolation. This is most evident in the two demonstrators made with the tighter PW strands where the rib features are partially filled with resin and there is almost no evidence of fibre movement.

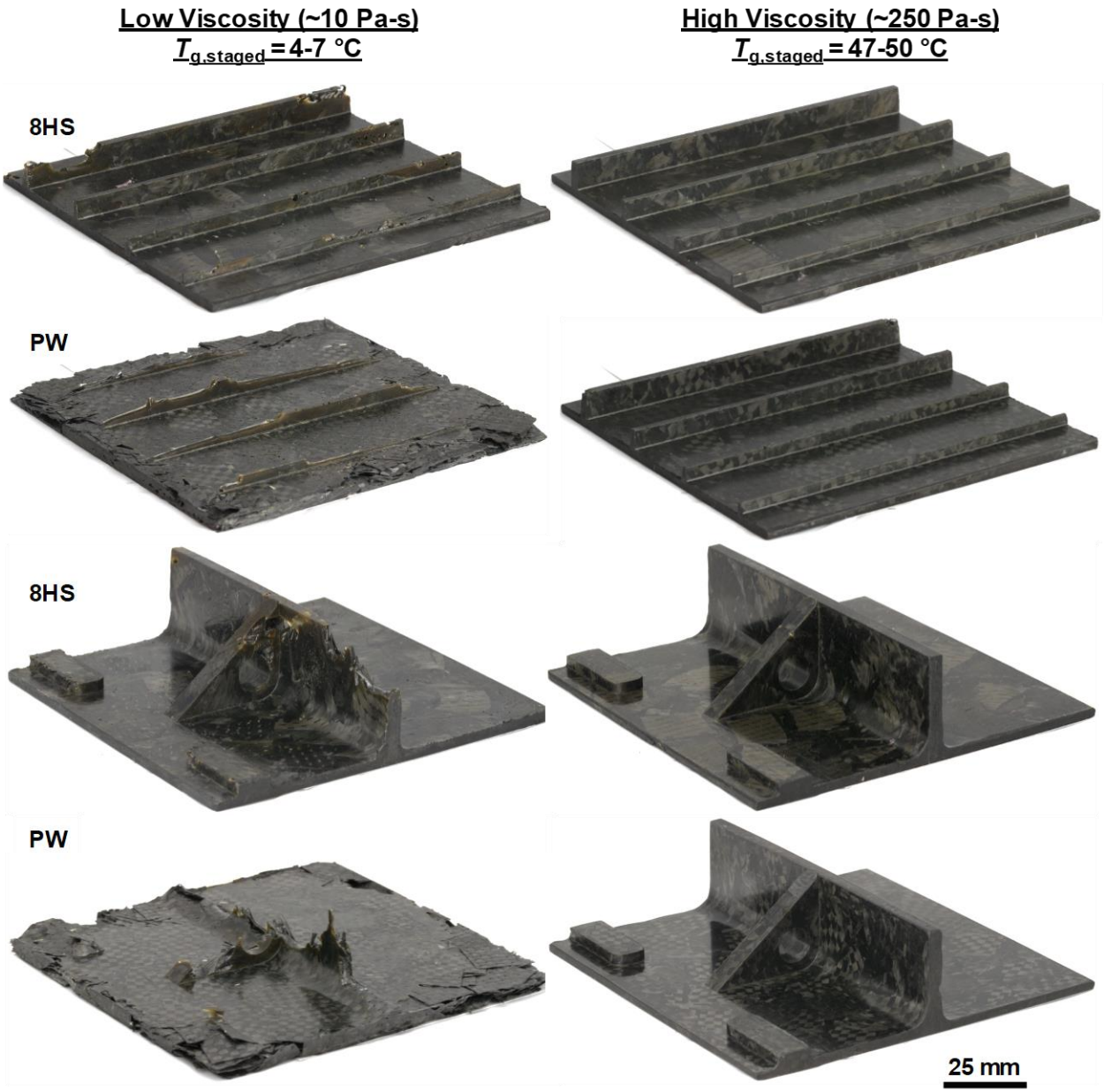

Figure 7-15. Demonstrator parts moulded at 6 MPa using lightly staged strands (left) and strands staged to an optimal state (right).

7.5 Material Hybridization

Discontinuous strand-based compounds suffer from a lack of strength and are more prone to high property variability when compared to continuous systems [71, 83]. These characteristics limit their potential in structural or even semi-structural aerospace applications. Strategic placement of continuous laminate groups within a discontinuous compression moulded component

has been shown to improve performance and produce more repeatable strand flow [159, 160]. The feasibility of this type of hybridization using the rPMC developed here was tested by adding a $[0_2]_T$ laminate group to the outer surface of the compound T-bracket's secondary rib side, a $[45_2]_T$ laminate group to the outer surface on the opposite rib side, and a [0/45]s laminate group to the panel's bottom. Cut-outs were included in the first of these groupings to allow for strands to flow into the secondary rib and raised bosses. By placing these staged laminate groups onto the preheated moulding surfaces as shown in Figure 7-16, their tackiness was increased enough such that were held securely in place. A charge of strands was then placed in the mould and the 9 MPa moulding cycle initiated. Both the laminate groups and strands used to make this hybrid demonstrator were comprised of the PW/5276-1 material.

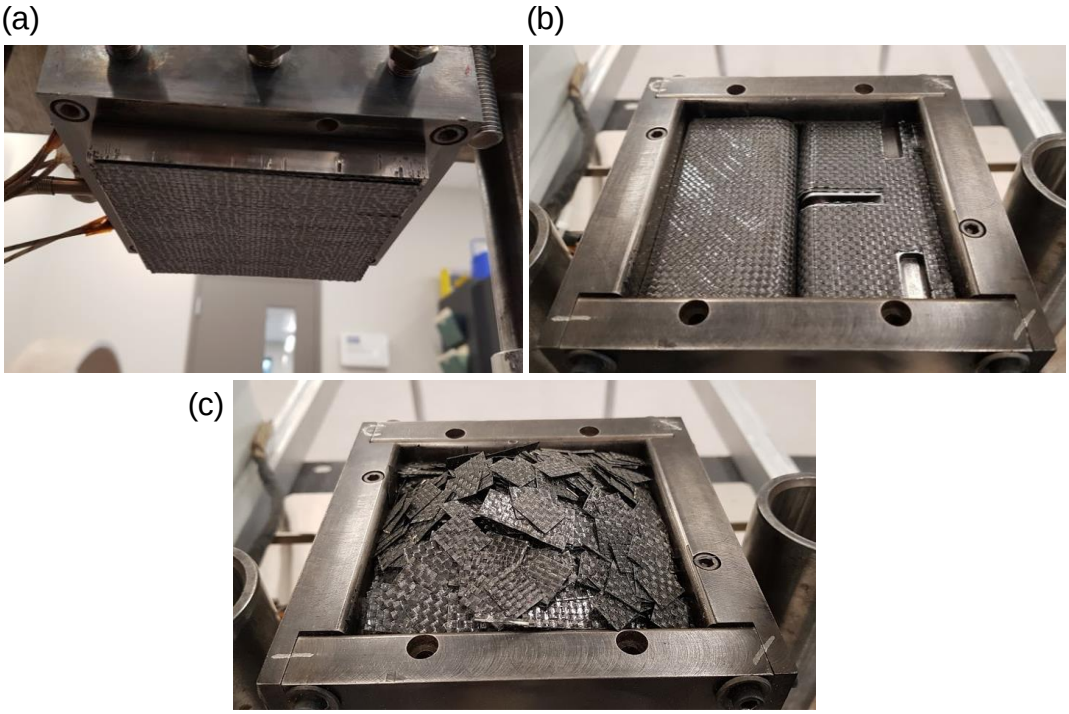

Figure 7-16. Continuous laminate groups successfully placed on the tooling surfaces corresponding to the T-bracket bottom (a) and rib sides (b), followed by strand charge placement (c).

A second type of material hybridization was also tested in which a mixture of 50 % PW strands and 50 % 8HS strands by weight was used to make another compound T-bracket at 9 MPa. Having the ability to join waste streams with the same, or with similar, resin systems in this way has value, as insufficient scrap supply often hinders the scaling of newly developed recycled materials.

The resulting hybrid parts are pictured in Figure 7-17. Other than both PW and 8HS strands being visible on the surface of the 50/50 strand hybrid bracket, it is visually identical to those previously shown in Figure 7-7 and Figure 7-8. If this type of hybridization were to be taken further, a rule of mixtures type approach would likely help to estimate the appropriate moulding pressure. Interestingly, the continuous-ply hybrid bracket had more difficulty filling at the corners of the main rib. This was likely caused by a narrowing of the space within the main rib through which strands normally flow. It was also clear that the continuous plies experienced some shear deformation during the moulding. The spacing between the secondary rib cut-out was noticeable larger and tow angles had deviated at the corners of the main rib.

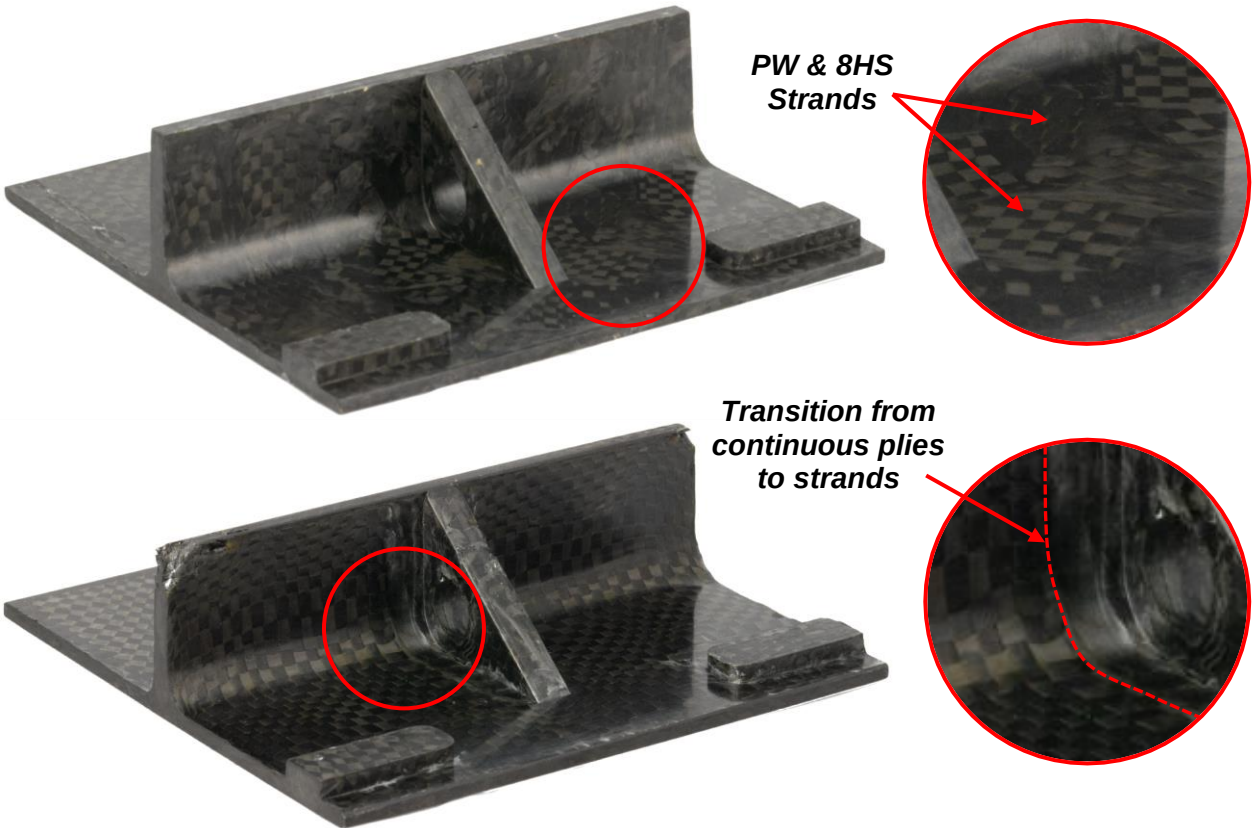

Figure 7-17. Pictures of the 50/50 strand hybrid (top) and continuous ply hybrid (bottom) brackets moulded at 9 MPa.

8
MECHANICAL TESTING

In this chapter, the results of a coupon-based mechanical characterization are presented. The method described in previous chapters for transforming uncured prepreg offcuts into a recycled prepreg moulding compound (rPMC) was applied to two batches of offcuts featuring the same 5276-1 epoxy matrix, but different fibre architectures. Large flat panels were manufactured using a standard hydraulic press, a 60-minute processing cycle, and a final target T_g of 100 °C. ASTM compliant coupons for tensile (D3039-15), flexural (D790-17), compression (D6641-14) and short-beam strength (D2344-13) testing were dry cut using a diamond saw. Fibre volume fraction, void content, and density measurements were performed according to D3171-15 and D792-13 standards. Results are presented following the guidelines of each ASTM standard, then compared with other aerospace materials in terms of specific strength and stiffness, as well as potential maximum service temperature.

8.1 Material Description

Two batches of rPMC were prepared using the offcuts characterized in Chapter 4 (resin cure, rheology, glass transition temperature), Chapter 5 (1-D flow-compaction), Chapter 6 (ageing) and Chapter 7 (advanced flow). The fact that each batch of offcuts recovered feature the same 5276-1 matrix, but two different fibre architectures makes it possible to assess the impact of strand architecture on the mechanical properties of manufactured panels. Due to a small difference in the as-received T_g of each offcut batch, different staging times were needed to obtain similar post-

staging T_g values. A detailed description of each rPMC batch is included in Table 8-1, as per ASTM reporting standards.

Table 8-1. rPMC specifications.

	Batch 1	**Batch 2**
Offcut Manufacturer	Cytec Solvay	Cytec Solvay
Offcut Source	Bell Helicopter	Bombardier Aerospace
Tow Count	3K	3K
Architecture	PW	8HS
Areal Weight	312 gsm	370 gsm
Matrix Type	Cycom 5276-1	Cycom 5276-1
Prepreg Matrix Content	36 % wt	42 % wt
Staging Time	145 min	134 min
Staging Temperature	120 °C	120 °C
Avg. Post-staging T_g	49.5 °C	47.7 °C
Staging Method	Convection oven + 2 aluminum plates (see Chapter 5)	
Strand Size	12.7 mm x 12.7 mm	

8.2 Specimen Preparation

8.2.1 Manufacturing

Four flat panels measuring approximately 380 x 380 mm were manufactured using the rPMCs described in Table 8-1 and a steel picture-frame style compression mould. The mould cavity featured a 2° draft angle in the horizontal (x-y) plane of the part to facilitate de-moulding once one side of the picture frame was removed. A machine drawing of the mould cavity is provided in Figure B-1. of Appendix B. Each of the four panels were cured at 140 °C for 45 min with a target final T_g of 100 °C. As part of the manufacturing process, the mould was preheated to the cure temperature using the heated platens of a 100-ton hydraulic press from Wabash. Three thermocouples that had been placed inside the mould cavity were used to ensure that the temperature was stable before removing the mould and applying several coats of the water-based release agent Chemlease 2627W (Chemtrend). A 565 g charge of rPMC was then spread evenly within the mould cavity, the top half was replaced, and the closed mould was moved back into the press. The final moulding pressure was applied by manually closing the Wabash press' pressure release valve. Figure 8-1 shows pictures taken of the released mould, rPMC charge placement, and a cured panel prior to de-moulding.

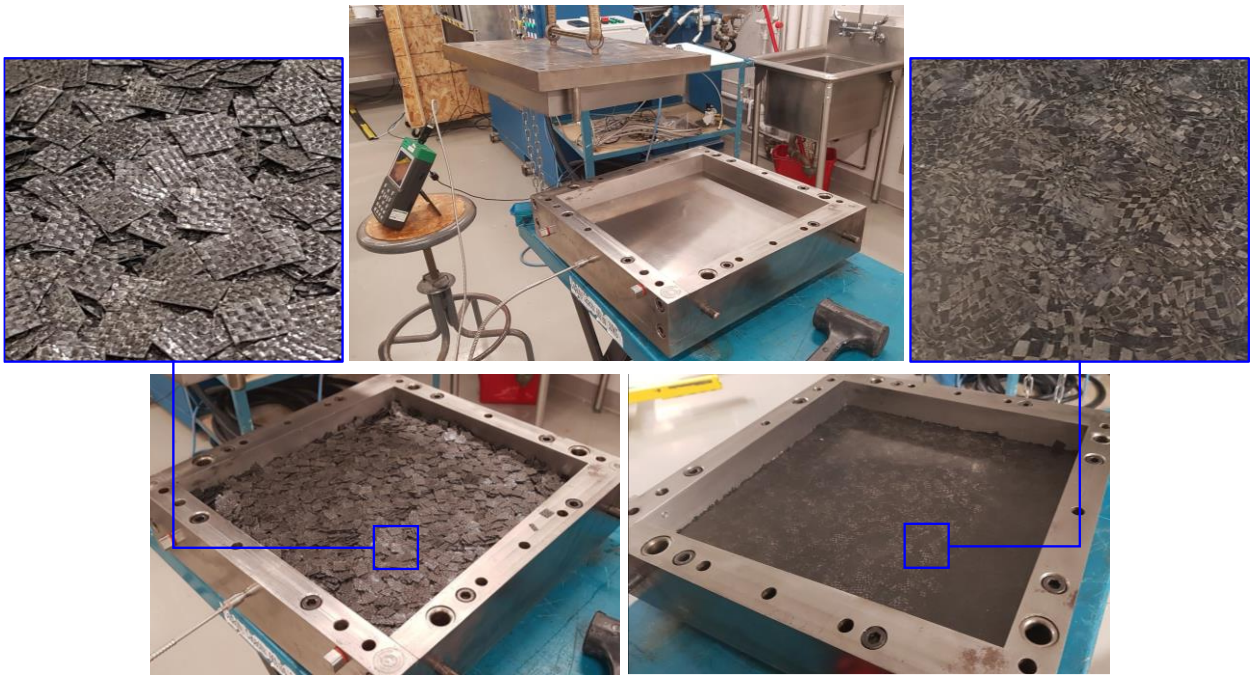

Figure 8-1. Pictures showing the preheated steel mould after the application of release agent (top-middle), after rPMC charge placement (left), and after cure (right).

General Observations & Defects

The first two panels, designated M23 and M26, were moulded under a pressure of 5.71 MPa. After the prescribed cure dwell (45 min at 140 °C), the press' water cooling system was used to quickly bring the temperature down to below 80 °C, ensuring that the panel would vitrify prior to demoulding. Visual inspection revealed peripheral regions on each panel that appeared hazy from a shallow angle and that felt somewhat rough compared to the part centre (Figure 8-2(left)).

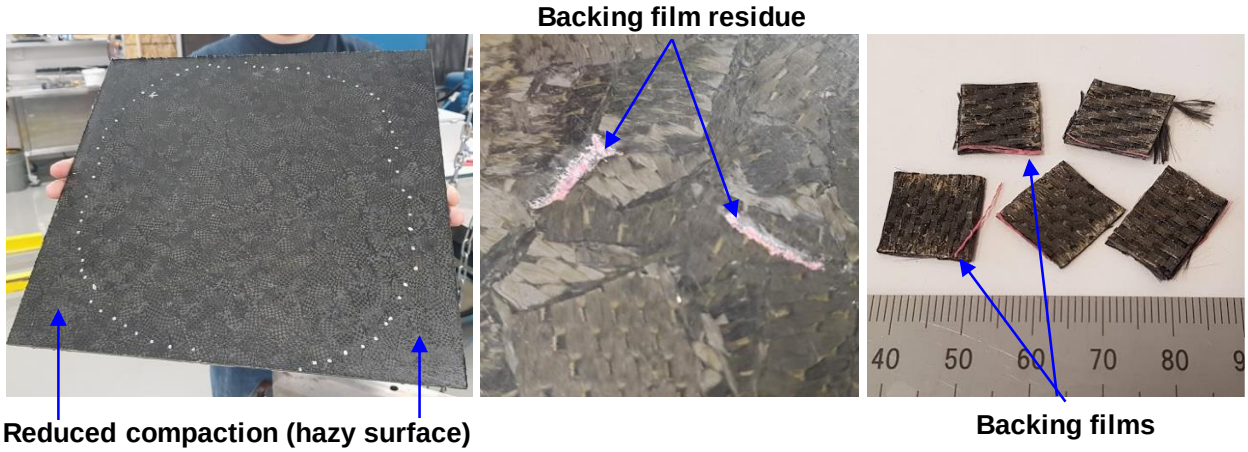

Figure 8-2. Pictures showing defects observed in panels M23 and M26: loss of compaction due to non-uniform cooling (left) and backing film remnants (middle & right).

Similar observations were reported by Landry [94], who hypothesized that non-uniform part cooling can cause large variations in material out-of-plane shrinkage. This phenomenon could then lead to regions of reduced part consolidation, or tool-part separation, depending on the severity of the temperature gradients and/or the magnitude of material shrinkage.

Figure 8-2(right) shows small pieces of backing film that were found clinging to the edges of rPMC strands from Batch 2 (8HS) following the staging and cutting operations. Despite removing as many of these remnants as possible prior to moulding, backing film residue was observed on the surface of the M26 panel as shown in Figure 8-2(middle). No backing film residue was found in any of the Batch 1 rPMC (PW), nor on any of the panels made using Batch 1 rPMC.

Alternate Moulding Scheme

Two additional panels (M34 & M40) were manufactured using a less aggressive cooling strategy to promote a more uniform temperature distribution within the parts while they are expected to shrink considerably. These panels were also moulded using a higher moulding pressure than M23 and M26 to reduce the likelihood of peripheral consolidation loss. The slow cooling strategy involved turning off the press' cartridge heaters at the end of the cure dwell, so that the system was allowed to cool down by natural convection, as shown in Figure 8-3. This clearly extends process cycle time by an amount that would be unacceptable in an industrial environment.

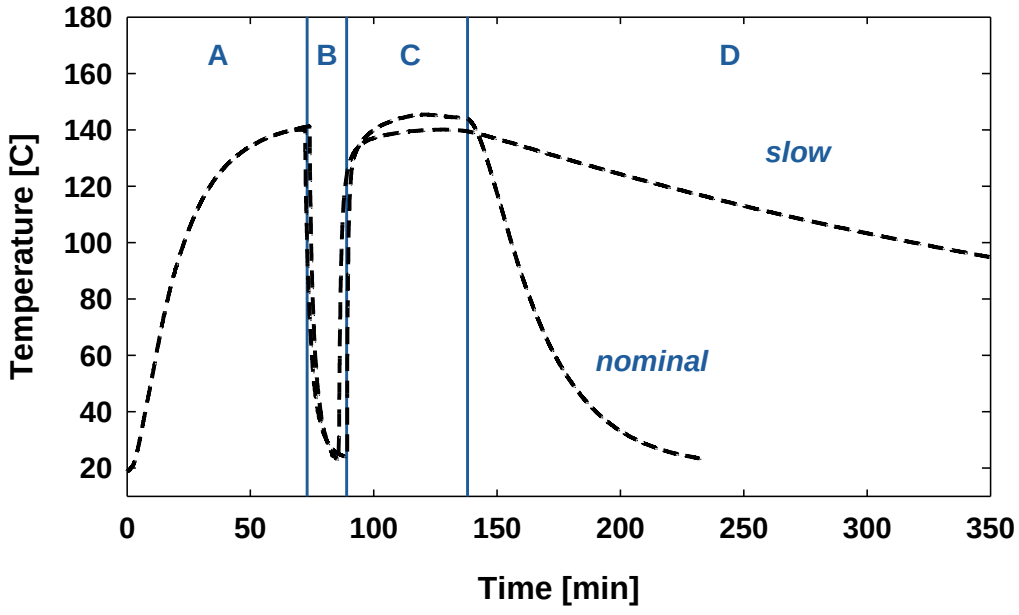

Figure 8-3. Thermocouple data from M26 (nominal) and M40 (slow-cooling) panel manufacture showing preheating (A), mould release (B), curing (C), and cooling (D).

A tool with a better thermal design including external insulation, internal cooling channels and heat transfer conduits would be necessary to bring down the cooling and reheat times to an acceptable level. Due to the combination of press capacity (100 tons or 892 kN) and part surface area (0.14 m^2), the moulding pressure was limited to 6.37 MPa. M34 and M40 were moulded at 6.04 MPa to avoid operating the press at its upper limit. Manufacturing parameters and panel inspection results are summarized in Table 8-2.

Table 8-2. Panel manufacturing parameter and inspection summary.

	M23	**M26**	**M34**	**M40**
Material	Batch 1	Batch 2	Batch 1	Batch 1
Cure Cycle	Nominal	Nominal	Slow Cooling	Slow Cooling
Pressure [MPa]	5.71	5.71	6.04	6.04
Surface Defects	HP, SP	BF, HP, SP	UC	UC
Thickness [mm]	2.60 ± 0.08	2.71 ± 0.05	2.59 ± 0.02	2.68 ± 0.02
ρ [g cm^{-3}]	1.55	1.53	1.55	1.55
V_f [%]	54.2	49.5	54.5	54.9
Void Content [%]	1.39	1.43	0.92	1.07
T_g [°C]	104.4	101.3	122.0	138.0

HP = hazy periphery; SP = surface pitting; BF = backing film residue; UC = lack of flow in corners

8.2.2 Coupon Preparation

Coupons were dry-cut using a table saw with a diamond encrusted blade. Each coupon was labelled using a permanent marker, then conditioned according to ASTM D5229. Special cutting patterns (Figure 8-4) were designed for M23 and M26 to avoid the regions with visible defects.

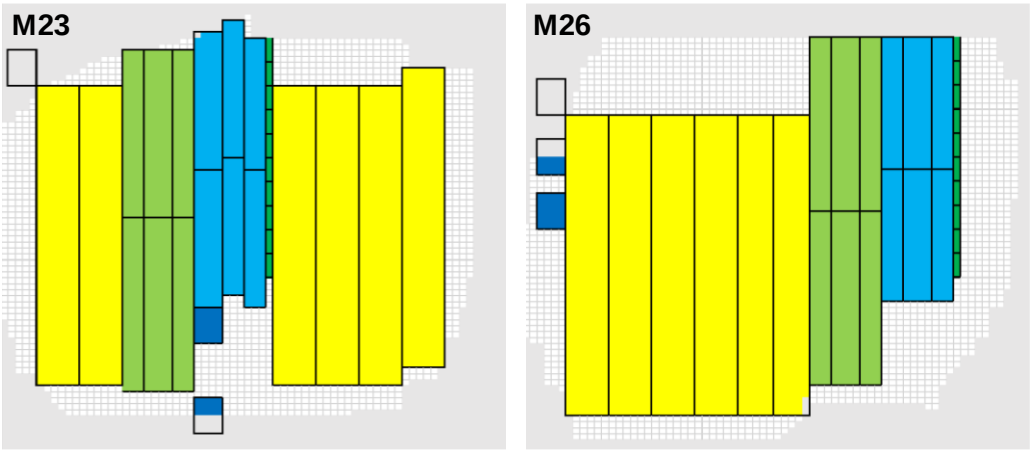

Figure 8-4. Cutting patterns designed to avoid panel defects: tensile (yellow), compression (light green), flexural (light blue), short-beam (green) and microscopy (blue and gray).

8.3 Tensile Properties

Tensile properties were measured according to the ASTM D3039-14 standard [161], using an Intron 5985 universal testing system with a 250 kN-capacity load cell. Each tensile specimen measured approximately 250 mm x 25 mm x 2.5 mm (length x width x thickness). No end-tabs were used, and all tests were performed at a speed of 2.0 mm/s. A biaxial knife-edge extensometer from Intron (13560-BIA) with a gauge length of 25 mm was used to measure specimen strain up until 1500 με. The extensometer was then removed, and each specimen was tested until failure.

Specimen instantaneous stress (σ_i) and ultimate tensile strength (F^{tu}) were calculated using Equations (8.1) and (8.2), respectively:

$$\sigma_i = \frac{P_i}{A}, \tag{8.1}$$

$$F^{tu} = \frac{P_{max}}{A}, \tag{8.2}$$

where P_i, P_{max}, and A are the instantaneous load, the load at failure, and a specimen's cross-sectional area, respectively. The tensile chord modulus (E^{chord}) and Poisson's ratio (ν) were calculated over a strain range of 500 – 1500 με using Equations (8.3) and (8.4):

$$E^{chord} = \frac{\Delta\sigma}{\Delta\varepsilon}, \tag{8.3}$$

$$\nu = \frac{-\Delta\varepsilon_t}{\Delta\varepsilon}, \tag{8.4}$$

where $\Delta\sigma$, $\Delta\varepsilon$, and $\Delta\varepsilon_t$ are the changes in specimen stress, longitudinal strain, and transverse strain along the chord length, respectively.

A summary of the tensile test results for each of the rPMC panels manufactured is presented in Table 8-3, including the number of specimens tested (n), average property values ($\bar{x}$), maximum and minimum property values (x_{max}, x_{min}), standard deviations (S_{n-1}) and coefficients of variation (CV %). Detailed results for each test performed including specimen dimensions, observed failure modes, pictures of tested specimens, stress-strain curves and longitudinal vs. transverse strain curves are included in Appendix C. Finally, the results summary shown in Table 8-3 is also presented graphically in Figure 8-5.

Table 8-3. Summary of tensile test results for each rPMC panel manufactured.

Panel	n	$\bar{x}$	x_{max}	x_{min}	S_{n-1}	CV %
Ultimate Tensile Strength, F^{tu} [MPa]						
M23	6	77.5	88.1	66.5	11.3	14.6
M26	6	79.6	96.5	59.5	15.9	20.0
M34	6	165.8	207.3	97.9	39.0	23.5
M40	6	136.1	166.6	117.6	18.1	13.3
Tensile Chord Modulus, E^{chord} [GPa]						
M23	6	35.2	37.5	33.0	1.7	4.8
M26	6	32.7	35.1	29.9	2.0	6.3
M34	6	52.7	70.3	39.4	11.5	21.9
M40	6	54.1	63.6	44.3	8.1	14.9
Poisson's Ratio by Chord Method, v						
M23	6	0.30	0.35	0.25	0.04	13.3
M26	6	0.33	0.39	0.25	0.05	15.9
M34	4	0.54	0.57	0.48	0.04	7.2
M40	6	0.44	0.52	0.36	0.06	14.3

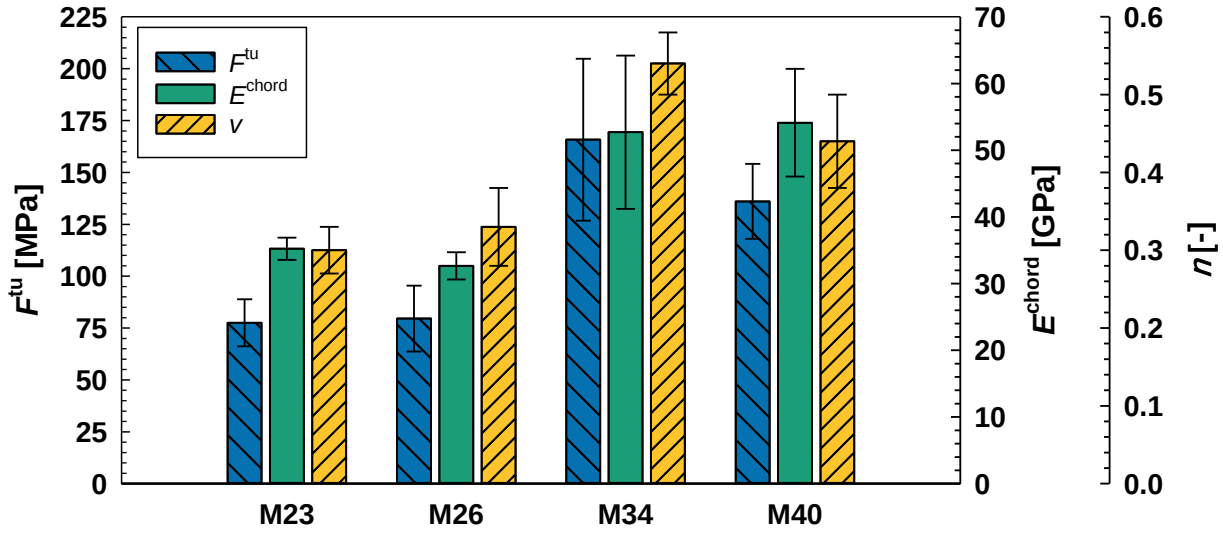

Figure 8-5. Summary of tensile test results for each rPMC panel manufactured.

Considering the amount of variation observed within each set of specimens tested from the two baseline panels (M23 & M26), the average tensile properties measured are quite similar. For example, the average tensile strength values of M23 and M26 differ by only 2.6 % (2.1 MPa), while the corresponding coefficients of variation range from 14.6 – 20.0 %. Similarly, a difference

of 7.5 % (2.6 GPa) was observed in the average chord moduli of the same two panels, which is on the same order of magnitude as the measured variations (4.8 – 6.3 %).

A large increase in tensile properties was observed for the two panels manufactured using the alternate moulding scheme (M34 & M40) in which slow cooling and higher moulding pressure were used (see Section 8.2.1). When compared to the Batch 1 rPMC baseline panel (M23), tensile strength increased by 75.6 – 113.9 % (58.6 – 88.3 MPa), chord modulus increased by 49.7 – 53.7 % (17.5 – 18.9 GPa), and Poisson's ratio increased by 46.7 – 80.0 % (0.14 – 0.24). These changes are likely due to the measured reduction in panel void content of 0.32 – 0.47 %, as well as the increase in final part T_g of 17.6 – 33.6 °C (Table 8-2). High sensitivity of mechanical properties to changes in the quantity, distribution, and morphology of voids is to be expected in strand-based rPMC, as load transfer must occur through the resin rich regions that surround adjacent strands. It is, therefore, consistent that the apparent mechanism of failure is strand pull-out or delamination.

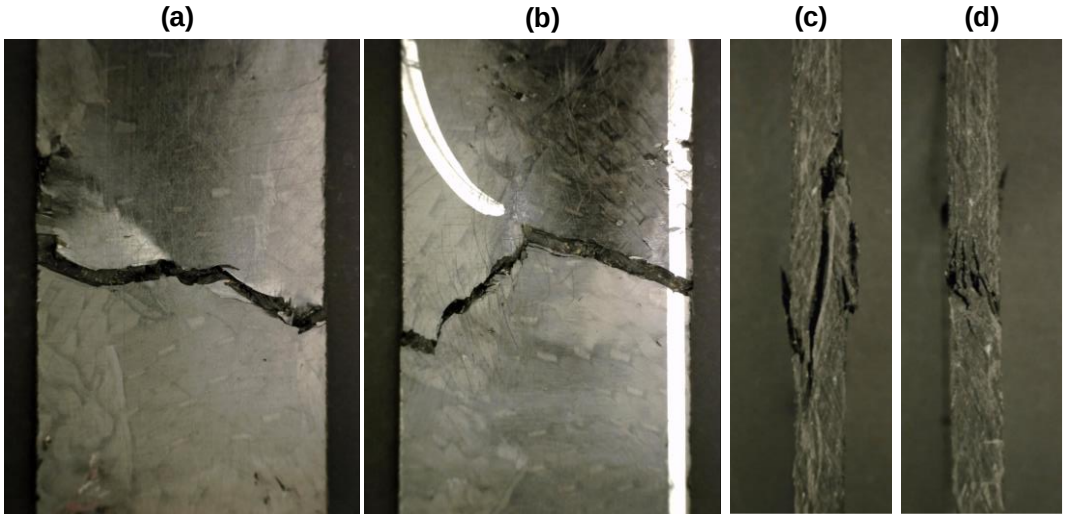

Figure 8-6. M26 specimen 6 top view (a), bottom view (b), left-side view (c), and right-side view (d). Reported failure mode: angled-gauge-middle.

The reduction in void content and the increase in T_g may also be responsible for changes to the type of failure path observed. All but one of the baseline specimens tested exhibited angled failure like the one shown in Figure 8-6. Specimens taken from the alternately processed panels, on the other hand, exhibited a mixture of both angled and lateral failures. The fracture paths of specimens that failed laterally appear to be more tortuous than those which exhibited angled failures (Figure 8-7). This may be an indication that the observed reduction in void content and surface imperfections has forced failure cracks to propagate along a more difficult path. However,

additional testing in the form of fractography would be needed to validate this hypothesis. It should also be noted that lateral failures did not correspond to higher failure stresses as expected based on this hypothesis.

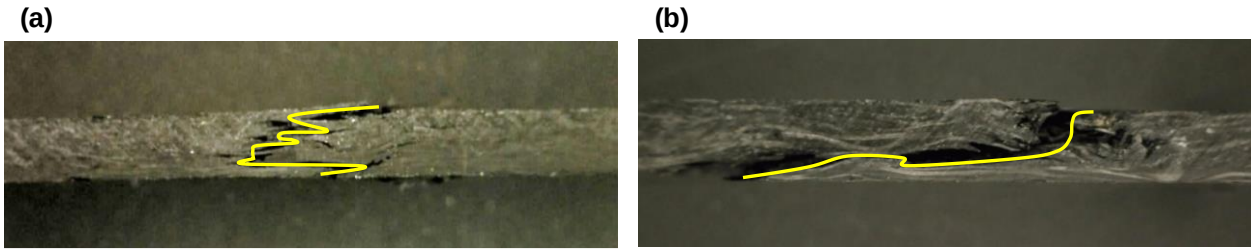

Figure 8-7 Side views of specimens M40-4 (a) and M40-3 (b) showing different failures.

8.4 Flexural Properties

Flexural properties were measured according to the ASTM D790-17 standard [162] using an Instron 5584 universal testing system with a 150 kN capacity load cell. Each flexural specimen measured approximately 110 mm x 13 mm x 2.5 mm (length x width x thickness) with a span ratio of 16:1, resulting in spans of 40 – 42 mm. All tests were performed at a speed of approximately 1.1 mm/s. A toe compensation was applied to the data using the Bluehill Universal testing software from Instron. A steel specimen 12.5 mm thick and 87.5 mm wide was tested over a 50 mm span to create a compliance correction curve for the fixture and testing frame used. This compliance correction is included in Appendix D for completeness.

Specimen flexural stress (σ_f) was calculated using Equations (8.1):

$$\sigma_f = \frac{3PL}{2bd^2}, \tag{8.5}$$

where P, L, b, and d are the instantaneous load, the support span, the specimen width and depth, respectively. A specimen's flexural strength (σ_{fM}) was taken as the maximum flexural stress observed during the bending test. Flexural strain (ε_f) was calculated using Equation (8.6):

$$\varepsilon_f = \frac{6Dd}{L^2}, \tag{8.6}$$

where D, d, and L are the maximum deflection at the centre of the beam, the specimen depth, and the support span, respectively. The flexural modulus of elasticity was calculated using Equation (8.7):

$$E_B = \frac{L^3 m}{4bd^3}, \tag{8.7}$$

where L, m, b, and d are the support span, the slope of tangent to the elastic portion of the load-deflection curve, the specimen width and depth, respectively.

As in the previous section, a summary of the flexural test results for each of the rPMC panels manufactured is presented in Table 8-4, including the number of specimens tested (n), average property values ($\bar{x}$), maximum and minimum property values (x_{max}, x_{min}), standard deviations (S_{n-1}) and coefficients of variation (CV %). These results are also shown graphically in Figure 8-8. Detailed results for each test performed including specimen dimensions, observed failure modes, pictures of tested specimens, and flexural stress-strain curves are included in Appendix D.

Table 8-4. Summary of flexural test results for each rPMC panel manufactured.

Panel	n	$\bar{x}$	x_{max}	x_{min}	S_{n-1}	CV %
Flexural Strength, σ_{fM} [MPa]						
M23	6	431.3	606.4	214.9	161.3	37.4
M26	6	293.9	499.2	184.4	112.0	38.1
M34	10	556.9	617.2	497.9	37.1	6.7
M40	10	402.8	580.0	232.6	126.8	31.5
Flexural Strain at Maximum Load, ε_{fM} [mm/mm]						
M23	6	0.0170	0.0187	0.0141	0.0017	9.8
M26	6	0.0171	0.0217	0.0103	0.0051	29.9
M34	10	0.0186	0.0228	0.0161	0.0021	11.2
M40	10	0.0152	0.0212	0.0095	0.0041	27.0
Tangent Modulus of Elasticity, E_B [GPa]						
M23	6	32.6	39.0	27.2	4.1	12.7
M26	6	28.9	37.1	20.9	5.4	18.8
M34	10	35.4	39.7	32.8	2.4	6.7
M40	10	32.1	39.6	24.9	4.9	15.3

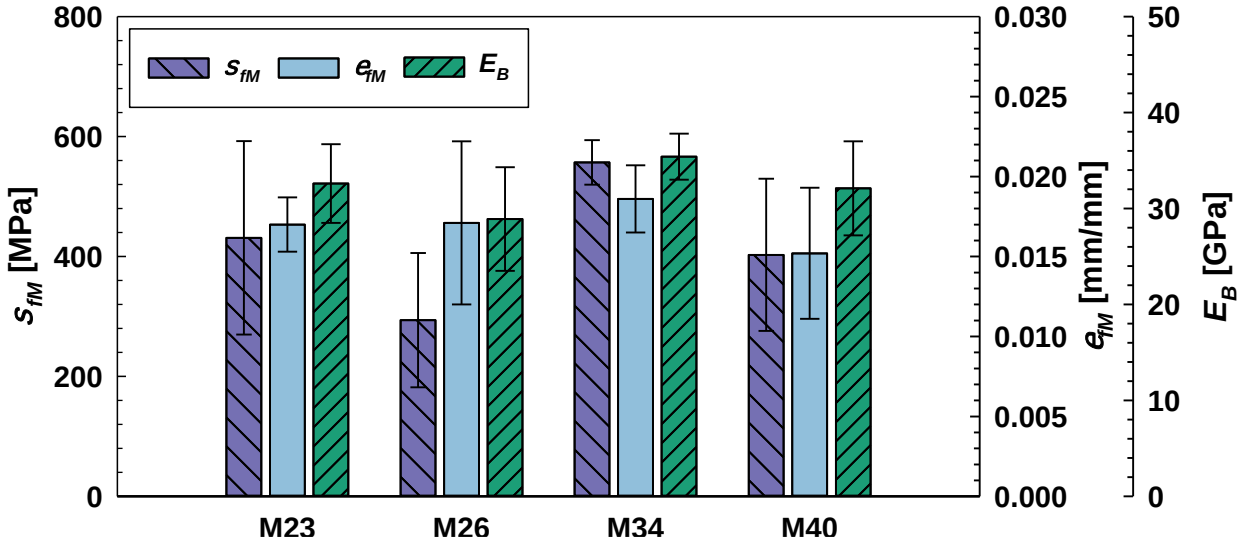

Figure 8-8. Summary of flexural test results for each rPMC panel manufactured.

Unlike the tensile results from the previous section, it is unclear what effect the modified moulding cycle has had, if any, on the flexural properties of the rPMC. All specimens tested experienced the same type of tensile failure on the bottom surface. Their does not seem to be a meaningful difference in the average values of either ε_{fM} or E_B when considering the amount of variability observed. Similarly, panels M23 and M40 exhibited almost identical flexural strengths, with 431.3 ± 161.3 MPa and 402.8 ± 126.8 MPa, respectively, despite a 0.32 % difference in void content and a 33.6 °C difference in T_g. The fact that M40, a panel that one would expect to behave the same as M34, exhibited much higher σ_{fM} suggests that some other aspect of the panel quality or structure is influencing panel-to-panel variability.

8.5 Compressive Properties

Compressive properties were measured according to the ASTM D6641-14 standard [163] using an Intron 5985 universal testing system equipped with a 250 kN capacity load cell. Each compression specimen measured approximately 140 mm x 13 mm x 2.5 mm (length x width x thickness), with a gauge length of 12.58 ± 0.82 mm. A testing speed of 1.30 mm/s was selected for all tests and no end-tabs were used.

The compressive strength (F^{cu}) of each specimen was calculated using Equation (8.8):

$$F^{cu} = \frac{P_f}{wh}, \tag{8.8}$$

where P_f, w, and h are the maximum load at failure, the specimen gauge width, and the specimen gauge thickness, respectively.

A summary of the compression test results for each of the rPMC panels manufactured is presented in Table 8-5, including the number of specimens tested (n), average property values ($\bar{x}$), maximum and minimum property values (x_{max}, x_{min}), standard deviations (S_{n-1}) and coefficients of variation (CV %). These results are also shown graphically in Figure 8-9. Detailed results for each test performed including specimen dimensions, observed failure modes, pictures of tested specimens, and compressive stress-displacement curves are included in Appendix E.

Table 8-5. Summary of compression properties measured according to ASTM D6641-14.

Panel	n	$\bar{x}$	x_{max}	x_{min}	S_{n-1}	CV %
Maximum Load at Failure, P_f [kN]						
M23	6	10.81	12.83	8.34	1.52	14.05
M26	6	8.61	10.37	7.50	1.06	12.29
M34	8	9.80	11.99	7.81	1.32	13.44
M40	9	10.28	13.55	7.97	1.54	15.01
Laminate Compressive Strength, F^{cu} [MPa]						
M23	6	307.8	363.6	235.9	42.5	13.8
M26	6	255.6	309.2	218.6	32.8	12.8
M34	8	272.7	333.5	217.8	36.6	13.4
M40	9	302.0	391.9	233.0	43.7	14.5

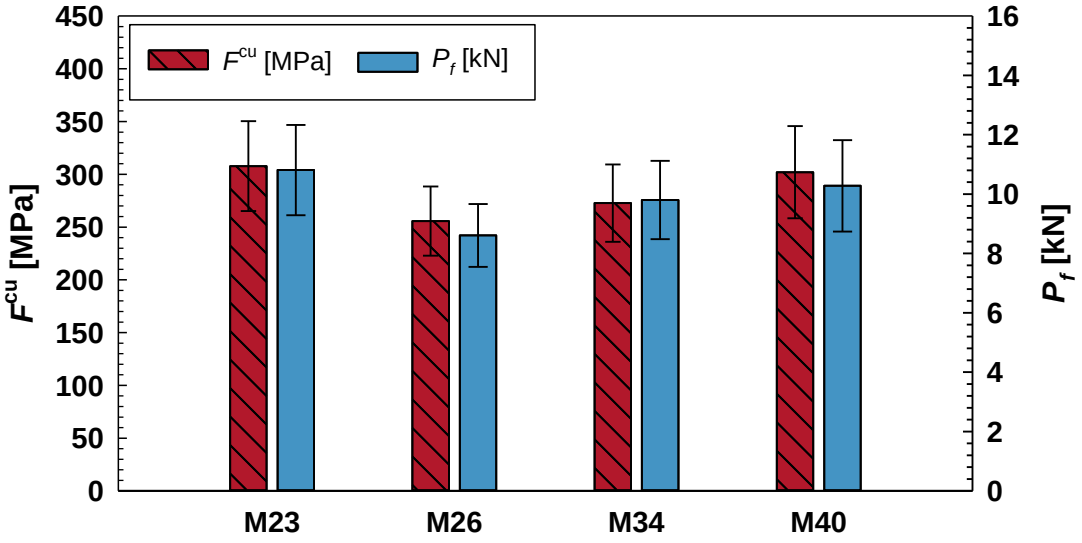

Figure 8-9. Summary of compression test results for each rPMC panel manufactured.

Compression specimens from each panel exhibited similar multi-mode failures, as shown in Figure 8-10. Compressive strength values were similar and repeatable with the measured coefficients of variation lying within a narrow range of 12.8 – 14.5 %. With the strength variations displayed in Figure 8-9 encompassing the average strength values from each set, it is difficult to see any meaningful difference from panel to panel.

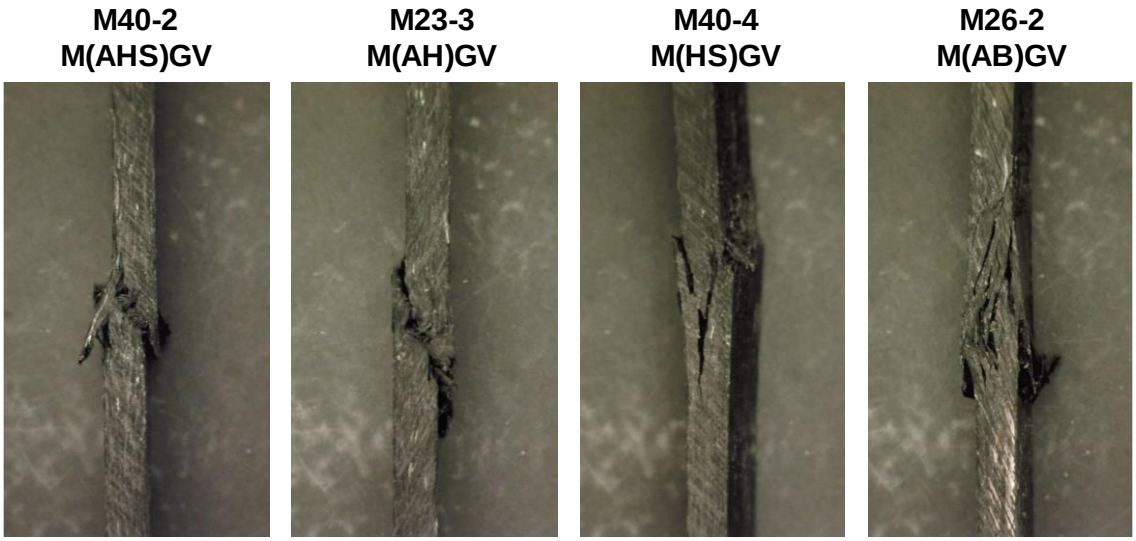

Figure 8-10. Representative compressive specimen failures.

Test Validity

According to the D6641-14 standard, specimens must fail within the gauge section in one of the accepted failure modes to be deemed valid (see Figure E-1.). Failure within the fixture grips, buckling of the gauge section, or excessive specimen bending as defined by Equation (8.9) invalidate the test results and reduce the ability to make comparisons with other datasets.

$$B_y = \frac{\varepsilon_1 - \varepsilon_2}{\varepsilon_1 + \varepsilon_2} \times 100 \tag{8.9}$$

Only one of the specimens tested (M40-1) experienced through-thickness cracking within the grips, and these initial cracks arrested prior to ultimate specimen failure which occurred in the gauge section. The use of back-to-back strain gauges on all specimens tested is necessary to completely rule out Euler-buckling and/or excessive bending. This approach represents a considerable investment in terms of instrumentation and labour and was deemed outside of the scope of this initial characterization. Instead, the standard's alternative and less stringent recommendations were used to assess the credibility of the compressive test results presented.

First, Equation (8.10) was used to estimate the theoretical Euler-buckling stress (F_{cr}) of a compression specimen:

$$F_{cr} = \frac{\pi^2 E_B}{\frac{{l_g}^2 A}{I} + 1.2\pi^2 \frac{E_B}{G_{xz}}}, \tag{8.10}$$

where E_B is the expected flexural modulus, l_g is the length of the gauge section, A is the cross-sectional area, I is the minimum moment of inertia of the specimen cross-section, and G_{xz} is the through-thickness interlaminar shear modulus, which was assumed to be 4 GPa [163].

Equation (8.10) gives an F_{cr} of 851 MPa when considering the average specimen dimensions, as well as the average flexural stiffness obtained in Section 8.4. This value is 117 % higher than the highest compressive strength observed (391.9 MPa). A more conservative approximation of F_{cr} was calculated by considering the dimensions of specimen M40-4, which was found to have the highest slenderness ratio (Equation (8.11)) of all the specimens tested, along with the lowest measured flexural stiffness [164]. This approach gave an F_{cr} of 629 MPa, which is still 60 % higher than the highest measured compressive strength.

$$\lambda = l_g \sqrt{\frac{A}{I}} \tag{8.11}$$

To prevent specimen buckling, the standard says that, "as a general guide, keeping the predicted value F_{cr} of buckling stress at least 20 % above the expected compressive strength is usually sufficient". It is therefore unlikely that the specimens tested here experienced Euler-buckling unless there was something consistently wrong with the specimen preparation and/or in the implementation of the D6641-14 test procedure. Back-to-back linear-pattern strain gauges (CEA-06-125UW-350) from Micro Measurements were used to validate this conclusion for one of the specimens tested (M40-9). Preparation of the specimen's surface was carried out according to the manufacturer's guidelines using the MCA-1 conditioner and MN5A neutralizer from Micro Measurements. The cyanoacrylate adhesive M-Bond 200 from the same product line was then used to secure the gauges.

Figure 8-11 (left) shows that the strains measured on each side of M40-9 decrease in a similar fashion during failure. Had the specimen buckled, the strain data would have rapidly

diverged with one side experiencing compression and the other tension. Considering that specimens also failed with similar values of F^{cu}, suggests that M40-9 did not experience buckling. Equation (8.9) was used to calculate the bending of M40-9, where ε_1 and ε_2 are the strain measurements of strain gauge 1 and 2, respectively, and the results are shown in Figure 8-11 (right). M40-9 experienced bending of approximately 60 % at the beginning of the test which was followed by a quick transition and stabilization to around 20 %. D6641 does not allow for more than 10 % bending if the test is to be considered valid; however, it also mentions that as much as 40 % bending may have little effect on the compressive strength [163].

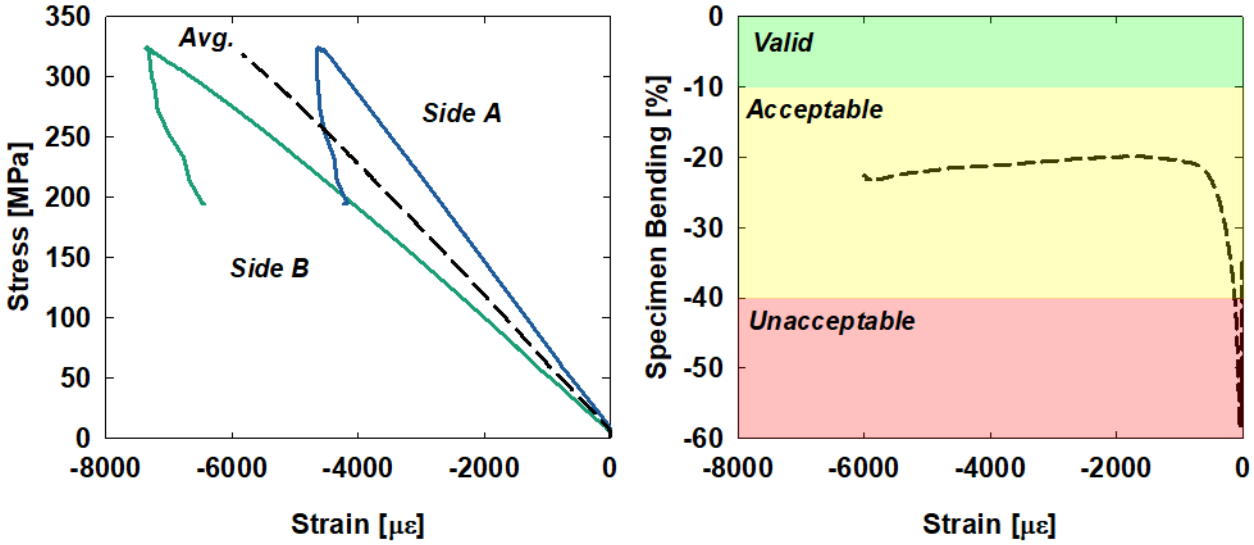

Figure 8-11. Strain data collected for each side of specimen M40-9 (left) and the calculated percent bending throughout the test (right).

Specimen compressive modulus (E^c) was estimated using the strain data collected from M40-9 and Equation (8.12):

$$E^c = \frac{P_2 - P_1}{(\varepsilon_{x2} - \varepsilon_{x1})wh}, \tag{8.12}$$

where P and ε_x correspond to the measured load and strain, respectively. A strain range of 1000 – 3000 με corresponding to the indices 1 and 2 was used to determine E^c. A modulus of 58.8 GPa was obtained by taking the average of the compressive modulus measured on side A (70.4 GPa) and side B (4.72 GPa).

8.6 Short-Beam Strength

Short-beam specimens measuring approximately 15.2 mm x 5.1 mm x 2.5 mm (length x width x thickness) were cut from each panel and tested in three-point bending according to the ASTM D2344-13 standard for short-bream strength [74]. Tests were performed at a speed of 1.0 mm/s using an Intron 5985 universal testing system with a 250 kN-capacity load cell[7]. The maximum testing load observed (P_m) was used to calculate a specimen's short-beam strength (F^{sbs}) according to Equation (8.13):

$$F^{sbs} = 0.75 \times \frac{P_m}{b \times h}, \tag{8.13}$$

where b and h are the specimen width and thickness, respectively.

A summary of P_m and F^{sbs} values are presented in Table 8-6, including the number of specimens tested (n), average property values ($\bar{x}$), maximum and minimum property values (x_{max}, x_{min}), standard deviations (S_{n-1}) and coefficients of variation (CV %). These results are also shown graphically in Figure 8-12. Detailed results for each test performed including specimen dimensions, observed failure modes, and load vs. displacement curves are included in Appendix F.

Table 8-6. Summary of short-beam test results for each rPMC panel manufactured.

Panel	n	$\bar{x}$	x_{max}	x_{min}	S_{n-1}	CV %
Maximum Test Load, P_m [N]						
M23	10	1067	1423	301	367	34.4
M26	10	611	846	392	163	26.6
M34	10	1246	1407	943	139	11.2
M40	10	1321	1546	1070	133	10.1
Short-Beam Strength, F^{sbs} [MPa]						
M23	10	57.7	81.0	14.9	20.8	36.0
M26	10	36.7	51.3	23.4	9.75	26.6
M34	10	70.1	78.7	53.0	7.83	11.2
M40	10	71.6	85.7	57.4	8.06	11.3

[7] Load cell accuracy is ± 0.5 % of the force reading down to 1/1000 of the load cell capacity (250 N).

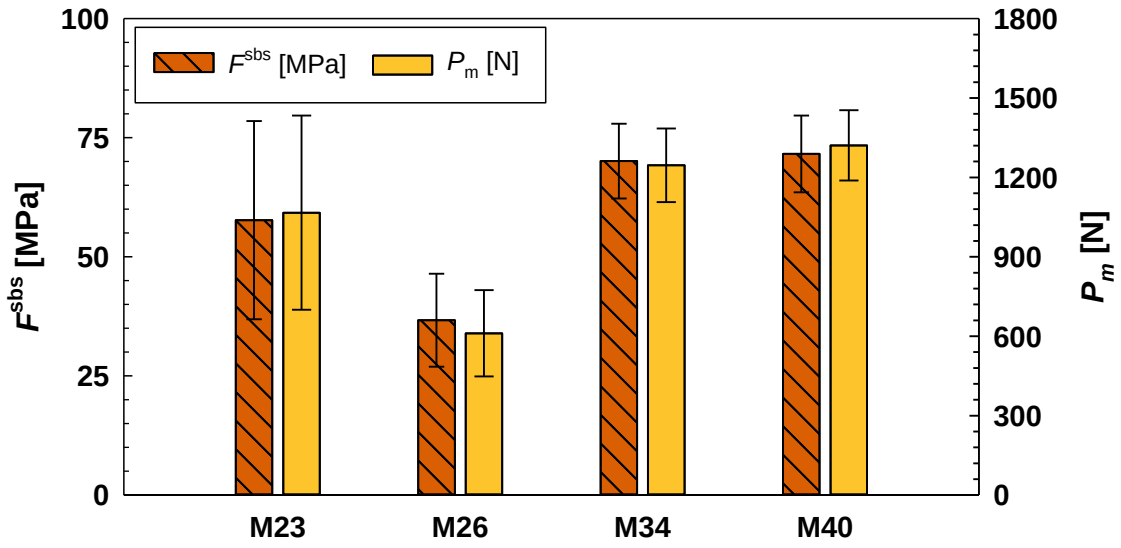

Figure 8-12. Summary of short-beam test results for each rPMC panel manufactured.

Unlike the results obtained in previous sections, short-beam strength values are not considered a material property. Instead, F^{sbs} is commonly used as an indicator of laminate quality, as short-beam specimen failure typically depends on interlaminar resin properties [74].

A difference of 44.5 % in average F^{sbs} was observed between M23 and M26 despite the two panels featuring similar void contents (1.39 %, 1.43 %) and final T_g values (104.4 °C, 101.3 °C). Two possible explanations for this discrepancy are that M26 was more susceptible to failure due to a lower fibre volume content, and/or that the use of strands with different architectures resulted in panels with significantly different mesostructures. M26 was also the only panel on which backing film residue was observed and, while no traces were seen on the short-beam specimens, this type of contamination could have contributed to a weakening of interlaminar shear strength.

Most of the specimens tested from the M23 and M26 panels failed in either tension on the bottom surface, or in compression on the upper surface. In contrast, the failures of M34 and M40 specimens all involved an aspect of interlaminar shear failure. This shift is clearly demonstrated in Figure 8-13 and reflects the changes in panel void content and surface defects previously discussed. Specimens from M34 and M40 also failed more repeatably with coefficients of variation of 11.2 % and 11.3 %, respectively in comparison with 36.0 % and 26.6 % for M23 and M26.

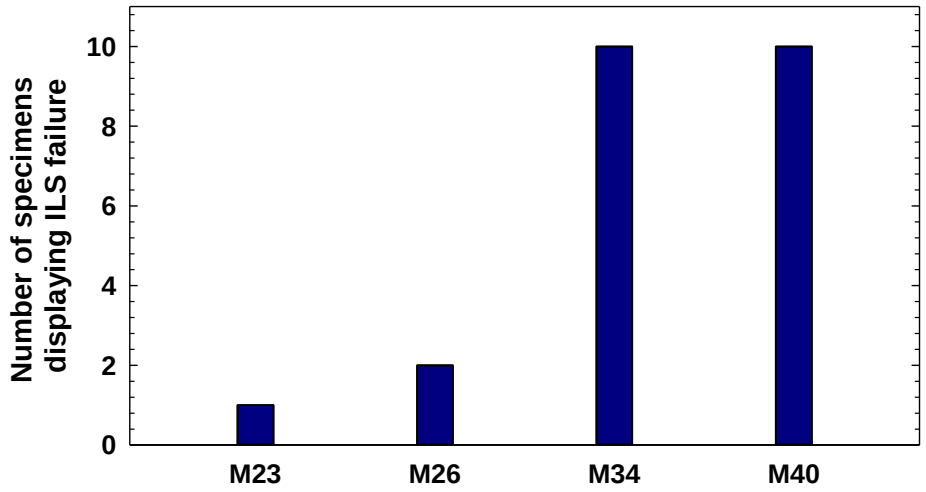

Figure 8-13. The number of specimens for each rPMC panel tested which exhibited interlaminar shear failure.

8.7 Testing Summary

In summary, four rPMC panels were manufactured from material with different strand architectures and using two different moulding strategies. Several aspects of panel quality that may have influenced the material's mechanical properties have been identified. These include the overall void content, the presence of surface defects, the final part T_g, and the average fibre volume content. It is not possible, however, to say with certainty which of these factors plays the most significant role without further testing.

A radial summary of the average properties of each panel is shown in Figure 8-14. Each category of this summary has been normalized relative to the maximum value measured, so that they are all shown in terms of percentage values. From this representation of the results, one can clearly see that the baseline panels are generally weaker and less stiff than the final two panels. M26 exhibits the lowest properties in almost all categories, which is likely tied to the fact that it features the lowest T_g, lowest V_f and highest void content. Figure 8-14 also reveals that the tensile properties and short-beam strength are sensitive to change in panel quality, while the flexural and compressive properties are less so.

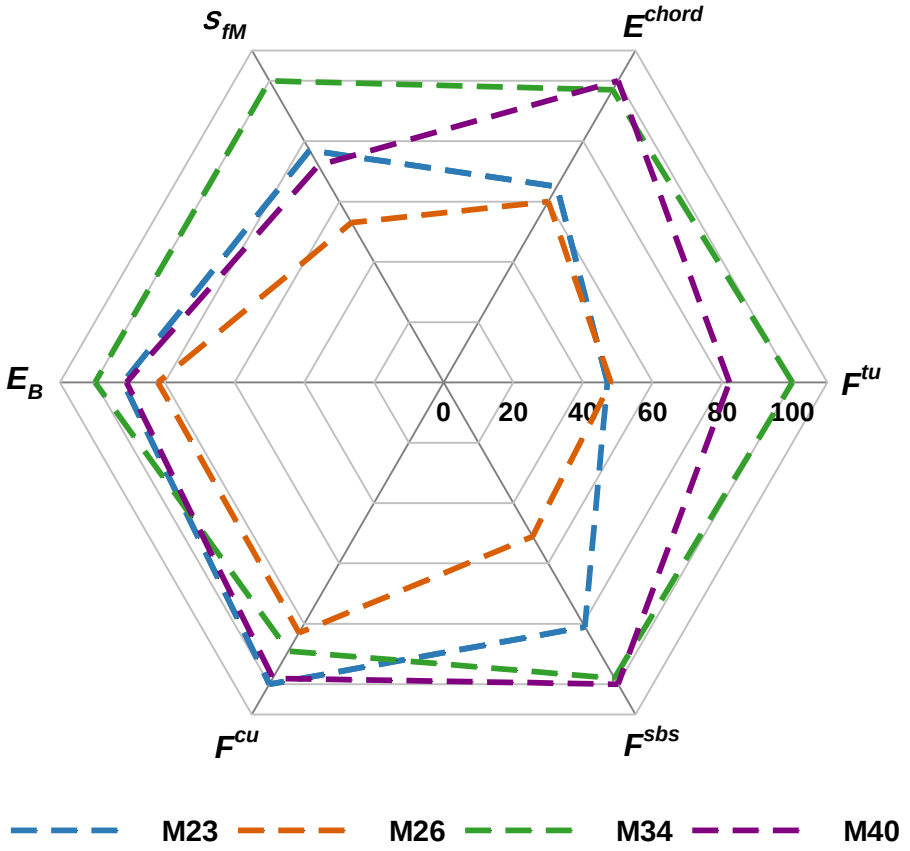

Figure 8-14. Radial summary of the rPMC panel testing. Each category is normalized to the higher value measured so that a visualization based on percentages is possible.

The panels tested displayed different amounts of variability depending on the property being measured. The coefficients of variation measured for each property-panel combination are shown in Figure 8-15. Tensile stiffness and short-beam strength are two properties for which very different amounts of variability were observed between the baseline panels and those processed using the alternate moulding strategy. In contrast, the variation in both the tensile and compressive strength data are fairly constant around 13.3 – 23.5 % and 12.29 – 15.01 %, respectively. Lastly, there does not seem to be a strong correlation between which panel specimens came from and the variability of both the flexural strength and flexural stiffness. The heterogeneous mesostructured inherent to strand-based composites is often cited as being the reason for highly variable mechanical properties like some of those presented in this section [83]. A prime example of this is the behaviours of M34 and M40, two panels that were manufactured from the same rPMC batch and with the same moulding cycle.

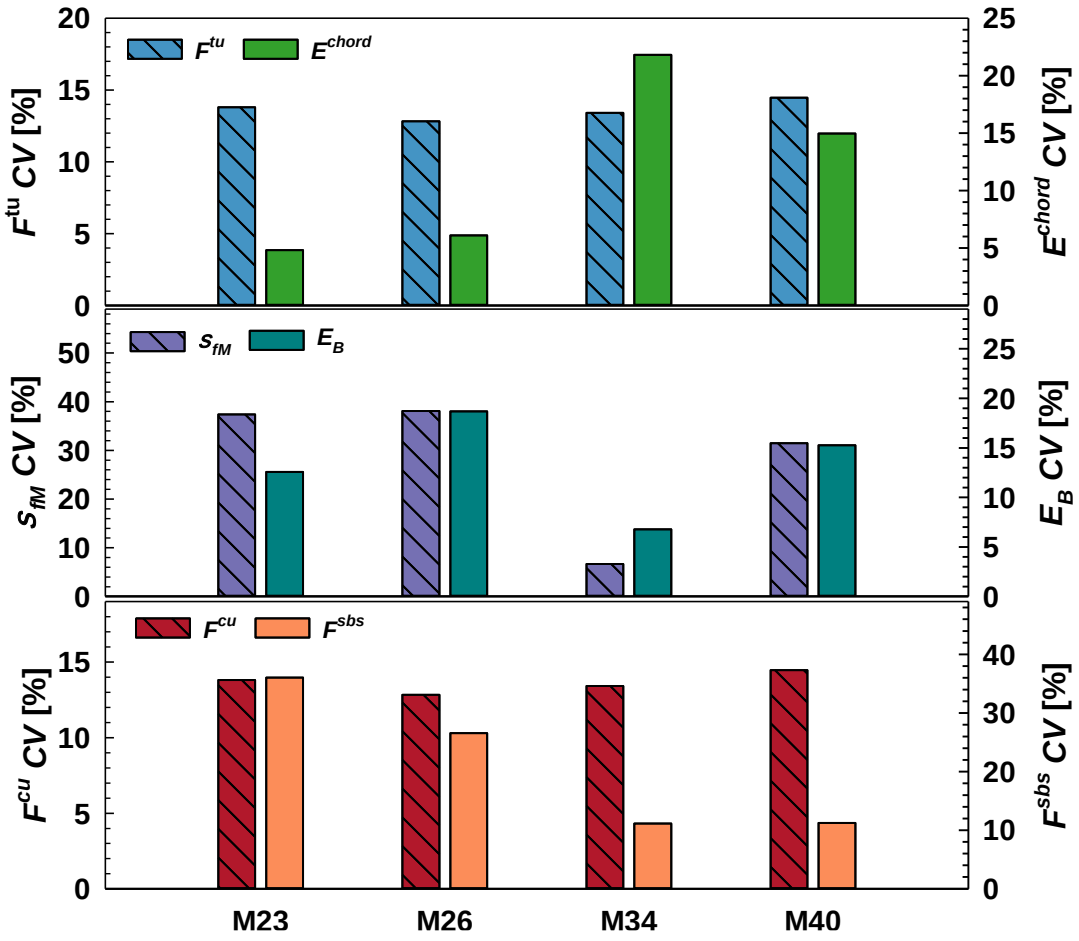

Figure 8-15. Variability of each property for each rPMC panel.

8.8 Property Comparison

Having presented a well-rounded mechanical characterization of the 5276-1 rPMC, the question remains: how do the rPMC properties compare with commercially available compression moulding compounds, as well as with more traditional composites and metals? The compression moulding systems used to provide this comparison include: Hexcel's HexMC-i/M77 which consists of unidirectional CF-epoxy prepreg strands measuring 50 mm long and 8 mm wide, Toray's Cetex MC1200 which consists of unidirectional CF-PEEK prepreg strands measuring 25.4 mm long, and AMC 8590 from Quantum Composites, a CF-vinyl ester bulk moulding compound with an approximate fibre length of 25 mm. Continuous-fibre laminates from NCAMP were also considered, including: a quasi-istropic layup of the CF/PW HexPly 8552 prepreg, a $[(\pm45)/0(\pm45)_2/90/(\pm45)]_s$ layup of the CF/PW 5320-1 vacuum bag only prepreg from Solvay, and an isotropic layup of the GF/8HS MTM45-1 prepreg from Solvay. Properties of the aerospace

metallic mainstay 7075-T6 aluminum were also considered. The averaged properties of the M34 and M40 panels were used for this comparison, as they more closely represent a defect free version of the rPMC. Figure 8-16, Figure 8-17, and Figure 8-18 show the specific tensile, compressive, and flexural properties, respectively, of the rPMC and the comparison materials.

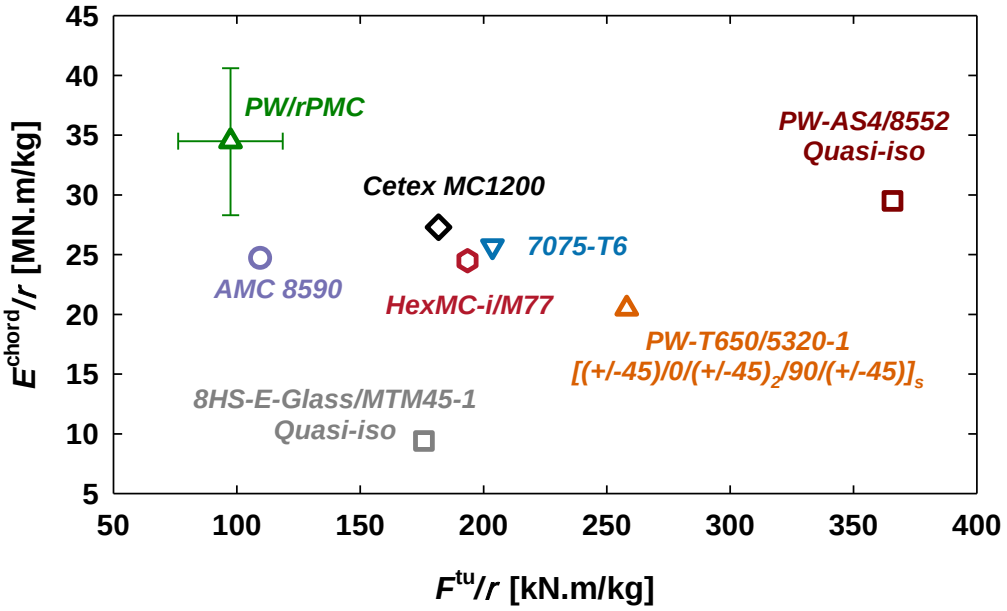

Figure 8-16. Specific tensile strength versus specific tensile modulus for the rPMC and for the comparison materials. The error bars represent standard deviations.

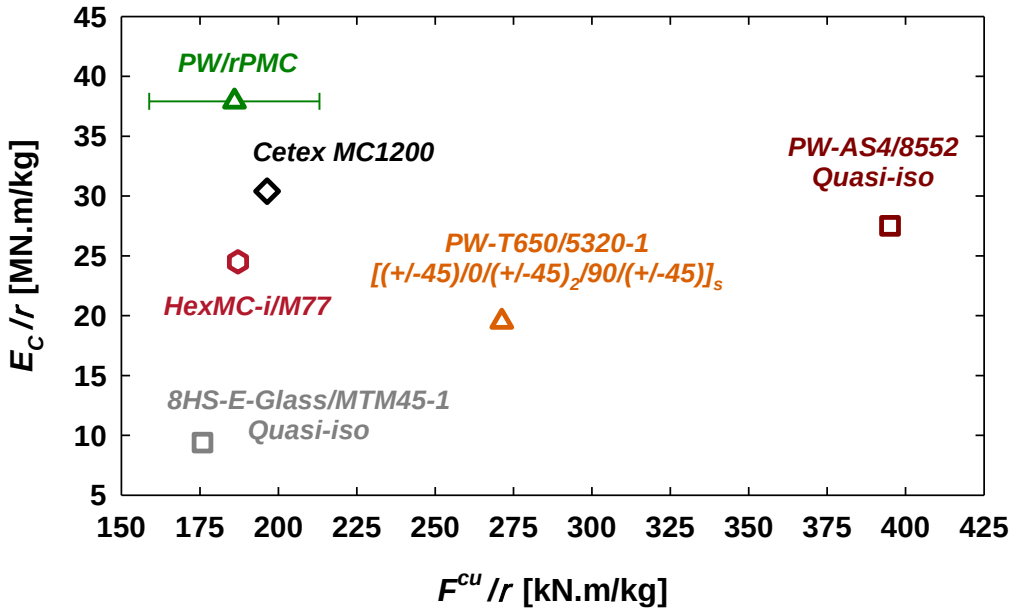

Figure 8-17. Specific compressive strength versus specific compressive modulus for the rPMC and for the comparison materials. The error bars represent standard deviations.

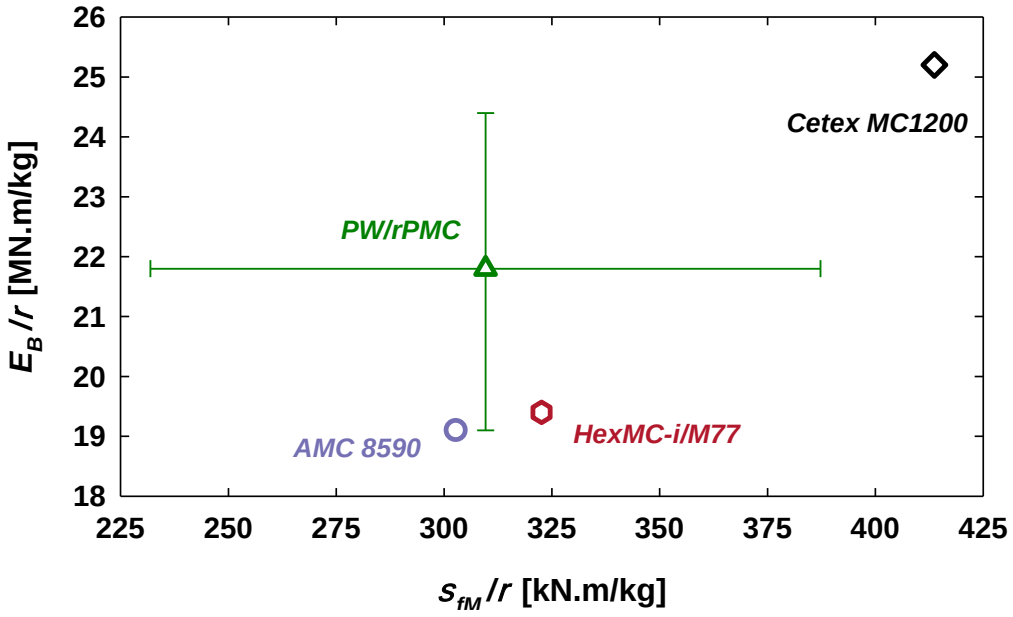

Figure 8-18. Specific flexural strength versus specific flexural modulus for the rPMC and for the comparison materials. The error bars represent standard deviations.

It comes as no surprise that the rPMC exhibits lower specific tensile strength than the other moulding compounds. Recall that the rPMC strand size is roughly 12.7 mm x 12.7 mm, while the effective fibre length of the other materials is between 25 – 50 mm. Selezneva [100] showed that increasing strand size from 12 – 50 mm can result in an increase in both tensile and compressive strength of up to 20 %. Furthermore, prepreg-based systems like Cetex MC1200 and HecMC are known to have potential fibre volume contents above 60 % [165]. The importance of interlaminar shear strength over fibre length may be why the same moulding compounds exhibit similar specific compressive and flexural strengths. Fibre properties and the potential of woven strand nesting may explain the rPMC's noticeably high specific stiffnesses. Only Cetex MC1200 boasts a higher specific stiffness in flexion. This result reinforces the notion that the rPMC developed here is suitable for stiffness-critical applications where the reduction of component mass is important, and not in instances where high strength is needed. The relevance of this type of material is further highlighted when part complexity is high, as manufacturing with the continuous materials shown here would not be possible. Finally, a combined property summary for just the compression moulding systems is given in Table 8-7 for completeness.

Since a material's service temperature plays a vital role in determining what applications it can be used for, an attempt was made to approximate this property for the materials discussed in this section. Glass transition temperatures were used to estimate the service temperatures of the composite systems, while the service temperature of 7075-T6 was chosen based on the drastic change in ultimate tensile strength and elongation a break that occurs near 150 °C (see Appendix G). Approximate service temperatures for each material based on this approach are presented in Figure 8-19. The compression moulding systems and 7075-T6 feature similar service temperatures in the range of 120 – 150 °C. Autoclave-cure systems, which usually benefit from an optional post-cure, feature a higher range around 180 – 200 °C. Attaining similarly high T_g is possible for the rPMC, as it features an autoclave curable matrix. However, this would require increasing the cure time, or implementing a post-cure cycle.

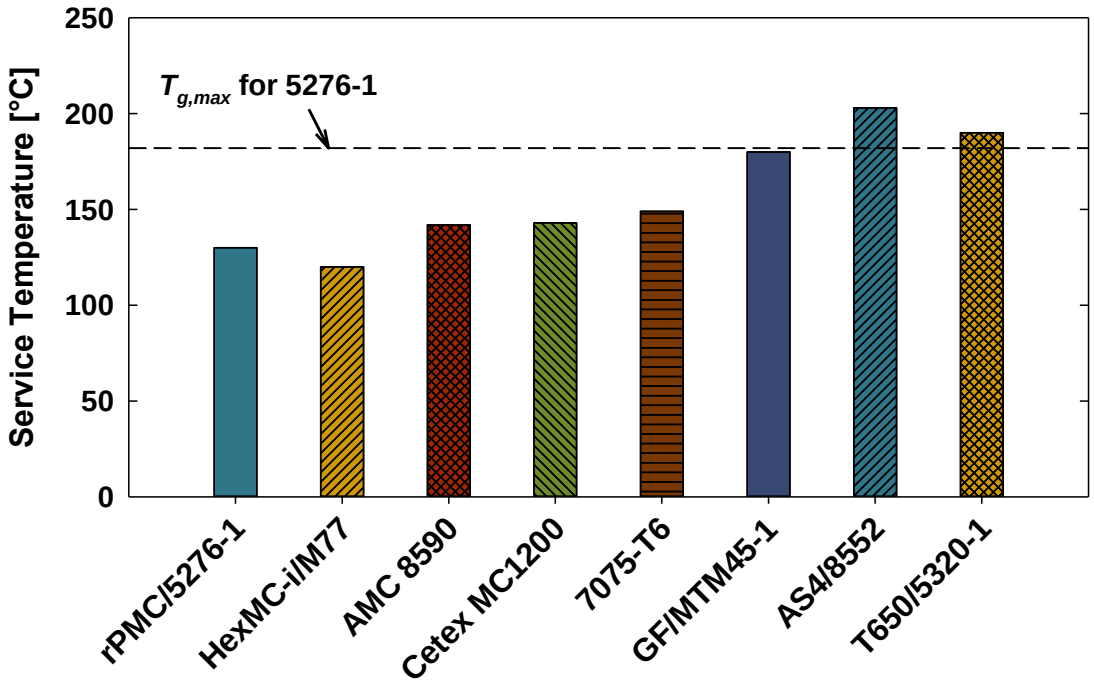

Figure 8-19. Approximation of each material's service temperature.

Table 8-7. Summary of specific property comparison for rPMC and commercially-available moulding compounds.

	rPMC[8]	HexMC-i/M77[166, 167]	AMC 8590[168]	Cetex MC1200[169]
Manufacturer	McGill	Hexcel	Quantum Composites	Toray
Matrix	5276-1	M77	Vinyl Ester	PEEK
Architecture	PW	UT	UT	UT
Strand Size [mm x mm]	12.7 x 12.7	50 x 8 mm	25 mm	25.4
F^{tu} [MPa]	151	300	162	289
F^{cu} [MPa]	288	290[9]	-	312
σ_{fM} [MPa]	480	500	448	658
E^{chord} [GPa]	53.4	38	36.5	43.4
E_c [GPa]	58.8[10]	38	-	48.3
E_B [GPa]	33.8	30	28.3	40
ρ [g/cm3]	1.55	1.55	1.48	1.59
T_g [°C]	130	120	142	143
Processing Temp. [°C]	140	150	138	385
Processing Time [min]	45	2	3-5	14.1
Moulding Pressure [MPa]	6.04	7-10	7	3.4 - 6.8
Shelf-life [months]	TBD	18	12	-
Out-life [days]	TBD	42	56	Indefinite

[8] rPMC properties were taken as the average of M34 and M40 testing data.
[9] ASTM D6484 used.
[10] Compressive stiffness taken from the one instrumented test performed.

9
CONCLUSIONS

9.1 Conclusions & Original Contributions

With an increasing need for pathways to recycle advanced composites in a number of growing sectors, the main objective of this thesis was to develop a methodology for transforming uncured prepreg manufacturing waste into an LDF compression moulding compound. To achieve this objective, the chemo-rheological and flow-compaction behaviours of recovered autoclave prepreg offcuts were studied using a variety of experimental techniques and an elevated temperature staging approach was defined for tailoring resin rheology and curing. Process scale-up trials were also performed to show the feasibility of producing geometrically-complex components using the developed rPMC and to obtain approximate mechanical performance allowables. The following conclusions and original contributions can be drawn from the work presented herein:

1. **Excitation of prepreg flow-compaction mechanisms during processing depends heavily on resin viscosity and rate of transverse deformation (mould closure rate).**
   A simplified (1D) compression moulding apparatus was used to study the effects of resin viscosity and transverse specimen deformation rate on the flow-compaction behaviour of 8 harness satin prepreg laminates. Resin percolation was the only mechanism observed when resin viscosity was low, while increasing viscosity progressively brought about a transition to shear flow dominance. Specimens were more likely to experience reduced

overall deformation when very slow mould closure rates were used. This was attributed to an increased probability of nesting between specimen plies.

Original contribution: A quantitative study of the relationship between resin viscosity and the type of flow-compaction mechanisms excited during the compression moulding of prepreg laminates was carried out. A novel technique for quantitatively measuring the magnitude of shear flow from cross-sectional optical micrographs was developed.

2. **Targeted changes to resin processing viscosity and requisite curing time can be achieved in a predictable way by adjusting the initial degree-of-cure through elevated temperature staging.**

   A simple elevated temperature staging technique was implemented using a convection oven and used to control the initial degree-of-cure of prepreg offcuts. Predictable and verifiable changes to the resin viscosity and necessary curing timeframe for a given moulding temperature were achieved using simple phenomenological models for resin cure, rheology, and glass transition temperature.

   Original contribution: A recycling framework based on controlled prepreg staging was developed (Figure 9-1). Unlike previous work found within the literature, this framework provides a way to achieve higher resin viscosities and shorter curing times without the addition of a new resin component. In addition, the resin behaviour models presented allow for unprecedented flexibility in selecting processing parameters such as cure temperature and cure time through manipulation of the post-staging degree-of-cure.

3. **Room-temperature ageing of the autoclave prepreg studied here brings about significant changes to the polymer's structure and properties.**

   An extended prepreg ageing study was carried out using a variety of experimental techniques including DSC, FT-IR, GPC, and Tack peel testing. Extended periods of room-temperature out-time were shown to cause progressive increases in glass transition temperature, decreases in the concentration of epoxy monomers, growth of lower molecular weight molecules, and shifting of viscoelastic behaviour.

   Original contribution: Multiple measurement techniques were used to develop a multifaceted understanding of the prepreg ageing process over an extended period (375 days). Ranking of the inspection techniques in terms of material, time, and money needed to perform a characterization was also presented.

4. **The specific properties of the 5276-1 rPMCs are comparable to those of similar virgin compression moulding compounds available on the commercial market.**

   Both 8 harness satin and plain weave versions of the rPMC developed here were used to manufacture flat plates from which mechanical testing coupons were obtained. ASTM standards were used to measure the specific tensile, compressive, and flexural properties of these coupons which were compared with the properties of several commercially available prepreg-based compression moulding compounds. The rPMCs were found to exhibit higher specific stiffnesses compared to the commercial systems despite having smaller strands (shorter fibre lengths). Furthermore, rPMC specific strengths were generally within the same range as the comparison materials.

   Original contribution: The recycling framework presented in this thesis was successfully implemented to manufacture large flat panels with high fibre volume fractions (~55 %) and low void contents (~ 1 %). Mechanical properties and glass transition temperatures similar to commercially available moulding compounds were achieved using a shortened processing cycle (140 °C for 45 min) when compared to the manufacturer's recommendation (177 °C for 120 min).

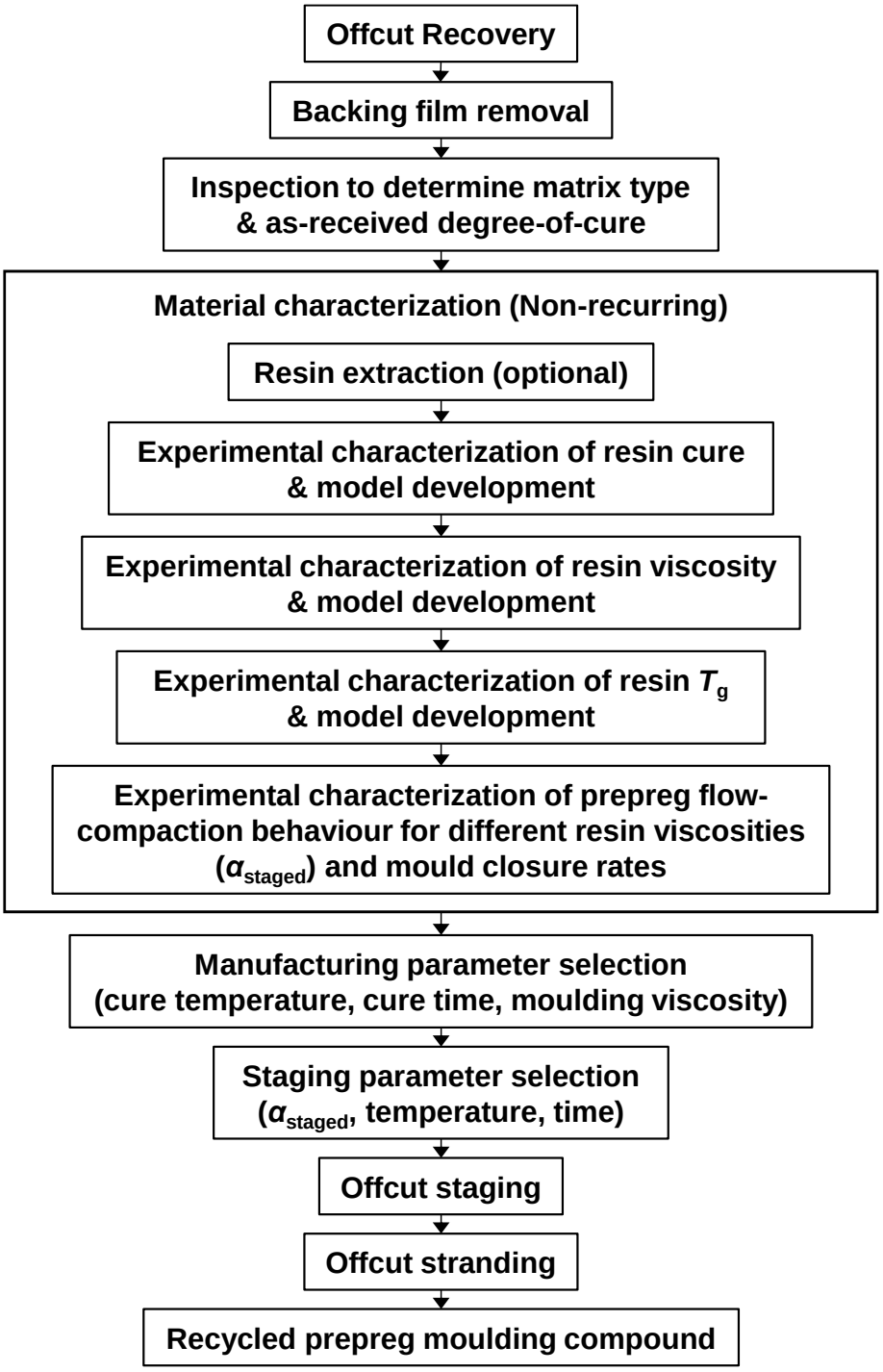

Figure 9-1. Recycling framework based on elevated temperature staging of recovered prepreg offcuts.

9.2 Future work

Suggested follow-up work based on the findings of this work include:

- Perform a more detailed study of viscosity evolution for neat resin specimens that have been stages to different degrees-of-cure.
- Further explore the relationship between the degree-of-cure values obtained by DSC (DiBenedetto) and FT-IR (Beer-Lambert) measurements.
- Develop a flow-compaction process map that includes different resin viscosities and prepregs of different fibre architecture (e.g. 8HS, PW, UD).
- Determine the impact of using a mixture of prepregs with similar matrix types to generate an rPMC with particular focus on the compound processability and resulting mechanical performance.
- Study the effect of advanced staging (close to gelation) on resin cohesion.
- Perform a detailed life cycle analysis on the rPMC compared to other materials.

REFERENCES

[1] Y. Leach. "Boeing 787 Dreamliner Completes First Flight." Boeing PRNewswire. https://boeing.mediaroom.com/2009-12-15-Boeing-787-Dreamliner-Completes-First-Flight (accessed June 3, 2019).

[2] D. Shukman. "Airbus A350 maiden flight close up." BBC News. https://www.bbc.com/news/av/business-22901267/airbus-a350-maiden-flight-close-up (accessed June 3, 2019).

[3] G. Marsh. "Airbus A350 XWB update." materialstoday.com. https://www.materialstoday.com/composite-applications/features/airbus-a350-xwb-update/ (accessed January 5, 2015).

[4] M. Duchesne, "Bombardier's CSeries Aircraft Completes Historic First Flight," ed: Bombardier, 2013.

[5] "New MC-21-300 commercial airliner has completed maiden flight," ed: United Aircraft Corporation, 2017.

[6] G. Marsh, "Bombardier throws down the gauntlet with CSeries airliner," *Reinforced Plastics*, vol. 55, no. 6, pp. 22-26, 2011, doi: https://doi.org/10.1016/S0034-3617(11)70181-3.

[7] G. Polek. "Second MC-21 Preparing for Flight Test." AINonline. https://www.ainonline.com/aviation-news/air-transport/2018-03-26/second-mc-21-preparing-flight-test (accessed June 3, 2019).

[8] G. Gardiner. "Teaming to define what automotive CFRP could be." CompositesWorld.com. https://www.compositesworld.com/articles/teaming-to-define-what-automotive-cfrp-could-be (accessed January 8, 2018).

[9] M. Legault. "Advanced hockey stick design delivers optimal performance." CompositesWorld.com. https://www.compositesworld.com/articles/advanced-hockey-stick-design-delivers-optimal-performance (accessed January 7, 2012).

[10] M. M. Shenoy, L. V. Smith, and J. T. Axtell, "Performance assessment of wood, metal and composite baseball bats," *Composite Structures*, vol. 52, no. 3, pp. 397-404, 2001, doi: 10.1016/S0263-8223(01)00030-7.

[11] P. Suciu. "The Perplexing Carbon Fiber Repurposing Problem." TechNewsWorld.com. https://www.technewsworld.com/story/76172.html (accessed September 18, 2012).

[12] M. Sauer, "Composites Market Report 2019

The global CF-und CC-Market 2019," Carbon Composites, 2019.

[13] "Supply and demand: Advanced fibers." CompositesWorld.com. https://www.compositesworld.com/articles/supply-and-demand-advanced-fibers (accessed June 18, 2020).

[14] S. Das, J. Warren, D. West, and S. Schexnayder, "Global Carbon Fiber Composites Supply Chain Competitiveness Analysis," Clean Energy Manufacturing Analysis Center, 2016.

[15] R. A. Witik, R. Teuscher, V. Michaud, C. Ludwig, and J.-A. E. Manson, "Carbon fibre reinforced composite waste: An environmental assessment of recycling, energy recovery and landfilling," *Composites Part A: Applied Science and Manufacturing,* vol. 49, pp. 89-99, 2013, doi: 10.1016/j.compositesa.2013.02.009.

[16] C. Ward and K. Potter, "In-process composite recycling in the aerospace industry," in *Management, recycling and reuse of waste composites*, V. Goodship Ed. Boca Raton, FL, USA: CRC Press LLC, 2010, ch. 17, pp. 458-494.

[17] "Global commercial aircraft deliveries fell in 2016 as Boeing again outsold Airbus; 2017 to be a peak." CAPA Centre for Aviation. https://centreforaviation.com/analysis/reports/global-commercial-aircraft-deliveries-fell-in-2016-as-boeing-again-outsold-airbus-2017-to-be-a-peak-321424 (accessed March 18, 2020.

[18] F. C. Campbell, A. R. Mallow, and C. E. Browning, "Porosity in carbon fiber composites an overview of causes," *Journal of advanced materials,* vol. 26, no. 4, pp. 18-33, 1995.

[19] J. C. Seferis, R. W. Hillermeier, and F. U. Buehler, "Prepregging and Autoclaving of Thermoset Composites," in *Comprehensive Composite Materials*, vol. 2, A. Kelly and C. Zweben Eds. Seattle, WA, USA: Elsevier, 2000, ch. 2.20.

[20] R. A. Witik, F. Gaille, R. Teuscher, H. Ringwald, V. Michaud, and J.-A. E. Manson, "Economic and environmental assessment of alternative production methods for composite aircraft components," *Journal of Cleaner Production,* vol. 29-30, no. 3-4, pp. 91-102, 2012, doi: 10.1016/j.jclepro.2012.02.028.

[21] G. Fernlund, C. Mobuchon, and N. Zobeiry, "Autoclave Processing," in *Comprehensive Composite Materials II*, vol. 2, C. Zweben and P. Beaumont Eds.: Elsevier, 2018.

[22] M. G. Bader, "Selection of composite materials and manufacturing routes for cost-effective performance," *Composites Part A: Applied Science and Manufacturing,* vol. 33, no. 7, pp. 913-934, 2002, doi: 10.1016/S1359-835X(02)00044-1.

[23] T. Centea and S. R. Nutt, "Manufacturing cost relationships for vacuum bag-only prepreg processing," *Journal of Composite Materials,* vol. 50, no. 17, pp. 2305-2321, 2016. [Online]. Available: http://journals.sagepub.com/doi/pdf/10.1177/0021998315602949.

[24] M. S. Wu, T. Centea, and S. R. Nutt, "Compression molding of reused in-process waste – effects of material and process factors," *Advanced Manufacturing: Polymer & Composites Science*, vol. 4, no. 1, pp. 1-12, 2018, doi: 10.1080/20550340.2017.1411873.

[25] "What-we-do." http://www.elgcf.com/about/what-we-do (accessed April 16, 2020).

[26] E. Worrell and M. Reuter, *Handbook of Recycling: State-of-the-art for Practitioners, Analysts, and Scientists*. Newnes, 2014.

[27] S. J. Pickering, "Thermal methods for recycling waste composites," in *Management, recycling and reuse of waste composites*, V. Goodship Ed. Boca Raton, FL, USA: CRC Press LLC, 2010, ch. 4, pp. 65-101.

[28] M. Blazso, "Pyrolysis for recycling waste composites," in *Management, recycling and reuse of waste composites*, V. Goodship Ed. Boca Raton, FL, USA: CRC Press LLC, 2010, ch. 5, pp. 102-121.

[29] C. H. Park and W. I. Lee, "Compression molding in polymer matrix composites," in *Manufacturing techniques for polymer matrix composites (PMCs)*, S. G. Advani and K.-T. Hsiao Eds. Oxford: Woodhead Publishing Limited, 2012, ch. 3.

[30] J. M. Henshaw, W. Han, and A. D. Owens, "An overview of recycling issues for composite materials," *Journal of Thermoplastic Composite Materials,* vol. 9, no. 1, pp. 4-20, 1996.

[31] S. J. Pickering, "Recycling technologies for thermoset composite materials-current status," *Composites Part A: Applied Science and Manufacturing,* vol. 37, no. 8, pp. 1206-1215, 2006, doi: 10.1016/j.compositesa.2005.05.030.

[32] S. Pimenta and S. T. Pinho, "Recycling carbon fibre reinforced polymers for structural applications: Technology review and market outlook," *Waste management,* vol. 31, no. 2, pp. 378-392, 2011.

[33] Y. Yang, R. Boom, B. Irion, D.-J. van Heerden, P. Kuiper, and H. de Wit, "Recycling of composite materials," *Chemical Engineering and Processing: Process Intensification,* vol. 51, pp. 53-68, 2012.

[34] G. Oliveux, L. O. Dandy, and G. A. Leeke, "Current status of recycling of fibre reinforced polymers: Review of technologies, reuse and resulting properties," *Progress in Materials Science,* no. 72, pp. 61-99, 2015.

[35] K. Makenji, "Mechanical methods for recycling waste composites," in *Management, recycling and reuse of waste composites*, V. Goodship Ed. Boca Raton, FL, USA: CRC Press LLC, 2010, ch. 9, pp. 217-252.

[36] T. Inoh, T. Yokoi, K.-I. Sekiyama, N. Kawamura, and Y. Mishima, "SMC recycling technology," *Journal of Thermoplastic Composite Materials,* vol. 7, no. 1, pp. 42-55, 1994.

[37] D. Perrin, E. Leroy, L. Clerc, A. Bergeret, and J. M. Lopez-Cuesta, "Treatment of SMC composite waste for recycling as reinforcing fillers in thermoplastics," in *Macromolecular Symposia*, 2005, vol. 221, no. 1: Wiley Online Library, pp. 227-236.

[38] J. Brandrup, M. Bittner, W. Michaeli, and G. Menges, *Recycling and recovery of plastics*. Hanser Munich, 1996.

[39] M. R. Gent, M. Menendez, J. Toraño, D. Isidro, and S. Torno, "Cylinder cyclone (LARCODEMS) density media separation of plastic wastes," *Waste Management,* vol. 29, no. 6, pp. 1819-1827, 2009, doi: 10.1016/j.wasman.2008.12.026.

[40] A. Bledzki and D. Kardasz, "Fast identification of plastics in recycling processes," *Polimery(Poland),* vol. 43, no. 2, pp. 79-86, 1998.

[41] C. Kouparitsas, C. Kartalis, P. Varelidis, C. Tsenoglou, and C. Papaspyrides, "Recycling of the fibrous fraction of reinforced thermoset composites," *Polymer composites,* vol. 23, no. 4, pp. 682-689, 2002.

[42] J. Scheirs, *Polymer recycling: science, technology, and applications*. Wiley New York, 1998.

[43] J. Palmer, O. R. Ghita, L. Savage, and K. E. Evans, "Successful closed-loop recycling of thermoset composites," *Composites Part A: Applied Science and Manufacturing,* vol. 40, no. 4, pp. 490-498, 2009, doi: 10.1016/j.compositesa.2009.02.002.

[44] G. Schinner, J. Brandt, and H. Richter, "Recycling carbon-fiber-reinforced thermoplastic composites," *Journal of Thermoplastic Composite Materials,* vol. 9, no. 3, pp. 239-245, 1996.

[45] A. Saccani, S. Manzi, I. Lancellotti, and L. Lipparini, "Composites obtained by recycling carbon fibre/epoxy composite wastes in building materials," *Construction and Building Materials,* vol. 204, pp. 296-302, 2019.

[46] X. Li, R. Bai, and J. McKechnie, "Environmental and financial performance of mechanical recycling of carbon fibre reinforced polymers and comparison with conventional disposal routes," *Journal of Cleaner Production,* vol. 127, pp. 451-460, 2016.

[47] J. A. T. Palmer, "Mechanical recycling of automotive composites for use as reinforcement in thermoset composites," PhD, School of Engineering, Mathematics and Physical Sciences, Exeter University, 2009.

[48] J. Scheirs, "Overview of commercial pyrolysis processes for waste plastics," in *Feedstock Recycling and Pyrolysis of Waste Plastics: Converting Waste Plastics into Diesel and Other Fuels*, J. Scheirs and W. Kaminsky Eds.: John Wiley & Sons, 2006, ch. 15, pp. 381-433.

[49] S. Naqvi, H. M. Prabhakara, E. Bramer, W. Dierkes, R. Akkerman, and G. Brem, "A critical review on recycling of end-of-life carbon fibre/glass fibre reinforced composites waste using pyrolysis towards a circular economy," *Resources, conservation and recycling,* vol. 136, pp. 118-129, 2018.

[50] L. Giorgini *et al.*, "Pyrolysis as a way to close a CFRC life cycle: carbon fibers recovery and their use as feedstock for a new composite production," in *Times of Polymers (TOP) and Composites*, USA, June 22-26 2014, vol. 1599: American Institute of Physics, in AIP Conf. Proc. (USA), pp. 354-7, doi: 10.1063/1.4876851.

[51] K.-W. Kim, J.-S. Jeong, K.-H. An, and B.-J. Kim, "A Low Energy Recycling Technique of Carbon Fibers-Reinforced Epoxy Matrix Composites," *Industrial & Engineering Chemistry Research,* vol. 58, no. 2, pp. 618-624, 2019, doi: 10.1021/acs.iecr.8b02554.

[52] B. J. Jody, J. A. Pomykala Jr, E. J. Daniels, F. L. Paulauskas, and M. G. Abdallah, "A process to recover carbon fibers from polymer matrix composite scrap," in *SAMPE*, Long Beach, CA, USA, May 16 - 20 2004, pp. 41-53.

[53] W. Kaminsky, "Fluidized bed pyrolysis of waste polymer composites for oil and gas recovery," in *Management, recycling and reuse of waste composites*, V. Goodship Ed. Boca Raton, FL, USA: CRC Press LLC, 2010, ch. 8, pp. 192-213.

[54] F. Meng, J. McKechnie, T. A. Turner, and S. J. Pickering, "Energy and environmental assessment and reuse of fluidised bed recycled carbon fibres," *Composites Part A:*

Applied Science and Manufacturing, vol. 100, pp. 206-214, 2017, doi: 10.1016/j.compositesa.2017.05.008.

[55] K. H. Wong, D. Syed Mohammed, S. J. Pickering, and R. Brooks, "Effect of coupling agents on reinforcing potential of recycled carbon fibre for polypropylene composite," *Composites Science and Technology,* vol. 72, no. 7, pp. 835-844, 2012, doi: 10.1016/j.compscitech.2012.02.013.

[56] K. H. Wong, T. A. Turner, and S. J. Pickering, "Challenges in developing nylon composites commingled with discontinuous recycled carbon fibre," presented at the 16th European Conference on Composite Materials, Seville, Spain, 2014.

[57] P. Feraboli, H. Kawakami, B. Wade, F. Gasco, L. DeOto, and A. Masini, "Recyclability and reutilization of carbon fiber fabric/epoxy composites," *Journal of Composite Materials,* vol. 46, no. 12, pp. 1459-1473, 2012, doi: 10.1177/0021998311420604.

[58] H. U. Sokoli, J. Beauson, M. E. Simonsen, A. Fraisse, P. Brøndsted, and E. G. Søgaard, "Optimized process for recovery of glass- and carbon fibers with retained mechanical properties by means of near- and supercritical fluids," *The Journal of Supercritical Fluids,* vol. 124, pp. 80-89, 2017, doi: 10.1016/j.supflu.2017.01.013.

[59] G. Jiang, S. J. Pickering, E. H. Lester, T. Turner, K. Wong, and N. Warrior, "Characterisation of carbon fibres recycled from carbon fibre/epoxy resin composites using supercritical n-propanol," *Composites Science and Technology,* vol. 69, no. 2, pp. 192-198, 2009.

[60] M. Roux, C. Dransfeld, N. Eguémann, and L. Giger, "Processing and Recycling of a Thermoplastic Composite Fibre/PEEK Aerospace Part," presented at the 16th European Conference on Composite Materials, Seville, Spain, 2014.

[61] N. Eguémann, "Etude du comportement mécanique de matériaux composites polymère PEEK/renfort fibre de carbone à architecture discontinue en plis," PhD, Université de Franche-Comté, 2013.

[62] D. Leblanc, B. Landry, M. Jancik, and P. Hubert, "Recyclability of randomly-oriented strand thermoplastic composites," presented at the ICCM 20, 2015.

[63] G. Gardiner. "Recycled thermoplastic composites for production." CompositesWorld.com. (accessed September 15, 2020).

[64] M. Buggy, L. Farragher, and W. Madden, "Recycling of composite materials," *Journal of Materials Processing Technology,* vol. 55, no. 3-4, pp. 448-456, 1995, doi: 10.1016/0924-0136(95)02037-3.

[65] W. Michaeli and A. Oelgarth, "New technologies for processing of non-cured prepreg waste preparation of high-strength DMC," presented at the International SAMPE Symposium and Exhibition, Anaheim, CA, USA, 1996.

[66] K. Pannkoke, M. Oethe, and J. Busse, "Efficient prepreg recycling at low temperatures," *Cryogenics,* vol. 38, no. 1, pp. 155-159, 1998, doi: 10.1016/S0011-2275(97)00127-6.

[67] G. Nilakantan and S. Nutt, "Reuse and upcycling of aerospace prepreg scrap and waste," *Reinforced Plastics,* vol. 59, no. 1, pp. 44-51, 2015, doi: 10.1016/j.repl.2014.12.070.

[68] B. C. Jin, X. Li, A. Jain, C. González, J. Llorca, and S. Nutt, "Optimization of microstructures and mechanical properties of composite oriented strand board from reused prepreg," *Composite Structures,* vol. 174, pp. 389-398, 2017, doi: 10.1016/j.compstruct.2017.05.002.

[69] T. Blanco, N. Colas, J. Sánchez, A. Ricardo, and N. Fanegas, "Reúso de prepreg aeronáutico sin curar," *Materiales Compuestos,* vol. 2, no. 3, pp. 1-5, 2018.

[70] S. Sultana, A. Asadi, J. Colton, and K. Kalaitzidou, "Composites made from CF prepreg trim waste tapes using sheet molding compounds (SMC) technology: Challenges and potential," *Composites Part A: Applied Science and Manufacturing,* vol. 134, 2020, doi: 10.1016/j.compositesa.2020.105906.

[71] G. Nilakantan and S. Nutt, "Reuse and upcycling of thermoset prepreg scrap: Case study with out-of-autoclave carbon fiber/epoxy prepreg," *Journal of Composite Materials,* vol. 52, no. 3, pp. 341-360, 2018, doi: 10.1177/0021998317707253.

[72] J. F. Unser, "Reuse of scrap prepreg," presented at the 42nd International SAMPE Symposium and Exhibition, Anaheim, CA, USA, May 4-8, 1997.

[73] C. S. R. de Souza *et al.*, "Reuse of Uncured Carbon Fiber/Epoxy Resin Prepreg Scraps: Mechanical Behavior and Environmental Response," *ACS Sustainable Chemistry & Engineering,* vol. 7, no. 2, pp. 2200-2206, 2019, doi: 10.1021/acssuschemeng.8b04852.

[74] *Standard Test Method for Short-Beam Strength of Polymer Matrix Composite Materials and Their Laminates,* D 2344-13, ASTM, USA, 2013.

[75] J. Sloan. "Boeing to supply ELG carbon fiber for recycling." CompositesWorld.com. https://www.compositesworld.com/news/boeing-to-supply-elg-carbon-fiber-for-recycling (accessed October 4, 2020).

[76] S. Mazza. "Gardena startup uses discarded rocket material to make skateboards, desks, briefcases and more." Daily Breeze. https://www.dailybreeze.com/2018/01/15/gardena-startup-uses-discarded-rocket-material-to-make-skateboards-desks-briefcases-and-more/ (accessed October 4, 2020).

[77] "Ryan Olliges: Founder of 121c boards." cnl. https://flounder-tunny-wen9.squarespace.com/nativeadmission/2015/7/29/ryan-olliges-founder-of-121c-boards.html (accessed October 4, 2020).

[78] E. Villalon and J. Grondin, "Method for providing a moulding composition and moulding composition," World Patent Patent WO 2017/109107 Al, June 29, 2019.

[79] "Lavoisier." https://www.lavoisier-composites.com/en/ (accessed October 5, 2020).

[80] K. Potter, "Understanding the origins of defects and variability in composites manufacture," presented at the ICCM 17, Edinburgh, UK, 2009.

[81] F. Nosrat Nezami, T. Gereke, and C. Cherif, "Active forming manipulation of composite reinforcements for the suppression of forming defects," *Composites Part A: Applied Science and Manufacturing,* vol. 99, pp. 94-101, 2017, doi: 10.1016/j.compositesa.2017.04.011.

[82] I. Y. Chang and J. F. Pratte, "LDF™ thermoplastic composites technology," *Journal of Thermoplastic Composite Materials,* vol. 4, no. 3, pp. 227-252, 1991.

[83] S. B. Visweswaraiah, M. Selezneva, L. Lessard, and P. Hubert, "Mechanical characterisation and modelling of randomly oriented strand architecture and their hybrids – A general review," *Journal of Reinforced Plastics and Composites,* vol. 37, no. 8, pp. 548-580, 2018, doi: 10.1177/0731684418754360.

[84] R. J. Sager *et al.*, "Effect of carbon nanotubes on the interfacial shear strength of T650 carbon fiber in an epoxy matrix," *Composites Science and Technology,* vol. 69, no. 7, pp. 898-904, 2009, doi: 10.1016/j.compscitech.2008.12.021.

[85] A. Levy and P. Hubert, "Interstand Void Content evolution in compression moulding of Randomly Oriented Strands (ROS) of thermoplastic composites," *Composites Part A (Applied Science and Manufacturing),* 2013.

[86] D. Ferré Sentis, L. Orgéas, P. J. J. Dumont, S. Rolland du Roscoat, M. Sager, and P. Latil, "3D in situ observations of the compressibility and pore transport in Sheet Moulding Compounds during the early stages of compression moulding," *Composites Part A: Applied Science and Manufacturing,* vol. 92, pp. 51-61, 2017, doi: 10.1016/j.compositesa.2016.10.031.

[87] H. Darcy, *Les fontaines publiques de la ville de Dijon: exposition et application*. Paris, 1856.

[88] P. Hubert, "Aspects of Flow and Compaction of Laminated Composite Shapes During Cure," Ph.D., Metals and Materials Engineering, University of British Columbia, 1996.

[89] I. Taketa, T. Okabe, H. Matsutani, and A. Kitano, "Flowability of unidirectionally arrayed chopped strands in compression molding," *Composites Part B: Engineering,* vol. 42, no. 6, pp. 1764-1769, 2011, doi: 10.1016/j.compositesb.2011.01.021.

[90] D. LeBlanc, "Compression Moulding of Complex Parts with Randomly-Oriented Strand Thermoplastic Composites," M.Eng, Mechanical Engineering, McGill University, Montreal, QC, Canada, 2014.

[91] J.-H. Bae, M.-G. Han, and S.-H. Chang, "Formability of complex composite structures with ribs made of long carbon-fiber-reinforced prepregs," *Composite Structures,* vol. 168, pp. 56-64, 2017, doi: 10.1016/j.compstruct.2017.02.033.

[92] M. I. Abdul Rasheed, "Compression molding of chopped woven thermoplastic composite flakes: a study on processing and performance," PhD, University of Twente, 2016.

[93] A. D. Evans, C. C. Qian, T. A. Turner, L. T. Harper, and N. A. Warrior, "Flow characteristics of carbon fibre moulding compounds," *Composites Part A: Applied Science and Manufacturing*, vol. 90, pp. 1-12, 2016, doi: 10.1016/j.compositesa.2016.06.020.

[94] C. B. Landry, "Experimental study and numerical simulation of defect formation during compression moulding of discontinuous long fibre carbon/PEEK composites," PhD, Mechanical Engineering, McGill University, Montreal, 2016.

[95] M. Van Wijngaarden, A. Jongbloed, and J. De Vries, "Thermoplastic compound compression molding," presented at the SAMPE Conference and Exhibition, Seattle, WA, United states, May 17-20, 2010.

[96] L. M. Martulli, L. Muyshondt, M. Kerschbaum, S. Pimenta, S. V. Lomov, and Y. Swolfs, "Carbon fibre sheet moulding compounds with high in-mould flow: Linking morphology to tensile and compressive properties," *Composites Part A: Applied Science and Manufacturing,* vol. 126, 2019, doi: 10.1016/j.compositesa.2019.105600.

[97] G.-P. Picher-Martel, "Compression Moulding of Randomly-Oriented Strands Thermoplastic Composites: A study of the flow and deformation mechanisms," PhD, Mechanical Engineering, McGill University, Montreal, QC, CA, 2014.

[98] A. J. Favaloro, D. E. Sommer, B. R. Denos, and R. B. Pipes, "Simulation of prepreg platelet compression molding: Method and orientation validation," *Journal of Rheology,* vol. 62, no. 6, pp. 1443-1455, 2018.

[99] G.-P. Picher-Martel, A. Levy, and P. Hubert, "Compression moulding of Carbon/PEEK Randomly-Oriented Strands composites: A 2D Finite Element model to predict the squeeze flow behaviour," *Composites Part A: Applied Science and Manufacturing,* vol. 81, pp. 69-77, 2016, doi: 10.1016/j.compositesa.2015.11.006.

[100] M. Selezneva, "Experimental and Theoretical Investigations of Mechanical Properties of Randomly-Oriented Strand (ROS) Composites," PhD, Mechanical Engineering, McGill University, Montreal, QC, Canada, 2015.

[101] S. Yamashita, K. Hashimoto, H. Suganuma, and J. Takahashi, "Experimental characterization of the tensile failure mode of ultra-thin chopped carbon fiber tape-reinforced thermoplastics," *Journal of Reinforced Plastics and Composites,* vol. 35, no. 18, pp. 1342-1352, 2016, doi: 10.1177/0731684416651134.

[102] Y. Wan and J. Takahashi, "Tensile properties and aspect ratio simulation of transversely isotropic discontinuous carbon fiber reinforced thermoplastics," *Composites Science and Technology,* vol. 137, pp. 167-176, 2016, doi: 10.1016/j.compscitech.2016.10.024.

[103] B. Landry and P. Hubert, "Experimental study of defect formation during processing of randomly-oriented strand carbon/PEEK composites," *Composites Part A: Applied Science and Manufacturing,* vol. 77, pp. 301-309, 2015.

[104] C. Collins, "Dimensional Stability in Compression-Moulded Discontinuous Long Fibre Carbon/PEEK Composites," MEng, Mechanical Engineering, McGill University, Montreal, Canada, 2018.

[105] P. Feraboli, E. Peitso, F. Deleo, T. Cleveland, and P. B. Stickler, "Characterization of prepreg-based discontinuous carbon fiber/epoxy systems," *Journal of Reinforced Plastics and Composites,* vol. 28, no. 10, pp. 1191-1214, 2009, doi: 10.1177/0731684408088883.

[106] M. Selezneva and L. Lessard, "Characterization of mechanical properties of randomly oriented strand thermoplastic composites," *Journal of Composite Materials,* vol. 50, no. 20, pp. 2833-2851, 2016.

[107] P. Feraboli, E. Peitso, T. Cleveland, P. B. Stickler, and J. C. Halpin, "Notched behavior of prepreg-based discontinuous carbon fiber/epoxy systems," *Composites Part A: Applied*

Science and Manufacturing, vol. 40, no. 3, pp. 289-299, 2009, doi: 10.1016/j.compositesa.2008.12.012.

[108] C. Qian, L. Harper, T. Turner, and N. Warrior, "Notched behaviour of discontinuous carbon fibre composites: comparison with quasi-isotropic non-crimp fabric," *Composites Part A: Applied Science and Manufacturing*, vol. 42, no. 3, pp. 293-302, 2011.

[109] N. Eguémann, L. Giger, K. Masania, C. Dransfeld, F. Thiebaud, and D. Perreux, "Processing of characterisation of carbon fibre reinforced PEEK with discontinuous architecture," presented at the 16th European conference on composite materials, Seville, Spain, 2014.

[110] *CYCOM® 5276-1 Epoxy Resin System*, Cytec Engineered Materials, 2012. Accessed: July 20, 2016.

[111] A. O. Siddiqui, P. Sudher, and B. V. S. R. Murthy, "Cure kinetics modeling of cyanate-ester resin system," *Thermochimica Acta*, vol. 554, pp. 8-14, 2013.

[112] D. Dykeman, "Minimizing Uncertainty in Cure Modeling for Composites Manufacturing," Ph.D., Materials Engineering, University of British Columbia, 2008.

[113] K. C. Cole, J. J. Hechler, and D. Noel, "A New Approach to Modeling the Cure Kinetics of Epoxy Amine Thermosetting Resins. 2. Application to a Typical System Based on Bis[4-(diglycidylamino)phenyl]methane and Bis(4-aminophenyl) Sulfone," *Macromolecules*, vol. 24, no. 11, pp. 3098-3110, 1991.

[114] N. A. Slesinger, "Thermal Modeling Validation Techniques for Thermoset Polymer Matrix Composites," Master of Applied Science, Materials Engineering, University of British Columbia, 2010.

[115] V. M. A. Calado and S. G. Advani, "Thermoset Resin Cure Kinetics and Rheology," in *Processing of Composites*, R. S. Davé and A. C. Loos Eds., 2000, ch. 2, pp. 32-107.

[116] J. Kratz, K. Hsiao, G. Fernlund, and P. Hubert, "Thermal models for MTM45-1 and Cycom 5320 out-of-autoclave prepreg resins," *Journal of Composite Materials*, vol. 47, no. 3, pp. 341-352, 2012.

[117] "COMPRO Model Documentation," Release 1.5.13 ed: Convergent Manufacturing Technologies Inc., 2017.

[118] *KE-1204 A/B*. Shin-Etsu Silicones of America, Inc. Accessed: November 2, 2017.

[119] L. Khoun, T. Centea, and P. Hubert, "Characterization methodology of thermoset resins for the processing of composite materials-case study: CYCOM 890RTM epoxy resin," *Journal of Composite Materials*, vol. 44, no. 11, 2010, doi: 10.1177/0021998309353960.

[120] J. Castro and C. Macosko, "Kinetics and rheology of typical polyurethane reaction injection molding systems," *SPE Tech. Pap*, vol. 26, pp. 434-438, 1980.

[121] P. J. Halley and M. E. Mackay, "Chemorheology of thermosets—an overview," *Polymer Engineering & Science*, vol. 36, no. 5, pp. 593-609, 1996.

[122] J. Barroeta Robles, "A Streamlined Characterization-Based Selection of Composite Material Systems for Space Structures," Master of Engineering, Mechanical Engineering, McGill University, 2018.

[123] L. E. Nielsen, "Cross-Linking–Effect on Physical Properties of Polymers," *Journal of Macromolecular Science, Part C,* vol. 3, no. 1, pp. 69-103, 1969.

[124] H. E. Adabbo and R. J. J. Williams, "The evolution of thermosetting polymers in a conversion–temperature phase diagram," *Journal of Applied Polymer Science,* vol. 27, no. 4, pp. 1327-1334, 1982.

[125] J. B. Enns and J. K. Gillham, "Time–temperature–transformation (TTT) cure diagram: Modeling the cure behavior of thermosets," *Journal of Applied Polymer Science,* vol. 28, no. 8, pp. 2567-2591, 1983.

[126] J. P. Pascault and R. J. J. Williams, "Glass transition temperature versus conversion relationships for thermosetting polymers," *Journal of Polymer Science Part B: Polymer Physics,* vol. 28, no. 1, pp. 85-95, 1990, doi: 10.1002/polb.1990.090280107.

[127] C. M. Ó Brádaigh, G. B. McGuinness, and S. P. McEntree, "Implicit finite element modelling of composites sheet forming processes," in *Composite Sheet Forming*, D. Bhattacharyya Ed., (Composite Materials Series, no. 11), R. B. Pipes, Ed., 1997, ch. 7.

[128] T. Centea, "Material-Processing-Quality Relationships During the Consolidation of Out-of-Autoclave Prepregs," Ph.D., Mechanical Engineering, McGill University, Montréal; Québec; Canada, 2012.

[129] L. Grunenfelder and S. Nutt, "Out-Time Effects on VBO(Vacuum Bag Only) Prepreg and Laminate Properties," *SAMPE Journal,* vol. 47, no. 5, pp. 6-12, 2011.

[130] A. W. Smith and P. Hubert, "A Unidimensional Flow and Consolidation Characterization of Recycled Prepregs," presented at the Canadian International Conference on Composite Materials, Ottawa, Canada, 2017.

[131] B. S. Hayes and L. M. Gammon, *Optical Microscopy of Fiber-Reinforced Composites*. ASM international, 2010.

[132] M. C. Waterbury and L. T. Drzal, "Determination of Fiber Volume Fractions by Optical Numeric Volume Fraction Analysis," *Journal of Reinforced Plastics and Composites,* vol. 8, no. 6, pp. 627-636, 1989, doi: 10.1177/073168448900800605.

[133] M. T. Cann, D. O. Adams, and C. L. Schneider, "Characterization of fiber volume fraction gradients in composite laminates," *Journal of composite materials,* vol. 42, no. 5, pp. 447-466, 2008.

[134] H. Yang and J. S. Colton, "Quantitative image processing analysis of composite materials," *Polymer composites,* vol. 15, no. 1, pp. 46-54, 1994.

[135] *Standard Test Methods for Constituent Content of Composite Materials*, D 3171-15, ASTM, USA, 2015.

[136] B. T. Astrom, *Manufacturing of polymer composites*. CRC Press, 1997.

[137] "TORELINA PPS Resin." https://www.toray.us/plastics/torelina/technical/tec_017.html (accessed December 19, 2019).

[138] M. Brillant and P. Hubert, "Out-of-autoclave processing of complex shape laminates," presented at the SAMPE Conference and Exhibition, Seattle, WA, USA, May 17-20, 2010.

[139] D. Bangarusampath, H. Ruckdäschel, V. Altstädt, J. K. Sandler, D. Garray, and M. S. Shaffer, "Rheology and properties of melt-processed poly (ether ether ketone)/multi-wall carbon nanotube composites," *Polymer,* vol. 50, no. 24, pp. 5803-5811, 2009.

[140] *ULTEM Resin 1000 - Americas*, Prospector, 2018. Accessed: June 4, 2020.

[141] D. Kim, T. Centea, and S. R. Nutt, "Out-time effects on cure kinetics and viscosity for an out-of-autoclave (OOA) prepreg: Modelling and monitoring," *Composites Science and Technology,* vol. 100, pp. 63-69, 2014, doi: 10.1016/j.compscitech.2014.05.027.

[142] S. K. Mazumdar, *Composites Manufacturing: Materials, Product, and Process Engineering*. Boca Raton, Florida, USA: CRC Press LLC, 2002.

[143] *Standard Test Method for Transition Temperatures and Enthalpies of Fusion and Crystallization of Polymers by Differential Scanning Calorimetry*, D 3418-15, ASTM, USA, 2015.

[144] J. Mijovic, A. Fishbain, and J. Wijaya, "Mechanistic modeling of epoxy-amine kinetics. 1. Model compound study," *Macromolecules,* vol. 25, no. 2, pp. 979-985, 1992.

[145] *Compendium of Chemical Terminology* (International Union of Pure and Applied Chemistry). 2014.

[146] J. F. Sprouse, B. M. Halpin Jr, and R. E. Sacher, "Cure Analysis of Epoxy Composites Using Fourier Transform Infrared Spectroscopy," Army Materials and Mechanics Research Center, 1978.

[147] R. E. Smith, F. N. Larsen, and C. L. Long, "Epoxy resin cure. II. FTIR analysis," *Journal of Applied Polymer Science,* vol. 29, no. 12, pp. 3713-3726, 1984.

[148] G. George, G. Cash, and L. Rintoul, "Cure monitoring of aerospace epoxy resins and prepregs by Fourier transform infrared emission spectroscopy," *Polymer International,* vol. 41, no. 2, pp. 169-182, 1996.

[149] X. Ramis, J. M. Salla, C. Mas, A. Mantecón, and A. Serra, "Kinetic study by FTIR, TMA, and DSC of the curing of a mixture of DGEBA resin and γ-butyrolactone catalyzed by ytterbium triflate," *Journal of Applied Polymer Science,* vol. 92, no. 1, pp. 381-393, 2004.

[150] E. G. Malawer and L. Senak, *Introduction to Size Exclusion Chromatography*, 2nd ed. (Handbook of Size Exclusion Chromatography and Related Techniques). Marcel Dekker, Inc., 2004.

[151] K. J. Ahn, L. Peterson, J. C. Seferis, D. Nowacki, and H. G. Zachmann, "Prepreg aging in relation to tack," *Journal of Applied Polymer Science,* vol. 45, no. 3, pp. 399-406, 1992, doi: 10.1002/app.1992.070450304.

[152] A. Endruweit *et al.*, "Characterisation of tack for uni-directional prepreg tape employing a continuous application-and-peel test method," *Composites Part A: Applied Science and Manufacturing,* vol. 114, pp. 295-306, 2018, doi: 10.1016/j.compositesa.2018.08.027.

[153] D. Budelmann, H. Detampel, C. Schmidt, and D. Meiners, "Interaction of process parameters and material properties with regard to prepreg tack in automated lay-up and

draping processes," *Composites Part A: Applied Science and Manufacturing,* vol. 117, pp. 308-316, 2019, doi: 10.1016/j.compositesa.2018.12.001.

[154] A. W. Smith, A. Endruweit, G. Y. H. Choong, D. S. A. De Focatiis, and P. Hubert, "Adaptation of Material Deposition Parameters to Account for Out-time Effects on Prepreg Tack," *Composites Part A: Applied Science and Manufacturing,* 2020, doi: 10.1016/j.compositesa.2020.105835.

[155] R. J. Crossley, P. J. Schubel, and D. S. A. De Focatiis, "Time-temperature equivalence in the tack and dynamic stiffness of polymer prepreg and its application to automated composites manufacturing," *Composites Part A: Applied Science and Manufacturing,* vol. 52, pp. 126-33, 2013, doi: 10.1016/j.compositesa.2013.05.002.

[156] M. L. Williams, R. F. Landel, and J. D. Ferry, "The temperature dependence of relaxation mechanisms in amorphous polymers and other glass-forming liquids," *J. Am. Chem. Soc.*, vol. 77, no. 14, pp. 3701-3707, 1955.

[157] G. Y. H. Choong, D. S. A. De Focatiis, and D. G. Hassell, "Viscoelastic melt rheology and time–temperature superposition of polycarbonate–multi-walled carbon nanotube nanocomposites," *Rheologica Acta,* vol. 52, no. 8, pp. 801-814, 2013, doi: 10.1007/s00397-013-0706-6.

[158] R. Mulvenna, "Standard Operating Procedure GPC/SEC," ed: Purdue University College of Engineering, 2014.

[159] S. B. Visweswaraiah, L. Lessard, and P. Hubert, "Interlaminar shear behaviour of hybrid fibre architectures of randomly oriented strands combined with laminate groups," *Composite Structures,* vol. 176, pp. 823-832, 2017, doi: 10.1016/j.compstruct.2017.06.002.

[160] D. M. Corbridge, L. T. Harper, D. S. A. De Focatiis, and N. A. Warrior, "Compression moulding of composites with hybrid fibre architectures," *Composites Part A: Applied Science and Manufacturing,* vol. 95, pp. 87-99, 2017, doi: 10.1016/j.compositesa.2016.12.018.

[161] *Standard Test Method for Tensile Properties of Polymer Matrix Composite Materials*, D 3039 - 14, ASTM, 2014.

[162] *Standard Test Method for Flexural Properties of Unreinforced and Reinforced Plastics and Electrical Insulating Materials*, D 790 - 17, ASTM, 2017.

[163] *Standard Test Method for Compressive Properties of Polymer Matrix Composite Materials Using a Combined Loading Compression (CLC) Test Fixture*, D 6641 - 14, ASTM, 2014.

[164] J. Chakrabarty, "Plastic Analysis of Beams and Frames," in *Theory of Plasticity*, J. Chakrabarty Ed. Oxford: Butterworth-Heinemann, 2006, ch. 4, pp. 233-322.

[165] P. Feraboli, T. Cleveland, M. Ciccu, P. Stickler, and L. DeOto, "Defect and damage analysis of advanced discontinuous carbon/epoxy composite materials," *Composites Part A: Applied Science and Manufacturing,* vol. 41, no. 7, pp. 888-901, 2010, doi: 10.1016/j.compositesa.2010.03.002.

[166] *HexMC®-i Moulding Compound*, Hexcel Corporation, 2019.

[167] *HexMC® M77*, Hexcel Corporation, 2013.

[168] *Quantum AMC® 8590 NT*, A. Schulman, 2018.

[169] *Toray Cetex® MC1200 PEEK*, Toray Advanced Composites, 2019.

APPENDIX A

Table A-1. T_g values measured by DSC for prepreg specimens subjected to increasing periods of out-time. Error bars represent the minimum and maximum values measured for batches 1 and 2, and standard deviations for Batch 3.

t_{out} [days]	*Batch 1*	*Batch 2*	*Batch 3*[*]
0	-3.08 ± 2.73	-1.44 ± 4.01	-0.20 ± 0.80
7	-1.27 ± 1.60	1.03 ± 1.97	4.00 ± 0.40
14	2.76 ± 0.65	5.92 ± 1.58	6.40 ± 0.40
21	5.66 ± 1.30	9.23 ± 0.85	8.30 ± 0.80
28	9.68 ± 0.19	13.92 ± 1.04	-
35	13.97 ± 1.79	21.01 ± 0.87	16.80 ± 0.70
42	18.66 ± 1.16	23.45 ± 1.61	-
49	20.85 ± 1.01	28.35 ± 1.23	-
56	23.67 ± 1.06	30.53 ± 2.17	-
70	29.93 ± 1.37	32.86 ± 1.17	-
92	-	35.98 ± 3.69	-
112	-	40.94[*]	-
147	-	40.54 ± 3.11	-
169	-	42.64 ± 6.52	-
282	-	49.09 ± 4.47	-
288	-	50.08 ± 2.53	-
372	-	55.86[*]	-
375	-	55.03 ± 1.65	-

[*]Only one data point collected

Table A-2. Summary of the average peak areas, degrees-of-cure, and $T_{g,t}$ obtained during the FT-IR ageing trials.

t_{out} [days]	A^t_{909}	α_t [-]	$T_{g,t}$ [°C]
0	20.69	0.014	-3.00
1	20.66	0.016	-2.81
4	20.62	0.018	-2.54
5	20.41	0.031	-1.07
6	20.42	0.030	-1.15
9[*]	*21.15*	*-0.014*	*-6.14*
10	19.80	0.067	3.29
11[*]	*20.32*	*0.036*	*-0.47*
15	19.31	0.097	6.84
16[**]	-	-	-
21	18.50	0.145	12.93
40	14.94	0.359	42.95
47[**]	-	-	-
53[**]	-	-	-
cured	4.03	1.000	182.00

[*] Repeatable specimen scans, but potential outliers.

[**] Unacceptable spectra scatter.

APPENDIX B

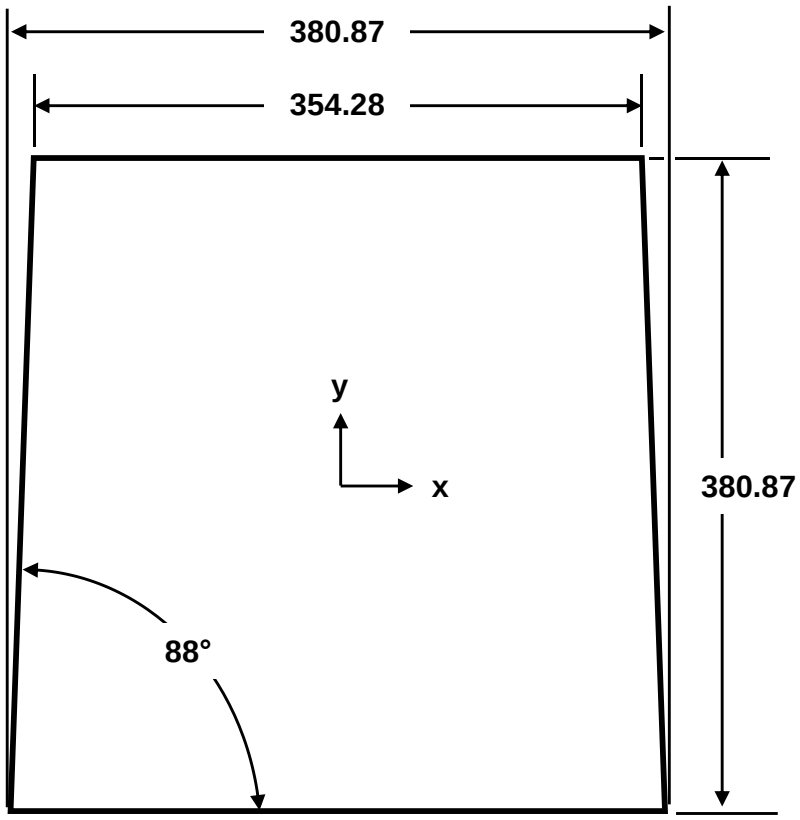

Figure B-1. Flat panel compression mould cavity dimensions (millimetres).

APPENDIX C

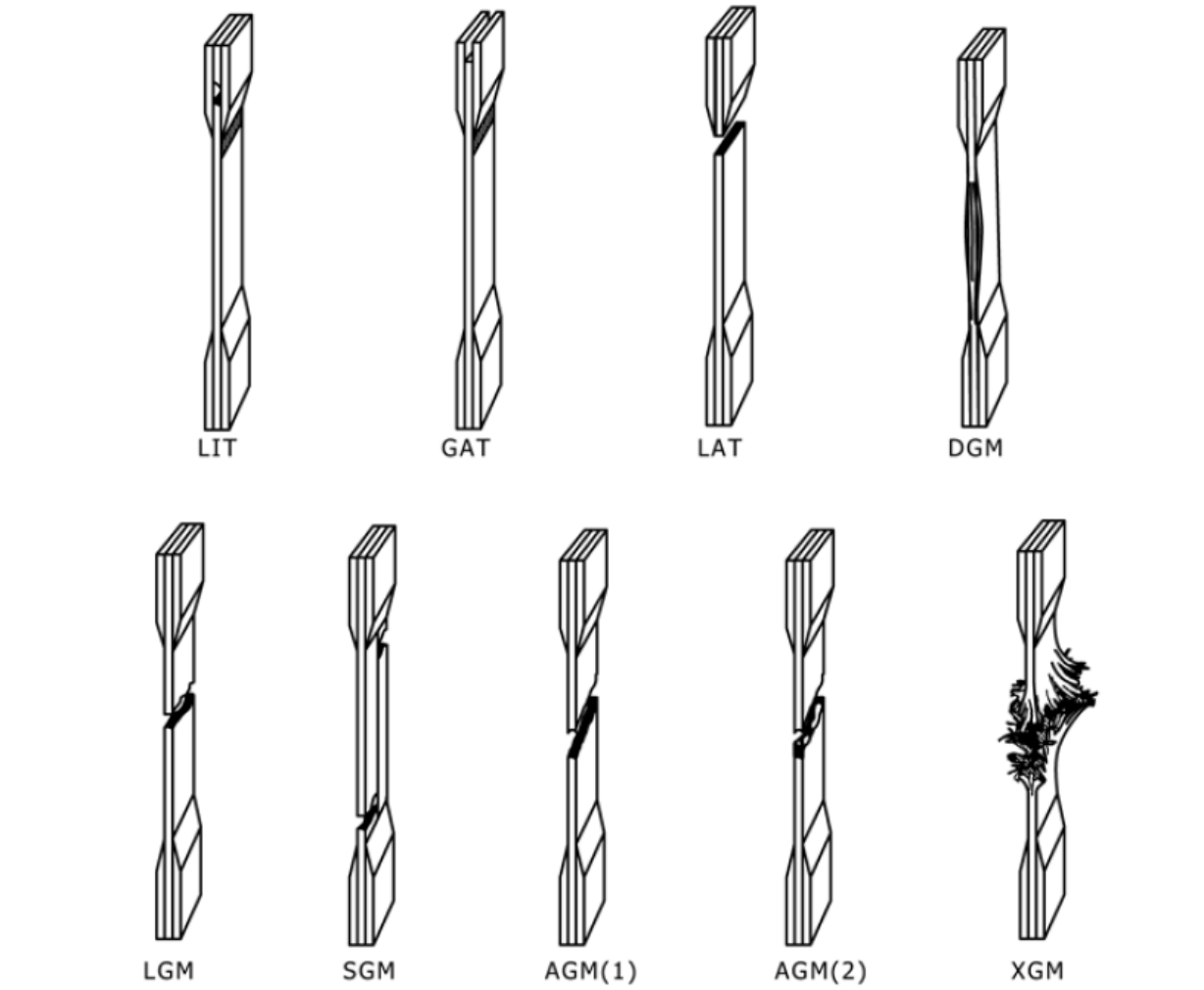

First Character

Failure Type	Code
Angled	A
edge Delamination	D
Grip/tab	G
Lateral	L
Multi-mode	M(xyz)
long. Splitting	S
eXplosive	X
Other	O

Second Character

Failure Area	Code
Inside grip/tab	I
At grip/tab	A
<1W from grip/tab	W
Gage	G
Multiple areas	M
Various	V
Unknown	U

Third Character

Failure Location	Code
Bottom	B
Top	T
Left	L
Right	R
Middle	M
Various	V
Unknown	U

Figure C-1. Tensile failure codes and typical failure modes taken from the D3039-14 standard [161].

Table C-1. D3039-14 results summary for M23 specimens.

	t [mm]	w [mm]	F^{tu} [MPa]	E^{chord} [GPa]	ν [-]	Failure Mode
Specimen 1	2.56	25.34	87.24	37.50	0.32	LGB
Specimen 2	2.51	25.31	88.36	34.38	0.30	AGM
Specimen 3	2.70	25.00	66.80	n/a	n/a	AGB
Specimen 4	2.69	25.20	66.50	35.94	0.35	AGT
Specimen 5	2.53	25.34	68.30	35.29	0.26	AGT
Specimen 6	2.59	24.99	88.08	33.03	0.25	AGT

Table C-2. D3039-14 results summary for M26 specimens.

	t [mm]	w [mm]	F^{tu} [MPa]	E^{chord} [GPa]	ν [-]	Failure Mode
Specimen 1	2.77	25.37	61.76	29.88	0.31	AGM
Specimen 2	2.75	25.35	82.57	31.86	0.31	AGM
Specimen 3	2.73	25.28	94.94	33.07	0.32	AGM
Specimen 4	2.69	25.31	82.28	34.85	0.39	AGM
Specimen 5	2.66	25.23	59.45	35.05	0.38	AAB
Specimen 6	2.64	25.40	96.47	31.33	0.25	AGM

Table C-3. D3039-14 results summary for M34 specimens.

	t [mm]	w [mm]	F^{tu} [MPa]	E^{chord} [GPa]	ν [-]	Failure Mode
Specimen 1	2.62	25.03	207.32	39.36	N/A	AGT
Specimen 2	2.62	25.01	174.75	40.82	N/A	M(DX)MV
Specimen 3	2.61	25.03	149.61	52.92	0.48	AWT
Specimen 4	2.60	25.08	97.91	54.50	0.56	LAV
Specimen 5	2.58	25.03	196.14	70.25	0.57	LWT
Specimen 6	2.56	24.93	168.77	58.47	0.55	AWT

Table C-4. D3039-14 results summary for M40 specimens.

	t [mm]	w [mm]	F^{tu} [MPa]	E^{chord} [GPa]	ν [-]	Failure Mode
Specimen 1	2.69	25.03	142.16	58.94	0.50	AGM
Specimen 2	2.70	25.03	139.19	60.48	0.52	LWT
Specimen 3	2.71	25.07	117.64	44.27	0.36	AGT
Specimen 4	2.70	25.07	131.64	51.74	0.46	LGT
Specimen 5	2.66	25.07	166.64	45.73	0.38	LGM
Specimen 6	2.65	25.02	119.05	63.56	0.44	LGT

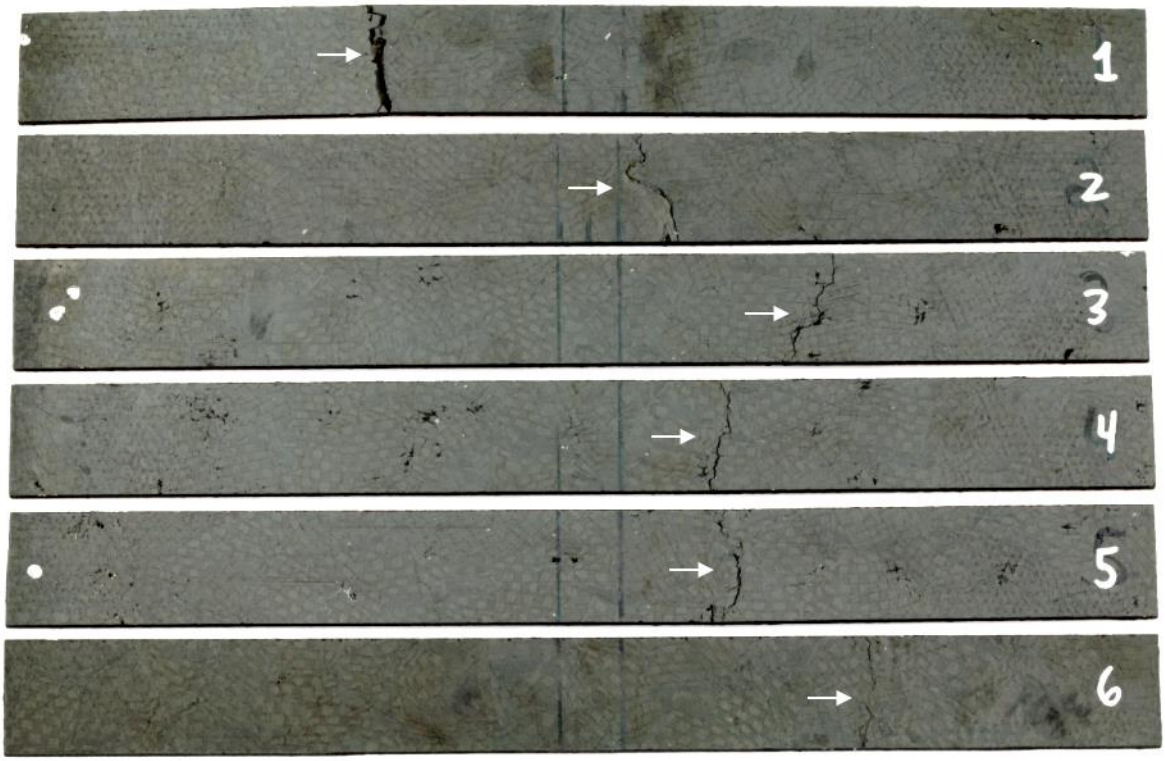

Figure C-2. Picture of tested M23 specimens; white arrows indicate the location of failure.

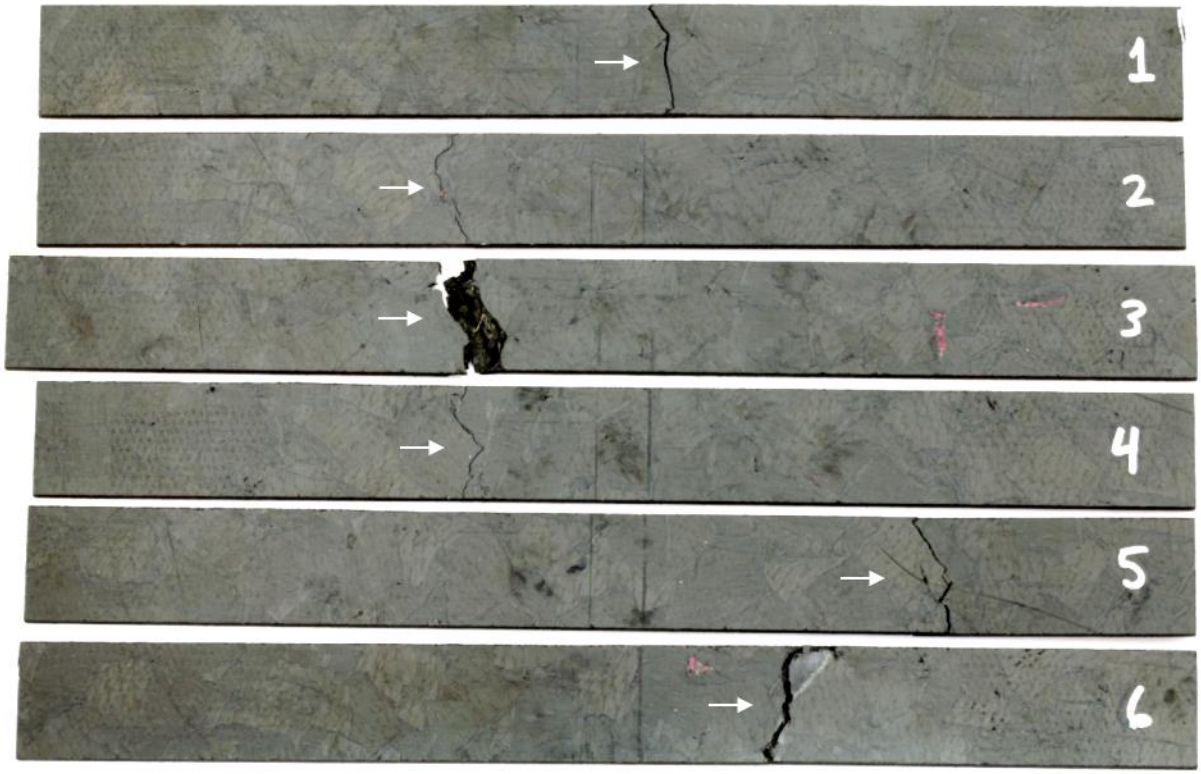

Figure C-3. Picture of tested M26 specimens; white arrows indicate the location of failure.

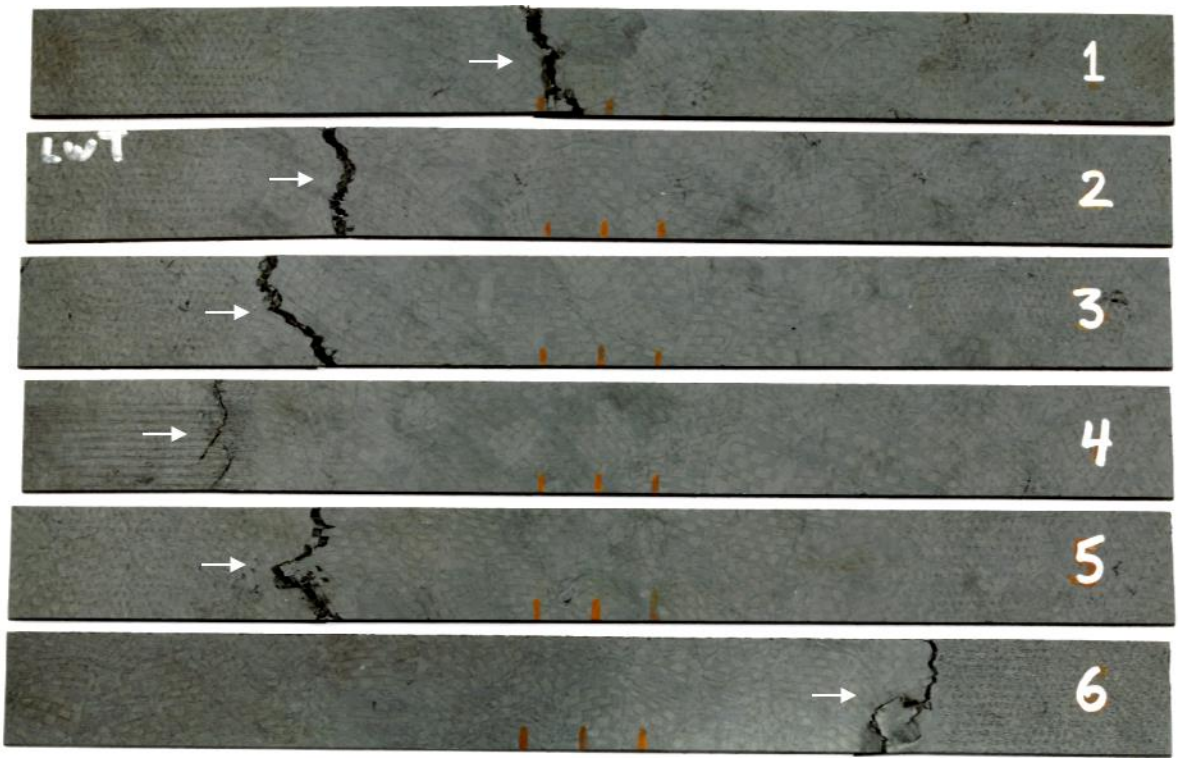

Figure C-4. Picture of tested M34 specimens; white arrows indicate the location of failure.

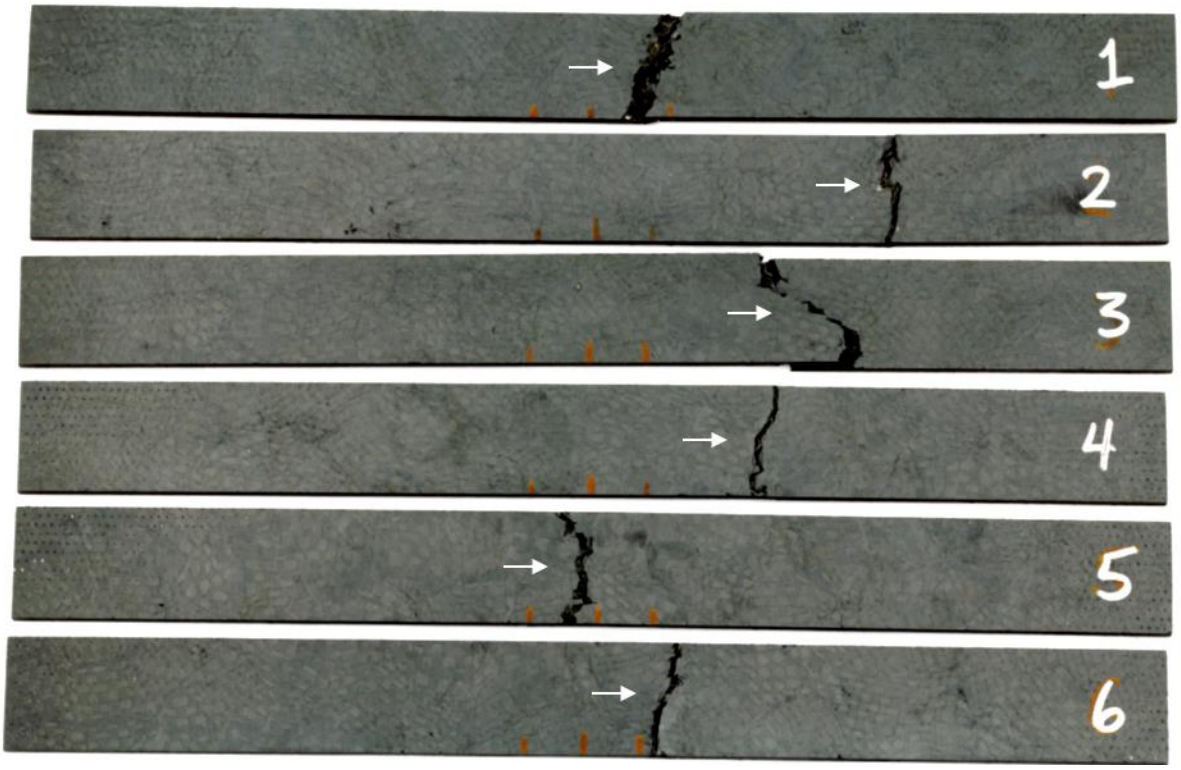

Figure C-5. Picture of tested M40 specimens; white arrows indicate the location of failure.

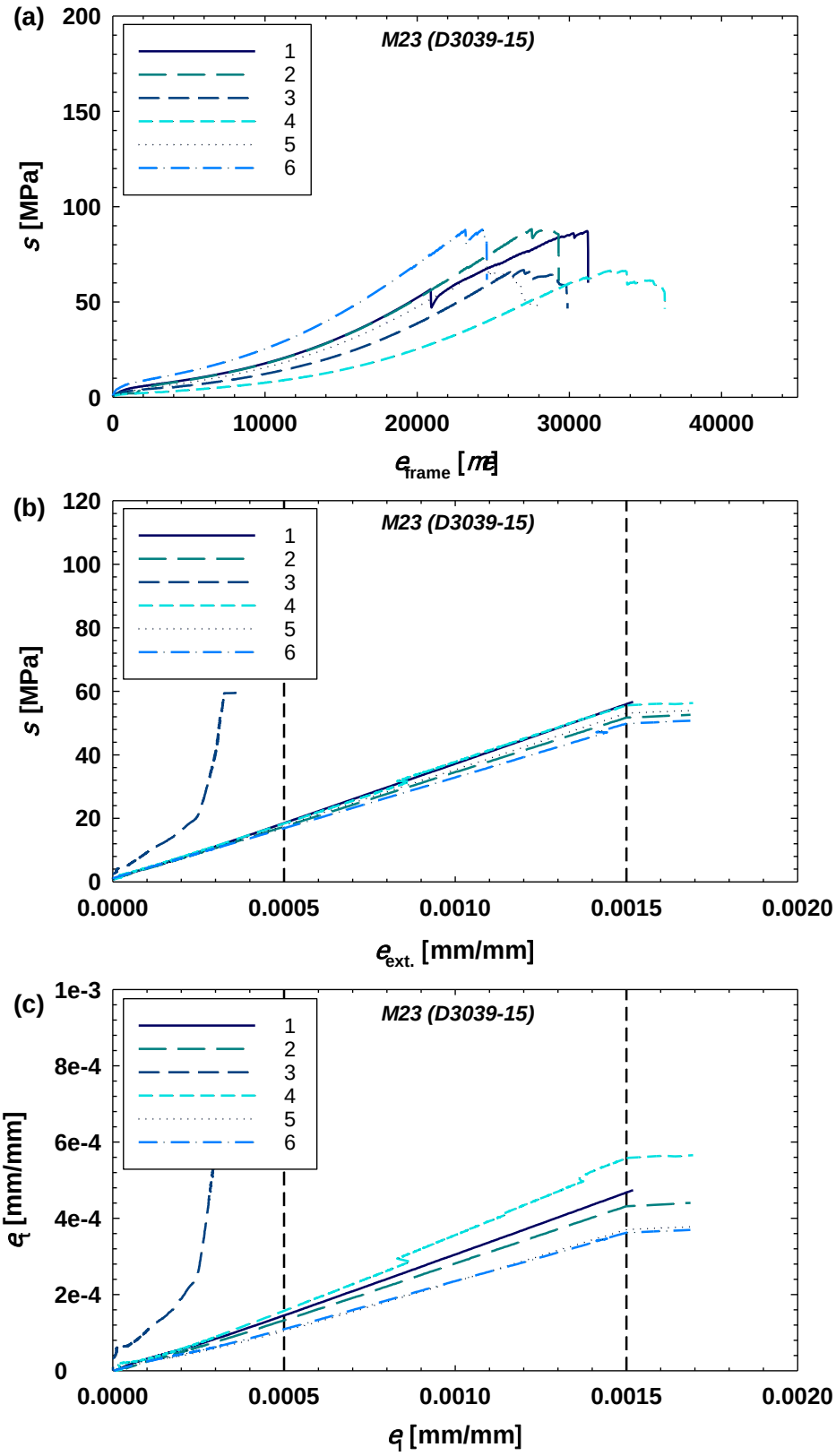

Figure C-6. Stress vs. frame strain (a), stress vs. extensometer strain (b), and longitudinal strain vs. transverse strain (c) for M23 specimens.

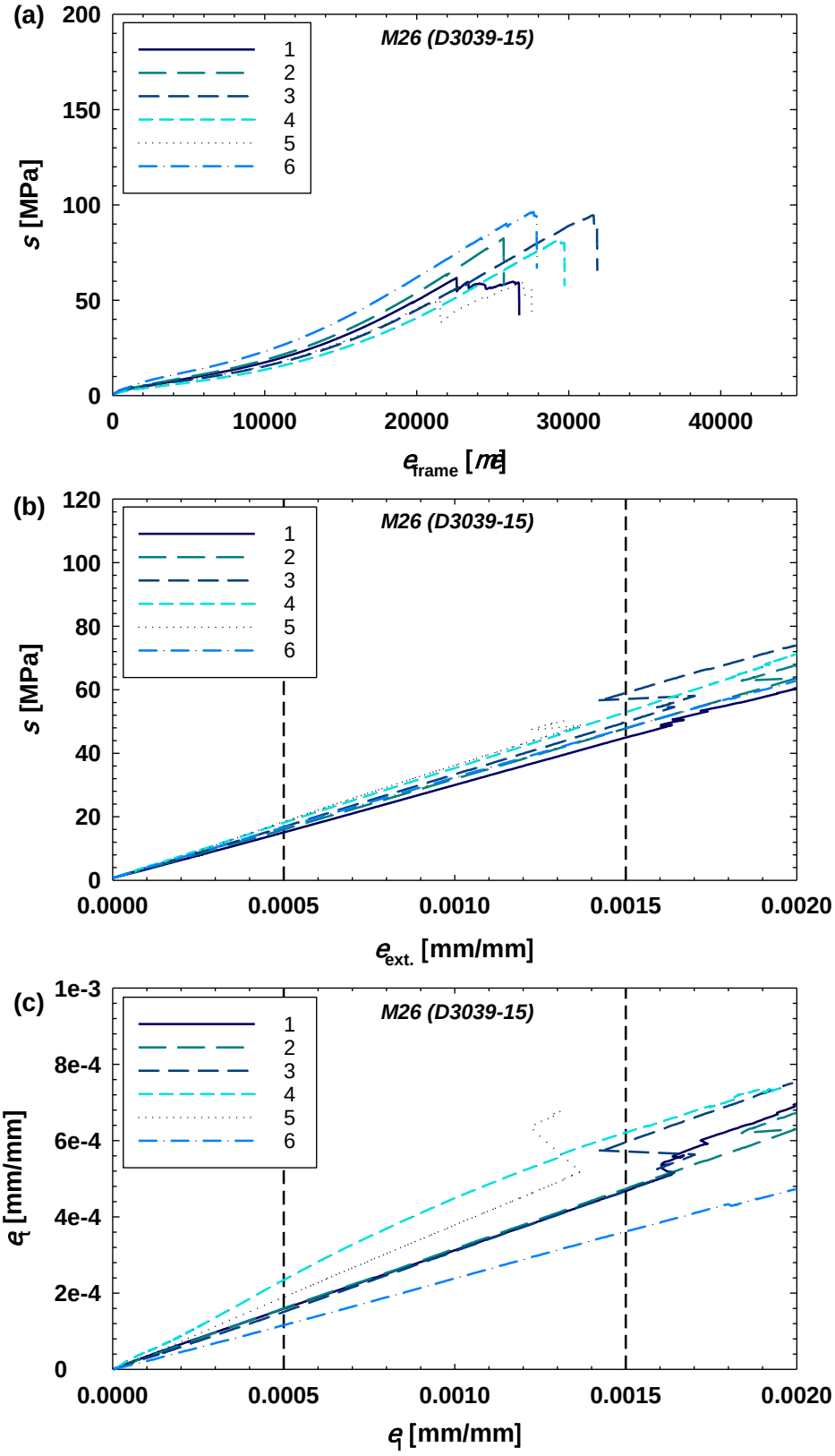

Figure C-7. Stress vs. frame strain (a), stress vs. extensometer strain (b), and longitudinal strain vs. transverse strain (c) for M26 specimens.

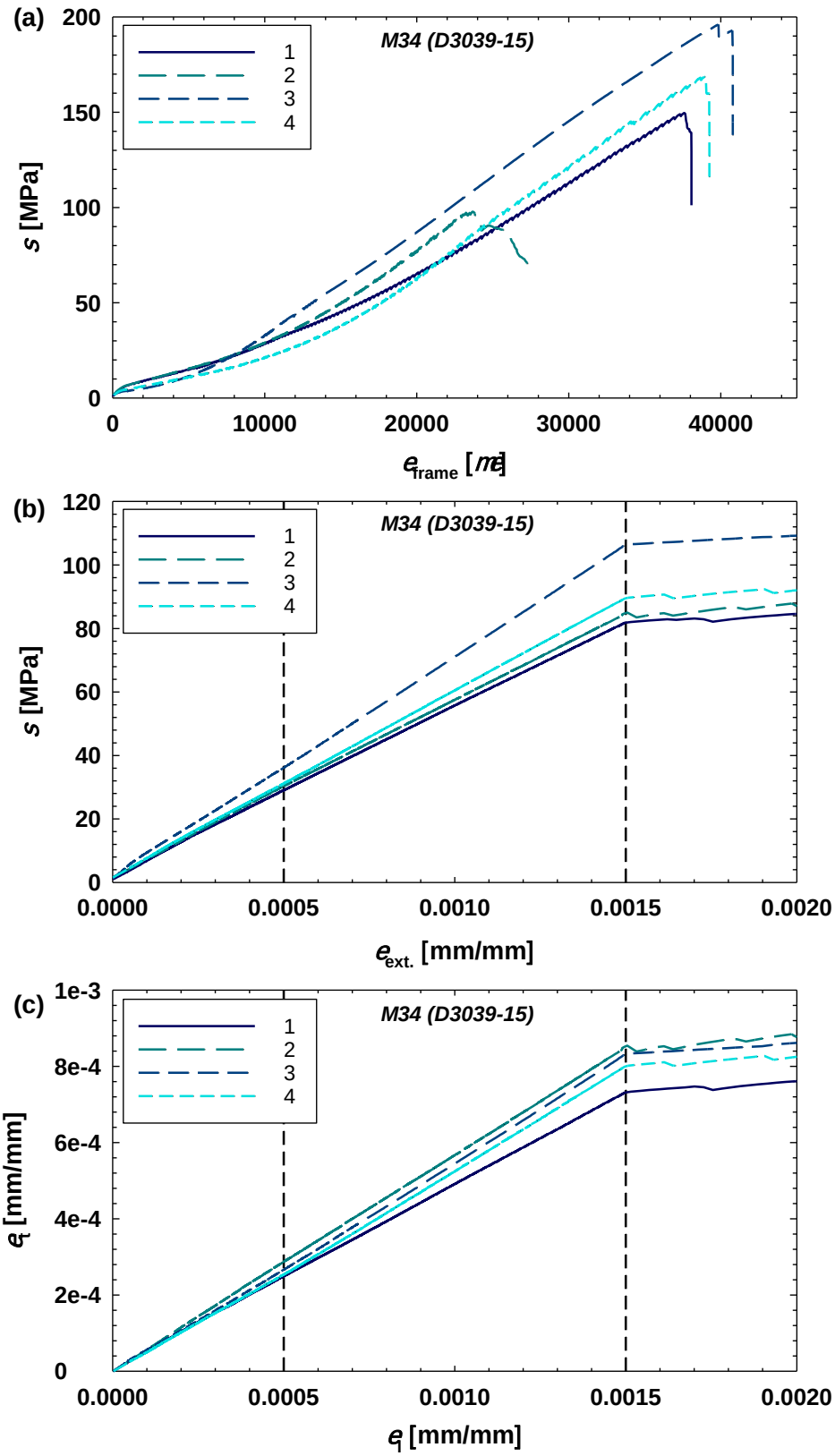

Figure C-8. Stress vs. frame strain (a), stress vs. extensometer strain (b), and longitudinal strain vs. transverse strain (c) for M34 specimens.

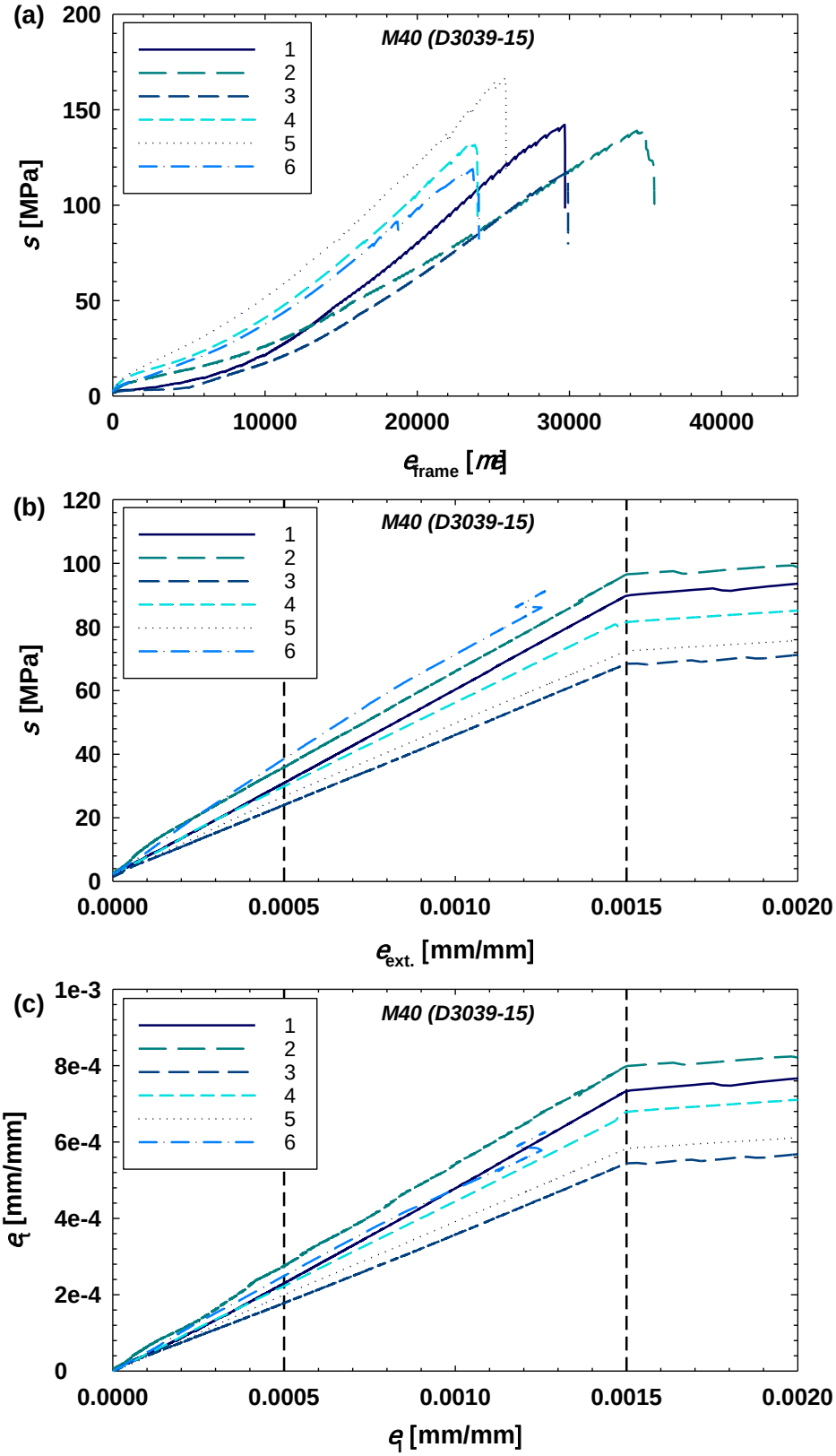

Figure C-9. Stress vs. frame strain (a), stress vs. extensometer strain (b), and longitudinal strain vs. transverse strain (c) for M40 specimens.

APPENDIX D

Table D-1. D790-17 results summary for M23 specimens; span = 42 mm.

	t [mm]	w [mm]	σ_{fM} [MPa]	ε_{fM} [mm/mm]	E_B [GPa]	Failure Mode
Specimen 1	2.62	13.17	501.42	0.0187	30.75	Tensile Break
Specimen 2	2.65	13.31	244.39	0.0141	30.14	Tensile Break
Specimen 3	2.70	13.39	606.35	0.0175	39.01	Tensile Break
Specimen 4	2.62	13.12	520.21	0.0176	33.91	Tensile Break
Specimen 5	2.62	13.12	214.94	0.0160	27.21	Tensile Break
Specimen 6	2.66	13.02	500.73	0.0181	34.53	Tensile Break

Table D-2. D790-17 results summary for M26 specimens; span = 40 mm.

	t [mm]	w [mm]	σ_{fM} [MPa]	ε_{fM} [mm/mm]	E_B [GPa]	Failure Mode
Specimen 1	2.47	13.05	499.21	0.0195	31.45	Tensile Break
Specimen 2	2.53	13.02	282.88	0.0103	30.04	Tensile Break
Specimen 3	2.48	13.19	328.36	0.0217	27.89	Tensile & Compressive Break
Specimen 4	2.41	13.20	226.28	0.0111	26.03	Tensile Break
Specimen 5	2.41	13.20	184.41	0.0214	37.10	Tensile Break
Specimen 6	2.51	13.09	242.50	0.0183	20.94	Tensile Break

Table D-3. D790-17 results summary for M34 specimens; span = 42 mm.

	t [mm]	w [mm]	σ_{fM} [MPa]	ε_{fM} [mm/mm]	E_B [GPa]	Failure Mode
Specimen 1	2.63	13.20	571.86	0.0194	35.26	Tensile Break
Specimen 2	2.62	13.20	587.58	0.0198	33.00	Tensile Break
Specimen 3	2.63	13.21	544.37	0.0165	36.37	Tensile Break
Specimen 4	2.62	13.16	558.86	0.0161	37.90	Tensile Break
Specimen 5	2.64	13.03	538.86	0.0191	32.78	Tensile Break
Specimen 6	2.64	13.17	570.00	0.0201	33.49	Tensile Break
Specimen 7	2.61	13.23	497.88	0.0162	37.34	Tensile Break
Specimen 8	2.61	13.21	617.16	0.0184	39.69	Tensile Break
Specimen 9	2.65	13.16	502.98	0.0177	34.74	Tensile Break
Specimen 10	2.65	13.22	579.89	0.0228	33.43	Tensile Break

Table D-4. D790-17 results summary for M40 specimens; span = 40 mm.

	t [mm]	w [mm]	σ_{fM} [MPa]	ε_{fM} [mm/mm]	E_B [GPa]	Failure Mode
Specimen 1	2.59	13.16	232.64	0.0095	24.93	Tensile Break
Specimen 2	2.52	13.16	500.25	0.0172	39.54	Tensile Break
Specimen 3	2.62	13.16	449.30	0.0212	27.87	Tensile Break
Specimen 4	2.48	13.03	386.01	0.0126	34.22	Tensile Break
Specimen 5	2.58	13.18	263.28	0.0097	30.43	Tensile Break
Specimen 6	2.54	13.16	580.00	0.0183	39.64	Tensile Break
Specimen 7	2.58	13.20	305.04	0.0144	28.09	Tensile Break
Specimen 8	2.47	13.14	461.04	0.0182	32.39	Tensile Break
Specimen 9	2.61	13.13	285.66	0.0121	29.48	Tensile Break
Specimen 10	2.55	13.16	564.63	0.0189	34.04	Tensile Break

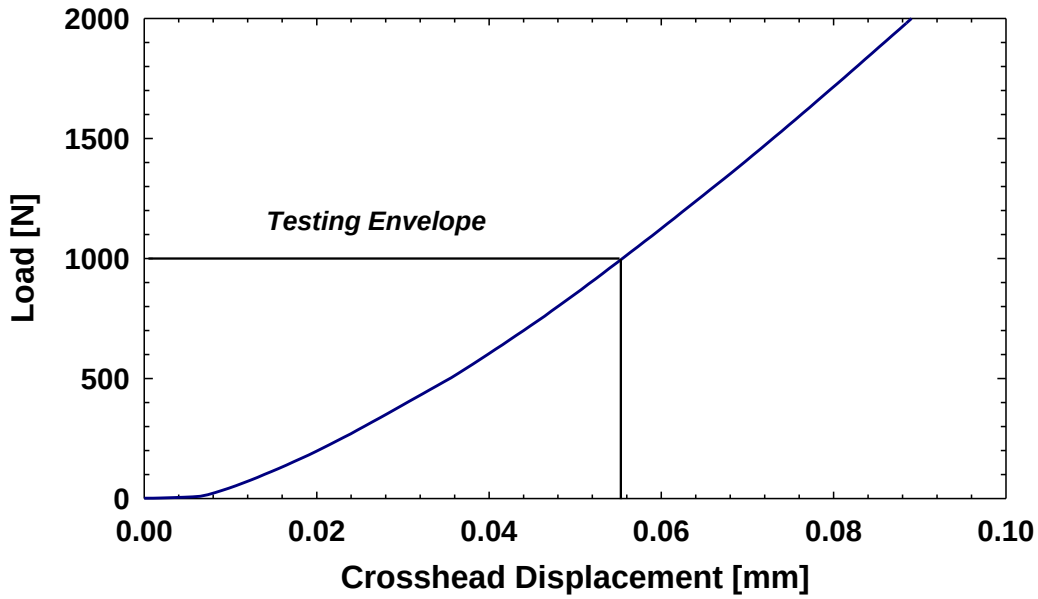

Figure D-1. Flexural compliance curve generated using a steel specimen measuring 12.5 mm by 87.5 mm with a 50 mm span. The blue region corresponds to the forces observed during specimen testing.

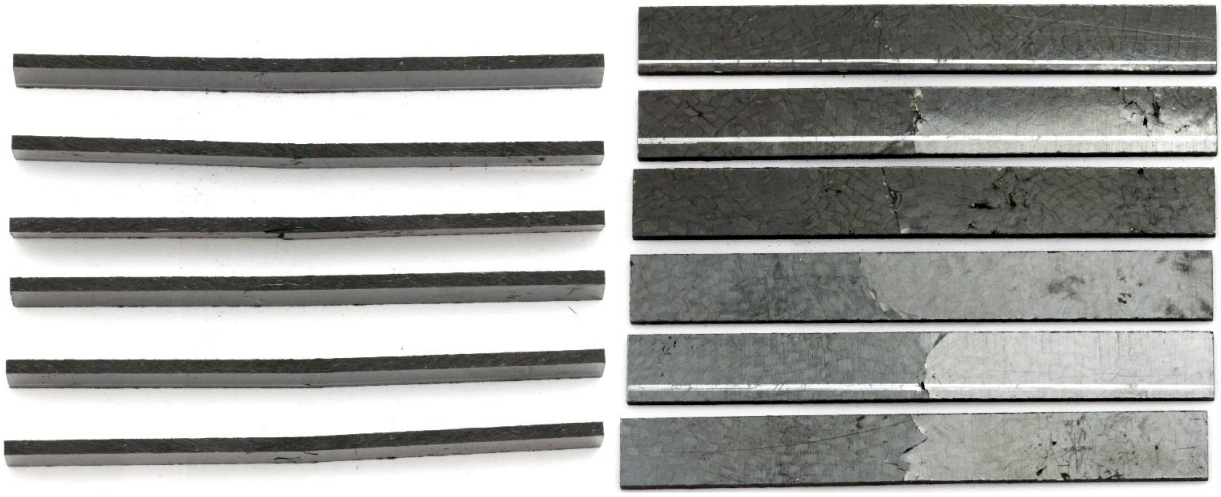

Figure D-2. M23 Side view (left) and bottom view (right) 1-6 (top-bottom).

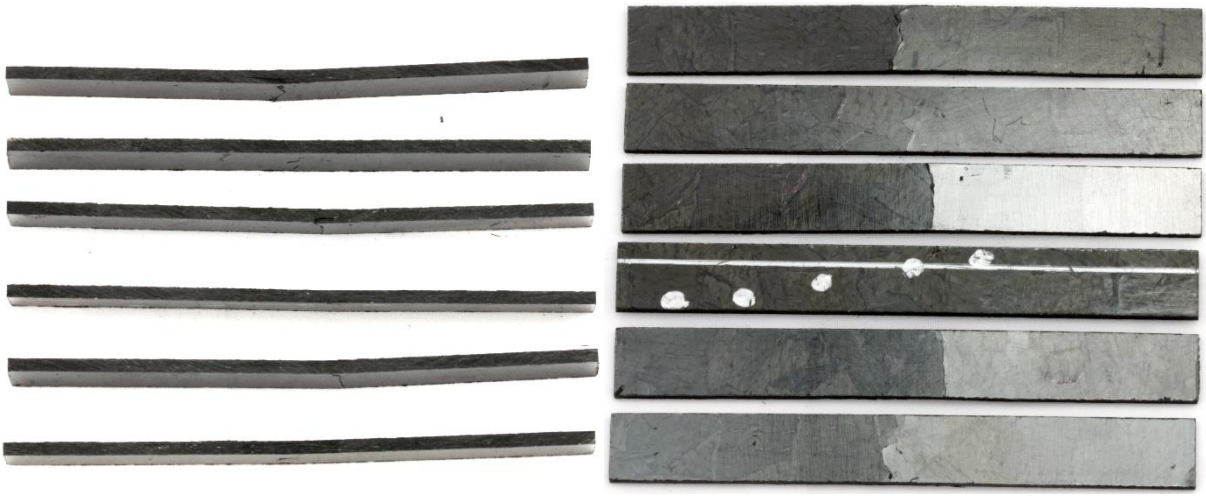

Figure D-3. M26 Side view (left) and bottom view (right) 1-6 (top-bottom).

Figure D-4. M34 Side view (left) and bottom view (right) 1-10 (top-bottom).

Figure D-5. M40 Side view (left) and bottom view (right) 1-10 (top-bottom).

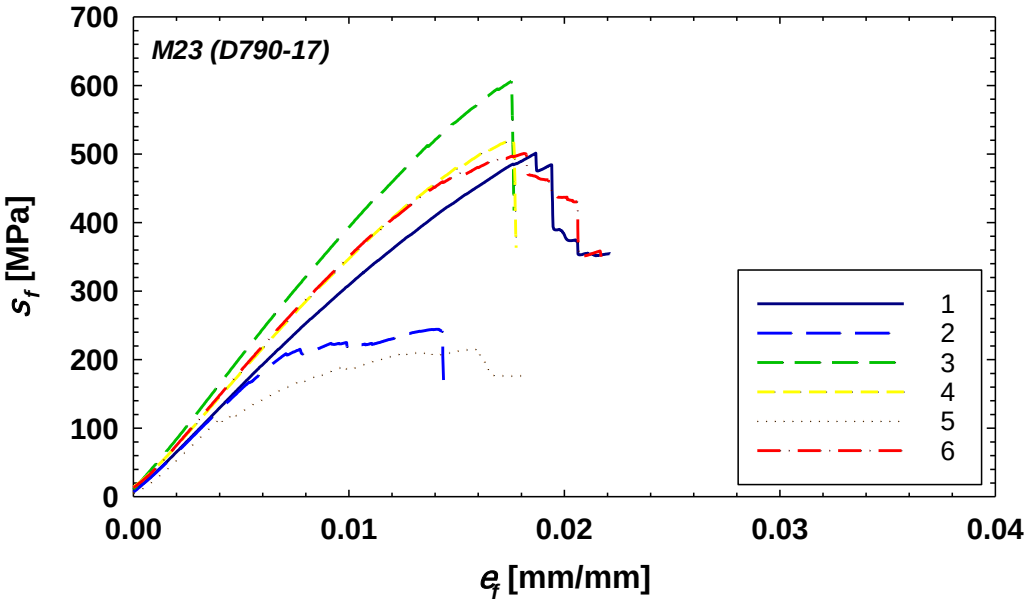

Figure D-6. Measured flexural stress versus compliance corrected flexural strain for M23 specimens.

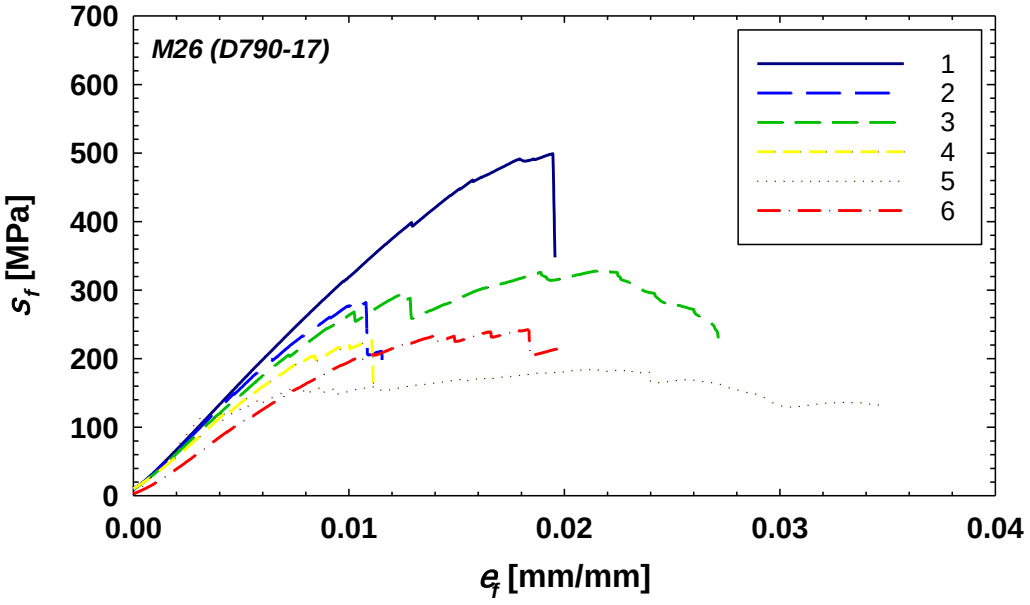

Figure D-7. Measured flexural stress versus compliance corrected flexural strain for M26 specimens.

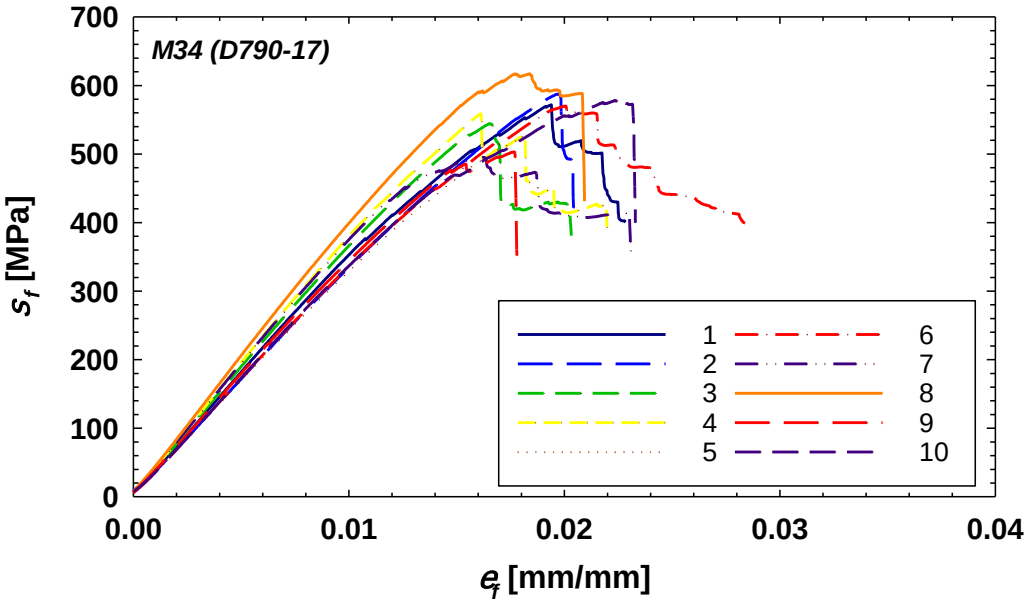

Figure D-8. Measured flexural stress versus compliance corrected flexural strain for M34 specimens.

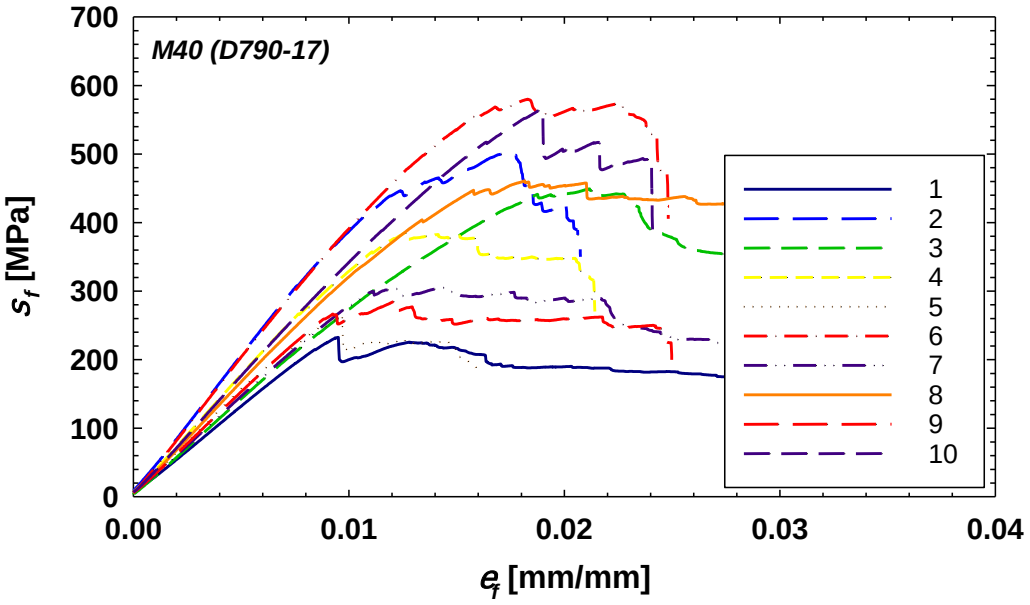

Figure D-9. Measured flexural stress versus compliance corrected flexural strain for M40 specimens.

APPENDIX E

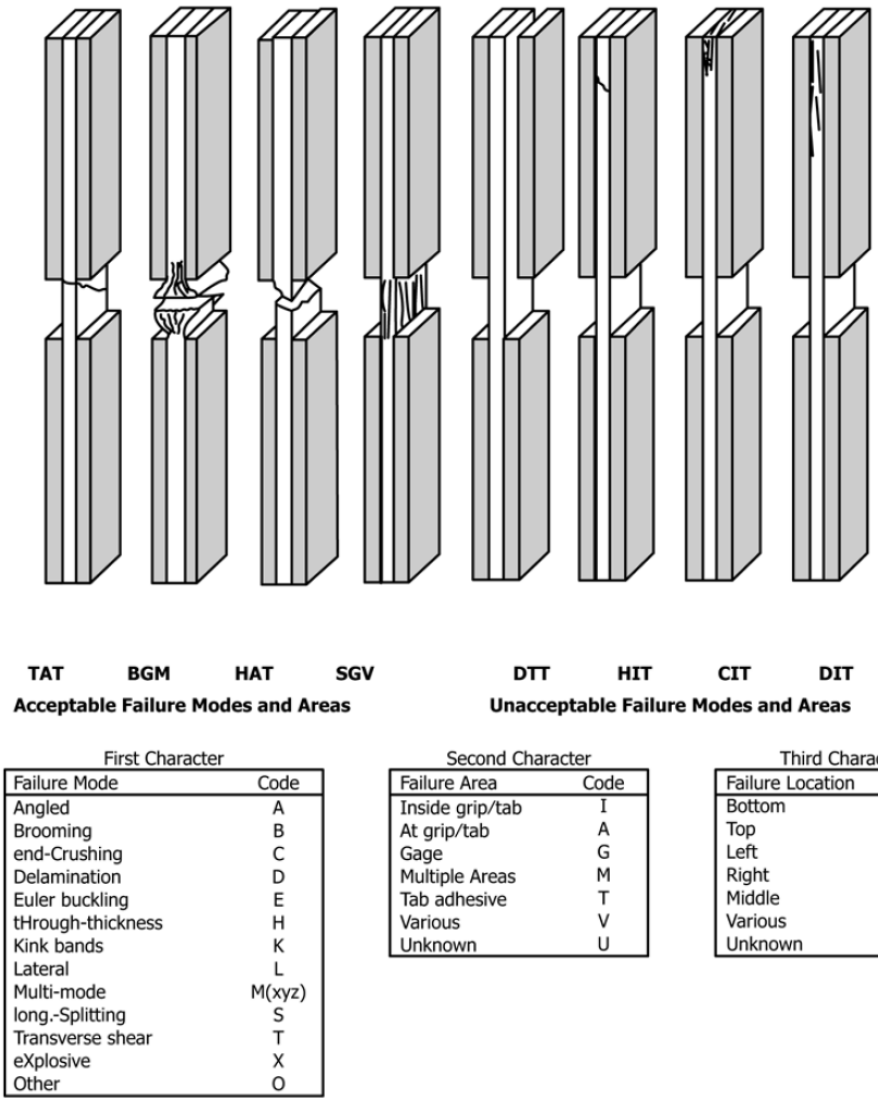

First Character

Failure Mode	Code
Angled	A
Brooming	B
end-Crushing	C
Delamination	D
Euler buckling	E
tHrough-thickness	H
Kink bands	K
Lateral	L
Multi-mode	M(xyz)
long.-Splitting	S
Transverse shear	T
eXplosive	X
Other	O

Second Character

Failure Area	Code
Inside grip/tab	I
At grip/tab	A
Gage	G
Multiple Areas	M
Tab adhesive	T
Various	V
Unknown	U

Third Character

Failure Location	Code
Bottom	B
Top	T
Left	L
Right	R
Middle	M
Various	V
Unknown	U

Figure E-1. Compressive failure codes and typical failure modes taken from the D6641-14 standard [163].

Table E-1. D6641-14 results summary for M23 specimens.

	t [mm]	w [mm]	l_{gauge} [mm]	P_f [kN]	F^{cu} [MPa]	Failure Mode
Specimen 1	2.71	13.15	10.50	11.73	329.5	M(ADH)GV
Specimen 2	2.65	13.19	11.45	11.16	319.1	M(ADH)GV
Specimen 3	2.67	13.23	12.04	8.34	235.9	M(AH)GV
Specimen 4	2.70	13.09	10.01	12.83	363.6	M(ABDH)GV
Specimen 5	2.66	13.23	11.81	10.43	295.9	M(AH)AB
Specimen 6	2.64	12.97	11.44	10.36	302.7	M(AD)VB

Table E-2. D6641-14 results summary for M26 specimens.

	t [mm]	w [mm]	l_{gauge} [mm]	P_f [kN]	F^{cu} [MPa]	Failure Mode
Specimen 1	2.56	13.25	12.35	7.79	229.3	M(AH)GT
Specimen 2	2.59	13.03	12.74	9.23	273.7	M(AB)GV
Specimen 3	2.50	13.74	12.49	7.50	218.6	AMB
Specimen 4	2.58	12.99	12.46	10.37	309.2	M(AB)AB
Specimen 5	2.56	12.95	12.50	8.16	245.7	M(AH)MB
Specimen 6	2.60	12.89	13.03	8.63	257.2	M(AH)VB

Table E-3. D6641-14 results summary for M34 specimens.

	t [mm]	w [mm]	l_{gauge} [mm]	P_f [kN]	F^{cu} [MPa]	Failure Mode
Specimen 1	2.73	13.17	13.13	11.99	333.5	M(AHS)GV
Specimen 2	2.75	13.14	13.12	8.68	240.3	AAB
Specimen 3	2.73	13.16	13.19	9.53	265.3	M(AHS)GV
Specimen 4	2.74	13.12	13.04	10.56	294.3	M(AHS)GV
Specimen 5	2.73	13.17	13.11	10.22	284.2	M(AHS)GV
Specimen 6	2.74	13.18	12.99	10.64	295.0	M(AHS)GV
Specimen 7	2.72	13.18	13.08	7.81	217.8	AAT
Specimen 8	2.73	13.14	12.96	9.01	251.4	M(AHS)GV

Table E-4. D6641-14 results summary for M40 specimens.

	t [mm]	w [mm]	l_{gauge} [mm]	P_f [kN]	F^{cu} [MPa]	Failure Mode
Specimen 1	2.61	13.23	13.05	13.55	391.9	1st - HIT, 2nd - HIB, 3rd - M(AHS)GV
Specimen 2	2.56	13.13	13.10	9.67	288.1	M(AHS)GV
Specimen 3	2.58	13.19	12.99	11.22	329.1	M(HS)GV
Specimen 4	2.54	13.18	13.12	9.80	292.9	M(HS)GV
Specimen 5	2.60	13.19	13.02	10.15	296.3	M(HS)GV
Specimen 6	2.59	13.20	13.02	7.97	233.0	M(AH)GV
Specimen 7	2.58	13.13	13.11	9.52	281.5	M(AH)GT
Specimen 8	2.60	13.16	12.97	9.62	281.0	M(AH)GV
Specimen 9	2.56	13.22	13.14	10.98	324.5	M(AHS)GV

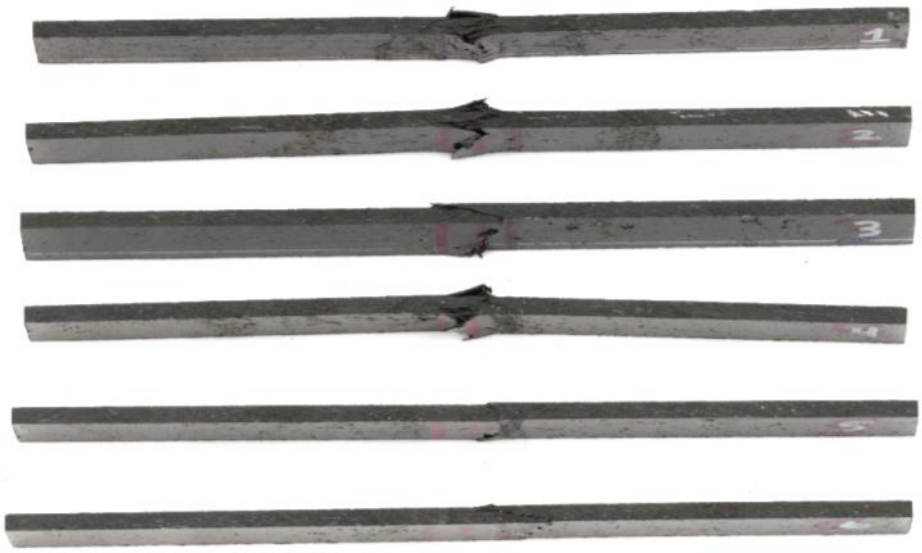

Figure E-2. M23 D6641-14 Compression Specimens 1-6 (top-bottom).

Figure E-3. M26 D6641-14 Compression specimens 1-6 (top-bottom).

Figure E-4. M34 D6641-14 Compression specimens 1-8 (top-bottom).

Figure E-5. M40 D6641-14 Compression specimens 1-9 (top-bottom).

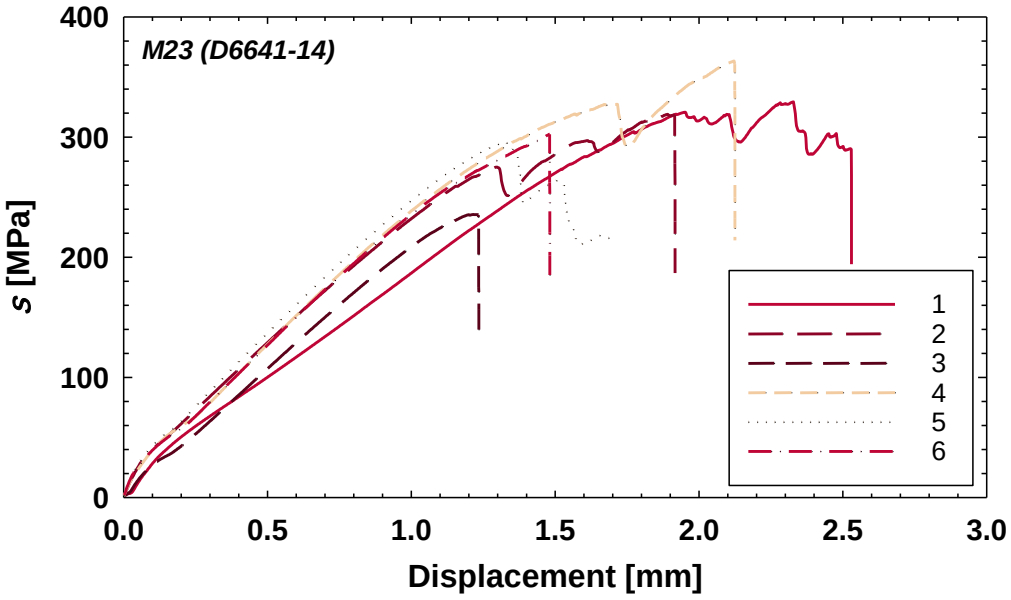

Figure E-6. Measured compressive stress versus displacement for M23 specimens.

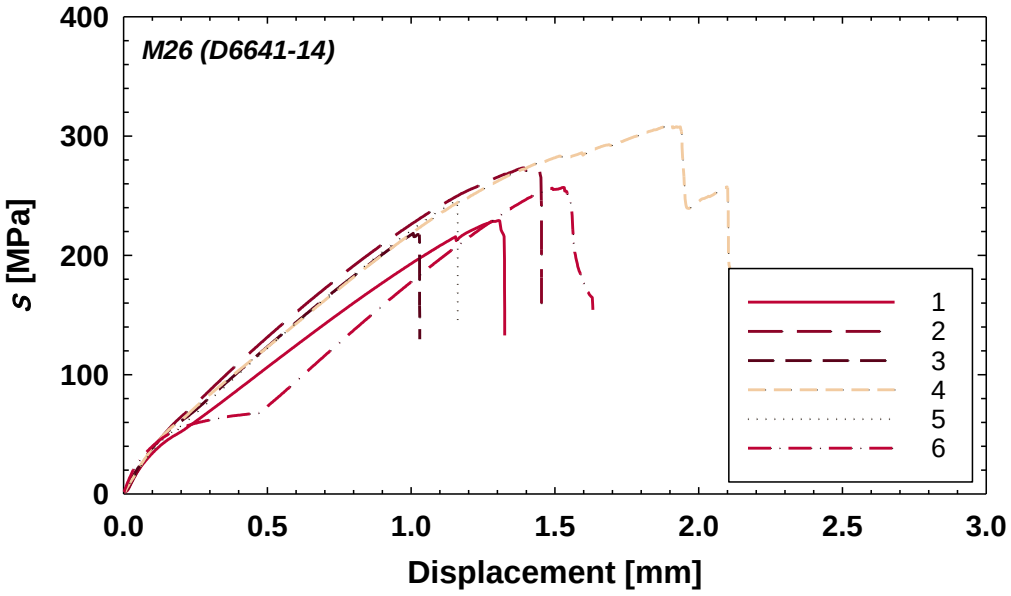

Figure E-7. Measured compressive stress versus displacement for M26 specimens.

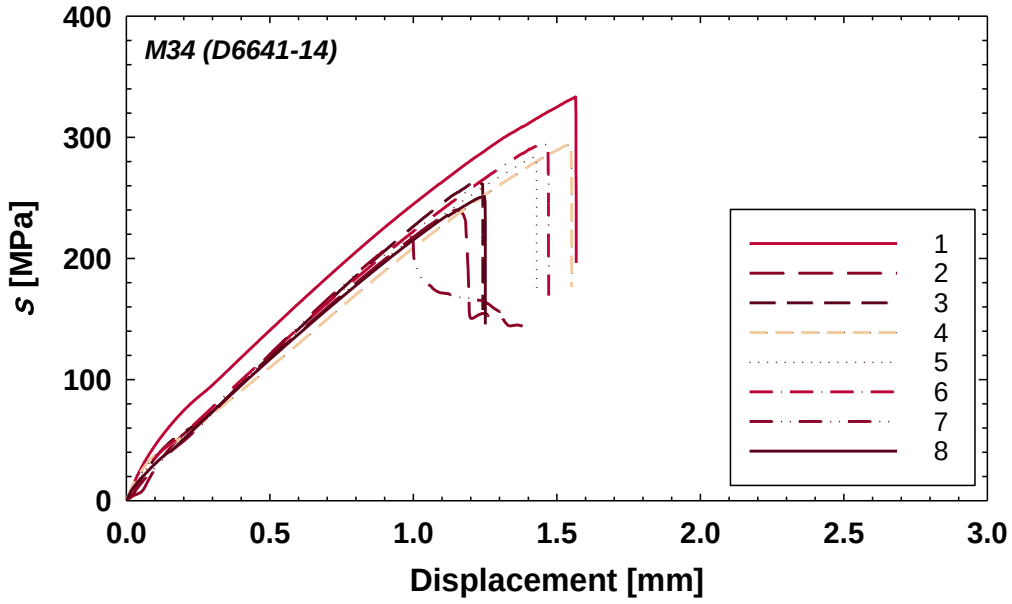

Figure E-8. Measured compressive stress versus displacement for M34 specimens.

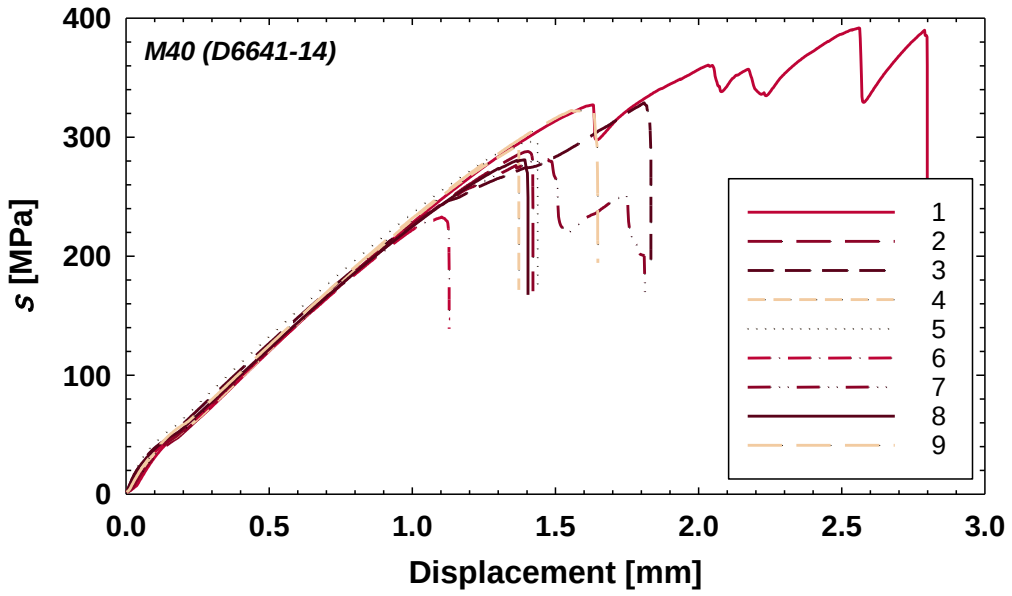

Figure E-9. Measured compressive stress versus displacement for M40 specimens.

APPENDIX F

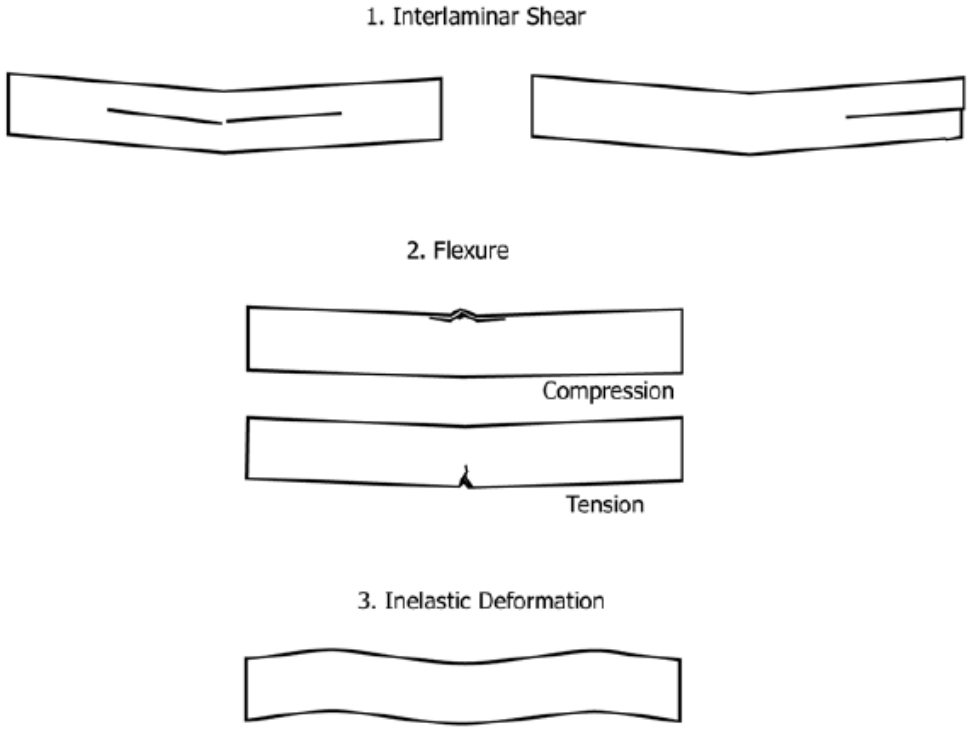

Figure F-1. Typical failure modes in the Short-Beam test: interlaminar shear (ILS), tension (T), compression (C) and inelastic deformation (ID) [74].

Table F-1. D2344-13 results summary for M23 specimens.

	t [mm]	w [mm]	P_m [N]	F^{sbs} [MPa]	Failure Mode
Specimen 1	2.80	5.04	822	43.7	T
Specimen 2	2.73	5.13	1346	72.0	T
Specimen 3	2.75	5.21	1356	71.0	C
Specimen 4	2.69	5.08	1382	76.0	C
Specimen 5	2.72	5.25	959	50.3	T
Specimen 6	2.75	5.11	1210	64.6	C
Specimen 7	2.70	4.89	1423	81.0	T
Specimen 8	2.66	5.01	1169	65.9	ILS
Specimen 9	2.96	5.11	301	14.9	T
Specimen 10	2.67	5.29	698	37.1	T

Table F-2. D2344-13 results summary for M26 specimens.

	t [mm]	w [mm]	P_m [N]	F^{sbs} [MPa]	Failure Mode
Specimen 1	2.53	5.02	532	31.5	T
Specimen 2	2.54	4.88	515	31.2	T
Specimen 3	2.52	5.00	829	49.3	ILS
Specimen 4	2.54	4.91	761	45.8	T
Specimen 5	2.53	4.93	538	32.3	T
Specimen 6	2.54	4.96	723	43.0	T
Specimen 7	2.52	4.90	462	28.1	ILS
Specimen 8	2.54	4.95	392	23.4	T
Specimen 9	2.51	4.94	513	31.0	T
Specimen 10	2.50	4.94	846	51.3	T

Table F-3. D2344-13 results summary for M34 specimens.

	t [mm]	w [mm]	P_m [N]	F^{sbs} [MPa]	Failure Mode
Specimen 1	2.67	5.03	1407	78.7	ILS
Specimen 2	2.62	5.06	1198	67.8	T and ILS
Specimen 3	2.67	5.06	1294	71.8	T and ILS
Specimen 4	2.66	4.98	1327	75.1	T and ILS
Specimen 5	2.66	5.07	1099	61.1	ILS
Specimen 6	2.65	5.05	943	53.0	ILS
Specimen 7	2.61	5.01	1280	73.5	C, T, ILS
Specimen 8	2.67	5.05	1396	77.8	T and ILS
Specimen 9	2.60	5.06	1244	70.9	T and ILS
Specimen 10	2.65	5.04	1267	71.2	T and ILS

Table F-4. D2344-13 results summary for M40 specimens.

	t [mm]	w [mm]	P_m [N]	F^{sbs} [MPa]	Failure Mode
Specimen 1	2.65	5.24	1275	68.9	T and ILS
Specimen 2	2.59	5.23	1546	85.7	T and ILS
Specimen 3	2.60	5.26	1446	79.4	T and ILS
Specimen 4	2.62	5.28	1235	66.9	T and ILS
Specimen 5	2.63	5.27	1226	66.4	T and ILS
Specimen 6	2.66	5.25	1324	71.3	T and ILS
Specimen 7	2.68	5.34	1318	69.0	T and ILS
Specimen 8	2.58	5.22	1423	79.3	T and ILS
Specimen 9	2.65	5.27	1070	57.4	T and ILS
Specimen 10	2.70	5.23	1346	71.6	T and ILS

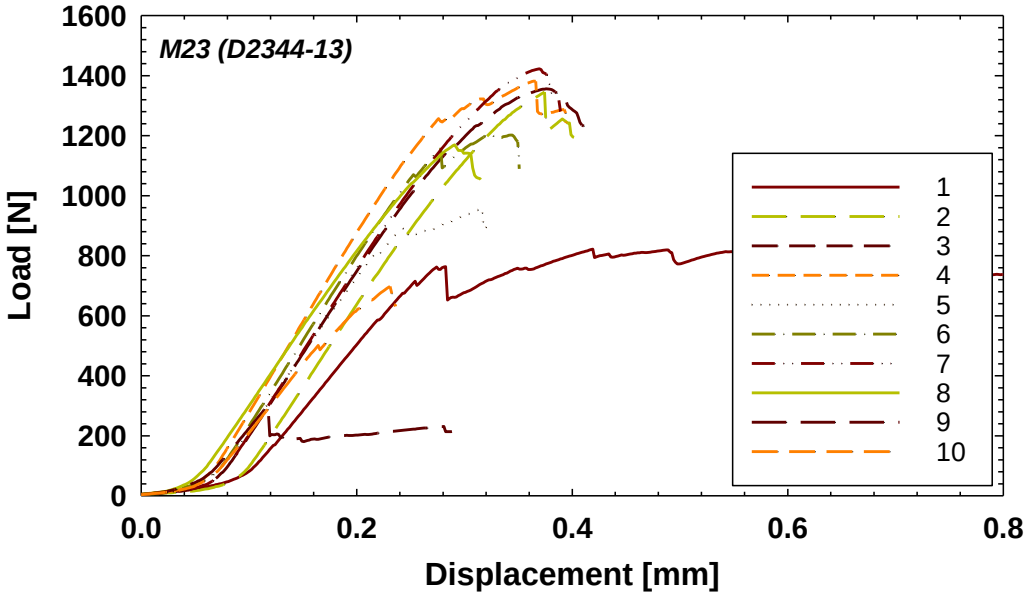

Figure F-2. Measured load versus displacement for M23 specimens.

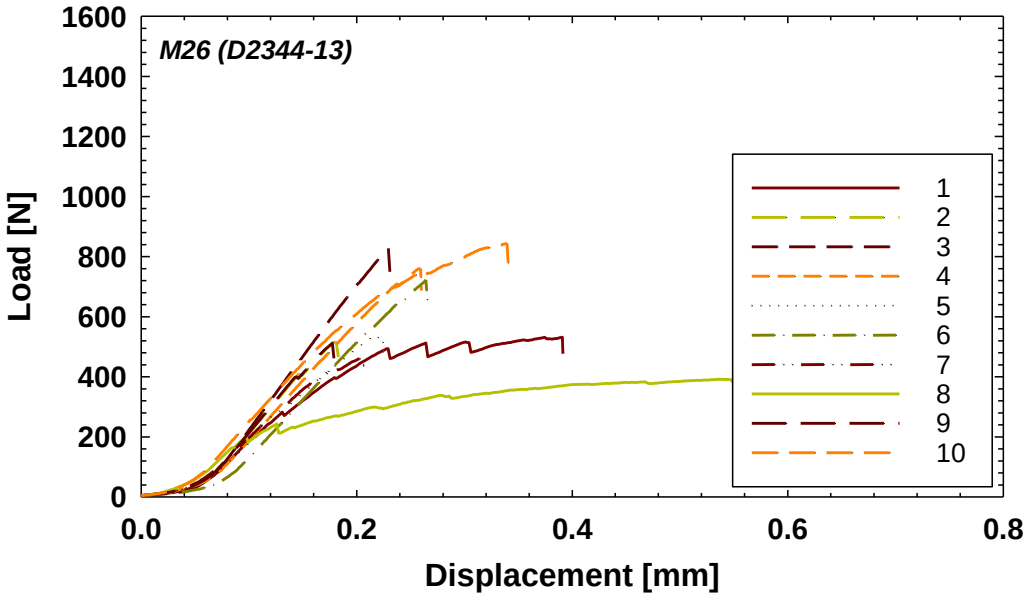

Figure F-3. Measured load versus displacement for M26 specimens.

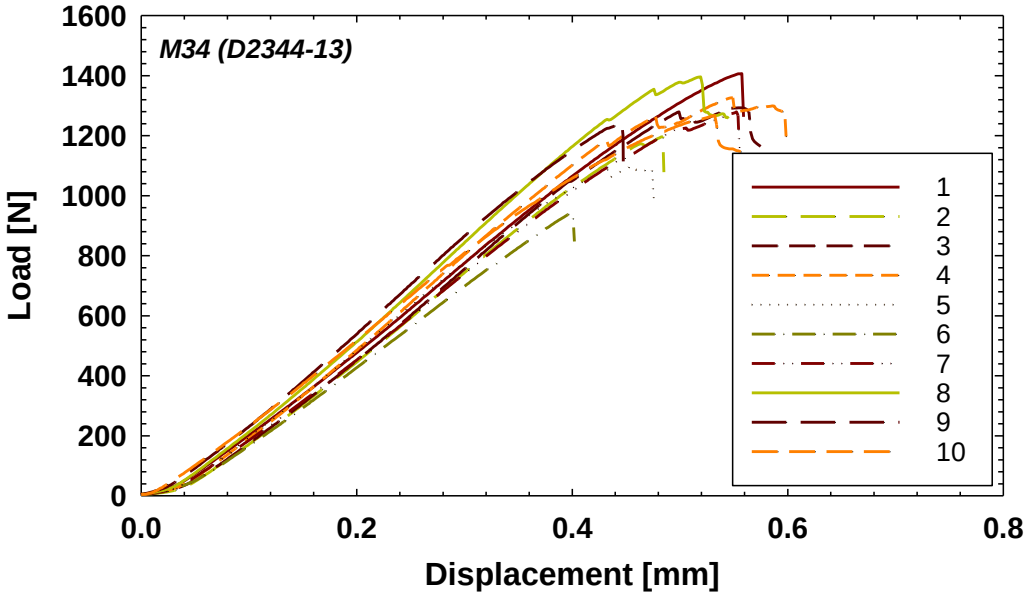

Figure F-4. Measured load versus displacement for M34 specimens.

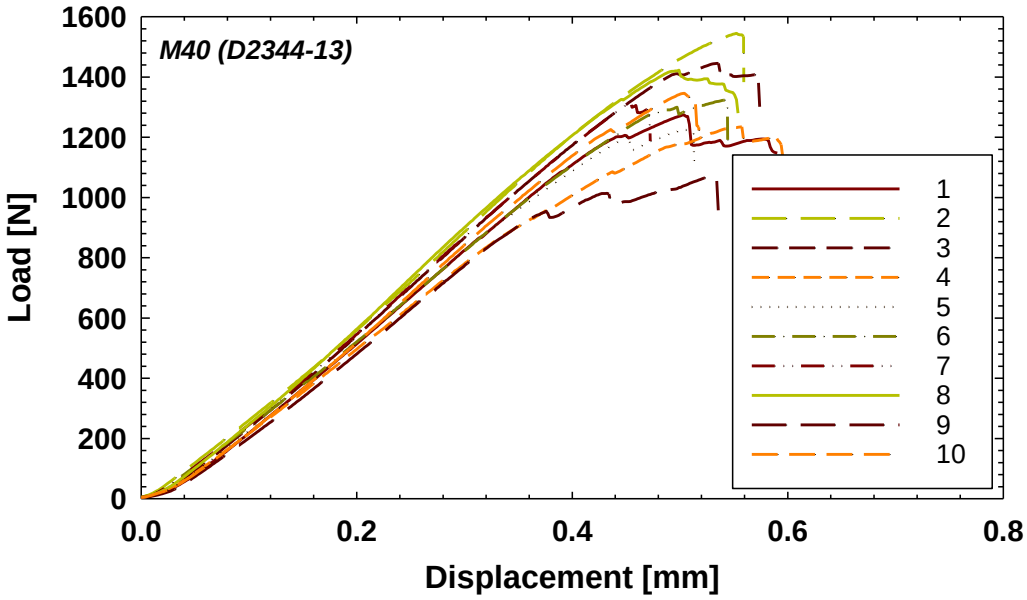

Figure F-5. Measured load versus displacement for M40 specimens.

APPENDIX G

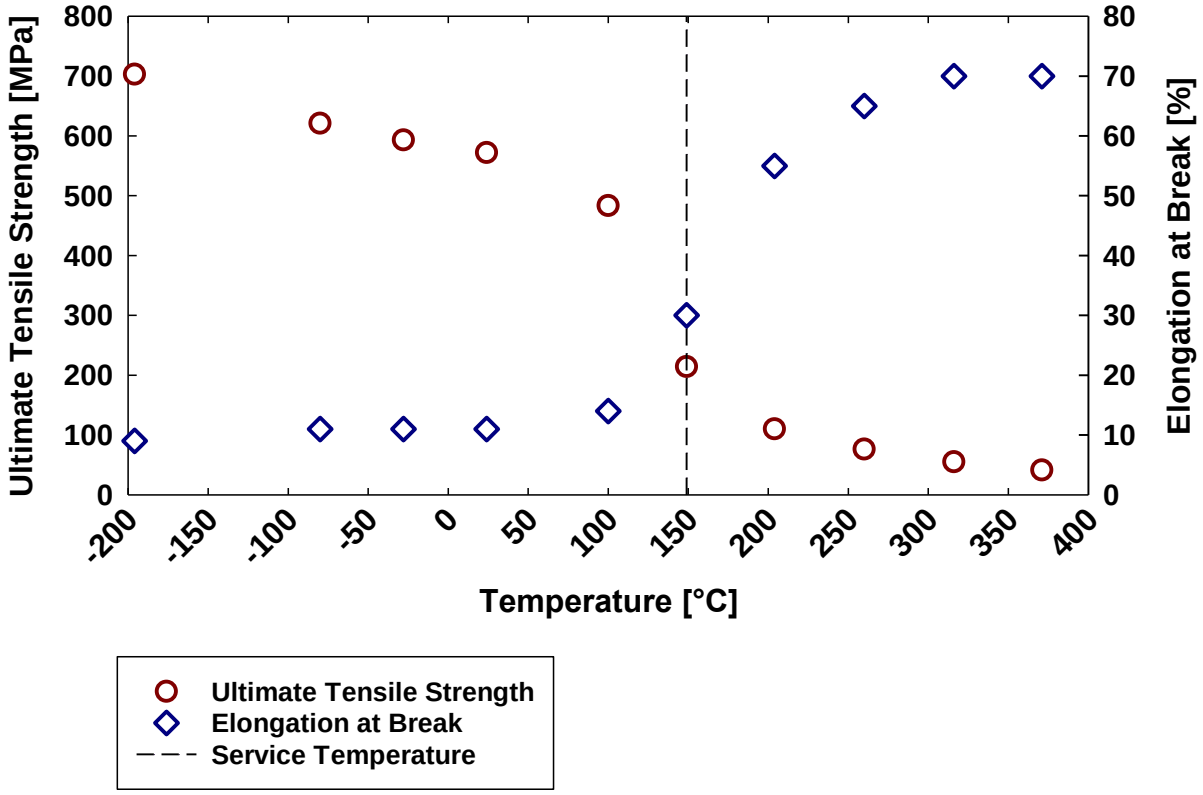

Figure G-1. Properties of 7075-T6 aluminum evolving with temperature showing a change in the material behaviour around 149 °C.